THE UNIVERSITY OF CHICAGO

BEYOND THE STANDARD MODEL PHENOMENA: FROM MODEL BUILDING TO SEARCHES

A DISSERTATION SUBMITTED TO
THE FACULTY OF THE DIVISION OF THE PHYSICAL SCIENCES
IN CANDIDACY FOR THE DEGREE OF
DOCTOR OF PHILOSOPHY

DEPARTMENT OF PHYSICS

BY
WEN HAN CHIU

CHICAGO, ILLINOIS
AUGUST 2023

TABLE OF CONTENTS

LIST OF FIGURES

LIST OF TABLES

ACKNOWLEDGMENTS

I would like to thank my advisor Lian-Tao Wang for everything that he has done for me during the past six years. The countless conversations that I had with him has taught me how I should think about problems and provided me a better understanding of what it is like to work in this field (while still being very entertaining).

I would also like to thank the members of my thesis committee: Marcela Carena, Young-Kee Kim, and Dam T. Son.

I appreciate the mentoring that the many postdocs of the group had provided. These include (in no particular order): Emmanuel Stamou, Jia Liu, Xiaoping Wang, Da Liu, Yiming Zhong, Christina Gao (unoffically), Elina Fuchs, Mattias Schlaffer, Sungwoo Hong, Seth Koren, and Henning Bahl. Many thanks to all of my collaborators on both successful and unsuccessful projects. This includes many of the postdocs that I had previously listed, Zhen Liu, and Matthew Low. I appreciate the time they spent answering my many dumb questions presented to them at the most inconvenient times.

I would like to thank my many friends that made my time spent at grad school much more fun.

Many thanks to Stuart Gazes and various course instructors for making the many years that I spent teaching more enjoyable. I would also like to thank Mark Oreglia for offering me an administrative role which provided me with much needed teaching relief during my last two years as a graduate student.

Lastly, I would like to thank my family for their support throughout this program.

ABSTRACT

The Standard Model (SM) of particle physics is an effective theory for describing the interactions of fundamental particles and their properties. In spite of countless experimental agreements with the predictions of the SM, we have good reason to believe that the SM is not a complete description of particle physics. This unknown description of particle physics which is beyond that of the SM is the focus of this dissertation.

We start by studying model-independent flavor non-universal UV effects at proton-proton colliders, low-energy flavor physics, and exotic Higgs decays. We then discuss the details of defining an arrival time for a jet to better search for long-lived particles which decay hadronically. Next, we study how an extended Higgs sector with an approximate $\mathbb{Z}_2$ symmetry can affect electroweak precision observables, collider experiments, and cosmology. Lastly, we study a framework for a dark matter model where the dark sector was described by an approximate conformal field theory at early times.

CHAPTER 1

INTRODUCTION

1.1 The Standard Model

1.1.1 Description of the Standard Model

The Standard Model (SM) is an anomaly-free, renormalizable, spontaneously broken gauge theory in 3 + 1 spacetime dimensions with the following symmetry breaking structure: $SU(3)_C \times SU(2)_L \times U(1)_Y \to SU(3)_Y \times U(1)_{EM}$. The gauge structure implies the existence of three types of massless vector fields; each in the adjoint representation of its corresponding gauge group. The particle content can be labeled by its representations under Lorentz, its representation under the gauge groups, and $U(1)_Y$ charge:

Field	Lorentz	$SU(3)_C$	$SU(2)_L$	$U(1)_Y$
Q_i	$(1/2, 0)$	**3**	**2**	$1/6$
u_i	$(0, 1/2)$	**3**	**1**	$2/3$
d_i	$(0, 1/2)$	**3**	**1**	$-1/3$
L_i	$(1/2, 0)$	**1**	**2**	$-1/2$
e_i	$(0, 1/2)$	**1**	**1**	-1
H	0	**1**	**2**	$1/2$

Table 1.1: The representations of the SM particle content labeled by the dimension of the representation and their hypercharges. The index $i = 1, 2, 3$ labels the generation of the particle

In addition to minimal coupling to the gauge sector, the SM contains Yukawa interactions and a Higgs potential

$$\mathcal{L} \supset -(y^u_{ij}\bar{u}_i\tilde{H}Q_j + y^d_{ij}\bar{d}_iH^\dagger Q_j + y^e_{ij}\bar{e}_iH^\dagger L_j + \text{h.c}) - V(|H|^2), \tag{1.1}$$

where

$$\tilde{H} = i\sigma_2 H, \quad V(|H|^2) = -\mu^2|H|^2 + \lambda|H|^4. \tag{1.2}$$

The tachyonic mass in the Higgs potential implies an instability near $H = 0$ and that the true ground state of the potential is at

$$|H|^2 = \mu^2/(2\lambda) \equiv v^2. \tag{1.3}$$

Without loss of generality, we can parametrize the components of the vacuum excitations of the Higgs field as

$$H \doteq \begin{pmatrix} \phi^+ \\ \frac{1}{\sqrt{2}}(v + h + i\phi^0) \end{pmatrix}. \tag{1.4}$$

For perturbations about this minimum, the original $SU(2)_L \times U(1)_Y$ subgroup of the SM is realized non-linearly. A $U(1)_{EM}$ subgroup of $SU(2)_L \times U(1)_Y$ is still realized linearly and is identified with the $U(1)$ corresponding to electromagnetism. The electromagnetic charge is a linear combination of its $SU(2)$ weight and $U(1)_Y$ charge. In addition, the originally massless gauge fields and chiral fermions gains mass terms. By diagonalizing these masses, we obtain the fields which corresponds to the physical quarks[1], leptons, W boson, Z boson, and photon. Due to the fact that there are separate left and right rotations in the quark sector across generations, there is physical mixing in the mass basis mediated by charged currents. This is characterized by the Cabibbo-Kobayashi-Masukawa (CKM) matrix.

A well known fact about the Standard Model is that the couplings for the Yang-Mills fields are asymptotically free [12]. For the weak interaction, due to the heavy mediators, this fact does not affect our ability to perform perturbative calculations at low energies. However, this is not true for the strong interaction. It is observed that low energy quantum chromodynamics (QCD) results in confinement; quarks and gluons form color-singlet bound states. This means that the external states in scattering experiments are hadrons and glueballs[2]. To perform perturbative calculations at low-energies, it was realized that

---

[1] Here, I'm using physical in a very loose sense.

[2] Glueballs have not been discovered experimentally as of writing.

confinement generates a non-zero vacuum expectation value for the quark condensate $\bar{q}q$. This in turn spontaneously breaks the approximate[3] chiral symmetry of the three lightest quarks: $SU(3)_L \times SU(3)_R \to SU(3)_V$. The pseudo-Nambu-Goldstone bosons corresponding to this symmetry breaking pattern is identified with the mesons. The low-energy baryonic degrees of freedom can be classified under its representation under Lorentz, $SU(3)_V$, and its $U(1)_{EM}$ charge.

1.1.2 (Un)Effectiveness of the Standard Model

Using the above model and 19 precisely measured experimental inputs, one can calculate various low-energy observables and differential cross sections corresponding to various scattering experiments. For the most part, there have been no experimental results within the Standard Model's prediction power that were significantly different from the Standard Model's prediction (*i.e.* $> 5\sigma$).

There are a handful of anomalies in experimental results. A subset of these include: the anomalous value of the muon anomalous magnetic moment, excesses in the KOTO experiment, and the CDF-II measurement of the W boson mass [13, 14, 15]. These experimental anomalies, if confirmed, could be an indication of physics beyond the Standard Model. This can be used as a motivation for building new models. An example in which we build a model to explain the W-mass anomaly is given in Chapter 4.

While experimental anomalies provide motivations for very particular BSM models, they are not the main reason why particle theorists are certain that the Standard Model of particle physics is incomplete. Below are a list of experimental observations that physicists are highly confident in that, if true, necessitates physics beyond the Standard Model.

- **Neutrino masses** The Standard Model only includes degrees of freedom which exists in nature. As we have yet to observe right-handed neutrinos, there is no mass term for

---

[3] This is exact in the massless limit.

neutrinos in the SM. However, the observation of neutrino oscillations indicates that at least two of the three known neutrino species have non-zero masses [16].

- **Matter-antimatter asymmetry** In the observable universe, it is an empirical fact that there is more matter than antimatter. This asymmetry can be produced in the early universe as long as there are processes which satisfy the Sakharov conditions [17]. While the SM does contain processes which satisfies the Sakharov conditions, it cannot generate a sufficiently large asymmetry.

- **Dark matter** There are copious indirect evidence for the existence of dark matter. This includes explaining galactic rotation curves, lensing observations, and large scale structure formation. Observationally, dark matter does not interact very strongly with baryons and structure formation necessitates cold dark matter. As such, none of the particles in the Standard Model can account for 100% of dark matter. Details on popular dark matter candidates and production mechanisms will be discussed later.

When modeling the effects of BSM on existing and future measurements, it is important to know whether or not new particles exists at the scale of the measurement. While the null result of various Large Hadron Collider (LHC) searches may seem to indicate that the answer is no, it is entirely possible that existing search strategies may completely miss the signal. In that case, it is imperative that new ideas are implemented to make full use of the High-Luminosity Large Hadron Collider (HL-LHC) dataset. The existing detectors at the LHC have been upgraded for the high luminosity run and other detectors have been added. An example of a strategy to improve sensitivity to long-lived particles which decay hadronically is provided in Chapter 3.

If there are indeed no new particles at the energy scale of a given experiment which contributes directly to said measurement, then the effects of ultraviolet (UV) physics can be effectively captured by treating the SM as an effective field theory. From the top-down point of view, an effective field theory is obtained when UV modes are integrated out of the path integral. This process has two effects. Firstly, it induces threshold corrections to relevant parameters of the theory (*e.g.* the Higgs mass parameter when a heavy scalar is integrated out). Secondly, it generates an infinite set of irrelevant operators suppressed by inverse powers of the heavy scale with known coefficients. Due to this scale suppression, operators which are more irrelevant will contribute less to a given physical observable than those that are less irrelevant.

As we generically do not know the underlying UV model, one typically takes a bottom-up approach. We augment the Standard Model with all possible gauge invariant irrelevant operators with unknown coefficients and unknown scale. Due to the scale suppression, it is generally sufficient to only include the leading irrelevant operator which contributes to a given observable. Due to the consistency of the SM predictions with experiments, any effects these irrelevant operators have on physical observables must be smaller than the experimental uncertainty. This allows us to impose constraints on the unknown coefficients and scale. An example exploring the reach of this unknown scale at HL-LHC and future colliders from flavor non-universal models is given in Chapter 2.

1.2 Dark Matter

In a previous section, we had briefly outlined the empirical evidence for the existence of dark matter. We will now review what we know about dark matter based on experimental results. We will start by going into detail about the evidence supporting the existence of dark matter before discussing constraints on its properties.

The initial evidence for dark matter originated in the mid 1900s when various physicists noted that the velocity of stars as a function of distance from the center of their host galaxy is much larger than expected based on the amount of luminous matter [18]. This suggested either the presence of non-luminous matter or Newtonian gravity is modified on galactic scales.

The latter hypothesis became disfavored with the observation of the bullet cluster. In this observation, the amount of baryonic matter from the two colliding galaxy clusters were measured by the light emitted by stars and scattering of gas. Gravitational lensing was used to determine the total mass distribution as throughout the collision event. The lensing observations are most easily modeled by the inclusion of additional non-luminous matter that scatters weakly with baryons and itself. This observation is used to set limits on dark matter self-interactions to $\sigma/m < 1 \text{ cm}^2/\text{g}$ [19].

In addition to astrophysical observations, cosmology also heavily favors the existence of dark matter. The cosmic microwave background (CMB) is a largely isotropic bath of thermal photons with $T \approx 2.7$ K believed to be from the surface of last scattering at recombination (when the expected thermal energy of electrons is insufficient to overcome the binding energy of hydrogen). This temperature can be used to infer how long ago recombination occurred. At this time, the over-densities of baryons and photons are largely correlated due to them initially being in equilibrium. One can then evolve the baryon over-densities under GR to determine when large scale structure could have formed under the hypothesis that baryons comprised a majority of matter in the universe. What one finds is that the earliest observed galaxies and large scale structure could not have possibly formed at the observed time. This implies the existence of additional matter that do not interact with photons to aid in structure formation. The size of large scale structure has been used to constrain the free-streaming length of dark matter in the early universe.

Using these early universe observations, one can perform fits to various cosmological models. Using PLANCK data, it was found that the standard model of cosmology, ΛCDM, fits extremely well and the cold dark matter makes up roughly 23% of the current energy density of the universe[20]. Based off of the dynamics of the Milky Way and the solar system's position in the galaxy, one can infer that the local dark matter density is roughly

$\rho_{\text{DM, local}} \sim 0.4$ GeV cm^{-3} [21].

If dark matter has some non-gravitational interactions with standard model particles, then this can in principle be detected via scattering with the local dark matter. The null result of various direct detection experiments have been used to set bounds on dark matter interaction with nucleons and electrons for dark matter masses comparable to their masses. For dark matter candidates with masses lighter than $\mathcal{O}$(keV), stars place stringent bounds on how strongly dark matter can interact with electrons. For lighter dark matter candidates, the Migdal effect can be used to constrain the interaction strength with electrons [22, 23].

Stars contain a high density of high energy electrons. If electrons have a non-zero coupling to dark matter, these high energy electrons can radiate dark matter. As dark matter is unlikely to scatter with electrons, they can free stream from the core to surface; contributing to anomalous cooling of stars.

1.2.1 Dark matter models

In addition to the model independent constraints, a dark matter model should contain both a stable/cosmologically long-lived dark matter candidate and a population mechanism for generic initial conditions. Here, I will list a sample of models and their population mechanism. I will also include references studying model-specific constraints.

- WIMPs are a class of dark matter models with weak scale masses (i.e. $\sim \mathcal{O}$(TeV)) and couplings populated by thermal freeze-out. A common WIMP candidate is the lightest supersymmetric particle (LSP) in a supersymmetric theory with R-parity. Generic WIMP models with weak scale couplings to nucleons and electrons are highly constrained by direct detection experiments. However, there are still various WIMP models that are still viable.[24, 25, 26]

- Fuzzy dark matter corresponds to dark matter candidates with mass $\sim \mathcal{O}(10^{-20}$ eV). From the light mass, cold fuzzy dark matter necessarily has very high number densities.

This generically rules out fermionic fuzzy dark matter candidates [27]. Common candidates include ultra-light axions, scalars, and dark photons. Fuzzy dark matter generally has the constraint that they cannot be produced via a thermal process. A common production mechanism is known as misalignment [28]. [29, 30, 31, 32, 33, 34, 35, 36, 37, 38]

- MACHOs are a class of non-particle dark matter. They generically include any form of dim or non-luminous astronomical object. One popular MACHO candidate are primordial black holes. They can be produced from overdensities in the early universe. From observations, only PBHs with mass $\sim 10^{-13}\ M_\odot$ or $\sim 10^{15}\ M_\odot$ can account for 100% of DM without being already ruled out [39]. [40]
- Freeze-in is a process in which dark matter is populated without ever being in thermal equilibrium. This is ensured by having a negligible initial population of dark matter and tiny portal coupling to the Standard Model. [41, 42]
- A list of other possible dark matter models and their corresponding constraints can be found in Refs. [43, 44, 45, 46, 47, 48, 49]

The above list provides a set of simplified models for experimentalists to target in their searches. However, an important question is whether they can be realized in a UV theory and whether or not the IR observables are sufficient to fully specify the model's predictions. In chapter 5, we will explicitly construct a framework for a UV model which sets up freeze-in while having very different predictions.

1.3 General model building considerations

In addition to empirical evidence of phenomena not explained by the Standard Model, there remains the question of what sets the free parameters of the Standard Model. When building a UV BSM model, one would ideally like to also address this. The question pertaining to the free parameters of the SM can be classified into the following:

- **Electroweak hierarchy problem** The mass of the Higgs boson is observed to be approximately 125 GeV. When integrating out massive degrees of freedom from a UV theory which couples to the Higgs, the Higgs mass parameter receives threshold corrections proportional to the square of the mass of the particle being integrated out [50]. If such a massive particle exists, then the Higgs mass parameter appears to be unnaturally small. Is there a mechanism which sets the Higgs mass to what we observe? There are two very popular classes of models which tries to address this. The first are composite Higgs models where the Higgs mass is set by an RG fixed-point rather than some relevant parameter in the Lagrangian that get corrected quadratically. The other is supersymmetry where additional scalar/fermionic partners are introduced to cancel the corresponding threshold correction.

- **Strong CP problem** The θ parameter parameterizes different Yang-Mills vacua which are topologically distinct. This choice of the Yang-Mills vacuum can be incorporated into the SM Lagrangian by introducing the θ-term: $\theta\text{tr}(G\tilde{G})$. A linear combination of θ and the phase of the Yukawa matrices (known as $\bar{\theta}$) characterizes the physical CP violation in the strong sector. From measurements of the neutron electric dipole moment, it can be inferred that $|\bar{\theta}| < 10^{-10}$. If these two are the only contributions to $\bar{\theta}$, then the supposedly free parameter θ is very close to the phase of the Yukawa matrices. Is there a physical mechanism which makes it so? Classes of solutions include spontaneous CP breaking (Nelson-Barr models) and the QCD axion.

- **Flavor problem** In the SM, we see a hierarchy of masses of the fermions across the generations. In addition, there also appears to be a hierarchy in terms of the mixing across generations. Is there a physical mechanism which generates this observation?

- **Grand unification** In the SM, the electromagnetic force and weak force unify. Does the electroweak force unify with the strong force as well at higher energies? If so, what is the underlying structure? Well known examples of GUT theories include $SO(10)$, $SU(5)$, and $SU(4) \times SU(2) \times SU(2)$. Recently, from the analysis of the (approximate) flavor symmetry in the Standard Model, it was proposed that there are only four possible embeddings [51].

1.4 Outline of the thesis

The outline of this thesis is as follows. Chapter 2 contains a study on an EFT description of models which affect the quark sector in a non-universal manner. In this study, we studied the reach of future hadron colliders have on these models. Chapter 3 contains a study on how best to define the arrival time of a jet in the context of displaced trackless jets in searches for long-lived particles. Chapter 4 studies a model in which the Standard Model has an additional Higgs in the $j = 1$ representation of $SU(2)_L$. In this extension, there is an approximate $\mathbb{Z}_2$ symmetry. Chapter 5 studies a model in which the dark sector is described by a conformal field theory during its production. In this study, we also show how the initial condition of freeze-in can be realized within this framework.

CHAPTER 2

EFT ANALYSIS OF FLAVOR MODELS

A large portion of this chapter is reprinted with permission from:

Wen Han Chiu, Zhen Liu, and Lian-Tao Wang. Probing flavor nonuniversal theories through Higgs physics at the LHC and future colliders. Phys.Rev.D 101 (2020) 3, 035045.

2.1 Introduction

The Standard Model (SM) is often perceived as complete with the discovery of the Higgs boson in 2012 [52, 53]. Below the electroweak (EW) scale, the predictive power of the SM is immense. It provides a mechanism for elementary particles to obtain masses and accurately predicts the rates of particle scattering. However, many puzzles remains to be explained. These include the origin of the electroweak scale and the flavor structure of the SM. These puzzles indicate the existence of new physics (NP) beyond the Standard Model (BSM).

For any BSM model, once all massive BSM particles above the EW scale have been integrated out, their effects will be encoded in the Wilson coefficients of higher-dimensional operators involving SM particles. In a flavor-universal theory, there is one dimension-5 operator and 59 dimension-6 operators up to hermitian conjugation [54]. For most processes accessible at colliders, the leading order correction to the SM is dimension-6.

The Higgs doublet is present in a large number of these operators. Hence, the constraint on the new physics scale, Λ_{NP}, is typically associated with processes involving either the Higgs or the longitudinal modes of the massive gauge bosons. These constraints can be obtained from future Higgs factories, where very clean measurements can be performed. Even in the scenario of cancellations among operators, it is still possible to probe new physics up to $\mathcal{O}(10)$ TeV [55, 56, 57, 58, 59, 60, 61, 62, 63, 64, 65].

In many of these existing studies and analyses of the Higgs physics at current and future colliders, they tend to focus on universal theories. Especially those involving electroweak precision observables (EWPO). However, in general, most BSM theories have couplings in which the third generation and the first two generations can be considerably different. These include models such as supersymmetry, composite Higgs, as well as quark flavor models [66, 67, 68, 69, 70, 71, 72, 73, 74, 75].

The constraints from LEP measurements on such new physics scenarios are rather weak. By comparison, the high center-of-mass energy at the Large Hadron Collider (LHC) leads to an enhancement of the new physics effect which scale with a higher power of energy compared to the background [76, 77, 78, 79, 80, 81, 82]. This can be further enhanced at future hadron colliders at higher energies, such as the 27 TeV high energy upgrade to the LHC [82, 83], and a pp collider in a 100 km tunnel with possible beam center of mass energy at 37.5 TeV [84, 85] and 100 TeV [86, 87, 84]. Moreover, the hadronic initial states imply good constraints on light-quark operators by virtue of high statistics from the parton distribution function (PDF). Hence, these hadronic colliders are the best place to search for flavor universality violations. In particular, for operators which modify the couplings between the first generation of quarks associated with the Higgs boson.

In this work, we will focus on probing flavor non-universal theories. We will present results involving the first generation up-type flavor operators, which generally has the best sensitivities at proton-proton colliders. The result can be extended to other operators via the appropriate parton luminosity rescaling and also possibly via the final state selection.

The structure of this chapter is as follows: in Sec. 2.2, we will introduce the new physics scenario we are considering in this chapter. In Sec. 2.3, we will present the projected constraints at both the High Luminosity (HL) LHC and potential future hadron colliders. The possible existing constraints from flavor physics will be discussed in Sec. 2.4. The complementarity of this study with exotic Higgs decay will be discussed in Sec. 2.5 and lastly, we will conclude.

2.2 Flavor non-universal scenario

The flavor non-universal operators in the Warsaw basis associated with the first generation are listed in Table 2.1 [54].

Operators
$\mathcal{O}_{Hu} = (iH^\dagger \overset{\leftrightarrow}{D}_\mu H)(\bar{u}_R \gamma^\mu u_R)$
$\mathcal{O}_{Hd} = (iH^\dagger \overset{\leftrightarrow}{D}_\mu H)(\bar{d}_R \gamma^\mu d_R)$
$\mathcal{O}^{(1)}_{HQ} = (iH^\dagger \overset{\leftrightarrow}{D}_\mu H)(\bar{Q} \gamma^\mu Q)$
$\mathcal{O}^{(3)}_{HQ} = (iH^\dagger \sigma^a \overset{\leftrightarrow}{D}_\mu H)(\bar{Q} \gamma^\mu \sigma^a Q)$

Table 2.1: The set of operators with an energy-enhanced contribution to the $pp \to Vh, VV$ amplitudes.

These operators can be classified using the so-called high energy primaries associated with a given diboson process [80, 88]. These are the coefficient of the term in the relevant diboson process's signal-to-background ratio with the largest energy scaling behavior. Hence, these are the primary observable in the high-energy limit. So if one wishes to constrain new physics using a diboson process at a hadron collider in a general EFT setup, the leading results in new physics constraints should be associated with one of the operators in Table 2.1.

The Wilson coefficient of $\mathcal{O}_{Hu}$ is the high-energy primary associated with $f_R \bar{f}_R \to W^+_L W^-_L$ and $f_R \bar{f}_R \to Z_L h$. There are existing studies in both of these channels, though only the WW channel has been studied in the flavor non-universal scenario [89, 90]. For the operators $\mathcal{O}^{(1)}_{HQ}$ and $\mathcal{O}^{(3)}_{HQ}$, the contribution to the WW channel is enhanced relative to Zh due to the inclusion of the t-channel diagram. As a result, one can expect more stringent constraints on the Wilson coefficients of these operators from the WW process.

To determine the overall reach in the parameter space of non-universal models through

Zh production, we focus on the contribution of $\mathcal{O}_{Hu}$. The result of the other operators can be parameterized and derived in a similar manner.

To begin, the effective Lagrangian with dimension-6 operators involving up type quarks is

$$\mathcal{L} = \mathcal{L}_{\text{SM}} + \frac{c_{Hu}}{\Lambda^2}(iH^\dagger \overleftrightarrow{D}_\mu H)(\bar{u}_{R,i} g_{ij} \gamma^\mu u_{R,j}), \tag{2.1}$$

where i, j are flavor indices. For now we focus on the scenario in which the only nonzero coupling is $g_{uu} = 1$. Moving to the mass eigenstate basis, we get

$$\mathcal{L} \supset \frac{c_{Hu}}{\Lambda^2}(iH^\dagger \overleftrightarrow{D}_\mu H)(\bar{u}'_{R,i} U^\dagger_{R,ij} g_{jk} \gamma^\mu U_{R,kl} u_{R,l}), \tag{2.2}$$

where U_R is the unitary matrix which, alongside U_L, diagonalizes the mass matrix. Due to the small charm fraction in the parton distribution functions and the typical smallness of the off-diagonal terms of the rotation matrices in most flavor models, we expect their contributions to be negligible. Hence, we will neglect the contribution from the off-diagonal terms for the Zh process. Moving to the EW broken phase, we have

$$i(H^\dagger \overleftrightarrow{D}_\mu H) \supset -\frac{g}{2c_w}(v+h)^2 Z_\mu. \tag{2.3}$$

This interaction term gives us the relevant Feynman rules for Zh:

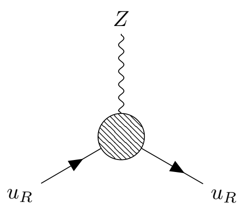

$$= -i\frac{gv^2}{2c_w}\frac{c_{Hu}}{\Lambda^2},$$

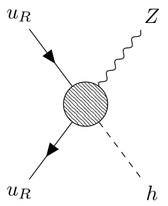

$$= -i\frac{gv}{c_w}\frac{c_{Hu}}{\Lambda^2} \tag{2.4}$$

where c_w and s_w (in later text) denote $\cos\theta_w$ and $\sin\theta_w$ of the Weinberg angle θ_w with $s_w^2 \simeq 0.23$, and g is the $SU(2)$ gauge coupling.

2.3 Detailed Analysis

To obtain projections on the sensitivities, one million $pp \to Zh$ events were generated in MG5_aMC with the operator implemented using a UFO file generated in FeynRules [91, 92, 93]. The Wilson coefficient normalized with a NP scale of 1 TeV, $c_{Hu}/\Lambda^2_{\text{TeV}}$, was varied from -1 to 1 in increments of 0.1. The data were then scaled to match the number of expected events for a given integrated luminosity. Next, the signal was split into bins of 150 GeV, matching roughly the energy resolution of the Zh system invariant mass over a large range. The number of signal events as a function of the Wilson coefficient was obtained by interpolation.

The SM background under 3 TeV was estimated using the 2017 ATLAS search on heavy resonances to Zh final state [94]. Above the 3 TeV threshold, the background was modeled by fitting the tail of the data to an exponential function, equivalent to a fixed selection efficiency for high invariant mass regions of the background.

Our signal Z and h with subsequent decays into dileptons and $b\bar{b}$ were multiplied by the corresponding decay branching fractions respectively, to match the final state of the ATLAS search. A $p_T > 300$ GeV cut and a $|\eta| < 2.5$ cut were applied to the Higgs. A universal cut efficiency was then imposed on the signal events to match the number of Standard Model events computed in the ATLAS search.

A binned likelihood test was performed by defining the significance, Z, of each bin as a function of the Wilson coefficients, e.g., $c_{Hu}/\Lambda^2_{\text{TeV}}$ for signal and background numbers of events of s and b, as

$$Z_i = \left[2\left((s+b)\ln\left[\frac{(s+b)(b+\delta_b^2)}{b^2+(s+b)\delta_b^2}\right] - \frac{b^2}{\delta_b^2}\ln\left[1+\frac{\delta_b^2 s}{b(b+\delta_b^2)}\right]\right)\right]^{1/2}, \tag{2.5}$$

where δ_b is the uncertainty [95]. The 2σ constraint up to a given center-of-mass energy, $\sqrt{\hat{s}}$, was computed by adding the significance of bins with $m_{Zh} < \sqrt{\hat{s}}$ in quadrature and solving for $\sum_i Z_i^2(c_{Hu}/\Lambda^2_{\mathrm{TeV}}) = 4$.

When calculating the sensitivities for future hadron collider, signal events were obtained in the same manner as the HL-LHC calculation. For the background, a differential rescaling was performed by computing the ratios of the parton luminosity at each mass bin using ManeParse 2.0 [96] and the NNPDF23_nlo PDF set [97] yielding a background estimate for $\sqrt{\hat{s}} < 14$ TeV. As the effective theory is only well-defined for energy scales below the cut-off, our constraints are physically meaningful if $\hat{s} < \Lambda^2$. Hence, only bins with $\hat{s} < \Lambda^2$ will be used in calculating the sensitivities.

For the uncertainty used in our analysis, a 5% universal systematic and statistical uncertainty was assumed. However, it should be noted that for bins with larger invariant masses, the theoretical uncertainty from the choice of factorization scale increases. This increase of uncertainty can be estimated by performing the analysis with the factorization and normalization scale set to be 0.5, 1, and 2 times m_T^2, where, m_T is the transverse mass of the system. We show the sensitivity to the new physics scale with these different choices of the scales in Fig. 2.1. The scale dependence of our sensitivity as discussed earlier, grows with center of mass energy, up to roughly 3% with the Zh center of mass energy at 4 TeV.

To take the scale dependence into account, we assumed the per bin PDF uncertainty is Gaussian and defined it as:

$$\delta_{\mathrm{PDF},i} = \frac{1}{2}\Big(\Big|n_i^{\frac{Q^2}{m_T^2}=1} - n_i^{\frac{Q^2}{m_T^2}=0.5}\Big| + \Big|n_i^{\frac{Q^2}{m_T^2}=1} - n_i^{\frac{Q^2}{m_T^2}=2}\Big|\Big), \tag{2.6}$$

where n_i is the number of events in the ith bin after imposing the appropriate cuts. This was added to our systematic uncertainty linearly.

The 95% C.L. sensitivity for the benchmark Wilson coefficient, $c_{Hu} = 1$, including the PDF uncertainties, are given in Fig. 2.2. Constraints on new physics scales up to about 3.3 TeV can be obtained for HL-LHC, 7.3 TeV for HE-LHC, 9.2 TeV for a 37.5 TeV FCC-hh, and 17.8 TeV for a 100 TeV FCC-hh.

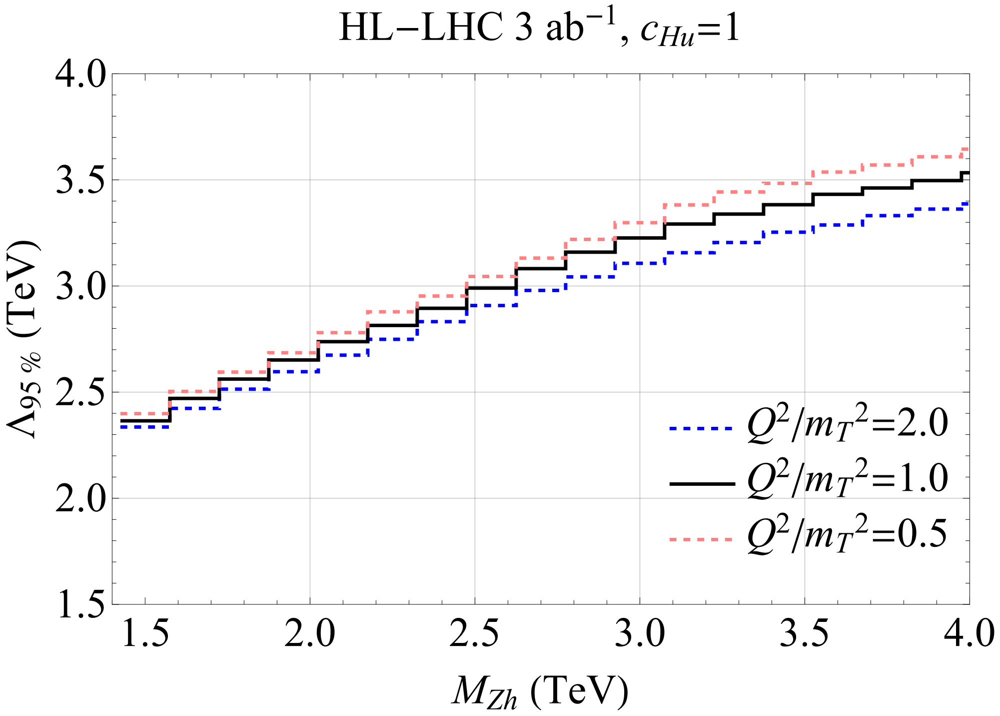

Figure 2.1: The effects of changing the scale factor on the constraints from HL-LHC with a reference value of $c_{Hu} = 1$.

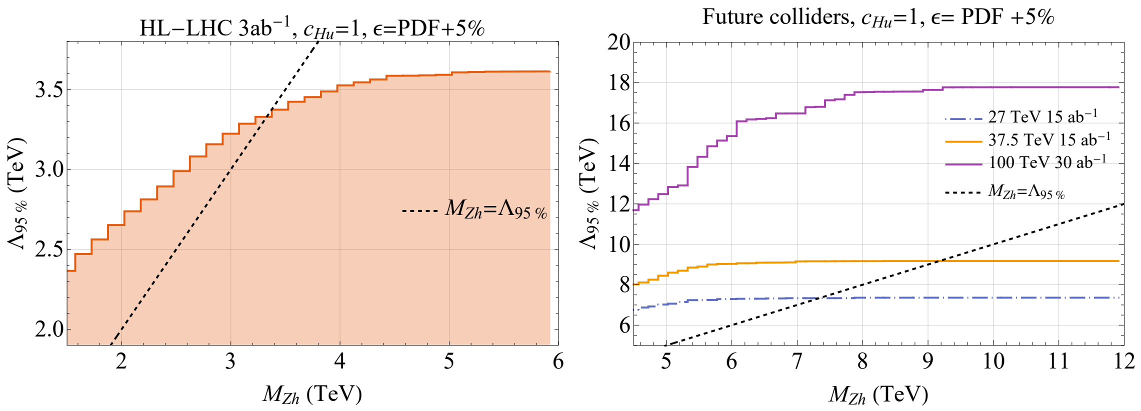

Figure 2.2: The constraints on the scale of new physics including PDF uncertainties probed by HL-LHC (left) and potential future hadron colliders (right) using the benchmark point of $c_{Hu} = 1$.

For regions of parameter space beyond our benchmark point, we redid the calculations with different values of c_{Hu}. The regions of parameter space that can be probed are given in Fig. 2.3. For comparison, the constraints from a corresponding lepton collider were also included in the plot. The LEP constraints were obtained by looking at the shift in

$g_R^{Z,u}$ induced by our operator and fitting to the number provided in Ref. [98]. The CEPC projections were obtained from Ref. [65], assuming flavor universality. This assumption will result in a more optimistic estimate as the EWPO will also receive contributions from the other generations. In addition, we also include the reach from $pp \to WW$ for HL-LHC by translating the constraint on $g_R^{Z,u}$ into a constraint on c_{Hu}/Λ^2 [89]. From the figure, we can see that Zh production is indeed competitive to other direct and indirect probes over a large range of parameter space.

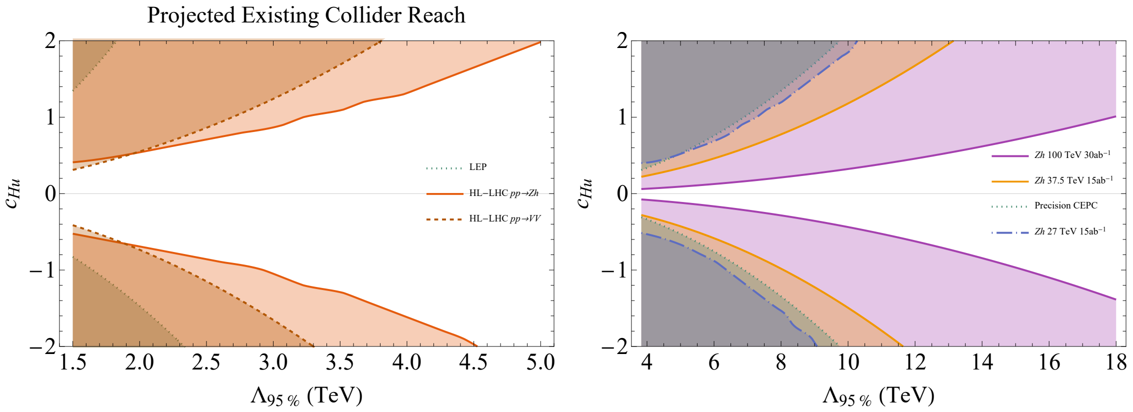

Figure 2.3: The constraints on the scale of new physics for models with different values of c_{Hu} which can be probed by Higgsstrahlung at HL-LHC (left) and potential future hadron colliders (right) using only bins satisfying $\hat{s} < \Lambda^2$. For comparison, the existing constraints from LEP and the reach from diboson at HL-LHC was also included for the HL-LHC plot while a next generation lepton collider reach was included for the future collider plot.

To ensure that neglecting dimension-8 operators is well justified, its contribution must be small relative to the dimension-6 operators. First, we can compute the change in the invariant matrix element in powers of $\hat{s}$.

$$\frac{\Delta|\overline{\mathcal{M}}|^2}{|\overline{\mathcal{M}}_{\text{SM}}|^2} = \frac{s_w^4 c_w^2}{e^2(32s_w^4 - 24s_w^2 + 9)} \left(144 \frac{c_w^2}{e^2} \frac{c_{Hu}^2}{\Lambda^4} \hat{s}^2 + 96 \frac{c_{Hu}}{\Lambda^2} \hat{s} \right), \tag{2.7}$$

where e is the electric coupling constant around 0.3.

Noting that the coefficient of the quadratic piece is an order of magnitude larger than the linear piece, the contribution from $|\mathcal{O}_{d=6}|^2$ will dominate once $c_{Hu}\hat{s}/\Lambda^2 \gtrsim \mathcal{O}(0.1)$. Given the same suppression of Λ^4, the contribution from dimension-8 operators should be estimated as well.

As dimension-8 operators do not generate any new vertices which contribute to Zh production at tree-level, they contribute by modifying the vertex factors in Eq. (2.4). So one can estimate the leading contribution by taking the linear piece in Eq. (2.7) and replacing

$$c_{Hu} \to c_{Hu} + \sum_{i,j} a_i c_{i,j} \frac{p_i \cdot p_j}{\Lambda^2}, \tag{2.8}$$

where the i, j indices denote the different legs in the Feynman diagram and a_i is some $\mathcal{O}(1)$ number.

So, in models where the Wilson coefficients of the dimension-8 operators are less than or comparable to the dimension-6 operators, the leading contribution from dimension-8 are estimated to be smaller than dimension-6 and dimension-6 squared. In cases where dimension-8 operators Wilson coefficients being larger than dimension-6, one should view our constraints as those on a given linear combination of the Wilson coefficient of dimension-6 and dimension-8 that can be absorbed into the dimension-6 operators. For instance, dimension-8 operators derived with additional $H^\dagger H$ insertions to the dimension-6 operators can be captured by redefining the dimension-6 operators' coefficients concerning the Zh process considered in this work. The estimation of the sensitivity to new physics scale Λ for Wilson coefficient of order unity remains the same.

2.4 Flavor physics constraints

The type of flavor models that we are looking at may have non-trivial constraints from flavor changing neutral currents (FCNC). This is due to the presence of flavor-mixing terms in the Lagrangian in the mass eigenbasis. The dominant constraint on up-type flavor mixing is through charm-number violating processes, in particular from $D_0 - \bar{D}_0$ mixing [99]. In order to have a rough estimate of what region of parameter space has been ruled out by existing measurements, we computed the leading order contribution from our operator.

From Eqs. (2.2) and (2.3), the operator which directly contributes to FCNC via $D_0 - \bar{D}_0$ mixing is

$$\mathcal{L}^{\Delta C=1} = -\frac{c_{Hu} M_Z v}{\Lambda^2} Z_\mu \bar{u}_R \gamma^\mu c_R (U^\dagger_{R,uu} U_{R,uc}).$$

Integrating out the Z propagator gives the effective operator:

$$\mathcal{L}^{\Delta C=2}_{\text{eff}} = 3\left(\frac{c_{Hu} v}{\Lambda^2}(U^\dagger_{R,uu} U_{R,uc})\right)^2 \bar{u}_R \gamma^\mu c_R \bar{u}_R \gamma_\mu c_R.$$

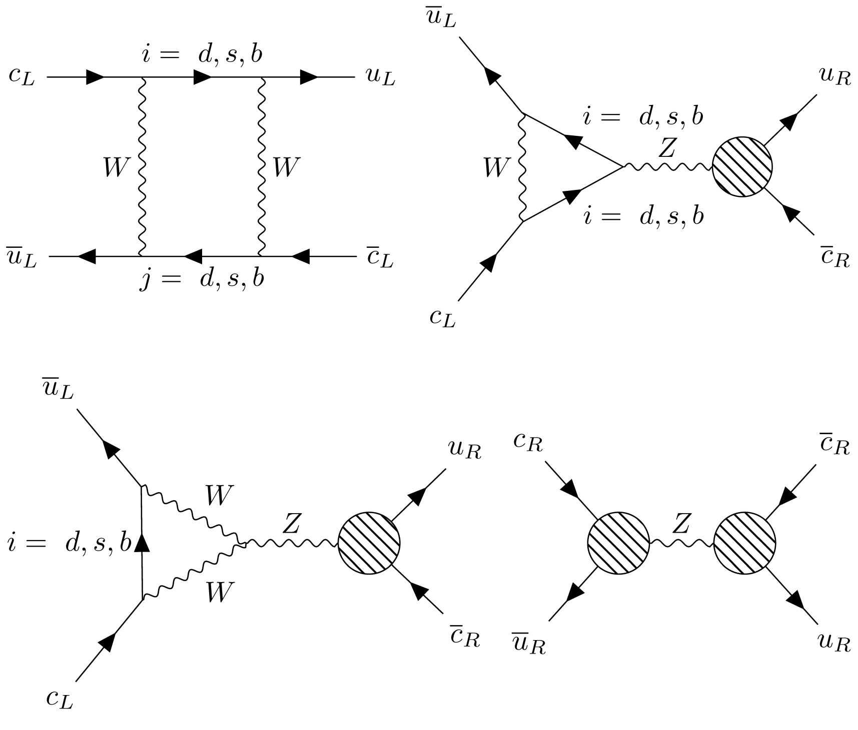

Figure 2.4: A subset of diagrams which contribute to $D_0 - \overline{D_0}$ mixing at leading order to illustrate the parametric dependence for each $\Delta C = 2$ effective operators.

From Fig. 2.4, it can be seen that at dimension-6, SM process contributes to the operator $\bar{u}_L \gamma^\mu c_L \bar{u}_L \gamma_\mu c_L$ while the SM-EFT cross terms contributes to operators of the form

$\bar{u}_L c_L \bar{u}_R c_R$. Thus, the leading contribution to the operator $\bar{u}_R \gamma^\mu c_R \bar{u}_R \gamma_\mu c_R$ is the EFT only term. The Wilson coefficient of this operator has been constrained in [99] using a global fit with all possible low-energy dimension-6 operators. As such, this should be viewed as a conservative estimate of the current constraint. Assuming that only our operator contributes to the observables used to derive these constraints, we obtain

$$3 \left| \frac{c_{Hu} v}{\Lambda^2} (U^\dagger_{R,uu} U_{R,uc}) \right|^2 \lesssim 5.7 \times 10^{-7} \left(\frac{1}{1 \text{ TeV}} \right)^2 . \tag{2.9}$$

This gives us a constraint on the Wilson coefficient of the operator that depends on the flavor model of interest. As a benchmark model (benchmark theory 1), suppose that $|U^\dagger_{R,uu} U_{R,uc}| = |V_{ud} V_{cd}|$, we get

$$\Lambda / \sqrt{c_{Hu}} \gtrsim 11 \text{ TeV}. \tag{2.10}$$

In addition, one could consider constraints from the operator $\bar{u}_L c_L \bar{u}_R c_R$. The dominant contribution comes from the bottom quark, so Wilson coefficient is on the order of

$$\begin{aligned} &\sim \frac{v^2}{M_Z^2} \frac{M_b^2}{M_W^2} \frac{1}{16\pi^2} \frac{c_{Hu}}{\Lambda^2} |V_{ub}| |V_{cb}| (U^\dagger_{R,uu} U_{R,uc}) \\ &\lesssim 1.6 \times 10^{-7} \left(\frac{1}{1 \text{ TeV}} \right)^2 . \end{aligned} \tag{2.11}$$

The constraints on our Wilson coefficient from this operator in benchmark theory 1 is $\Lambda / \sqrt{c_{Hu}} \gtrsim 0.16$ TeV, clearly weaker than the previous one.

These flavor constraints appear to be very strong in a generic flavor violating theory. However, we can consider models where the operator under considerations applies to the first two generations universally, maintaining a $U(2)^2$-flavor symmetry in the quark sector (benchmark theory 2). These types of models can be motivated due to the large mass gap between the second and third generation [74, 75]. In this scenario, $g_{ij} = \text{diag}(1, 1, 0)$. The

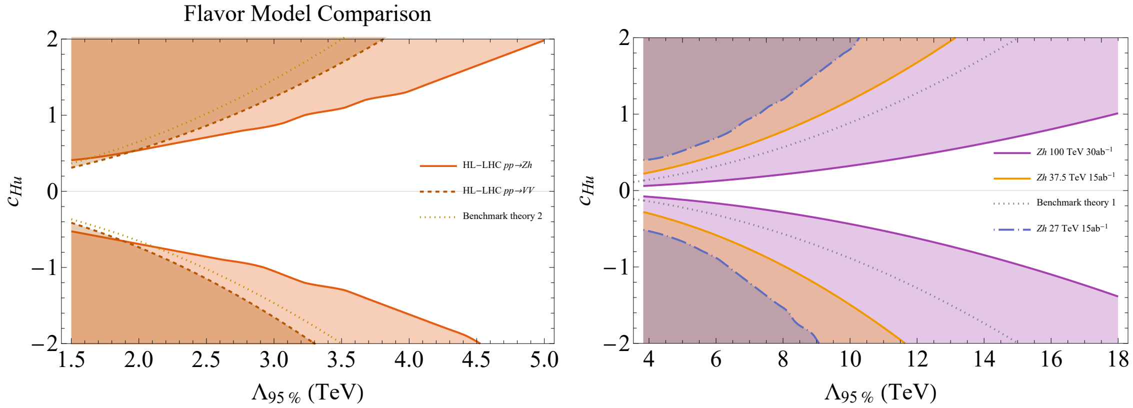

Figure 2.5: The flavor constraints (unfilled, dotted curves) plotted on top of the HL-LHC (left) and potential future hadron collider (right) constraints. Benchmark theory 1 refers to the fully flavor non-universal theory with the choice of $|U^\dagger_{R,uu}U_{R,uc}| = |V_{ud}V_{cd}|$. Benchmark theory 2 refers to the theory which is universal across the first 2 generations with a similar choice for the right-handed rotations.

LHC constraints are not expected to change by much due to the limited charm fraction in the large x region. In the mass eigenstates, we now have

$$\mathcal{L}^{\Delta C=1} \to -\frac{c_{Hu}M_Z v}{\Lambda^2} Z_\mu \bar{u}_R\gamma^\mu c_R \left(U^\dagger_{R,uu}U_{R,uc} + U^\dagger_{R,uc}U_{R,cc}\right).$$

As U_R is unitary, the term in the parenthesis is equal to $-U^\dagger_{R,ut}U_{R,tc}$. Due to the smallness of the corresponding CKM elements, this quantity is naturally small in most flavor models. This relaxes the constraints given by Eq. (2.9) by a factor of about $\mathcal{O}(10^{-3})$ for a similar benchmark point and hence relax the constraints on the Wilson coefficient to be

$$\Lambda/\sqrt{c_{Hu}} \gtrsim 0.4 \text{ TeV}. \tag{2.12}$$

The $U(2)$-flavored quark sectors also modifies $\Gamma(Z \to c\bar{c})$; which has been measured to about 1.6% accuracy [100]. In the small charm mass limit, the fractional change in the $Z \to c\bar{c}$ width is given by:

$$\frac{\Delta\Gamma(Z\to c\bar{c})}{\Gamma(Z\to c\bar{c})} \approx \frac{2g_R\Delta g_R}{g_L^2+g_R^2} \approx -0.0615\frac{c_{Hu}}{\Lambda^2_{\text{TeV}}} \tag{2.13}$$

For comparison, constraints for the benchmark flavor models were plotted on top of the collider constraints. From Fig. 2.5, the reach from WW production is comparable to the region ruled our by FCNCs for the partial universal theory (benchmark theory 2). Higgsstrahlung at a 37.5 TeV pp collider with 15 ab^{-1} of integrated luminosity is comparable to the region ruled out by existing FCNC measurements for the fully flavor non-universal theory (benchmark theory 1).

2.5 Complementarity to Higgs Exotic Decay

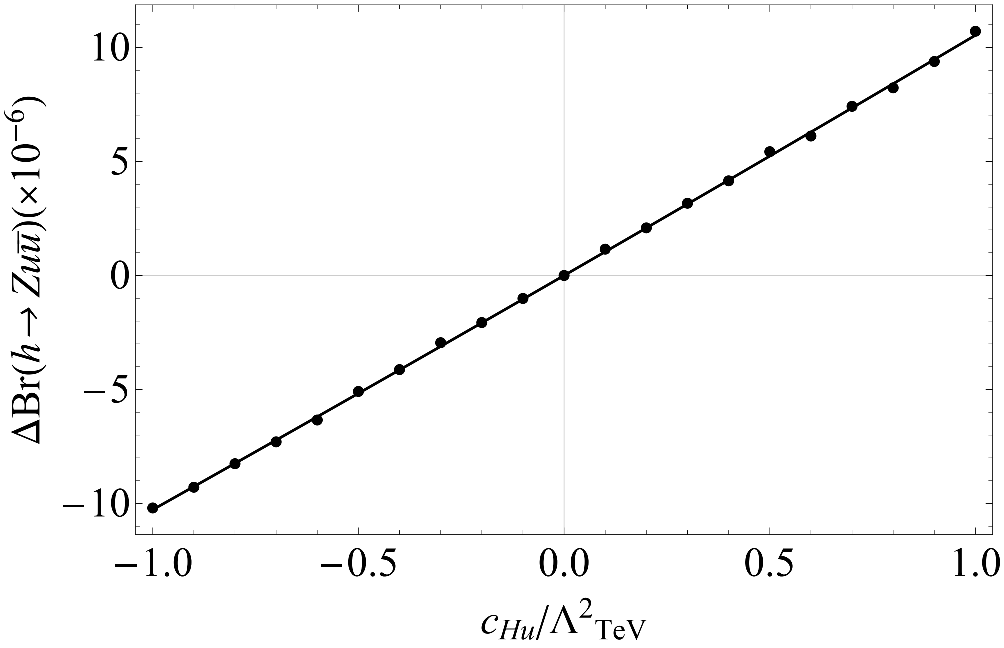

Figure 2.6: The modifications to the Higgs decays into an on-shell Z boson and quark anti-quark pairs from the operator under consideration.

The Higgs physics exotic decays [101] are also modified by these operators. The operator $\mathcal{O}_{Hu}$ contributes directly to $h\to Zu\bar{u}$ decay through the addition of the two diagrams in Fig. 2.7. The first by shifting g_R and the second by generating a contact term.

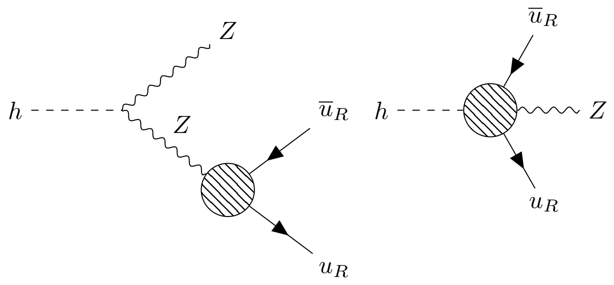

Figure 2.7: The additional diagrams contributing to $h \to Zu\bar{u}$.

The shift on the branching ratio was computed using the same model file with MG5_aMC, shown in Fig. 2.6 as a function of the Wilson coefficient over operator scale squared. We can see the interference term dominance and generically the shift of the order 10^{-5}-10^{-6}. The future lepton collider Higgs factories will produce around one million Higgs bosons in a clean environment. In principle, the modification can be measured as an exclusive mode, especially with charm-quark flavor tagging. Furthermore, in contrast to the $H \to ZZ^*$, this channel would exhibit different kinematic features.

Assuming an upper limit in this channel of 10^{-5} and 3×10^{-6}, we can probe $c_{Hu}/\Lambda^2_{\text{TeV}}$ up to order unity and 0.3, respectively. With a dedicated search, this may further improve. Although not competitive to the high energy probes, this channel does provide a complementary probe to the same physics and will help reveal the nature of the underlying physics.

2.6 Conclusion and outlook

By parameterizing the effects of new physics with non-renormalizable operators, we have studied the potential reach of the HL-LHC and future colliders which modify the Z, h, and quark couplings in flavor non-universal models. Using a binned-likelihood test, we determined that Zh production is the optimal diboson process to yield constraints on the dimension-six operator, $\mathcal{O}_{Hu}$ and $\mathcal{O}_{Hd}$, beating the constraints from LEP and the WW production at the HL-LHC. With a detailed analysis, we computed the projected sensitivity of the Zh process on these operators at the HL-LHC, HE-LHC, and FCC-hh. In comparison with the flavor constraints and future lepton collider projection, our results show that the Zh process yields competitive sensitivities .

Depending on the choice of right-handed rotations, a portion of the parameter space for flavor non-universal models not excluded by existing FCNC measurements can be tested by the Higgsstrahlung process. For instance, Higgsstrahlung can exclude a significant portion of the first 2 generation partial universal theories compared with what is currently excluded by measurements. This study also shows the exotic Higgs decay searches at future Higgs factories are complementary to the high energy Zh process. Should future measurements establish any deviations in quark couplings, our proposed measurements will help reveal the flavor nature of the underlying new physics.

CHAPTER 3

TIMING JETS

This chapter is reprinted with permission from:
Wen Han Chiu, Zhen Liu, Matthew Low, and Lian-Tao Wang. Jet timing. JHEP 01 (2022) 014.

3.1 Introduction

The time at which a particle arrives at a particular detector layer is a piece of independently measurable and valuable information. Measuring the time of a lepton, a photon, or a hadron has been used extensively at the Large Hadron Collider (LHC) to great effect.[1] Recently, it was shown that timing information is vital in the search for long-lived particles (LLPs) [108]. The upgraded electronics at the high-luminosity LHC will significantly improve the timing resolution for various subdetectors, reaching tens of picoseconds in some cases, extending the sensitivity of LLP searches even further. For instance, particle timing can improve prompt detection of beyond the Standard Model (BSM) physics [109], enable LLP mass and lifetime determination [110, 111, 112, 113], and enhance other various BSM searches [114, 115, 116, 117, 118, 119, 120, 121, 122, 123, 124, 125, 126, 127, 128, 129, 130, 131, 132, 133, 134, 135, 136, 137, 138, 139].

Obtaining similar information for final-state quarks and gluons, however, is much more challenging. These particles undergo showering and hadronization before arriving at the detector as a collection of particles, with a corresponding collection of arrival times. A jet is the standard object that combines these particles into a single object that can be used in analyses and searches. In momentum-space variables, summing the four-vectors of the

---

[1] Timing has been used in existing searches for heavy stable charged particles [102, 103], stopped particles [104, 105], and non-pointing photons [106, 107], where spatial information is unavailable or ineffective.

constituents provides a natural definition of the four-vector of the jet. Unfortunately, there is not an obvious choice for the definition of the arrival time of a jet.

The selection of a proper jet time definition is pivotal. A proper definition will enable efficient separation of the Standard Model (SM) prompt background and BSM long-lived signatures. A poor definition, on the other hand, will not allow us to take full advantage of the precision timing capabilities at the level of $30 - 40$ picoseconds, that will be part of upgrades to ATLAS [140], CMS [141], and LHCb [142]. Already, CMS has demonstrated sensitivity to delayed jets in their search for displaced gluinos [143].

Beyond just performance, a proper definition of jet time may help identify exciting properties of quantum chromodynamics (QCD), enable new jet tagging possibilities, and provide additional inputs for machine learning applications. Even pileup suppression may benefit substantially from an effective usage of jet time because generically pileup vertices have a spread both in space and in time. At the high-luminosity LHC any improvements to pileup suppression are indispensable.

The purpose of this chapter is to explore a variety of definitions of jet time and characterize their performances. As with any measurement tool, there are two aspects: accuracy and precision. For jet time, as we will discuss in detail later, the "correct" time is somewhat ambiguous. The precision, or resolution, is well-defined and will be the main criterion in comparing different approaches.

The structure of the chapter is as follows. In Sec. 3.2 we provide a brief overview of various possible definitions of jet time. The general behavior, both for prompt jets and delayed jets, is discussed in Sec. 3.3. In Sec. 3.4 we perform an in-depth numerical study of the behavior of each jet time definition, paying special attention to the dependence on the event geometry. Finally, our conclusions are in Sec. 3.5 along with outlook for future studies. Several appendices are included for cross-checks and studies of additional effects. We discuss the behavior of jet time when endcaps are also used to measure arrival times in App. 3.A, the impact of pileup and jet grooming in App. 3.B, the effects of detector resolution in App. 3.C, and the impact of hadronization in App. 3.D.

3.2 Definitions for Jet Time

In this section we briefly describe the definitions of jet time that we study. More detailed descriptions will follow in Sec. 3.3 and simulation results will be shown in Sec. 3.4.

We first define our notation. A single particle i has a four-momentum $(E_i, \vec{p}_i)$ and a particle time t_i, which is the time that it crosses a particular layer of the detector. A jet J is a set of particles which we write as $J = \{i\}$. While a particle has an unambiguous time, the jet has a set of times $\{t_i\}$ associated to it. In the same way that it is often useful to treat the jet as a single four-vector, *e.g.* in new physics searches, it is also useful to be able to assign a jet a single time t_J, that we call the jet time.

There are a number of possibilities that can be used. One can choose a single constituent i' in the jet and use its particle time $t_{i'}$ to represent the jet time. Jet time definitions of this type include:

- *median time*: take t_J to be the median value of the particle times $\{t_i\}$,
- *hardest time*: take t_J to be the time t_{i_h}, that corresponds to the time of the constituent i_h with the largest transverse momentum,
- *random time*: take t_J to be a randomly-drawn value of the particle times $\{t_i\}$.

The median time has been used by CMS in their search for gluinos with displaced decays [143]. The hardest particle in a jet is likely to be very close to the jet axis so it may be a good proxy for the time of the jet. We do not expect choosing a random particle time as the jet time to perform well, but it is useful as a baseline comparison.

Another option is to calculate t_J from a weighted sum of $\{t_i\}$, similar to a jet shape.

Generically, this would take the form[2]

$$t_J^{(\alpha,\beta,\gamma)} \propto \sum_{i\in\text{jet}} (p_{T,i})^{\alpha} (\Delta R_i)^{\beta} t_i^{\gamma}, \tag{3.1}$$

where ΔR_i is the $\eta\phi$-distance between particle i and the jet axis. The two simplest versions of a weighted sum are the average time where $(\alpha, \beta, \gamma) = (0, 0, 1)$ and the p_T-weighted time where $(\alpha, \beta, \gamma) = (1, 0, 1)$:[3]

- *average time*: take t_J to be

  $$t_J^{\text{average}} = \frac{1}{N} \sum_{i=1}^{N} t_i, \tag{3.2}$$

  where there are N particles in the jet,

- *p_T-weighted time*: take t_J to be

  $$t_J^{p_T} = \frac{1}{H_{T,J}} \sum_{i=1}^{N} p_{T,i} t_i, \qquad H_{T,J} = \sum_{i=1}^{N} p_{T,i}, \tag{3.3}$$

  where $H_{T,J}$ is a normalization factor.

Finally, one could simply disregard the particles times, treat the jet as a single particle, and calculate its time based on the jet kinematics. There are two variations depending on whether the jet is treated as a massless particle or massive particle:

- *null time*: treat the jet J as a massless particle and calculate its crossing time using the three-momentum $\vec{p}_J$ of the jet (assuming knowledge of the production vertex),
- *kinematic time*: treat the jet J as a massive particle and calculate its crossing time

---

[2] A number of alternatives are possible, such as particle energy E in place of p_T or angle θ in place of ΔR. In a brief survey, we did not find these to outperform the variables used in Eq. (3.1).

[3] We briefly studied a few additional cases such as p_T^2-weighted but did not see an improvement over the p_T-weighted time or average time. An optimization of α, β, and γ is beyond the scope of this work.

using the four-momentum $(E_J, \vec{p}_J)$ of the jet (assuming knowledge of the production vertex).

Since these definitions do not utilize the information available from timing measurements, we do not expect them to be optimal. They are useful, however, to determine what constitutes good performance from a jet time definition. In particular, the null time represents the crossing time if the parton did not undergo showering and hadronization and will serve as a useful reference time.[4]

After having chosen a definition for t_J we also need to choose a metric to evaluate which definition is the most useful. For a jet time definition, we will compare the relative time difference $\Delta t/t_{\text{ref}}$ defined as

$$\frac{\Delta t}{t_{\text{ref}}} = \frac{t_J - t_J^{\text{ref}}}{t_J^{\text{ref}}}, \tag{3.4}$$

to determine a good choice.

Each jet has a different value of $\Delta t/t_{\text{ref}}$ so that a sample of jets will lead to a distribution for the relative time difference. The mean of this distribution corresponds to the accuracy of the jet time definition while the width corresponds to the precision, or resolution, of the definition. Since the choice of t_{ref} is arbitrary it is not obvious that the mean of the distribution is important (not to mention that constant offsets can be corrected in practice). The width of the distribution, on the other hand, is a robust indicator of a stable time definition. For that reason, the width of the relative time difference distribution will be used as the figure of merit when comparing definitions.

3.3 General Behavior

In this section, we study analytically the general behavior of the various jet time definitions. We start with the prompt case where the majority of particles originate from the origin

---

[4] Note that while for prompt jets the null time is computable in data, for delayed jets the null time requires the location of the displaced vertex so it is not always computable in data.

and then we move on to the delayed case where the majority of particles originate from a displaced decay.

3.3.1 Prompt Particles

For prompt particles we assume that the particles originate at $t = 0$ from the origin of the detector $\vec{x} = \vec{0}$.[5] As a detector model, we will consider an infinite cylinder with radius r_T.[6] The time t_i of a particle i with four-momentum $(E_i, \vec{p}_i)$ is then given by

$$t_i = \frac{r_T}{c} \frac{E_i}{p_{T,i}}, \tag{3.5}$$

where c is the speed of light.

For a massless particle this simplifies to

$$t_i = \frac{r_T}{c} \frac{|\vec{p}_i|}{p_{T,i}} = \frac{r_T}{c} \cosh \eta_i, \tag{3.6}$$

which is a good approximation for particles in a high-momentum jet.

The jet times coming from a single particle within the jet are similarly calculated. For the median, hardest, and random times, the time of the jet is given by the time of the median-time particle i_m, the hardest particle i_h, or a random particle i_r, respectively, and is

$$t_J^{\{\text{median,hardest,random}\}} = t_{\{i_m, i_h, i_r\}} = \frac{r_T}{c} \cosh \eta_{\{i_m, i_h, i_r\}}. \tag{3.7}$$

With the cylindrical detector, the null and kinematic times of the jet, with four-momentum

---

[5] In reality and in simulation, there are displacements from processes like B-hadron decays. These have a negligible impact on our analysis.

[6] The differences when endcaps are included are discussed in App. 3.A.

$(E_J, \vec{p}_J)$, can also be calculated. The null time of a jet is

$$t_J^{\text{null}} = \frac{r_T}{c}\frac{|\vec{p}_J|}{p_{T,J}} = \frac{r_T}{c}\cosh\eta_J, \tag{3.8}$$

while the kinematic time of a jet is

$$t_J^{\text{kinematic}} = \frac{r_T}{c}\frac{E_J}{p_{T,J}} = t_J^{\text{null}}\frac{E_J}{|\vec{p}_J|}. \tag{3.9}$$

In the limit of small jet mass these definitions differ by $\mathcal{O}(m_J^2/\vec{p}_J{}^2)$.

The average and p_T-weighted times follow the definitions in Eqs. (3.2) and (3.3).

Prompt Relative Time Difference

For jet times using a single particle (median, hardest, and random times), with a time t_i, the relative time difference using Eqs. (3.7) and (3.8) is

$$\frac{\Delta t}{t_{\text{ref}}} = \frac{t_i - t_J^{\text{null}}}{t_J^{\text{null}}} = \frac{\cosh\eta_i}{\cosh\eta_J} - 1. \tag{3.10}$$

When the particle i points along the same direction as the jet axis, the relative time difference is always zero. When there is a fixed angular distance $\Delta\eta$ between the particle i and the jet axis, however, the relative time difference changes with η_J. Due to the detector geometry, as the jet becomes more forward, the relative time difference will grow.

The furthest that a particle i can be from the axis of the jet is approximately given by the jet radius R_{jet}. Therefore, for a given η_J there is a maximum relative time difference given by

$$\left.\frac{\Delta t}{t_{\text{ref}}}\right|^{\max} = \frac{\cosh(\eta_J \pm R_{\text{jet}})}{\cosh\eta_J} - 1, \tag{3.11}$$

where the + applies for positive η_J and the − applies for negative η_J.

The minimum is similar except that for $|\eta_J| < R_{\text{jet}}$ there is a stronger bound that comes from the fact that $\eta_i = 0$ for a massless particle corresponds to the fastest time possible since it is the shortest path from the origin. The bound for $|\eta_J| < R_{\text{jet}}$ consequently only depends on η_J. We find

$$\left.\frac{\Delta t}{t_{\text{ref}}}\right|^{\min} = \begin{cases} \operatorname{sech}\eta_J - 1, & |\eta_J| < R_{\text{jet}}, \\ \frac{\cosh(\eta_J \mp R_{\text{jet}})}{\cosh\eta_J} - 1, & \text{else.} \end{cases} \tag{3.12}$$

Eqs. (3.11) and (3.12) taken together specify boundaries in the space of pseudorapidity vs. relative time difference. The different jet time definitions will have different distributions within these boundaries. Fig. 3.1 illustrates these boundaries graphically.

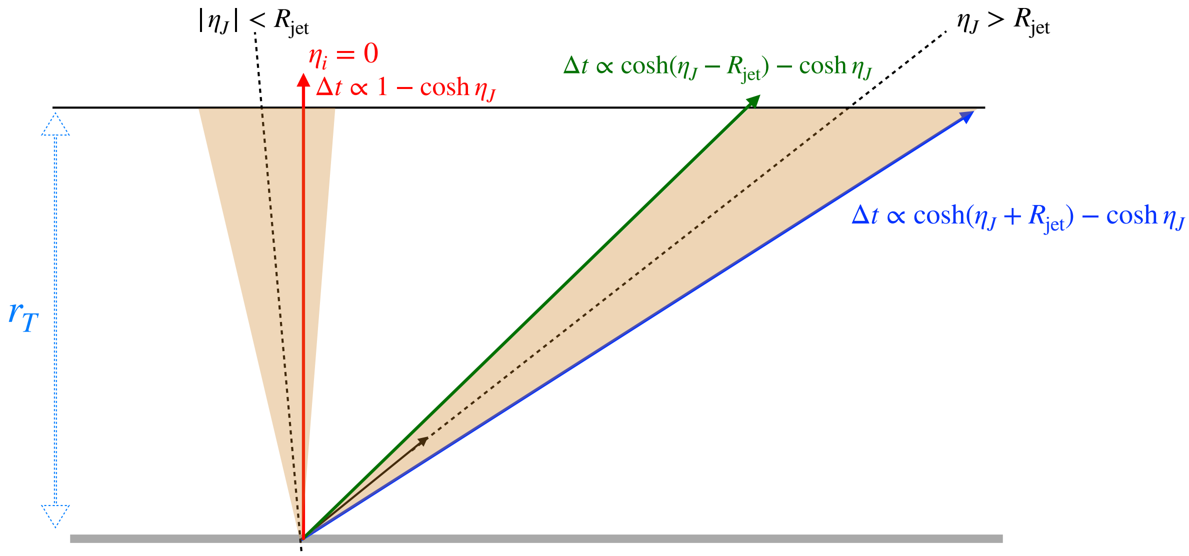

Figure 3.1: The slowest particle time, Eq. (3.11), follows the high $|\eta|$ boundary of the jet (blue). The fastest particle time, Eq. (3.12), follows the low $|\eta|$ boundary of the jet (green) or the $\eta = 0$ line (red).

At $\eta_J = 0$ the minimum of $\Delta t/t_{\text{ref}}$ is 0 while the maximum is $\cosh(R_{\text{jet}}) - 1 > 0$ which means that the relative time difference cannot be negative. Therefore, for very central jets we expect the relative time difference distributions to skew towards positive values since there is more available phase space. For less central jets we do not expect a strong preference for positive or negative values based only on phase space.

For the kinematic time rather a bound, one can relate the relative time difference to a kinematic quantity. From Eqs. (3.8) and (3.9) we find that for the kinematic time

$$\frac{\Delta t}{t_{\mathrm{ref}}} = \frac{E_J}{|\vec{p}_J|} - 1 = \frac{1}{\beta_J} - 1, \tag{3.13}$$

where β_J is the velocity. Since $\beta_J \leq 1$ the relative time difference for the kinematic time is always non-negative. This is expected since the kinematic time points in the same direction as the null time, but adjusts for the mass of the jet.

Next, we move to the relative time difference for the p_T-weighted time. This has a simple form given our cylindrical detector model. The p_T-weighted time is

$$t_J^{p_T} = \frac{1}{H_{T,J}} \sum_{i=1}^{N} p_{T,i} t_i = \frac{1}{H_{T,J}} \sum_{i=1}^{N} \frac{r_T}{c} E_i = \frac{r_T}{c} \frac{E_J}{H_{T,J}}, \tag{3.14}$$

and the corresponding relative time difference is

$$\frac{\Delta t}{t_{\mathrm{ref}}} = \frac{E_J}{H_{T,J}} \frac{p_{T,J}}{|\vec{p}_J|} - 1 = \frac{E_J}{|\vec{p}_J|} \frac{p_{T,J}}{H_{T,J}} - 1. \tag{3.15}$$

Written in the form after the second equality we recognize the factor $E_J/|\vec{p}_J| \geq 1$ from Eq. (3.13). The other factor $p_{T,J}/H_{T,J}$ is the ratio of the jet p_T to the scalar sum of the constituent p_T values. Since $p_{T,J}$ is a vector sum we have $p_{T,J}/H_{T,J} \leq 1$. The distribution at a given η_J is determined by the η-dependence of each of these two terms.

For small mass jets $E_J/|\vec{p}_J| \approx 1 + m_J^2/\vec{p}_J{}^2$ and schematically for QCD jets the mass is $\langle m_J^2 \rangle \sim R^2\, p_{T,J}^2 \sim R^2\, \vec{p}_J{}^2\, \mathrm{sech}^2\eta_J$ [144]. Consequently, $E_J/|\vec{p}_J| \sim 1 + R^2\, \mathrm{sech}^2\eta_J$ which peaks at $\eta_J = 0$ and reduces as $|\eta_J|$ grows. The other quantity $p_{T,J}/H_{T,J}$ depends on the energy distribution in the jet and is not strongly correlated with η_J. Therefore, we expect that the relative time distribution for the p_T-weighted time to be positively-skewed for central jets and switch over to negatively-skewed as the jets become more forward.

3.3.2 Delayed Particles

Next, we study the jet time behavior for delayed particles. Our benchmark scenario involves a mother particle M that travels a macroscopic distance, then decays into two daughter particles D and $\widetilde{D}$. We assume that M and $\widetilde{D}$ are unobserved while D is colored and results in a jet due to showering and hadronization.[7] In our numerical study we take M as a gluino, $\widetilde{D}$ as a gravitino, and D as a gluon.

Let the mother M have four-momentum $(E_M, \vec{p}_M)$ and decay at the displaced vertex $\vec{x}_M$ at a time t_M. The daughter D showers and hadronizes into a delayed jet. A particle i in the delayed jet has a four-momentum $(E_i, \vec{p}_i)$ and originates from $\vec{x}_M$ at t_M. Let the vector pointing from $\vec{x}_M$ to where i crosses the detector be $\vec{x}_i$.[8]

If particle i is measured, but the displaced vertex is not identified, then i will be assumed to have come from the origin, having traveled along $\vec{x}_i{}' = \vec{x}_M + \vec{x}_i$. This is illustrated in Fig. 3.2. We call the kinematics computed using $\vec{x}_i{}'$ the observed kinematics and those using $\vec{x}_i$ the truth kinematics.

	four-vector	assumed trajectory
truth	$(E_i, \vec{p}_i)$	$\vec{x}_i$
observed	$(E_i, \vec{p}_i{}')$	$\vec{x}_i{}'$

(3.16)

For transverse displacements $\gtrsim$ 10 cm the tracking efficiency is $\lesssim 40\%$ in CMS and drops off further above 50 cm [145]. Conservatively, we assume that the displaced vertex is not

---

[7] If M or $\widetilde{D}$ (or both) are colored, they will propagate as color-neutral R-hadrons. They will be unobserved if the resulting R-hadrons are electrically-neutral.

[8] For simplicity we neglect the effects of curvature in the magnetic field of the detector. For a magnetic field of 3.8 T the effect on the measurement of time or momentum is less than 1% for particles with $p_T >$ 2.5 GeV. In App. 3.B where we study pileup, we do include curvature induced by the magnetic field.

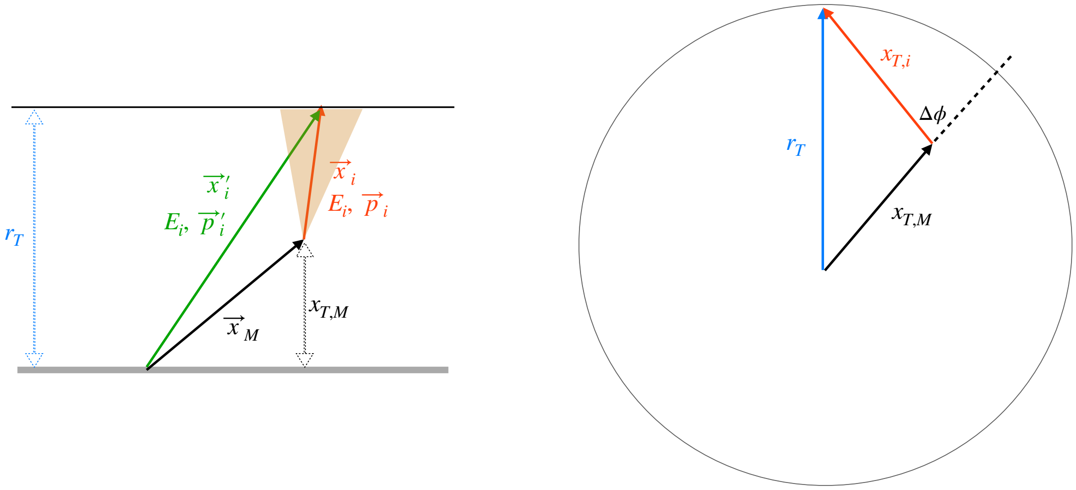

Figure 3.2: The mother particle M travels along $\vec{x}_M$ and decays to a delayed jet (shaded brown). The daughter particle i travels along $\vec{x}_i$ until it crosses the detector. If the displaced vertex is not identified then i is assumed to have traveled along $\vec{x}_i{}'$.

identified and work with the observed kinematics. Jet times that do not use the p_T values of particles in the time definition, *e.g.* the median time, are mostly insensitive to whether the truth or observed kinematics are used.

In the following, we begin by studying the three primary effects which control the performance of the timing of a delayed jet.

Observed Kinematics

For a massless particle i, if it is prompt its time is fully specified by its pseudorapidity η_i (see Eq. (3.6)). When i is delayed, its time depends now on its pseudorapidity η_i, the pseudorapidity of the mother η_M, the azimuthal angle difference $\Delta\phi = \phi_i - \phi_M$, the speed of the mother β_M, and the transverse decay location of the mother $x_{T,M}$:

$$\eta_M,\ \eta_i,\ \Delta\phi,\ \beta_M,\ x_{T,M}. \tag{3.17}$$

The transverse distance $x_{T,i}$ traveled by i is calculated to be

$$x_{T,i} = \sqrt{r_T^2 - x_{T,M}^2 \sin^2(\Delta\phi)} - x_{T,M}\cos(\Delta\phi). \tag{3.18}$$

The observed kinematics, $({p_{T,i}}', {\eta_i}', {\phi_i}')$, can be computed in terms of the variables in Eq. (3.17) and $x_{T,i}$. The observed pseudorapidity ${\eta_i}'$ is found from solving

$$r_T \sinh({\eta_i}') = x_{T,M}\sinh(\eta_M) + x_{T,i}\sinh(\eta_i). \tag{3.19}$$

In terms of the true transverse momentum $p_{T,i}$, the observed transverse momentum ${p_{T,i}}'$ is

$${p_{T,i}}'\sqrt{1 + \left(\frac{x_{T,M}}{r_T}\sinh(\eta_M) + \frac{x_{T,i}}{r_T}\sinh(\eta_i)\right)^2} = p_{T,i}\cosh(\eta_i). \tag{3.20}$$

Finally, the observed azimuthal angle ${\phi_i}'$ is

$$\tan({\phi_i}') = \frac{x_{T,M}\sin(\phi_M) + x_{T,i}\sin(\phi_i)}{x_{T,M}\cos(\phi_M) + x_{T,i}\cos(\phi_i)}. \tag{3.21}$$

Jets are clustered using the observed kinematics. The time t_i of a particle i is not impacted by using observed kinematics because the arrival time of a particle is an independent measurement. Since $\vec{x}_i$ and ${\vec{x}_i}'$ cross the detector at the same location, the effect on clustering using observed kinematics is nearly negligible (comparable to the difference between different jet algorithms).

The primary impact of using observed kinematics is on jet time definitions that utilize p_T information. We expect the p_T-weighted time to be impacted at a noticeable level (the size of this effect will be studied in Sec. 3.4). The hardest time could be affected if which jet constituent is the hardest changes under the observed kinematics. In practice, this is rare due to the hierarchical nature of the parton shower. The median time, likewise, is minimally affected.

Effective Radius

The radius of a jet, R_{jet}, is a parameter in the jet finding algorithm that determines which particles are included in the same jet. It determines the catchment area of a jet in $\eta\phi$-space which is approximately a circle with radius R_{jet} for cone-like algorithms used on isolated jets [146].

When choosing a jet radius there are trade-offs. If the radius is too small, then particles coming from the showering of a hard particle could fall outside a particular jet and the jet will not be a useful proxy for the underlying hard quark or gluon. If the radius is too large, the jet is more susceptible to contamination like underlying event and pileup [144].

One consequence for prompt jets of using a fixed R_{jet} for jet finding is that an optimal jet radius may be different for central jets as compared to forward jets. This is because for a fixed R_{jet} in $\eta\phi$-space, the corresponding angular distance, $\Delta\theta$, between a pair of particles is smaller for forward jets than for central jets. Physically, if a set of central particles within a jet with radius R_{jet} were shifted to larger $|\eta|$ values, then they may not all fit within a radius R_{jet} anymore.

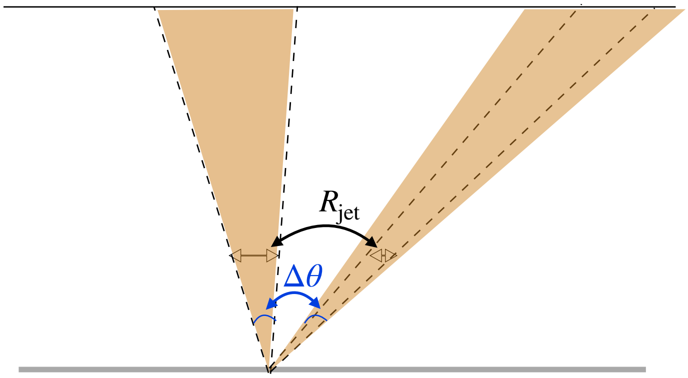

Figure 3.3: Illustration of $\Delta\theta$ effect for prompt jets. The dashed lines depict jets with the same R_{jet} while the shaded regions depict jets with the same $\Delta\theta$.

In the prompt case, we consider the effective radius of the jet to be the angular distance

$\Delta\theta$ that is required to keep ΔR fixed. This means that forward jets have a smaller effective radius than central jets because for fixed ΔR the required $\Delta\theta$ distance shrinks. See Fig. 3.3 for an illustration. Variable R jets were proposed to account for this by letting the jet radius grow at larger $|\eta|$ by scaling the radius inversely with transverse momentum [147].

In contrast, for delayed jets we consider the effective radius of a jet to be the true ΔR distance that is required to keep observed ΔR fixed. There are two factors that alter the effective radius for delayed jets. The first is that a non-zero value of $x_{T,M}$ means the jet originates closer to the detector radius r_T. The same way that the image from a projector is smaller as you move the projector closer to the screen, a fixed observed ΔR value corresponds to a larger true ΔR value as $x_{T,M}$ grows. See Fig. 3.4 for an illustration.

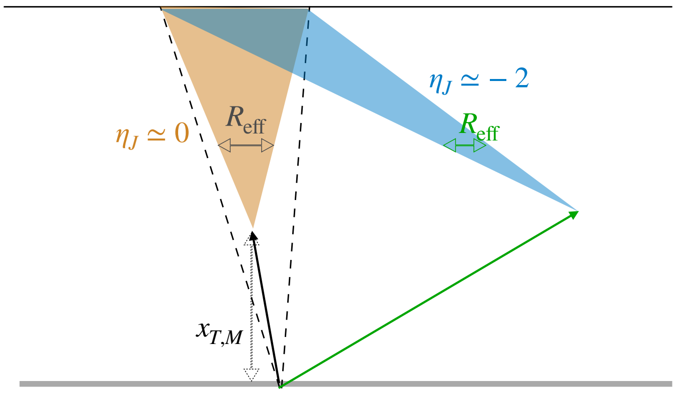

Figure 3.4: Illustration of R_{eff} effect for delayed jets. The brown shaded region has a larger R_{eff} compared to the dashed lines because $x_{T,M}$ is larger. The blue shaded region shows both the effect of shifting and tilting.

The second effect is that both η_J and η_M can vary. Changing η_J tilts the direction of the jet and generally causes the effective radius to shrink with η_J similar to the prompt case. Changing η_M is not a tilt, but rather a shift of the origin point of the particles. Due to the geometry of $\eta\phi$-space the effective radius generally increases as $|\eta_M|$ grows.

The effective radius can be estimated numerically. As shorthand we write the observed pseudorapidity of a jet as ${\eta_J}' = f(\eta_M, x_{T,M}, \eta_J)$ where the function is found in Eq. (3.19). We define the effective jet radius as R_{eff} and find it by solving

$$R_{\text{jet}} = f\left(\eta_M, x_{T,M}, \eta_J + \frac{1}{2}R_{\text{eff}}\right) - f\left(\eta_M, x_{T,M}, \eta_J - \frac{1}{2}R_{\text{eff}}\right). \tag{3.22}$$

The definition is not rigorous but rather is meant to provide intuition for the general behavior. We also set $\Delta\phi$ zero in the above for simplicity. In Fig. 3.5 we plot R_{eff} as a function of η_J for several sample points of $x_{T,M}$ and η_M with fixed jet radius $R_{\text{jet}} = 0.5$.

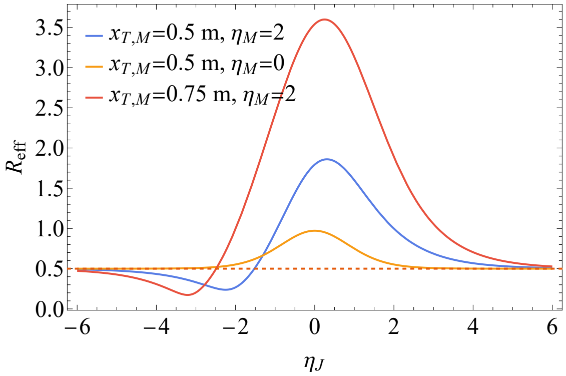

Figure 3.5: The effective radius, R_{eff}, as a function of η_J with $x_T = 0.5$ m and $\eta_M = 2$ (blue solid line), $x_T = 0.5$ m and $\eta_M = 0$ (yellow solid line), and $x_T = 0.75$ m and $\eta_M = 2$ (red solid line). A fixed value of 0.5 is also shown (red dashed line).

For isolated QCD jets, we expect the jet properties to change slowly with respect to increasing R_{eff}. In a typical parton shower there are both more and higher momentum particles near the center of the jet. Including additional soft particles further from the jet axis will not perturb the jet four-vector by much. When R_{eff} decreases the jet properties should change faster as more and higher momentum particles are excluded.

Daughter Time Fraction

The third effect is the fraction of time that comes from time of flight of the daughter i as compared to the time of flight of the mother, as shown in Fig. 3.6. Intuitively, when the mother travels more of the distance from the origin to the detector, there is less variation among the times of the particles in a jet. Consequently, the distribution of jet times becomes narrower.

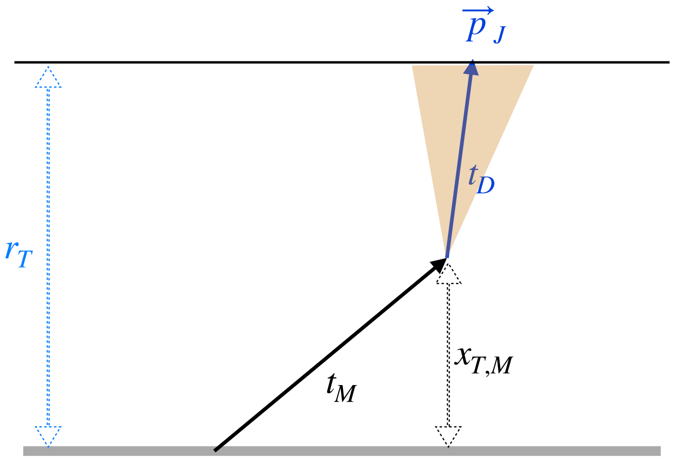

Figure 3.6: The time of flight of the mother particle is t_M and the time of flight of a daughter particle is t_D.

The time of a delayed particle i is

$$t_i = t_M + \frac{|\vec{x}_i|}{c}\frac{E_i}{|\vec{p}_i|} = t_M + \frac{x_{T,i}}{c}\frac{E_i}{p_{T,i}}. \tag{3.23}$$

The null time of a jet, which we continue to use as the reference time, is

$$t_J^{\text{null}} = t_M + \frac{x_{T,J}}{c}\frac{|\vec{p}_J|}{p_{T,J}} = t_M + \frac{x_{T,J}}{c}\cosh\eta_J. \tag{3.24}$$

Let us first consider the relative time difference for the median time so that $i = i_m$. We have

$$\frac{\Delta t}{t_{\rm ref}} = \frac{t_i - t_J^{\rm null}}{t_J^{\rm null}} = \frac{\left(t_M + \frac{x_{T,i}}{c}\frac{E_i}{p_{T,i}}\right) - \left(t_M + \frac{x_{T,J}}{c}\frac{|\vec{p}_J|}{p_{T,J}}\right)}{t_M + \frac{x_{T,J}}{c}\frac{|\vec{p}_J|}{p_{T,J}}}. \tag{3.25}$$

We set $t_D \equiv (x_{T,J}/c)(|\vec{p}_J|/p_{T,J})$, representing the “null" time from the daughter segment. If we approximate $x_{T,i} = x_{T,J}$ (*i.e.* the jet is narrow) and particle i as massless, then we find

$$\frac{\Delta t}{t_{\rm ref}} = \frac{t_D}{t_M + t_D}\left(\frac{\cosh\eta_i}{\cosh\eta_J} - 1\right). \tag{3.26}$$

The first factor is the fraction of the particle's time that is traveled by the daughter and the second factor we recognize from Eq. (3.10) as the prompt distribution evaluated at particle i's true pseudorapidity. As the distance the daughter travels, $x_{T,J}$, shrinks, so does the spread in $\Delta t/t_{\rm ref}$.

Delayed Relative Time Difference

Here we briefly review our expectations for the relative time difference in delayed jets. Recall that for single particle measures, like the median or the hardest, the prompt relative time is given by

$$\frac{\Delta t}{t_{\rm ref}} = \frac{\cosh\eta_i}{\cosh\eta_J} - 1. \tag{3.27}$$

The three effects that cause the delayed distribution to differ from Eq. (3.27) are:

- the daughter time fraction,
- the effective radius of the jet,
- the difference between observed and truth kinematics.

Let us now contrast a few jet time definitions to assess the impact of each delayed effect on the relative time distribution. We start with the hardest time. The difference in observed kinematics should have a negligible effect except in rare instances when the hardest particle in a jet changes between observed and truth kinematics. The effective radius should also have a minimal effect because the hardest particle in a jet tends to be near the jet axis. The daughter time fraction, however, is an irreducible effect.

From Eq. (3.26) we see that the delayed distribution inherits the prompt dependence on the daughter's true pseudorapidity, but with an additional suppression from the fact that spread between particles occurs over a smaller distance. The suppression comes from the prefactor

$$\frac{t_D(x_{T,M}, \eta_i)}{t_D(x_{T,M}, \eta_i) + t_M(x_{T,M}, \eta_M, \beta_M)}. \tag{3.28}$$

The times scale with their respective pseudorapidities, $t_M \propto \cosh(\eta_M)$ and $t_D \propto \cosh(\eta_i)$, so that the prefactor is closest to 1 when $\eta_D \approx 0$ and $|\eta_i|$ is large, and closest to 0 when $\eta_i \approx 0$ and $|\eta_D|$ is large. The prefactor can range from 0 to 1 and it plays a large role in the relative time difference distribution.

Next, we consider the median time. Again, we expect the observed kinematics to have a negligible effect on the relative time difference. The effective radius, however, can now have an impact because each particle has an equal effect on the median time of a jet. As R_{eff} grows, particles further from the jet axis are included in the jet and in the calculation of the jet time. Being far from the jet axis, these particles act like noise for the particle time distribution leading to more variation in the relative time difference distribution. Conversely, a shrinking R_{eff} will tend to narrow the distribution somewhat. The daughter time fraction is irreducible and has an $\mathcal{O}(1)$ effect on the median time.

Finally, we consider the p_T-weighted time. The daughter time fraction is again a driving effect. The impact of the effective radius should be smaller than in the median case, because particles far from the jet axis are typically soft so their contribution to the p_T-weighted time is suppressed by their p_T. The observed kinematics, however, can now have a large effect.

The p_T-weighted time for delayed jets is

$$t_J^{p_T} = \frac{1}{H_{T,J}'} \sum_{i=1}^{N} p_{T,i}' t_i, \qquad H_{T,J}' = \sum_{i=1}^{N} p_{T,i}'. \tag{3.29}$$

From Eq. (3.20) we see that the ratio $p_{T,i}'/p_{T,i}$ is independent of momentum. This means in the infinitely-narrow jet limit the p_T-weighted time is not affected by the observed kinematics. Beyond this limit, the effect of using the observed p_T can be large if the variation of $p_{T,i}'/p_{T,i}$ is large over the area of the jet.

The ability to accurately identify displaced vertices can eliminate the impact of the observed kinematics. Such an upgrade would be expected to improve the performance of the p_T-weighted time, but have a small effect on the hardest time and the median time.

3.4 Numerical Results

In this section, we compute the relative time differences for several jet time definitions in simulated data. Results will be compared with the derived behaviors from Sec. 3.3 and are found to follow the predicted trends.

3.4.1 Simulation Details

For prompt jets, we generate $pp \to Z' \to q\bar{q}$ events, where $q = u, d$, using Pythia v8.240 [148] at a center of mass energy of $\sqrt{s} = 14$ TeV and with a Z' mass of $m_{Z'} = 1$ TeV. Initial state radiation (ISR) and multiparton interactions (MPI) are turned off. Particles with $p_T < 0.5$ GeV or with $|\eta| > 4$ are discarded. Particles are clustered into anti-k_T jets [149] with $R_{\text{jet}} = 0.5$ using FastJet v3.3.2 [150]. The results are presented at particle-level without any detector resolution or time resolution included. The impact of these effects is shown in App. 3.C to be small.

For delayed jets, we generate $pp \to \tilde{g}\tilde{g} \to (g\tilde{G})(g\tilde{G})$ at parton-level using MadGraph5 v2.7.3 [91] at a center of mass energy of $\sqrt{s} = 14$ TeV and with particle masses of $m_{\tilde{g}} = 2$ TeV and $m_{\tilde{G}} = 10^{-16}$ TeV.[9] Events are showered with Pythia with ISR and MPI turned off. Particles with an observed transverse momentum below ${p_T}' < 0.5$ GeV or with an observed pseudorapidity $|\eta'| > 4$ are discarded, where a cylindrical detector with a radius of $r_T = 1$ m is used.

In both the prompt and delayed samples, hadronization is turned off. In Pythia, when there are both prompt and displaced particles, due to the hadronization procedure, some particles that descend from the displaced gluon can be assigned to the prompt vertex. Using unhadronized events avoids the issue of determining to which vertex a hadron should be assigned. In App. 3.D we compare the relative time distributions, in a prompt sample, with and without hadronization and find that the impact is at most a few percent.

3.4.2 Prompt Jets

We first look at prompt jets because the prompt distributions are inputs to understanding the delayed distributions. In each event we only consider the hardest jet and require that it has $p_T > 250$ GeV.

In Fig. 3.7 (left) we show the distribution of $\Delta t/t_{\text{ref}}$ for jets with $|\eta_J| < 0.5$ for the jet time definitions of p_T-weighted, median, hardest, average, and random. As expected, selecting a random particle in the jet to represent the jet time yields the widest distribution. Its distribution skews towards positive relative times because $\eta_J = 0$ corresponds to the fastest possible time, meaning there is more phase space for positive values. The other time definitions have narrower distributions but still skew towards positive values. The median, hardest, and average times have comparable performance, while the p_T-weighted time has the narrowest distribution.

From Fig. 3.7 we see that each $\Delta t/t_{\text{ref}}$ distribution peaks near zero, but that the mean

---

[9] Whether using gluon-initiated or light quark-initiated jets does not give rise to qualitative differences.

depends on the range of η_J used. The width of the distributions is an indicator of the resolution of a method and a useful figure of merit. Since these distributions are non-Gaussian, the 1σ standard deviation does not fully characterize the shapes, and in particular does not provide useful information about the tails. For that reason, we use the 3σ width (*i.e.* the bounds of the integral containing 99.7% of events) for comparison.[10] With this as the resolution, the p_T-weighted time performs 5 times better than the hardest time and 6 times better than the median time.

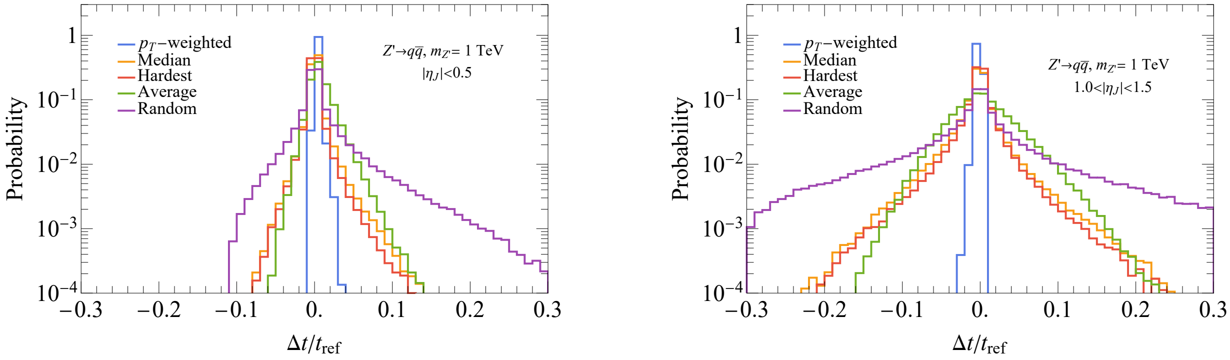

Figure 3.7: The relative time difference distribution in prompt jets for $|\eta_J| < 0.5$ (left) and for $1.0 < |\eta_J| < 1.5$ (right).

In Fig. 3.7 (right) we look at the relative time distribution for jets with $1.0 < |\eta_J| < 1.5$. The same pattern is present here where the random time is the widest distribution, followed by the median, hardest, and average times with similar widths, and the p_T-weighted time with the narrowest distribution. Again, comparing the resolutions, we find that the p_T-weighted time is 16 times better than the hardest time and 17 times better than the median time. The distributions of the median and hardest times widen noticeably in this $1.0 < |\eta_J| < 1.5$ range, as compared to $|\eta_J| < 0.5$, as predicted by Eqs. (3.11) and (3.12). The p_T-weighted time instead depends on the interplay between $E_J/|\vec{p}_J|$ and the ratio of transverse momentum to the scalar sum of the constituents' transverse momenta.

---

[10] In fact, we use the minimum width that contains 99.7% of the events rather than width centered at the mean because of the asymmetric nature of the distributions.

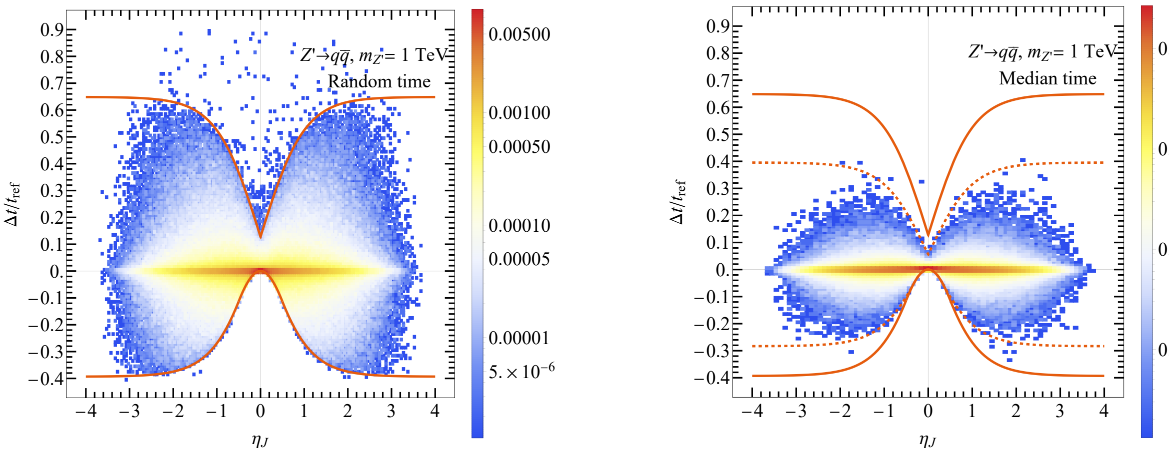

Figure 3.8: The relative time difference vs. η_J distribution for random time (left) and median time (right). The solid red curves depict the bounds from Eqs. (3.11) and (3.12). The dashed red curve depicts the same bounds for a jet of radius $(2/3)R_{\mathrm{jet}}$.

To better understand the difference between η_J regions, we look at the two-dimensional distribution of $\Delta t/t_{\mathrm{ref}}$ vs. η_J. Fig. 3.8 shows this distribution for random time with the bounds from Eqs. (3.11) and (3.12) overlaid. The majority of events fill out the region between the bounds with a few events above the maximum, due to mass effects, and a few events below the minimum due to the fact that particles can be slightly farther than R_{jet} from the jet axis.

Fig. 3.8 (right) shows $\Delta t/t_{\mathrm{ref}}$ vs. η_J for the median time. The red solid lines are the boundaries from Eqs. (3.11) and (3.12). This distribution clusters closer around $\Delta t/t_{\mathrm{ref}}$ values near zero. In fact, the dashed lines are boundaries for a jet with radius $(2/3)R_{\mathrm{jet}}$ which corresponds to the empirical observation that the behavior of the median time is similar to choosing a random particle from a narrower jet.

In Fig. 3.9 we show the same distribution for the p_T-weighted time. Here, we see that the behavior predicted by Eq. (3.15) does appear in the simulation. The positive relative time differences near $\eta_J = 0$ result from the $E_J/|\vec{p}_J|$ factor. The shape in that region even follows $\mathrm{sech}^2(\eta_J)$ as discussed in Sec. 3.3.1. As $|\eta_J|$ grows past ≈ 2 the $E_J/|\vec{p}_J|$ factor approaches

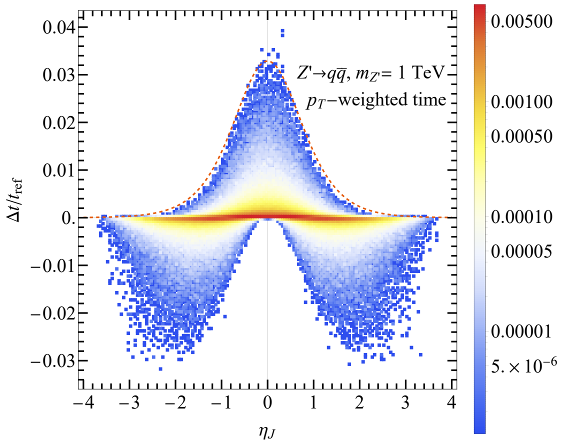

Figure 3.9: The relative time difference vs. η_J distribution for p_T-weighted time. The dashed red curve depicts the relation in Eq. (3.15).

unity and the $p_{T,J}/H_{T,J}$ factor determines the shape. Both of these factors have a narrow distribution leading to an overall narrow distribution for the relative time difference for the p_T-weighted time.

3.4.3 Delayed Jets

For delayed jets the parameter space expands from η_J to η_M, η_J, $\Delta\phi$, β_M, and $x_{T,M}$. To study a delayed sample, we vary the values for η_M, η_J, and $x_{T,M}$ and fix $\Delta\phi = 0$ and $\beta_M = 0.4$. The effect of non-zero $\Delta\phi$ has been discussed in our analytic estimates in Section 3.3.2.

In every event, there are two gluinos, each of which decay to a gluon leading to a hard jet. One of these gluinos is forced to decay outside of the detector while the other gluino is set to have velocity β_M and decays at a transverse distance $x_{T,M}$ to a gluon that points along η_J at parton-level. This same event is then re-showered many times to produce a sample of jets.

We consider only the hardest jet (that originates from inside the detector) in the event and require it to have an observed $p_T{}' > 50$ GeV. In order to identify effects that are dependent on the event topology, we discard events that differ by more than 0.25 in pseudorapidity or 0.25 in azimuthal angle before and after showering.

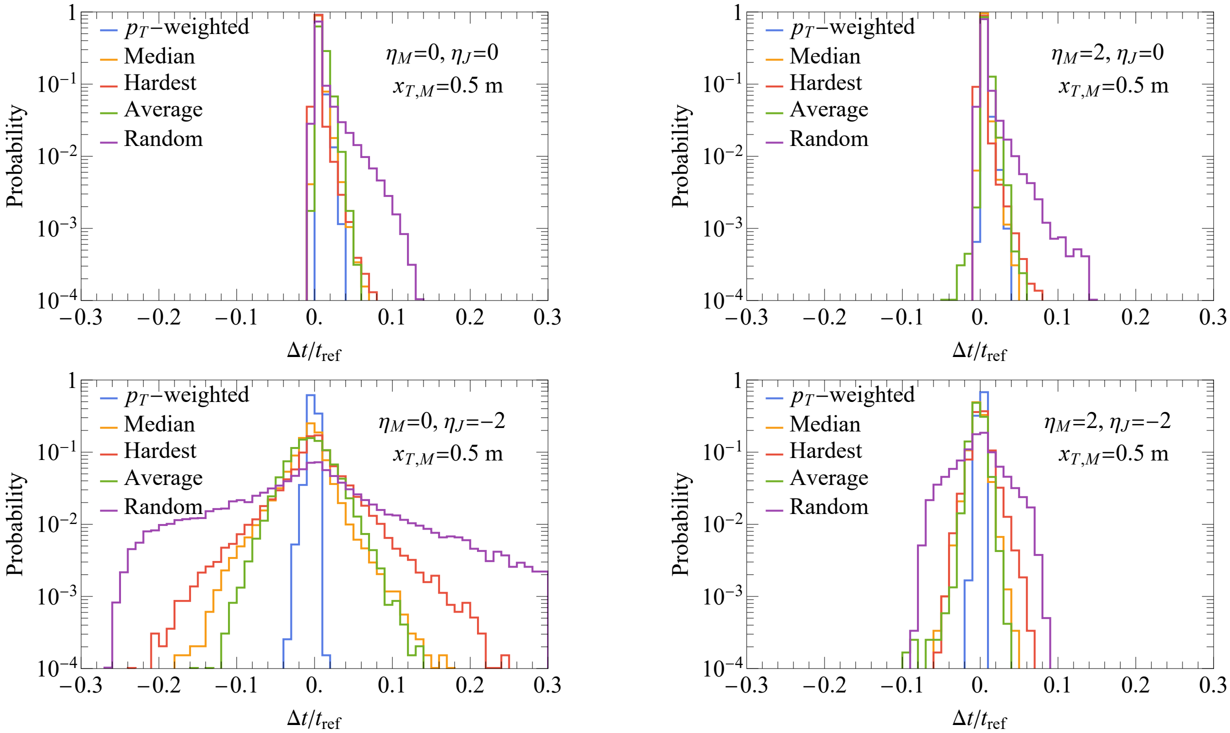

Figure 3.10: The relative time difference distribution for $(\eta_M, \eta_J) = (0, 0)$ (top left), $(\eta_M, \eta_J) = (2, 0)$ (top right), $(\eta_M, \eta_J) = (0, -2)$ (bottom left), and $(\eta_M, \eta_J) = (2, -2)$ (bottom right) for $x_T = 0.5$ m.

We first look at distributions of $\Delta t/t_{\mathrm{ref}}$ in Fig. 3.10 for $x_{T,M} = 0.5$ m. The top left plot shows the p_T-weighted, median, hardest, average, and random times with $(\eta_M, \eta_J) = (0, 0)$. Much like the prompt case, every definition skews positive since $\eta_J = 0$ corresponds to fastest possible arrival time. The distributions are narrower than the prompt case due to the decrease in variation in arrival time as captured by the daughter time fraction in Eq. (3.28).

Fig. 3.10 (top right) shows the $\Delta t/t_{\mathrm{ref}}$ distributions for $(\eta_M, \eta_J) = (2, 0)$ which corresponds to a forward gluino that decays to gluon that travels perpendicular to the beamline, directly to the detector. From Eq. (3.26) we expect this distribution to be similar to the prompt distribution for central jets. Compared to the $(\eta_M, \eta_J) = (0, 0)$, this point has a smaller daughter time fraction and is narrower as expected.

The bottom left of Fig. 3.10 shows $\Delta t/t_{\text{ref}}$ distributions for $(\eta_M, \eta_J) = (0, -2)$. Here the gluino travels perpendicular to the beamline then decays to a backward pointing gluon. The observed pseudorapidity for the gluon is $\eta_J{}' = -1.3$. Focusing first on the p_T-weighted time, we see that the distribution is slightly wider than the prompt case, Fig. 3.9, despite a slight suppression of ≈ 0.6 from the daughter time fraction. This is due to a sizable variation between the observed and truth kinematics. The median and hardest distributions do not differ much from their prompt counterparts.

Fig. 3.10 (bottom right) shows the distributions for $(\eta_M,\ \eta_J) = (2, -2)$. In this case, each distribution is very narrow. This is primarily a consequence of the jet having $R_{\text{eff}} = 0.27$.[11] While the p_T-weighted distribution is still narrow, the difference is not as large as for other jet times because of the discrepancy between observed and truth kinematics for this configuration.

In Fig. 3.11 we show a scan over η_J in the x-direction and η_M in the y-direction for the p_T-weighted, median, and hardest times. Here, we observe the general trend primarily follows Eq. (3.26). Changing η_J we see that distribution width tends to track with the corresponding pseudorapidity for the prompt distribution. The slight narrowing at large $|\eta_M|$ is due to the changing daughter time fraction, as in Eq. (3.28). The few deviations from this pattern are caused by larger changes in the effective radius and additionally from the observed kinematics for the p_T-weighted time. Fig. 3.12 shows a scan over η_J in the x-direction and η_M in the y-direction for different values of $x_{T,M}$. The distributions are narrow over the full parameter space.

The parameter scans in Figs. 3.11 and 3.12 are useful for emphasizing a few physics points. Firstly, the p_T-weighted time is consistently better than other jet time definitions across the variation of key kinematics, namely η_M and η_J. Secondly, the p_T-weighted time has a

---

[11] Note that because the particles in a jet are not uniformly distributed, excluding particles that are farther from the jet axis does result in a narrower relative time difference distribution.

different spread at different kinematical points which means one should compute calibrations and efficiencies at each point rather than using a single value over all of parameter space.

3.5 Conclusions

The time of a jet is a theoretically ambiguous and yet experimentally highly relevant quantity. The time profile of a jet provides a new independent probe of jet properties, potentially deepening our understanding of QCD. Experimentally, the jet time is an observable with strong discrimination power in searches for long-lived particles. Like how the jet clustering algorithm itself defines a jet using a collection of particles, the choice of jet time definition determines its properties and performance. A useful definition should have predictable behavior, give the closest representation to the parton-level information, and, more importantly, minimize the spread in arrival time.

In this work, we primarily studied five definitions of jet time. The first was the p_T-weighted time where the jet time is a p_T-weighted sum of the jet constituent arrival times. The second was the median time which uses the median constituent time as the jet time. The third was the hardest time where the time of the highest p_T constituent is used as the jet time. The fourth was the average time where the jet time is taken as the average of the constituent times. The fifth was the random time where the time of a constituent was randomly chosen to be used as the jet time.

To evaluate the various definitions, we both predicted and computed in simulation the relative time difference of a definition compared to the time it would take a massless parton to travel along the jet's trajectory. The width of the relative time difference distribution tells us how precisely the jet time can be measured. For prompt jets, we showed that the performance depends on the pseudorapidity of the jet. Due to the geometry of the detector barrel, all jet time definitions have wider distributions as the jets become more forward. We found that the p_T-weighted jet time consistently has the best performance. For instance, for central jets with $1.0 < |\eta| < 1.5$, the p_T-weighted time has a 16-fold improvement over the (next-best-performing) hardest time. For central jets with $|\eta| < 0.5$, the p_T-weighted time has a 5-fold improvement over hardest time.

For delayed jets, the full kinematics of the event affects the performance. Specifically, the direction of the mother particle, the direction of the jet, and the transverse decay location of the mother particle determine the behavior of the jet times. We show that delayed jet timing behavior can be understood through three effects. The first is the daughter time fraction which is the fact that as the displaced vertex gets closer to the detector there is less distance for the constituents to travel and consequently less spread in their times. The second is the effective radius of the jet that is an effect of the displaced vertex. The third is the that observed p_T differs from the true p_T, which occurs when the displaced vertex is not identified. Just as for prompt jets, the p_T-weighted time has the best performance over the full parameter space. Furthermore, the strong dependence on the event kinematics emphasizes the importance of having an efficiency map that depends on the long-lived particle's direction, its decay location, and the direction of the daughter jet.

This work is the first study that looks at the impact of different definitions of jet time. There are many related directions that can be explored. For instance, finding the jet time definition that is most amenable to direct calculation may help reduce theory uncertainties. More practically, given the trigger computation complexity budget, it would be useful to understand the best alternative jet time definition for a low-level delayed jet trigger. On the analysis side, studies could be done on the interplay between jet time and pileup and grooming. Other new physics models with different event topologies would be interesting to study. More detailed signal-specific studies are needed to evaluate the direct impact of using the jet time in new physics searches. We are optimistic that the jet time has the potential to be a standard tool in long-lived particle searches in the near future.

3.A Finite Length Detectors

In the main text, we consider a detector with only a barrel capable of timing measurements. If one includes endcaps, then the timing distributions are different for jets with times that the endcaps would measure.

If the pseudorapidity at which the barrel connects to the endcap is η_{EC}, then the arrival time of a particle i at the endcap is

$$t_i^{\mathrm{endcap}} = \frac{z_{\mathrm{EC}}}{c} \frac{1}{\tanh \eta_i}, \tag{3.30}$$

where $z_{\mathrm{EC}} = r_T \cosh \eta_{\mathrm{EC}}$. If all of the jet's constituents lie solely in the endcap, the trajectory that yields the shortest (largest) arrival time is now the most forward (central) constituent.

For jets with constituents in the intermediate region, the trajectory that yields the largest arrival time is always the trajectory intersecting the barrel-endcap corner. Depending on the jet axis, the shortest arrival time can be a constituent that intersects the barrel or the endcap.

In Fig. 3.13 we show the maximum and minimum relative time differences (for a single-particle measure) for $r_T = 1$ m and a total barrel length of $L = 6$ m which corresponds to $\eta_{\mathrm{EC}} = 1.76$.[12] Once all jet constituents lie within the endcap, the allowed spread in relative time difference sharply drops for prompt jets.

3.B Pileup and Grooming

We simulate pileup by overlaying n_{PU} soft QCD vertices onto our hard event. The number of pileup events is Poisson distributed, with $\langle n_{\mathrm{PU}} \rangle = 140$ and a cutoff at 200 vertices. The pileup vertices follows a Gaussian spread in both z and t, with $\sigma_z = c\sigma_t = 60$ mm [153]. The events with pileup include all of the detector effects discussed in App. 3.C.

---

[12] This yields the approximate inner geometry of the CMS and ATLAS electromagnetic calorimeters [151, 152].

The relative time differences without any form of pileup mitigation are shown in Fig. 3.14 for $|\eta_J| < 0.5$ (left) and $1.0 < |\eta_J| < 1.5$ (right). The average time distribution gets distorted for the $|\eta_J| < 0.5$ bin, and the peak shifts away from zero considerably. Like those from pileup, low-energy particles have a smaller curvature radius from the magnetic field and are therefore delayed more than higher-energy particles. Since a sizable fraction of a jet's constituents can come from pileup, this causes the average time to shift considerably. The same reasoning is responsible for the broadening of the distributions of the median and p_T-weighted times. The hardest time is affected very little.

The $1.0 < |\eta_J| < 1.5$ bin shows less impact from pileup as can be seen, for example, by the peak of the average time distribution remaining close to zero. Similarly, the distributions of the other times broaden slightly, but their peaks do not shift. This is the result of the p_T cut restricting to more energetic particles at larger pseudorapidities.

For pileup mitigation, we use an idealized version of charged hadron subtraction [154] where we assume all charged pileup can be removed. The remaining particles were then clustered into $R_{\text{jet}} = 0.5$ anti-k_T jets and trimmed [155] with $R_{\text{sub}} = 0.2$ and $f_{\text{cut}} = 0.03$. The choice of keeping R_{jet} the same is to ensure that the jet times with and without pileup mitigation are directly comparable.

The distributions for the $|\eta_J| < 0.5$ bin are shown in Fig. 3.15. The improvement is predominantly due to the removal of soft charged pileup particles by charged hadron subtraction. These constituents are the ones that are mainly delayed by mass effects and the magnetic field. Trimming plays a minor role because R_{sub} is not significantly smaller than R_{jet} and the number of pileup vertices is large. More aggressive trimming may improve results slightly.[13]

---

[13] One could also study the performance using pileup mitigation techniques that are better suited to large values of $\langle n_{\text{PU}} \rangle$ such as jet cleansing [156], constituent subtraction [157], PUPPI [158], soft killer [159], or PUMML [160]. This is beyond the scope of this work.

3.C Detector Effects

In this section we show the effects of implementing a simple detector model. We first implement time resolution, followed by time and spatial resolution. The effects are shown in a prompt sample for $|\eta_J| < 0.5$ in Fig. 3.16 and for $1.5 < |\eta_J| < 2.0$ in Fig. 3.17.

For time resolution, we round each particle's time to the nearest multiple of 30 ps. This is the expected resolution of LHC upgrades [140, 141, 142]. The effect on the $\Delta t/t_{\text{ref}}$ distribution can be seen by comparing the left plots (no timing resolution) to the center plots (30 ps timing resolution) in Figs. 3.16 and 3.17. In both cases, the time resolution has a negligible effect on the shape of the distribution.

For spatial resolution, we consider an $\eta \times \phi$ grid of 0.05×0.05 cells. The four-momenta are replaced with a massless four-vector with the same energy as the particle, and the direction shifted pointing to the center of the corresponding $\eta\phi$-cell. If multiple particles fall into the same cell and the same time window, their energies are added, and they are combined into a single cell. The effect on the $\Delta t/t_{\text{ref}}$ distribution can be seen in Fig. 3.16 (right) and Fig. 3.17 (right).

In the $|\eta_J| < 0.5$ bin, we see that spatial resolution does not significantly affect the timing distributions. By contrast, the $1.0 < |\eta_J| < 1.5$ bin has a noticeable broadening in the p_T-weighted distribution and moderate broadening in the median and hardest distributions. This is because the fractional momentum resolution induced by the spatial resolution increases with $|\eta|$. This impacts both the momentum of the jets and their constituents.

Lastly, we considered the impact of including a 4T magnetic field. In this case, the particles were hadronized (in order to get the correct electric charge of the hadrons), and at the same time and spatial resolution was applied. The effect on the relative time distribution for both bins are shown in Fig. 3.18. There is a very slight positive pull in the $|\eta_J| < 0.5$ bin (left) while the $1.0 < |\eta_J| < 1.5$ bin (right) has no noticeable change. This difference is due to the $p_T > 0.5$ GeV cut imposed on the constituents. As η increases, the energy required to pass the p_T cut also increases. The shift in arrival time due to the change in path length is inversely proportional to the energy.

3.D Hadronization

In this study the events are not hadronized to ensure that Pythia assigns the correct vertex to each delayed particle. Fig. 3.19 compares the relative time difference for prompt jets with and without hadronization for the p_T-weighted time (left), median time (center), and hardest time (right) in the range $1.0 < |\eta_J| < 1.5$. Of the three, only the median time shows a slight observable change.

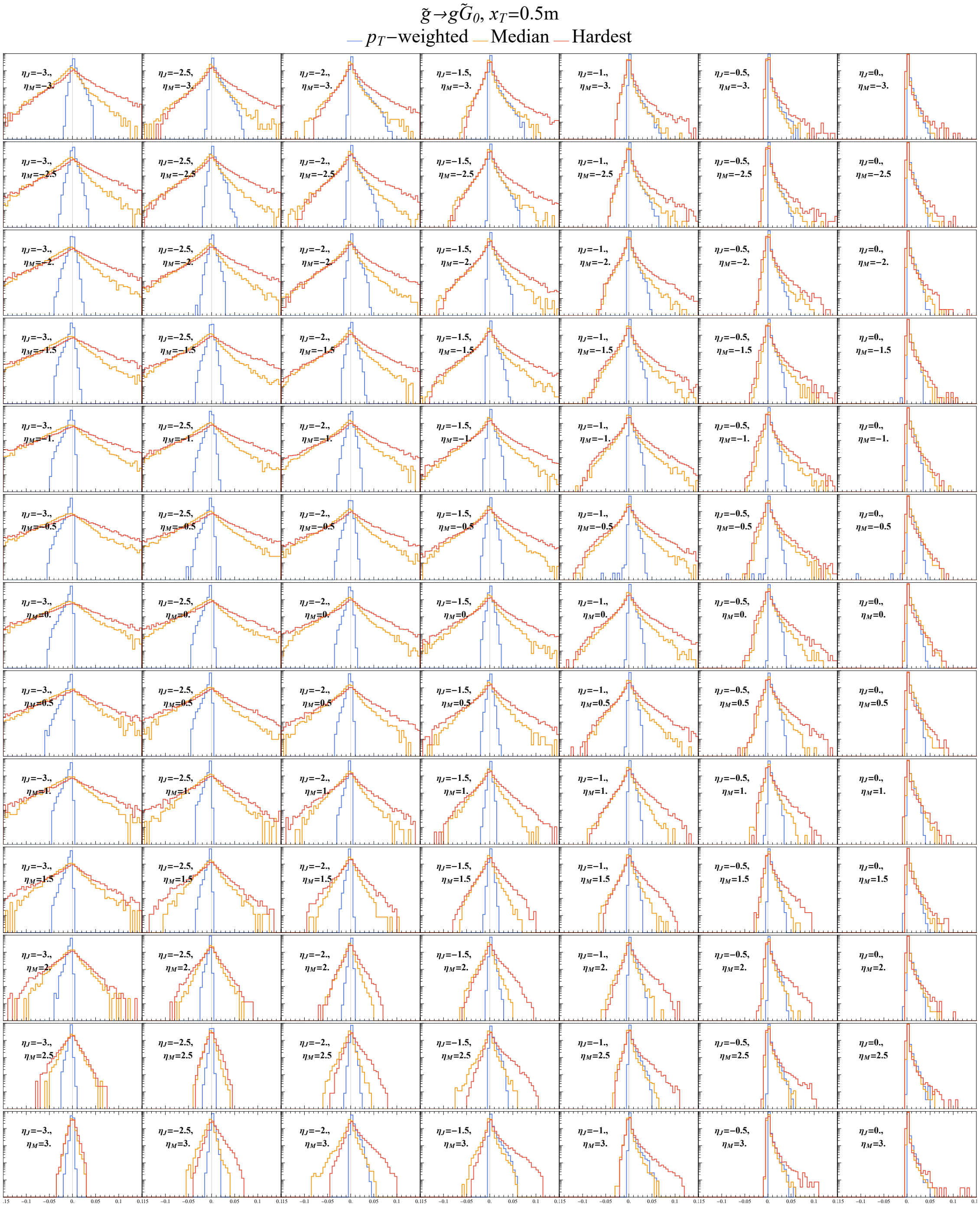

Figure 3.11: The relative time difference distribution for the p_T-weighted (blue), median (yellow), and hardest (red) times as a function of η_J (x-axis) and of η_M (y-axis) with a transverse decay location of $x_{T,M} = 0.5$ m. The vertical axis in each plot is in log-scale and ranges from 10^{-5} to 1.

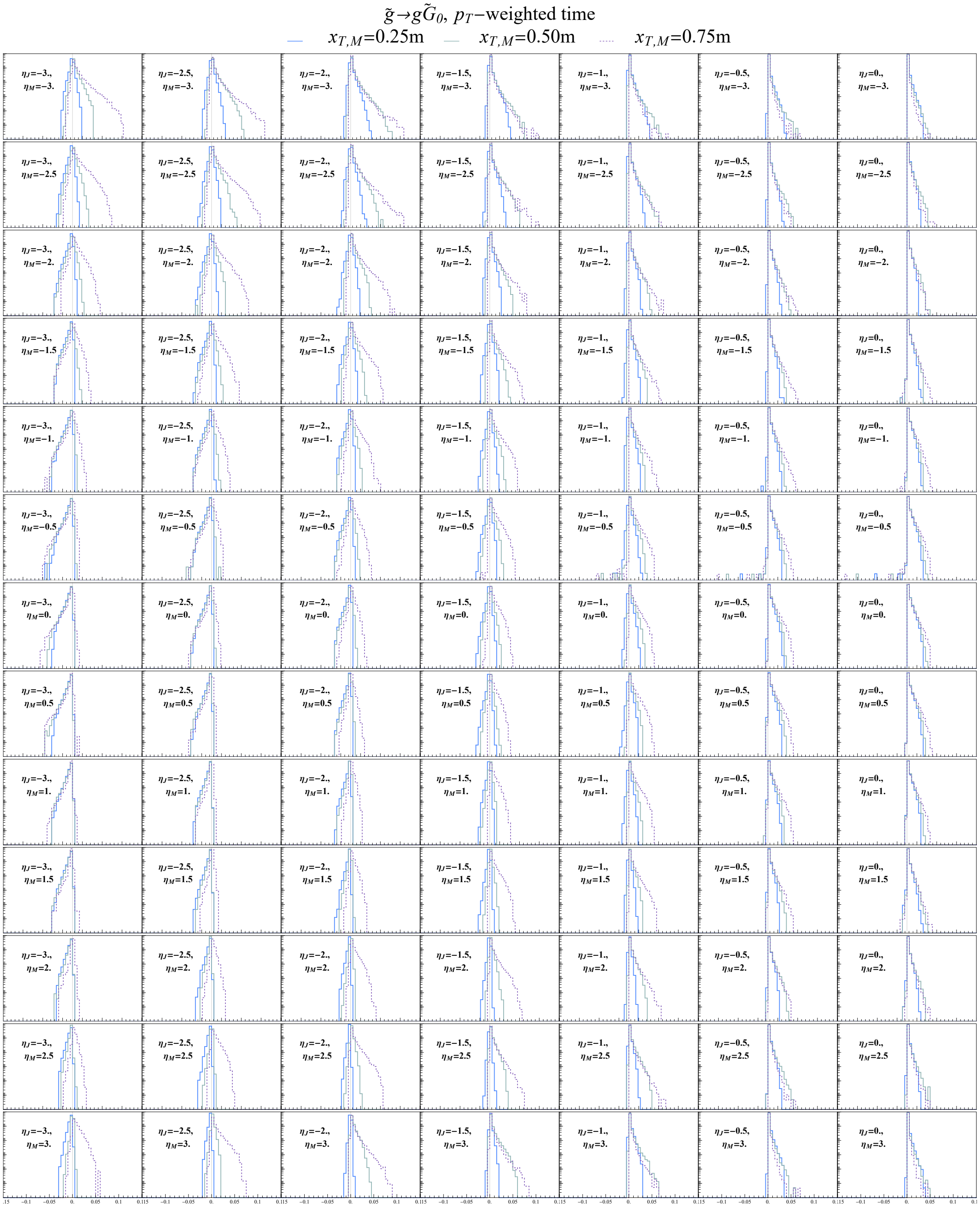

Figure 3.12: The relative time difference distribution for $x_{T,M} = 0.25$ m (blue), $x_{T,M} = 0.50$ m (gray), and $x_{T,M} = 0.75$ m (purple dashed) times as a function of η_J (x-axis) and of η_M (y-axis) for the p_T-weighted time. The vertical axis in each plot is in log-scale and ranges from 10^{-5} to 1.

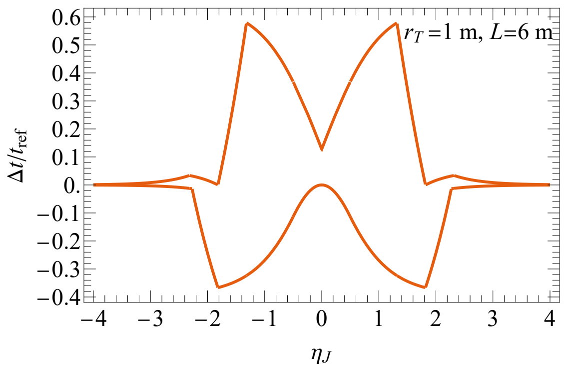

Figure 3.13: The boundaries for the relative time difference as a function of η_J. This can be compared with the boundaries in Fig. 3.8.

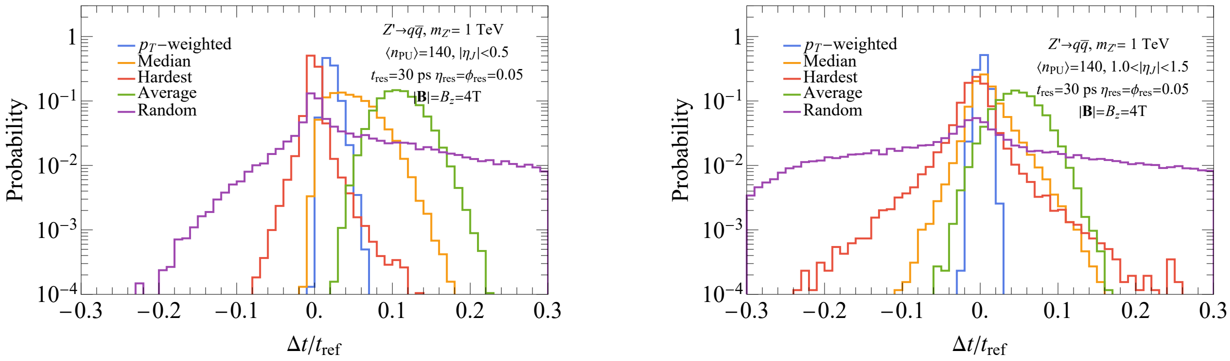

Figure 3.14: The relative time difference distribution for $|\eta_J| < 0.5$ (left) and $1.0 < |\eta_J| < 1.5$ (right) with pileup and no subtraction. The $|\eta_J| < 0.5$ plot can be compared with Fig. 3.18 (left) and the $1.0 < |\eta_J| < 1.5$ plot can be compared with Fig. 3.18 (right).

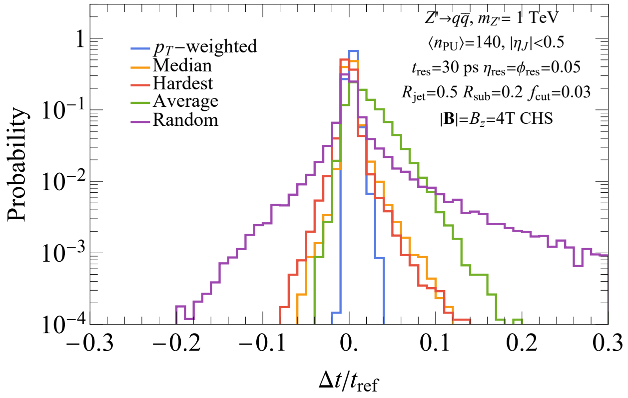

Figure 3.15: The relative time difference distribution for $|\eta_J| < 0.5$ with pileup, charged hadron subtraction, and trimming. This can be compared with Fig. 3.14 (left).

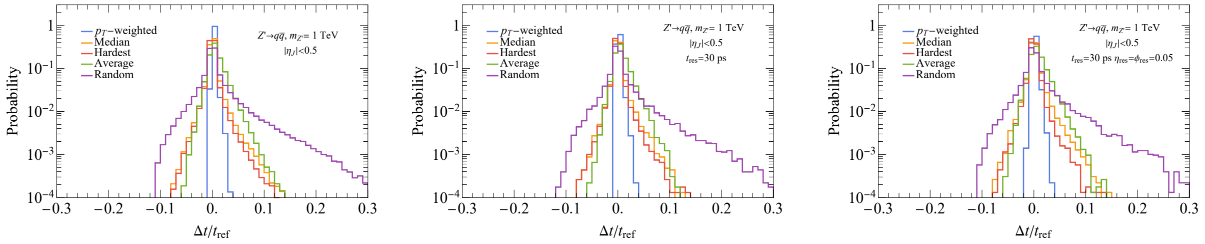

Figure 3.16: The relative time difference distribution for $|\eta_J| < 0.5$ with no detector effects (left), with time resolution added (center), and with time and spatial resolution added (right).

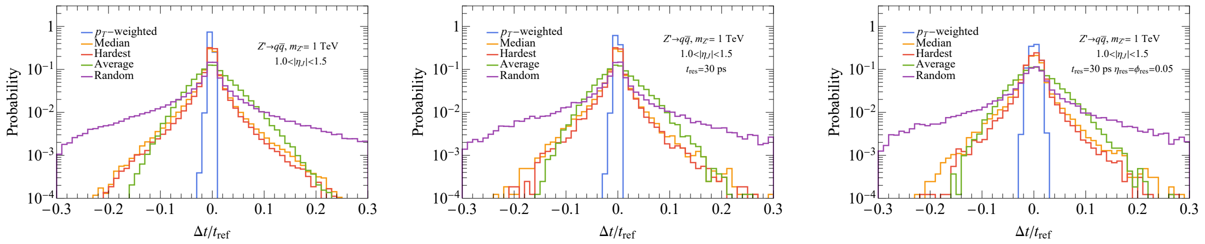

Figure 3.17: The relative time difference distribution for $1.0 < |\eta_J| < 1.5$ with no detector effects (left), with time resolution added (center), and with time and spatial resolution added (right).

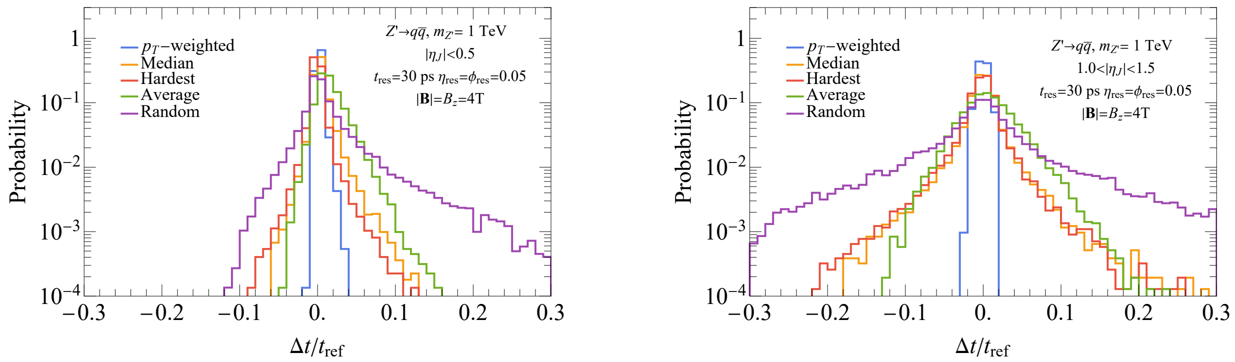

Figure 3.18: The relative time difference distribution for $|\eta_J| < 0.5$ (left) and $1.0 < |\eta_J| < 1.5$ (right) with a magnetic field. The $|\eta_J| < 0.5$ plot can be compared with Fig. 3.16 (right) and the $1.0 < |\eta_J| < 1.5$ plot can be compared with Fig. 3.17 (right).

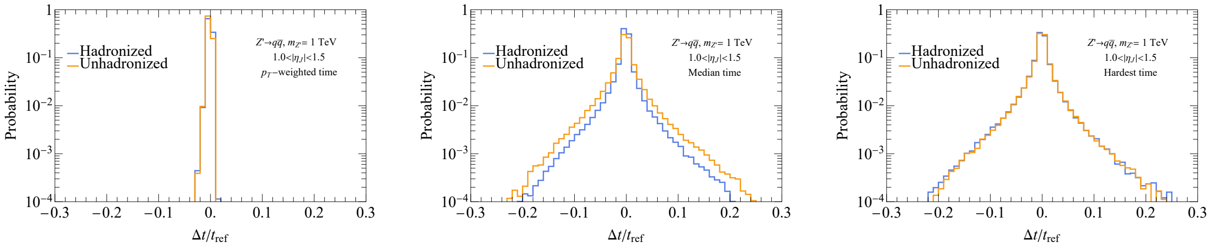

Figure 3.19: The relative time difference distributions with and without hadronization for the p_T-weighted time (left), median time (center), and hardest time (right) with $1.0 < |\eta_J| < 1.5$.

CHAPTER 4

MODELING EXPERIMENTAL ANOMALIES

This chapter is reprinted with permission from:

Henning Bahl, Wen Han Chiu, Christina Gao, Lian-Tao Wang, and Yiming Zhong. Tripling down on the W boson mass. Eur.Phys.J.C 82 (2022) 10, 944.

4.1 Introduction

Recently, the CDF-II experiment [14] measured the W boson mass to be

$$m_{W,\text{CDF-II}} = 80.4335 \pm 0.0094 \text{ GeV}. \tag{4.1}$$

This suggests a 7σ derivation from the Standard Model (SM) prediction [3],

$$m_{W,\text{SM}} = 80.357 \pm 0.006 \text{ GeV}. \tag{4.2}$$

The CDF-II measurement of m_W is also in tension with the measurements from the previous collider experiments at $\sim 2.6\sigma$ [3, 161]. The discrepancy might be due to some unknown experimental systematical uncertainties, but it could also be a hint for new physics [162, 163, 164, 165, 166, 167, 168, 169, 170, 171, 172, 173, 174, 175, 176, 177, 178, 179, 180, 181, 182, 183, 184, 185, 186, 187, 188, 189, 190, 191, 192, 193, 194, 195, 196, 197, 198, 199, 200, 201, 202, 203, 171, 204, 205, 206, 207, 208, 209, 210, 211, 212, 213, 214, 215, 216, 217, 218, 219, 220, 221, 222, 223, 224, 225, 226, 227, 228, 182, 229, 230, 231, 232, 233, 234, 235, 236, 237, 238, 239, 240, 241, 242, 243, 244, 245, 246]. A class of new physics solutions contain extensions to the Standard Model (SM) Higgs sector, whereby the new Higgs states provide additional sources of custodial symmetry breaking [162, 163, 164, 165, 166, 167, 168, 169, 170, 171, 172, 173, 174, 175, 176, 177, 178, 179, 180, 181, 182, 183, 184]. In a particular class of models, the correction to the W mass from new physics enters at the one-loop level. The new physics scale is then predicted to be around a few hundreds of GeV. This is particularly interesting since it could give rise to signals in LHC new physics searches. The new physics in this class are generically in some $SU(2)_L$ multiplet. The correction to the W mass requires that the masses of the different members of the multiplet receive different custodial symmetry breaking contributions from the electroweak symmetry breaking. Hence, some of the couplings between the new physics and the Higgs need to be sizable, and there need to be significant mass splittings within the multiplet. Both of these features have interesting phenomenological consequences.

In this chapter, we explore the phenomenology of the Higgs Triplet Model (HTM), with hypercharge $Y = 1$, in the context of electroweak precision measurements, direct collider searches, and Higgs precision measurement in light of the CDF-II W mass measurement. The prediction of this model for the W mass has been investigated in Ref. [175]. We go beyond the existing works by investigating the compatibility of the $m_{W,\mathrm{CDF-II}}$ preferred triplet spectra with the measurements of the effective weak mixing angle and Higgs precision data as well as by providing a comprehensive analysis of possible signatures at the Large Hadron Collider (LHC). Furthermore, we explore the situation that the new Higgs triplet is approximately inert. This can be achieved naturally by imposing an approximate $\mathbb{Z}_2$ symmetry, which can be broken softly. In this case, its lightest neutral states can be candidates for a fraction of stable dark matter or decaying dark matter. We explore the CDF-II measurement's impact on those dark matter candidates.

The chapter is organized as follows: in Section 4.2, we briefly review the Higgs Triplet Model; in Section 4.3, we calculate the HTM's correction to the W mass at the one loop and give the preferred mass spectra for the new Higgses from the CDF-II measurement. We explore the phenomenology of this spectra in various aspects, including their contributions to the effective weak mixing angle in Section 4.4, the compatibility with the Higgs precision measurement in Section 4.5, the bounds and discovery channels from the LHC direct searches in Section 4.6, and their cosmological implications in Section 4.7. We conclude in Section 4.8. In the appendices, we give details of the self-energy corrections and the SM fitting formula and discuss the soft $\mathbb{Z}_2$ breaking limit, the unitarity and vacuum stability bounds, the Landau pole, and the decoupling limit of the HTM.

4.2 Higgs Triplet Model

In the HTM, the Higgs sector contains an isospin doublet Φ with hypercharge $Y = \frac{1}{2}$ and an isospin triplet Δ with $Y = 1$.[1] They can be parameterized as

$$\Phi = \begin{pmatrix} G^+ \\ \frac{v_\phi + h + iG^0}{\sqrt{2}} \end{pmatrix}, \quad \Delta = \begin{pmatrix} \frac{H^+}{\sqrt{2}} & H^{++} \\ \Delta^0 & -\frac{H^+}{\sqrt{2}} \end{pmatrix} \quad \text{with } \Delta^0 = \frac{v_\Delta + H + iA}{\sqrt{2}}, \tag{4.3}$$

where v_ϕ and v_Δ are the vacuum expectation values (vev's) of the doublet and triplet field obeying

$$v^2 \equiv v_\phi^2 + 2v_\Delta^2 \approx (246\,\text{GeV})^2. \tag{4.4}$$

In addition to the SM-like Higgs boson, the scalar sector contains six new Higgs bosons (degrees of freedom): the $\mathcal{CP}$-even H boson, the $\mathcal{CP}$-odd A boson, the singly-charged $H^\pm$ bosons, and the doubly-charged $H^{\pm\pm}$ bosons.

In this model, the tree level W and Z boson masses are given by

$$m_W^2 = \frac{g^2}{4}v^2, \quad m_Z^2 = \frac{g^2}{4c_W^2}(v^2 + 2v_\Delta^2), \tag{4.5}$$

where $c_W^2 \equiv \cos^2\theta_W$ and θ_W is the weak mixing angle. If we take the Z boson mass as

---

[1] Alternatively, one can also consider a adding a $Y = 0$ triplet to the SM. In this model, M_W receives a positive tree-level shift allowing to easily fit the CDF-II anomaly (see e.g. Refs. [185, 173]).

an input, the expected W boson mass is naively smaller than the SM prediction at the tree level

$$m_W = m_{W,\mathrm{SM}}^{\mathrm{tree}} \left(1 - \frac{v_\Delta^2}{v^2}\right) + \Delta m_W, \tag{4.6}$$

where Δm_W denotes loop corrections.

However, as we shall see below, a mass splitting between the new Higgs states can correct the W mass at the loop level with an opposite sign compared to the tree level correction. To explain the CDF-II result, it is preferred that the 1-loop correction dominates over the tree level correction, i.e., $v_\Delta \ll v$. Assuming the difference between the CDF-II measurement and the SM prediction mainly comes from the loop correction Δm_W, i.e.,

$$\frac{v_\Delta^2}{v^2} \ll \frac{m_{W,\mathrm{CDF-II}} - m_{W,\mathrm{SM}}}{m_{W,\mathrm{SM}}}\ , \tag{4.7}$$

this restricts $v_\Delta \ll 7.6$ GeV. To be concrete, we assume that $v_\Delta < 1$ GeV in the rest of the chapter. For simplicity, we will work in the limit $v_\Delta = 0$ for the calculation of the W mass correction, effective weak mixing angle, the Higgs di-photon rate, and the trilinear Higgs coupling (see below). Note that deviations from this limit will be suppressed by powers of $v_\Delta^2/v^2 \lesssim 2 \times 10^{-5}$ and will be ignored.

4.2.1 The Inert Triplet

The limit of $v_\Delta = 0$ can be realized in a strict sense by imposing a $\mathbb{Z}_2$ symmetry, under which Φ is $\mathbb{Z}_2$-even and Δ is $\mathbb{Z}_2$-odd. This $\mathbb{Z}_2$ can also be used to forbid the neutrino yukawa term typically seen in the Type-II seesaw model. The general gauge invariant potential is then given by

$$
\begin{aligned}
V(\Phi,\Delta) = {} & m^2\Phi^\dagger\Phi + M^2\mathrm{Tr}(\Delta^\dagger\Delta) \\
& + \lambda_1\left(\Phi^\dagger\Phi\right)^2 + \lambda_2\left[\mathrm{Tr}(\Delta^\dagger\Delta)\right]^2 + \lambda_3\mathrm{Tr}\left[(\Delta^\dagger\Delta)^2\right] \\
& + \lambda_4\left(\Phi^\dagger\Phi\right)\mathrm{Tr}(\Delta^\dagger\Delta) + \lambda_5\Phi^\dagger\Delta\Delta^\dagger\Phi,
\end{aligned}
\tag{4.8}
$$

where all the parameters in the potential can be taken to be real. The minimization of the potential yields

$$
m^2 = -\lambda_1 v^2, \quad v_\Delta = 0. \tag{4.9}
$$

In terms of the physical states, the quadratic part of the Higgs potential is

$$
\begin{aligned}
V(\Phi,\Delta) \supset {} & \frac{1}{2}(2\lambda_1 v^2)h^2 + \frac{1}{2}\left(M^2 + \frac{\lambda_4 v^2}{2}\right)\left(A^2 + H^2 + 2H^{++}H^{--} + 2H^+H^-\right) \\
& + \frac{1}{4}\lambda_5 v^2\left(A^2 + H^2 + H^+H^-\right) .
\end{aligned}
\tag{4.10}
$$

Then, the mass spectrum is given by

$$
\begin{aligned}
m_h^2 &= 2\lambda_1 v^2, \\
m_A^2 = m_H^2 &= M^2 + (\lambda_4+\lambda_5)\frac{v^2}{2}, \\
m_{H^+}^2 &= M^2 + \lambda_4\frac{v^2}{2} + \lambda_5\frac{v^2}{4}, \\
m_{H^{++}}^2 &= M^2 + \lambda_4\frac{v^2}{2}.
\end{aligned}
\tag{4.11}
$$

We can substitute the Higgs potential parameters m^2, M^2, λ_1, λ_5 by v, m_h^2, $m_{A,H}^2 = m_A^2 = m_H^2$, $m_{H^+}^2$, and $m_{H^{++}}^2$, where $v = (\sqrt{2}G_F)^{-1/2} \simeq 246$ GeV and $m_h \simeq 125$ GeV. The free parameters in this model are thus given by

$$
m_{A,H}, \quad m_{H^+}, \quad m_{H^{++}}, \quad \lambda_2, \quad \lambda_3, \quad \lambda_4 \tag{4.12}
$$

$$\boxed{\begin{array}{lll} \alpha_{\rm em}^{-1} = 137.035999084, & m_Z = 91.1876\ \text{GeV}, & G_F = 1.166378 \cdot 10^{-5}\ \text{GeV}^{-2}, \\ m_t = 172.76\ \text{GeV}, & m_h = 125.09\ \text{GeV}, & \alpha_s(m_Z^2) = 0.1179, \\ \Delta\alpha = 0.0591577. & & \end{array}}$$

Table 4.1: Input parameters used in computation. Note that $\Delta\alpha$ is the sum of the hadronic contribution $\Delta\alpha^{(5)}_{\rm had}(m_Z^2) = 0.02766$ and the leptonic contribution $\Delta\alpha_{\rm lept} = 0.031497687$ [11].

with the condition that

$$m_{H^+}^2 - m_{H^{++}}^2 = m_{A,H}^2 - m_{H^+}^2 = \frac{\lambda_5 v^2}{4}. \tag{4.13}$$

I.e., the coupling λ_5 controls the splitting of the mass spectrum. For the rest of the discussion, the model with $\lambda_5 > 0$ ($\lambda_5 < 0$) will be referred to as the type-I (II) Higgs triplet model, which has a mass ordering of $m_{H^{++}} < m_{H^+} < m_{A,H}$ ($m_{A,H} < m_{H^+} < m_{H^{++}}$), respectively.

4.3 One-loop corrected W boson mass

If H^{++}, H^+ and H, A have sizable mass splittings, i.e., if $|\lambda_5|$ is large, the HTM provides additional sources of custodial symmetry breaking, therefore correcting the W mass differently than the Z mass. We summarize our results below. Note that we perform this calculation in the limit $v_\Delta = 0$. Finite values for v_Δ compatible with the upper bound of Eq. (4.7) will only induce negligible small shifts of m_W. All necessary self-energy corrections are listed in App. 4.A (see also Ref. [247]). Tab. 4.1 lists all of the input parameters [3] used in the computation.

To determine the W mass from the measurement of the Fermi coupling constant G_F, we note that,

$$G_F = \frac{\pi \alpha_{{\rm em},0}}{\sqrt{2} m_{W,0}^2 s_{W,0}^2} \left(1 + \frac{\Pi_{WW}(0)}{m_W^2} + \delta_{VB} \right), \tag{4.14}$$

where terms with 0 subscripts are the bare parameters, Π_{WW} is the self-energy of the W, and δ_{VB} are the vertex and the box diagram corrections to the muon decay process. Rewriting this expression in terms of the physical parameters, one gets at the one-loop level that

$$G_F = \frac{\pi\alpha_{\rm em}}{\sqrt{2}m_W^2 s_W^2}\left(1+\frac{\delta\alpha_{\rm em}}{\alpha_{\rm em}}-\frac{\delta m_W^2}{m_W^2}-\frac{\delta s_W^2}{s_W^2}+\frac{\Pi_{WW}(0)}{m_W^2}+\delta_{VB}\right)\equiv\frac{\pi\alpha_{\rm em}}{\sqrt{2}m_W^2 s_W^2}(1+\Delta r), \tag{4.15}$$

where $\delta\alpha_{\rm em}$, δm_W^2, and δs_W^2 are the counterterms for the fine-structure constant $\alpha_{\rm em}$, the W mass, and weak mixing angle $s_W \equiv \sin\theta_W$, respectively. The counterterm of s_W^2 can be expressed in terms of the W and Z mass counterterms, which we define in the on-shell scheme,

$$\delta s_W^2 = -\delta c_W^2 = -c_W^2\left(\frac{\delta m_W^2}{m_W^2}-\frac{\delta m_Z^2}{m_Z^2}\right). \tag{4.16}$$

The $\alpha_{\rm em}$ counterterm, which we also define in the on-shell scheme, is given by

$$\frac{\delta\alpha_{\rm em}}{\alpha_{\rm em}} = \Pi'_{\gamma\gamma}(0)+2\frac{c_W}{s_W}\frac{\Pi^{\rm 1PI}_{Z\gamma}(0)}{m_Z^2}, \tag{4.17}$$

where $\Pi'_{\gamma\gamma}(0)\equiv d\Pi_{\gamma\gamma}(p^2)/dp^2|_{p^2=0}$. Combining everything, Δr is at the one-loop level given by

$$\begin{aligned}\Delta r = {}&\Pi'_{\gamma\gamma}(0)+\frac{\Pi^{\rm 1PI}_{WW}(0)-{\rm Re}\Pi^{\rm 1PI}_{WW}(m_W^2)}{m_W^2}+\frac{c_W^2}{s_W^2}\left(\frac{{\rm Re}\Pi^{\rm 1PI}_{WW}(m_W^2)}{m_W^2}-\frac{{\rm Re}\Pi^{\rm 1PI}_{ZZ}(m_Z^2)}{m_Z^2}\right)\\&+2\frac{c_W}{s_W}\frac{\Pi^{\rm 1PI}_{Z\gamma}(0)}{m_Z^2}+\delta_{VB}.\end{aligned} \tag{4.18}$$

The vertex and box diagram corrections to the muon decay, δ_{VB}, are given by (see e.g. Ref. [248])

$$\delta_{VB} = \frac{\alpha_{\rm em}}{4\pi s_W^2}\left(6+\frac{7c_W^2+3s_W^2}{2s_W^2}\ln c_W^2\right), \tag{4.19}$$

where we neglected the contributions proportional to the electron and muon Yukawa couplings.

Based on Eq. (4.15), we can then write

$$m_W^2 = m_Z^2 \times \left(\frac{1}{2} + \sqrt{\frac{1}{4} - \frac{\pi \alpha_{\text{em}}}{\sqrt{2} G_F m_Z^2} \left(1 + \Delta r(m_W)\right)} \right), \tag{4.20}$$

which we can iterate to solve for m_W.

For the numerical implementation, we follow the procedure outlined e.g. in [249]. We split Δr into three parts: the one-loop SM contributions that depend on m_W as an input ($\Delta r_{\text{SM},W}$), the remaining one-loop and higher-order SM contributions ($\Delta r_{\text{SM, rest}}$), and the beyond-the-Standard-Model (BSM) contributions (Δr_{BSM}),

$$\Delta r = \Delta r_{\text{SM},W}(m_{W,\text{BSM}}) + \Delta r_{\text{SM, rest}} + \Delta r_{\text{BSM}}. \tag{4.21}$$

The quantity $\Delta r_{\text{SM, rest}}$ is given by

$$\Delta r_{\text{SM, rest}} = \Delta r_{\text{SM}} - \Delta r_{\text{SM},W}(m_{W,\text{SM}}), \tag{4.22}$$

where $m_{W,\text{SM}}$ is computed from the fitting formula given in Ref. [250] (see App. 4.B). The fitting formula can also be used to obtain a number for Δr_{SM} (i.e., $\Delta r_{\text{SM}} \simeq 0.03807$). Combining the Eqs. (4.21) and (4.22) together yields

$$\Delta r(m_{W,\text{BSM}}) = \Delta r_{\text{SM}} - \Delta r_{\text{SM},W}(m_{W,\text{SM}}) + \Delta r_{\text{SM},W}(m_{W,\text{BSM}}) + \Delta r_{\text{BSM}}, \tag{4.23}$$

This equation consistently combines the full HTM one-loop corrections with the SM higher-order corrections, which are crucial for a precise result.

In the left (right) panel of Fig. 4.1, we show the resulting numerical value for m_W as a function of $|\lambda_5| = \lambda_5$ ($|\lambda_5| = -\lambda_5$) and $m_{\text{lightest}} = m_{H^{++}}$ ($m_{\text{lightest}} = m_{A,H}$) for the type-I (II) HTM.[2] In both panels, we depict the CDF measured (PDG) value as a brown

---

[2] A plot showing m_W as a function of the mass difference between the doubly- the singly-charged Higgs

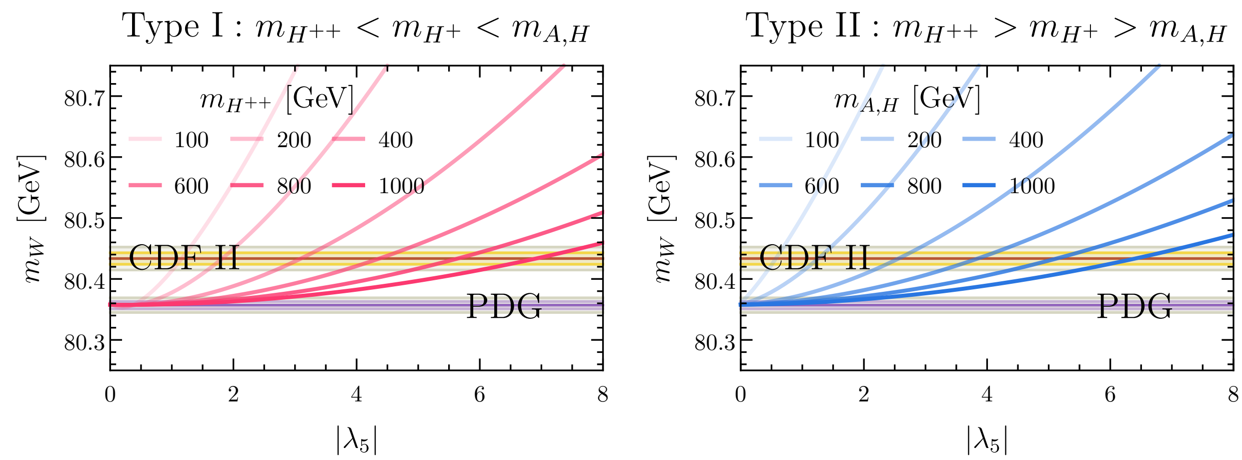

Figure 4.1: One-loop corrected W boson mass m_W as a function of the coupling $|\lambda_5| = 4|m^2_{H^+} - m^2_{H^{++}}|/v^2$ for various masses of the lightest state in the HTM. We assume the mass hierarchy of the new states following $m_{H^{++}} < m_{H^+} < m_A$ ($m_{H^{++}} > m_{H^+} > m_A$) in the left (right) panel. Different curves in each panel represent different masses for the lightest state. The brown (dark purple) line represent the CDF II measured (PDG) value and the yellow (purple)/gray band shows the $1\sigma/2\sigma$ intervals.

(dark purple) line, the 1σ region as a yellow (purple) band, and the 2σ region as gray bands. For a fixed value of the lightest BSM state m_{lightest}, the one-loop corrected W boson mass increases with $|\lambda_5|$. For a fixed shift in the W mass, a heavier m_{lightest} requires a larger value of $|\lambda_5|$. With the same m_{lightest}, the type-I model needs a larger value of $|\lambda_5|$ to obtain the same W mass shift compared to the type II.

The largish value of $|\lambda_5|$ required for large choices of m_{lightest} could potentially cause the appearance of a Landau pole close to the electroweak scale. As we show in App. 4.E, no Landau pole appears below ~ 10 TeV. This makes the additional contribution from the UV completion above the Landau pole subleading in comparison to those considered here.

Furthermore, we scan m_{lightest} and λ_5 to pinpoint the parameter regions predicting a m_W value close to the CDF-II measurement. The resulting mass spectra for the new Higgs states are shown in Fig. 4.2. The first, third, and fifth (second, fourth, and sixth) panels respectively represent the spectra for the type-I (II) HTM that yield the m_W value measured

---

bosons alongside a discussion of the decoupling of the BSM states can be found in App. 4.F.

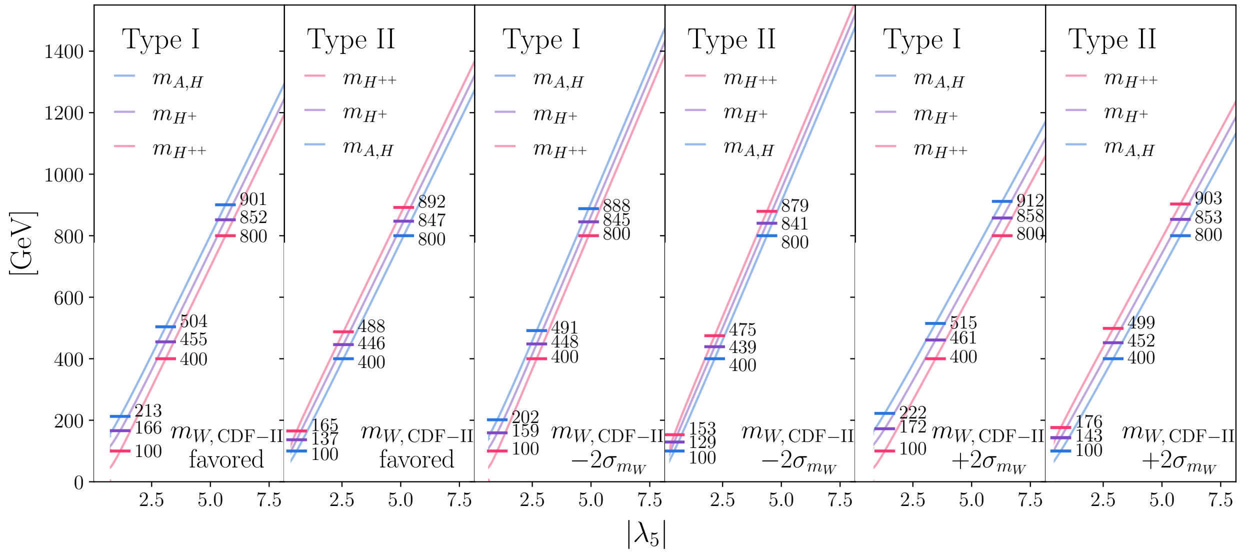

Figure 4.2: Mass spectrum of the new Higgs states for a given $|\lambda_5|$ that yields the CDF-II measured central values of m_W, $m_W - 2\sigma_{m_W}$, or $m_W + 2\sigma_{m_W}$ for the type-I and type-II HTM. We exclude the mass spectrum that corresponds $m_{H^{++}} < 42.9\,\text{GeV}$ (excluded by Z decays [1]) for the type-I model and that corresponds to $m_{A,H} < m_h/2 = 62.5\,\text{GeV}$ (excluded by Higgs precision measurement, see Sec. 4.5.2) for the type-II model. In each panel, we explicitly show three sets of benchmark values.

by CDF-II, the CDF-II value plus two times the experimental one-sigma uncertainty, and the CDF-II value minus two times the experimental one-sigma uncertainty. The blue, purple, and red lines in each panel represent the corresponding values of $m_{A,H}$, m_{H^+}, and $m_{H^{++}}$, respectively. We also explicitly show three sets of benchmark values for each scenario. For the type-I HTM, we do not show the mass spectrum corresponding to $m_{H^{++}} < 42.9\,\text{GeV}$ since it is excluded by the measurement of Z boson decays [1]. For the type-II HTM, we do not show the mass spectrum corresponding to $m_{H,A} < m_h/2 = 62.5\,\text{GeV}$ given it is excluded by the precision measurement of exotic Higgs decays as we discuss in Sec. 4.5.2. Note that there are stronger yet model-dependent constraints on the HTM mass spectrum from direct collider searches. We will summarize them in detail in Sec. 4.6.

4.4 Effective weak mixing angle

After obtaining the preferred spectra of the HTM, we assess whether these are compatible with the electroweak precision data by computing the effective weak mixing angle, $\sin^2\theta_{\text{eff}}$. In this computation, α_{em}, M_Z, and G_F are chosen as inputs. Experimentally, $\sin^2\theta_{\text{eff}}$ is defined as the ratio of the leptonic vector current to the leptonic axial current at the Z pole. The deviation from the tree-level value of the mixing angle, s_W^2, can be parameterized by $\Delta\kappa$, where

$$\sin^2\theta_{\text{eff}} = s_W^2(1+\Delta\kappa). \tag{4.24}$$

At one-loop, $\Delta\kappa$ obtains contributions from $A-Z$ mixing, corrections to the weak mixing angle, and corrections to the axial/vector vertices,

$$\begin{aligned}\Delta\kappa = & -\frac{c_W}{s_W}\left(\frac{\text{Re}\Pi^{\text{1PI}}_{Z\gamma}(m_Z^2)}{m_Z^2}\right) - \frac{c_W^2}{s_W^2}\left(\frac{\text{Re}\Pi^{\text{1PI}}_{WW}(m_W^2)}{m_W^2} - \frac{\text{Re}\Pi^{\text{1PI}}_{ZZ}(m_Z^2)}{m_Z^2}\right) \\ & + \frac{v_l}{v_l-a_l}\left(\frac{F_V^l(m_z^2)}{v_l} - \frac{F_A^l(m_z^2)}{a_l}\right),\end{aligned} \tag{4.25}$$

where v_l and a_l are the tree-level vector and axial couplings respectively, and $F^l_{V,A}$ are the form-factors for the leptonic vector/axial currents. Since the extra Higgs bosons do not couple to the SM fermions, they do not contribute to $F^l_{V,A}$.

We compute the SM contribution to $\sin^2\theta_{\text{eff}}$ with the help of the SM fitting formula. Similar to the treatment of Δr, we split $\Delta\kappa$ into three pieces,

$$\Delta\kappa = \Delta\kappa_{\text{SM},W}(m_{W,\text{BSM}}) + \Delta\kappa_{\text{SM, rest}} + \Delta\kappa_{\text{BSM}}\ . \tag{4.26}$$

$\Delta\kappa_{\text{SM, rest}}$ is determined via

$$\Delta\kappa_{\text{SM}} = \Delta\kappa_{\text{SM},W}(m_{W,\text{SM}}) + \Delta\kappa_{\text{SM, rest}}, \tag{4.27}$$

where $\Delta\kappa_{\rm SM} \simeq 0.03640$ is computed from the fitting formula given in Ref. [251] (see App. 4.B) and $\Delta\kappa_{{\rm SM},W}(m_{W,{\rm SM}}) \simeq 0.03628$ is Eq. (4.25) restricted to the SM contribution only, which explicitly depends on m_W.

In Fig. 4.3, we check whether the parameter space of the HTM that predicts m_W close to the CDF-II value is compatible with the measured effective mixing angle. The upper (lower) row of Fig. 4.3 shows the resulting $\sin^2\theta_{\rm eff}$ vs. m_W plot for a given $m_{\rm lightest}$ in the interval $[100~{\rm GeV}, 1000~{\rm GeV}]$ and $|\lambda_5| \in [0, 10]$ for the type-I (II) HTM. For each panel, we highlight the CDF-II (PDG) m_W value as the brown (dark purple) vertical lines while the yellow (purple) and gray vertical bands show the 1σ and 2σ ranges, respectively. The dark green horizontal lines in the left column represent the world-average value for the effective weak mixing angle [2, 3] while the green and gray horizontal band shows 1σ and 2σ range respectively. For comparison, we show in the right column the value of the single most precise effective weak mixing angle measurement obtained by the SLD collaboration [2].

In the limit of $|\lambda_5| = 0$, the type-I/II HTM predicts a W boson mass that agrees well with the world-averaged value. The effective weak mixing angle also agrees well with its world-average. As $|\lambda_5|$ increases, the resulting m_W increases while the resulting $\sin^2\theta_{\rm eff}$ decreases.[3] On the other hand, a change in $m_{\rm lightest}$ has a less significant impact (at least for $m_{\rm lightest} \gtrsim 400\,{\rm GeV}$). Note that a heavier $m_{\rm lightest}$ yields a larger deviation from the world average for $\sin^2\theta_{\rm eff}$ for the type-I model while it yields a smaller departure for type II. For the type-I model, the parameter space that explains $m_{W,\text{CDF-II}}$ is consistent with the world averaged value of $\sin^2\theta_{\rm eff}$ within 2σ level. For the type-II model, the two measurements are inconsistent at the 2σ level for the $m_{\rm lightest}$–$|\lambda_5|$ parameter space that we scanned. If we instead compare $\sin^2\theta_{\rm eff}$ to the value measured by the SLD collaboration [2], we find that the parameter space explaining $m_{W,\text{CDF-II}}$ is consistent with the measured $\sin^2\theta_{\rm eff}$ within the 2σ level for both type-I and -II mass hierarchies.

---

[3] In the limit of small $|\lambda_5|$, the correction to both the W mass and effective mixing angle is sensitive to the sign of λ_5. In particular, this results in the turning behavior seen for the type-I HTM.

In the Two-Higgs-doublet model (2HDM), for which also large upwards shift of m_W with respect to the SM prediction can be realized, a quite similar correlation between the predictions for m_W and $\sin^2\theta_{\text{eff}}$ is known to exist (see e.g. Ref. [167]). In comparison to the 2HDM, the type-I triplet model provides a slightly better fit of the effective weak mixing angle measurements if the the lightest BSM state is close to the electroweak scale; in contrast, the type-II triplet model provides a slightly worse fit if the lightest BSM state is close to the electroweak scale.

4.5 Precision measurement of the Standard Model Higgs

For $v_\Delta \simeq 0$, the tree-level couplings of the SM-like Higgs boson are only modified negligibly with respect to the SM. Significant effects can, however, occur a the loop level or through the presence of new exotic decay modes.

4.5.1 Higgs-photon coupling and Higgs self-coupling

We define the ratio of the coupling between the SM-like Higgs boson and photon to the SM predicted coupling by

$$\kappa_\gamma^2 \equiv \frac{\Gamma_{H\to\gamma\gamma}}{\Gamma^{\text{SM}}_{H\to\gamma\gamma}}.$$

For the triplet model, it is given by

$$\kappa_\gamma^2 = \frac{\left|\frac{4}{3}F_{1/2}(\tau_t) + \ldots + Q^2_{H^{\pm\pm}}\frac{v^2\lambda_{hH^{\pm\pm}H^{\mp\mp}}}{m_h^2}F_{\pm}(\tau_{H^{\pm\pm}}) + Q^2_{H^{\pm}}\frac{v^2\lambda_{hH^{\pm}H^{\mp}}}{m_h^2}F_{\pm}(\tau_{H^{\pm}})\right|^2}{\left|\frac{4}{3}F_{1/2}(\tau_t) + \ldots\right|^2}, \tag{4.28}$$

where Q denotes the electric charge; $\tau_f \equiv m_h^2/(4m_f^2)$; and the ellipsis denotes subleading SM contributions. The scalar couplings are given by

$$\lambda_{hH^{\pm\pm}H^{\mp\mp}} = -v\lambda_4, \quad \lambda_{hH^{\pm}H^{\mp}} = -v(\lambda_4 + \lambda_5/2). \tag{4.29}$$

The loop functions $F_{1/2}$ and $F_{\pm}$ have the form

$$F_{1/2}(\tau) = \frac{(\tau-1)f(\tau)+\tau}{\tau^2}, \quad F_{\pm}(\tau) = \frac{\tau - f(\tau)}{\tau} \tag{4.30}$$

with

$$f(\tau) = \begin{cases} \arcsin^2(\sqrt{\tau}) & \text{if } \tau \le 1, \\ -\frac{1}{4}\left(\ln\frac{1+\sqrt{1-1/\tau}}{1-\sqrt{1-1/\tau}} - i\pi\right)^2 & \text{if } \tau > 1. \end{cases} \tag{4.31}$$

We evaluate the LHC constraints set on the triplet couplings through modifications of the $H \to \gamma\gamma$ rate by employing `HiggsSignals` [252, 253].

In addition to the di-photon rate, we also evaluate loop corrections to the trilinear Higgs self-coupling, which can receive large quantum corrections in the presence of large scalar couplings potentially excluding otherwise unconstrained parameter space (see e.g. Ref. [254]).

We compute the one-loop correction using `FeynArts` [255] and `FormCalc` [256] with the necessary model file derived using `FeynRules` [257, 93]. For this calculation, we renormalize the SM-like Higgs boson mass in the on-shell scheme. The SM-like vev is also renormalized in the on-shell scheme by renormalizing the W and Z boson masses as well as the electric charge in the on-shell scheme.

We compare the predicted value for the trilinear Higgs self-coupling normalized to the SM tree-level value, κ_λ, to the strongest current bound of $-1.0 \le \kappa_\lambda \le 6.6$ [258] (at 95% CL). This bound is based on searches for the production of two Higgs bosons and assumes that this production mechanism is only affected by a deviation of the trilinear Higgs self-coupling from its SM value. While quantum corrections to double-Higgs production are not only induced by corrections to the trilinear Higgs self-coupling, evaluating the one-loop corrections to the trilinear Higgs self-coupling takes into account all one-loop corrections to double Higgs production leading in powers of scalar couplings. Since the scalar couplings are responsible for the dominant deviation from the SM, this justifies applying the bound of Ref. [258].

The constraints in the $(m_{H^{++}}, m_{H^+})$ parameter plane due to modifications of κ_γ and κ_λ are shown in Fig. 4.4. The blue shaded region shows the excluded parameter space by measurements of the Higgs di-photon rate (demanding compatibility at 95% CL); the orange shaded region is excluded by the constraint on the trilinear Higgs couplings (at 95% CL). Moreover, we show the constraints set by perturbative unitarity (green hashed region) and by the (meta-)stability of the electroweak vacuum (red hashed region), which we evaluate as detailed in App. 4.D. Note that we set $\lambda_4 = 0$ and $\lambda_2 = \lambda_3 = 1$ in drawing the plots.[4]

For the left panel of Fig. 4.4, we concentrate on the type-I hierarchy. Almost the complete lower right half of the parameter plane is excluded by requiring metastability of the electroweak vacuum. Perturbative unitarity excludes large differences between $m_{H^{++}}$ and m_{H^+}. Measurements of the Higgs to di-photon rate additionally exclude a portion of the parameter space around $m_{H^{++}} \sim 300\,\text{GeV}$ and $m_{H^{++}} \sim 450\,\text{GeV}$ unconstrained by perturbative unitary and vacuum stability. The experimental measurements of the Higgs trilinear coupling are, so far, not precise enough to probe parameter space unconstrained by perturbative unitarity and vacuum stability in the considered scenario. We find, the parameter space favored by the CDF-II measurement of m_W (red narrow band) with $m_{H^{++}} \gtrsim 250\,\text{GeV}$, which lies close to the diagonal, to not lie in the parameter space excluded by the above mentioned constraints. In addition to the constraints discussed above, we also show the

---

[4] Larger values for λ_4 tighten the constraints from $h \to \gamma\gamma$. Larger values for $\lambda_{2,3}$ tighten the perturbative unitarity constraint while relaxing the vacuum stability constraint.

LHC constraints on $m_{H^{++}}$ if H^{++} decays promptly (gray band) or if it is detector stable (gray dash line). These constraints are discussed in detail in Sec. 4.6.2 below.

For type II (see the right panel of Fig. 4.4), the constraints set by the Higgs couplings, perturbative unitarity and vacuum stability are unchanged. The parameter space favored by the CDF-II m_W measurements (blue narrow bands) is, however, shifted downwards with respect to the type-I hierarchy. As a result, the parameter space favored by the CDF-II m_W measurements lies at the boundary of the region excluded by demanding vacuum stability. The parameter space favored by $m_{W,\text{CDF-II}}$ is only accessible for $m_{H^{++}} \lesssim 350\,\text{GeV}$. Note, however, that the evaluating of the vacuum stability constraint relies on various assumptions (see App. 4.D).

4.5.2 Exotic decays of the Higgs boson

For the type-I HTM, the branching ratio for $h \to H^{++}H^{--}$ depends on λ_4 (see Eq. 4.29). This coupling needs to be small ($\lesssim 1$ for $m_{\text{lightest}} \sim \mathcal{O}(100)$ GeV) in order to evade constraints from the di-photon decay rate of the SM-like Higgs boson. This leads to negligibly small exotic decay modes for the SM-like Higgs boson (if at all kinematically accessible). The situation is quite different for the type-II HTM. In this case, the exotic decay modes of the SM-like Higgs boson are mainly given by $h \to HH$, $h \to AA$, and $h \to H^+H^-$ once they are kinetically accessible. Their branching ratios mostly depend on λ_5 (4.29), which needs to be large to explain the CDF-II measurement of m_W.

We compute the branching ratio for the SM-like Higgs boson decays to the BSM Higgs states for the type-II model as a function of $m_{A,H}$ for the parameter space that explains $m_{W,\text{CDF-II}}$. We find the resulting branching ratio to lie between 80%−97% if the decay modes are kinematically accessible ($m_{A,H} < m_h/2$). Such a large branching ratio for the exotic decays is in tension with the Higgs precision measurements from the LHC. For example, the ATLAS experiment places a 95% CL constraint of $\text{Br}(h \to \text{BSM}) = \text{Br}(h \to \text{inv}) + \text{Br}(h \to$

undetected) $< 49\%$ [259]. A similar constraint has also been placed by CMS experiment [260]. These constraints exclude the type-II model if neutral states are lighter than $m_h/2$.

4.6 Direct searches at the LHC

In this Section, we study potential LHC signals of the new scalars with a spectrum preferred by $m_{W,\mathrm{CDF-II}}$. As we have demonstrated in the previous sections, an explanation of the W mass deviation in the context of the HTM points to new Higgs bosons below a TeV which makes them targets for direct searches at the LHC. As a guide for the dedicated experimental searches in the future, the main goal of this section is to highlight the promising search channels with distinct signatures. Of course, some of the LHC searches designed to look for different signal processes would also have sensitivity to the signals considered here. To this end, we recast some of the most relevant searches. Instead of providing detailed limits on the model, our focus is to obtain an indication whether the parameter space has been thoroughly covered. As we will show later in this section, most of the parameter space remains open. We expect dedicated searches designed specifically for the signature described in this section will be much more sensitive. For the rest of this section, we start by discussing the various production channels for the BSM states. We then differentiate between three situations for the decays of the BSM Higgs states resulting in distinct collider signatures: a promptly-decaying lightest BSM state, a detector-stable lightest BSM state, a long-lived lightest BSM state.

4.6.1 Production

In the absence of additional Yukawa-type interaction terms and for $v_\Delta \ll v$, the exotic Higgs states are dominantly produced via electroweak pair production as shown in the upper row of Fig. 4.5.

In order to obtain an overview of the rate of the various production channels, we computed the next-leading-order (NLO) pair production cross sections for both mass hierarchies using a modified version of the TYPE-II SEESAW model file [261] (derived using `FeynRules 2.3` [93]) and `MG5aMC@NLO v2.9.10` [91]. The dependence of the production cross sections on the lightest BSM state mass in the respective model type is shown in Fig. 4.6. Here, we have chosen the mass spectrum such that we can reproduce the CDF-II central value for m_W as shown in Fig. 4.2.

For type I (see left panel of Fig. 4.6), the $pp \to H^{\pm\pm}H^{\mp}$ channel mediated by a W boson has the largest cross section of up to ~ 1 pb for $m_{H^{++}} \sim 100$ GeV. The $pp \to H^{\pm\pm}H^{\mp\mp}$ production cross section is of similar size (especially for lower mass values). Less important are the $pp \to H^{\pm}H + H^{\pm}A$, $pp \to HA$, and the $pp \to H^{\pm}H^{\mp}$ production channels.

The overall behavior is similar for type II (see right panel of Fig. 4.6). As a consequence of H and A being the lightest BSM Higgs bosons, the $pp \to H^{\pm}H + H^{\pm}A$ and $pp \to HA$ channels have, however, now the largest cross sections given their larger phase spaces. Their cross sections reach ~ 1 pb for $m_{H,A} \sim 100$ GeV.

In our discussion of potential search strategies at the LHC below, we will only focus on the production channels with the largest cross sections.

4.6.2 Detection signatures

In order to correctly reproduce the W mass measured by CDF-II, the triplet vev v_Δ generically needs to be small. Given the size of v_Δ is controlled by the amount of soft breaking, a small value can be naturally achieved. If the triplet vev is exactly zero, the lightest triplet state is stable. This implies that the choice of v_Δ directly affects the lifetime of the lightest state, thus affecting the detection signature at the LHC. We discuss the cosmological implications in Sec. 4.7.

In Fig. 4.7, we show this lifetime of the lightest state for different choices of v_Δ ranging from 10^{-8} GeV to 1 GeV for the type-I/II HTM. For $v_\Delta \sim 10^{-4}$ GeV, the lifetime of the lightest state is generically of the order of the B-meson lifetime. As such, any decay products of the lightest state will be tagged as displaced. For $v_\Delta \sim 10^{-8}$ GeV, the lifetime is generically orders of magnitude greater than the radius of the detector. In this case, the lightest state is unlikely to decay within the detector volume.

We further show the decay branching ratio of H and A for type-II model in Fig. 4.8 (assuming a small but finite v_Δ).[5] Generically, the branching ratio of the dominant decay mode is always very close to one. This dominant decay mode depends on whether or not the preferred final state is kinematically accessible. For the $\mathcal{CP}$-even BSM Higgs boson, H, the important thresholds are the hh and WW mass thresholds. For the $\mathcal{CP}$-odd Higgs boson, A, the important threshold is the Zh mass threshold. Below the lowest mass threshold, they both predominantly decay to $b\bar{b}$ due to the bottom Yukawa inherited from its mixing with the SM Higgs doublet.

In the remainder of the section, we discuss the qualitatively different LHC signatures for the three different lifetime domains: prompt decay of the lightest state, detector-stable lightest state, long-lived lightest state.

The lightest state promptly decays

An overview of the main LHC search channels for a promptly decaying lightest BSM state for the type-I and type-II HTM can be found in Tab. 4.2.

For type-I HTM, the production process with the largest cross section is $pp \to H^{\pm\pm}H^{\mp}$. The singly-charged Higgs boson then decays to a doubly-charged Higgs boson via emission of a W boson, $H^{\mp} \to H^{\mp\mp}W^{\pm}$. All doubly-charged Higgs bosons will then promptly decay into a pair of W bosons, $H^{\pm\pm} \to W^{\pm}W^{\pm}$, with branching ratio ≈ 1. (c.f., the lower left diagram of Fig. 4.5.) As such, the corresponding search channel will be a final state of five W bosons. These W bosons could be off-shell depending on the masses.

---

[5] Branching ratios for the lightest state in the type-I HTM, H^{++}, can be found in e.g. in Ref. [1].

Type I, Prompt	
Main Channels	Example Signature
$pp \to H^{\pm\pm}H^{\mp} \to H^{\pm\pm}(H^{\mp\mp}W^{\pm}) \to 5W^{(*)}$	$5\ \ell + \not{E}_T$
$pp \to H^{++}H^{--} \to (W^{+}W^{+})(W^{-}W^{+})$	$4\ \ell + \not{E}_T$
$pp \to H^{\pm}H(A) \to H^{\pm}(H^{\pm}W^{\mp}) \to (H^{\pm\pm}W^{\mp})(H^{\pm\pm}W^{\mp}W^{\mp}) \to 7W^{(*)}$	$7\ell + \not{E}_T$

Type II, Prompt		
$m_{H,A}$	Main Channels	Example Signature
$\lesssim 250$ GeV	$pp \to H^{\pm}H/A \to W^{\pm(*)}b\bar{b}b\bar{b}$	monolepton+up to 4 b-jets+$\not{E}_T$
	$pp \to HA \to bbbb$	up to 4 b-jets
$\gtrsim 250$ GeV	$pp \to H^{\pm}H/A \to (W^{\pm}H/A)H/A,\ H/A \to hh/Z$	multi b-jets + leptons+$\not{E}_T$
	$pp \to HA \to Zhhh$	up to 6 b-jets + leptonic Z

Table 4.2: Summary of main channels and example search signatures for additional Higgs bosons of the HTM that promptly decay at the LHC. The upper and lower tables consider the type-I and II HTM, respectively. See text for more details.

No dedicated searches for this channel exist so far. To nevertheless gain an estimate for the LHC sensitivity for this signature, we use `CheckMATE 2.2` [262, 148, 263, 150, 264, 149, 265] to recast a large set of existing searches on a set of benchmark points. `CheckMATE` will generically summarize the result with $r = S/S_{95}$, where S is the number of signal events and S_{95} is the 95% C.L. limit on the number of signal events for the given analysis. For statistically limited searches, one would expect r to scale as $\sqrt{\int \mathcal{L}dt}$. We will use this naive scaling to make statements about potential reach with searches involving more data.

We find that $m_{H^{++}} = 150$ GeV can be excluded by recasting the multi-lepton final state search of Ref. [266] (i.e., by the B02 signal region). Based on this channel, one could potentially expect to fully close the gap of $84\,\text{GeV} \leq m_{H^{++}} \leq 200\,\text{GeV}$ between the searches for doubly-charged Higgs boson pair production based, as described below. We also checked a benchmark point of $m_{H^{++}} = 350$ GeV. Here, we expect four on-shell W bosons and one off-shell W boson in the final state. This benchmark is not constrained, for example, by using the search of Ref. [266] in the G05 signal region. Applying the naive integrated luminosity based rescaling indicates that the full high-luminosity (HL)-LHC dataset (3 ab^{-1}) can exclude this mass point; albeit with an analysis that is not dedicated to searching for a doubly-charged Higgs.

In the type-I HTM, the process with the second largest cross section is doubly-charged Higgs boson pair production, $pp \to H^{\pm\pm}H^{\mp\mp}$. The corresponding search channel involves a final state of four W bosons. A dedicated search for this signature has been performed by ATLAS using 13 TeV data [267, 268] . Their search excludes doubly charged Higgs promptly decaying into W bosons with masses $200\,\text{GeV} \leq m_{H^{++}} \leq 350\,\text{GeV}$. Studies recasting 8 TeV ATLAS data excludes the mass range $m_{H^{++}} < 84\,\text{GeV}$ [1, 269].

Another significant production process for the type-I HTM is $pp \to H^{\pm}H/A$. The neutral Higgs boson in the type-I HTM decays to a singly-charged Higgs boson via $W^{(*)}$ emission with a branching ratio close to one. ($H/A \to W^{\mp}H^{\pm}$, c.f., the lower left diagram of Fig. 4.5.) Fully decaying all of the extra Higgs bosons will generate a final state of seven $W^{(*)}$ bosons. The corresponding experimental final state will contain various jets, leptons and missing transverse energy. We have checked a benchmark point with $m_{H^{++}} = 350$ GeV using the search in Ref. [270] in signal region SR12, and found that it is not sensitive to this point.

For the type-II HTM, the production process with the largest cross section is $pp \to H^{\pm}H/A$. The singly-charged Higgs boson will decay to H/A via W boson emission, $H^{\pm} \to W^{\pm}H/A$; both H and A have roughly the same probability of being produced. From Fig. 4.8, the neutral Higgs boson will likely decay to either to a heavy fermion pair or a pair of SM bosons. As before, all of these SM bosons could be off-shell. For this scenario, we ran `CheckMATE` for both $m_H = 100$ GeV and $m_H = 300$ GeV. We find both benchmark values to be allowed using the built-in 13 TeV run analyses. The $m_H = 100$ GeV benchmark point scenario yielded $r \approx 0.6$ using the search of Ref. [271] in the $3b1j$ signal region. As this study only used 3.2 fb^{-1} of 13 TeV data, one could potentially exclude the benchmark (i.e., cases where di-boson decays are kinematically forbidden) at 2σ using a dedicated search with existing data. The $m_H = 300$ GeV benchmark point yielded $r \approx 0.1$ using the search of Ref. [270]. Even with the full HL-LHC dataset, it seems unlikely that a re-analysis could exclude this parameter point based on naive rescaling alone. This analysis is not dedicated to this particular search. It does not make use of the h or Z in the final state.

For the type-II HTM with a light H/A, $pp \to HA$ production can be sizable. For $m_H = 100$ GeV, recasting Ref. [271] in the same signal regions as the previous production mode yielded $r \approx 0.4$. Once again, naive luminosity based scaling indicates that existing data is potentially sufficient to exclude this. For $m_H = 300$ GeV, we obtained $r \approx 0.02$ using [271] in the $4b1j$ signal region. Accounting for the differences in integrated luminosity used in this and Ref. [270], the exclusion reach comparable to the previous production mode. It should be noted that this production mode ensures a Z boson in the final state. Reconstructing it can potentially reduce the background.

The lightest state is detector stable

In this section, we consider the case in which the lightest member of the Higgs triplet is stable on detector timescales. This can be achieve with a small $v_\Delta \lesssim 10^{-8}$ GeV.

In type I, if the lightest state is detector stable, charged tracks in multiple subsystems of the detector are a generic signature. ATLAS presented a search for such tracks excluding doubly-charged particles masses below 1050 GeV [272]. The unexcluded mass regions will typically require very large values of λ_5 to give the desired shift in the W mass as shown in Fig. 4.2.

In type II, starting with the $pp \to H^\pm H/A$ production, a generic final state consists of W^* and missing transverse energy (MET). As such, the search channels are either monolepton + MET or dijet + MET. Recasting existing searches using `CheckMATE` did not yield any exclusions for the $m_H = 100$ GeV benchmark point. $pp \to H^{\pm\pm}H^\mp$ production leads to a different final state with more visible particles. The final state consists now out of three $W^{(*)}$ boson. The final state signature could be three charged leptons + MET, two charged leptons + jets + MET, monolepton + jets + MET, or jets + MET. We will focus on the three charged lepton signature. Our recasting with this benchmark show that current searches, such as the one in Ref. [266], is not yet sensitive. Naively rescaling based on the full HL-LHC integrated luminosity shows that this analysis barely misses the exclusion. Lastly, for $pp \to HA$ production, the main search channel is a mono-jet or mono-photon + MET signature (with the jet or photon originating from initial-state radiation). Current available searches, such as Ref. [271] in the MET1j signal region, are not sensitive. This scenario can potentially be excluded using the full HL-LHC dataset.

The lightest state is long-lived

If the charged particle decays before reaching the muon spectrometer, the previously mentioned ATLAS charged track search [272] is not sensitive to it. If the particle decays in the inner tracker, the signal caused by doubly-charged Higgs bosons will be disappearing tracks plus delayed multi-lepton/multi-jet final states. Depending on the initial state, one may also expect prompt off-shell W bosons. These prompt jets/leptons could be used to tag the events provided that the intrinsic jet time spread is sufficiently low [273]. It should also be noted that recently ATLAS found am anomalously large ionization energy loss [274]. A highly boosted, long-lived, doubly-charged particle is a potential explanation to explain this excess [275] suggesting that $H^{\pm\pm}$ could be a good candidate. A large partonic center-of-mass energy could provide the desired boost. A detailed study should be performed to determine the viability of the HTM as an explanation for the dE/dx anomaly.

For the neutral Higgs states, Ref. [276] could be recasted for pair production of the neutral Higgs. However, the only hard objects in this production mode are delayed objects. Generically, we expect a search strategy involving prompt jets/lepton tagging + delayed jets/leptons to be better. Furthermore, for $m_A > 215$ GeV, the dominant decay mode involves an on-shell Z boson. Reconstructing a delayed Z boson will be a good signal to search for.

4.7 Cosmological implications

For sufficiently small v_Δ, the lifetime of the lightest states in type-II, H and A, could be longer than the age of the Universe. Given H and A are electrically neutral, they could provide a good candidate for dark matter or a massive relic. To explain the m_W value measured by CDF-II, a large $|\lambda_5|$ is needed. This requires H and A to strongly couple to h. Such strong couplings yield a small relic density for H/A if they are produced through the standard thermal freeze-out. The large couplings also lead to large scattering cross sections between H/A and nucleons as well as the production of significant amounts of electromagnetic or hadronic energy if they are not cosmologically stable.

We first compute the thermal relic density for A and H using `MadDM 3.2` [277]. The upper panel of Fig. 4.9 shows the resulting sum of the relative relic abundances for H and A with respect to that of cold dark matter, $f_\chi \equiv \Omega_{H+A}/\Omega_c$ as a function of $m_{A,H} \equiv m_H \simeq m_A$[6] for model parameters that explains the CDF-II measured m_W within 2σ. The relative relic abundance of A and H ranges from 10^{-7} to 10^{-1} of the total dark matter abundance. It reaches a maximum of 7% around $m_{A,H} \approx m_W$ and converges to $\sim 1\%$ for $m_{A,H} > 700\,\text{GeV}$. The dips around $m_{A,H} = m_Z/2$ and $m_{A,H} = m_h/2$ correspond to the resonant enhancement of the annihilation cross sections. Note that the parameter space below $m_{A,H} < m_h/2$ (shaded in gray) is excluded by Higgs precision measurements at the LHC (see Sec. 4.5.2). If we restrict $m_{H,A}$ to be away from the resonant region of $m_h/2$, i.e. $m_{H,A} > 63\,\text{GeV}$, the relative abundance f_χ varies from 0.08% to 7%.

To discuss the observational signatures of the massive relic, we consider two scenarios according to the lifetime of H and A: (i) H and A are cosmologically stable and (ii) H and A are cosmologically unstable.[7] For the parameters that explain $m_{W,\text{CDF-II}}$, the lifetime

---

[6] The mass splitting between H and A is at $\mathcal{O}(v_\Delta^2/v^2)$. It is negligible for the value of v_Δ we are interested in.

[7] We do not consider the scenario where A is stable and H is unstable given the small difference in their lifetimes for a fixed v_Δ compared to the cosmological timescales.

of H and A mostly depends on the size of v_Δ and weakly depends on $m_{H,A}$. Besides the two parameters, the observational signature of the massive relic additionally depends on f_χ, which is determined by $m_{A,H}$ as shown in the upper left panel of Fig. 4.9.

4.7.1 Stable massive relic

For scenario (i), H/A could enter dark matter direct detection experiments on Earth and leave imprints even if they are subdominant components of dark matter. Given H/A are thermally produced in the early universe, their lifetime coincides with the age of the Universe. To realize the stable relic scenario, the lifetime for H/A needs to be longer than the age of universe today $\tau_{H,A} \gtrsim \tau_U = 10^{18}\,\text{sec}$. A stronger constraints on $\tau_{A,H}$ comes from the observations of the diffused γ-ray backgrounds [278, 279, 280, 9]. Observations from Fermi-LAT telescope restrict the decaying time of dark matter $\tau_\chi \gtrsim 10^{28}\,\text{sec}$ if it consists all the dark matter [9]. We translate this bound into $\tau_{H,A} \gtrsim 10^{28} f_\chi\,\text{sec}$ if only an f_χ fraction of dark matter decays visibly. This is shown as the brown shaded region in the right panel of Fig. 4.9. To satisfy the constraint, v_Δ needs to be small. In the right panel of Fig. 4.9, we explicitly show the value of v_Δ for a given lifetime for A with mass $m_A = 1.5\,\text{TeV}$ as the blue upper ticks. For the $m_{A,H}$ parameter space we consider, we find that setting

$$v_\Delta \lesssim 10^{-16}\,\text{eV}$$

guarantees the cosmological stability.

We use `MadDM 3.2` [277] to compute the spin-independent direct detection cross section for A and H. The lower panel of Fig. 4.9 shows the corresponding sum of the spin-independent direct detection cross section between the nucleon and H/A, weighted by the relative abundance. In the computation, we assume the relative abundance f_χ between the massive relic and cold dark matter stays the same for the local dark matter environment (with cold dark matter density $\rho_{\text{local}} = 0.3\,\text{GeV/cm}^3$). Besides, the two share the same velocity distribution. The resulting weighted cross section (blue band), which is favored to explain $m_{W,\text{CDF-II}}$, is ranging from $10^{-49}\,\text{cm}^2$ to $10^{-44}\,\text{cm}^2$ for $m_{A,H}$ ranging from 30 GeV to 1.5 TeV. In the same panel, we also show 95% CL constraint from the LUX-ZEPLIN (LZ) experiment with 5.5 ton·60 day exposure, where we scale up the cross section by 1.96/1.64 to estimate 95% CL limit based on the 90% CL limit reported in [4]. Note that most of the parameter space to explain $m_{W,\text{CDF-II}}$ is excluded by the LZ experiment together with the Higgs precision measurement. One exception is a fine-tuned parameter space with $m_{A,H}$ slightly above $m_h/2$, which could be excluded by future direct detection experiments or Higgs precision measurements. Otherwise, an additional mechanism is needed to further deplete its relic abundance to make this case viable.

4.7.2 Decaying massive relic

If H and A are not cosmologically stable, they could decay into the Standard Model particles through their couplings to the SM-like Higgs boson. The decays could inject significant amount of electromagnetic or hadronic energy into the Standard Model plasma in the early universe or intergalactic medium in the late universe, depending on the their lifetimes. This could lead to various observational signature in astrophysics and cosmology, such as those from Big Bang Nucleosynthesis (BBN) [281, 6, 7], Cosmic Microwave Background (CMB) [282, 283, 284, 7, 8], and galactic and extragalactic diffuse γ-ray background observations [278, 279, 280, 9], even if they are subdominant components of dark matter.

In the right panel of Fig. 4.9, we summarize current cosmological constraints on visibly-decaying massive relic from BBN [6], CMB (combining constraints from anisotropy [7] from Planck 2018 and spectra distortion ([8]) from COBE/FIRAS), and isotropic γ-ray background [9] as yellow, green, and brown shaded regions, respectively. To get the BBN constraints, we take the constraints on massive relic χ with $m_\chi = 1\,\text{TeV}$ that decaying to $b\bar{b}$

from Ref. ([6]) [8]. This constraints are representative for massive relic that mostly decaying to hadronic energy. As shown in Ref. [6], lighter relic ($m_\chi = 30\,\mathrm{GeV}$ and $m_\chi = 100\,\mathrm{GeV}$) or other hadronic energy-dominant decay channels ($\chi \to \bar{u}u, \bar{t}t, gg, WW$) share similar constraints. Constraints for massive relics decaying to electromagnetic energy, e.g. $\chi \to e^+e^-$, are generically weaker than those for relics decaying to hadronic energy. In our scenario explaining the CDF-II m_W measurement, the dominant decay channels of H (A) are $b\bar{b}$, WW, and hh (bb and Zh), depending on the kinematic accessibility (c.f. Fig. 4.8). All these decay channels generate significant amount of hadronic energy. Hence the BBN constraint we quoted are applicable.

In the same panel, we highlight a light blue band to show the range of the relative abundance for $m_{H,A} > 63\,\mathrm{GeV}$ (away from the fine-tuned mass region) whose corresponding parameters explain $m_{W,\text{CDF-II}}$. For such an abundance range (0.08%–7%), the strongest constraints for the decaying relic come from BBN, which restrict $\tau_{A,H} \lesssim 50\,\mathrm{sec}$. To satisfy this constraint, the value of v_Δ needs to be large. In the right panel of Fig. 4.9, we explicitly show the value of v_Δ for a given lifetime of A with mass $m_A = 65\,\mathrm{GeV}$ as the red upper ticks. For the $m_{A,H}$ parameter space we consider, we find that

$$v_\Delta \gtrsim 1\,\mathrm{eV}$$

guarantees that A and H evade all the cosmological constraints for a visibly-decaying massive relic in the scenario which explains the CDF-II m_W measurement. Note that $v_\Delta \geq 1\,\mathrm{eV}$ corresponds to $c\tau_{H,A} \lesssim 1\,\mathrm{km}$. Such decay signal could be searched at the long-lived particle search facilities at the LHC.

---

[8] The original constraints are expressed in the variable $m_\chi n_\chi/s$ where $m_\chi n_\chi$ is the density of the massive relic and s is the entropy density. We translate the constraints into those on f_χ.

4.8 Summary of the chapter

In this work, we studied the HTM with hypercharge $Y = 1$ in light of the recent CDF-II W mass measurement. The HTM can be realized with two distinct types of spectra: type I for which $m_{H^{++}} < m_{H^+} < m_{H,A}$, and type II for which $m_{H^{++}} > m_{H^+} > m_{H,A}$. First, we derived the mass spectrum of the additional Higgs bosons (for both type I and type II) preferred by the CDF-II m_W measurement. For this mass spectra, we then checked the compatibility with experimental measurements of the effective weak mixing angle and Higgs precision data (i.e., measurements of the Higgs di-photon rate, constraints on the Higgs trilinear coupling and constraints on exotic decay channels of the SM-like Higgs boson). For the type-I HTM, we find that mass spectra (as shown in the first, third, and fifth panel of Fig. 4.2) with the lightest state mass $m_{H^{++}} \gtrsim 250\,\text{GeV}$ explain the observed $m_{W,\text{CDF-II}}$ while being consistent with the measurements of the effective weak mixing angle and Higgs precision measurements, while also satisfying the theoretical constraints of perturbative unitarity and vacuum stability. For the type-II HTM, we find that mass spectra (as shown in the second, fourth, and sixth panel of Fig. 4.2) with the lightest state mass $62.5\,\text{GeV} \lesssim m_{H,A} \lesssim 350\,\text{GeV}$ explain the observed $m_{W,\text{CDF-II}}$ while being consistent with the Higgs precision measurements, perturbative unitarity, and vacuum stability. For type II, we, however, find a mild tension with the world average measurement of $\sin^2_{\theta_\text{eff}}$ at the 2σ level, while still being well consistent with the single-most precise measurement of the effective weak mixing angle by the SLD collaboration.

Direct searches at the LHC provide stronger yet model-dependent constraints on the HTM. The model dependence mainly originates from the decay length of the lightest state, which is mostly controlled by the value of v_Δ and m_lightest (c.f. Fig. 4.7). We classified the LHC signatures according to if the lightest state promptly decays, if it is detector-stable, or it is long-lived. We investigated the collider phenomenology for each of these cases and pointed out a number of promising discovery channels that the LHC could be sensitive to (summaries of those channels can be found in Tabs. 4.2). Current LHC searches are most sensitive to the type-I HTM with a prompt decay of the lightest state (excluding $200\,\mathrm{GeV} < m_{H^{++}} < 350\,\mathrm{GeV}$) or detector-stable lightest state (excluding $m_{H^{++}} < 1050\,\mathrm{GeV}$). A dedicated analysis using current data can also exclude a promptly decaying doubly-charged Higgs with $m_{H^{++}} \sim 150$ GeV by studying the $H^{\pm\pm}H^{\mp}$ production channel. The case of a long-lived lightest state is so far largely unconstrained for type I. Dedicated searches with the existing data could effectively cover the parameter space for the type-II HTM, especially given the constrained mass range for which the CDF-II measurement can be explained while evading other constraints (see above).

Furthermore, we explored the scenario that the new Higgs triplet is approximately inert. In this case, its lightest neutral state can be a candidate for a sub-dominate fraction of stable dark matter if $v_\Delta \lesssim 10^{-16}\,\mathrm{eV}$ or decaying dark matter if $v_\Delta \gtrsim 1\,\mathrm{eV}$. The former scenario is almost fully constrained by current dark matter direct detection experiments such as the LZ experiment. The later scenario remains possible.

4.A Self-energy corrections

We take the one-loop contributions to self energies from Ref. [247], setting $v_\Delta = 0$, in the computation of m_W and $\sin^2\theta_{\text{eff}}$. We listed all the relevant formula here for readers' convenience. The corrections are parameterized in terms of $g^2 = e^2/s_W^2$ and $g_Z^2 = e^2/(s_W^2 c_W^2)$.

The BSM contributions to the vector-boson self energies are given by

$$\Pi_{WW}^{\text{1PI, BSM}}(p^2) = \frac{g^2}{16\pi^2}\Big(B_5(p^2, m_{H^{++}}^2, m_{H^+}^2) + \frac{1}{2}B_5(p^2, m_{H^+}^2, m_H^2) + \frac{1}{2}B_5(p^2, m_{H^+}^2, m_A^2)\Big), \tag{4.32}$$

$$\Pi_{ZZ}^{\text{1PI, BSM}}(p^2) = \frac{g_Z^2}{16\pi^2}\Big((c_W^2 - s_W^2)^2 B_5(p^2, m_{H^{++}}^2, m_{H^{++}}^2) + s_W^4 B_5(p^2, m_{H^+}^2, m_{H^+}^2) + B_5(p^2, m_H^2, m_A^2)\Big), \tag{4.33}$$

$$\Pi_{\gamma\gamma}^{\text{1PI, BSM}}(p^2) = \frac{e^2}{16\pi^2}\big(4B_5(p^2, m_{H^{++}}^2, m_{H^{++}}^2) + B_5(p^2, m_{H^+}^2, m_{H^+}^2)\big), \tag{4.34}$$

$$\Pi_{\gamma\gamma}^{\prime\text{1PI, BSM}}(p^2) = \frac{e^2}{16\pi^2}\big(4B_5'(p^2, m_{H^{++}}^2, m_{H^{++}}^2) + B_5'(p^2, m_{H^+}^2, m_{H^+}^2)\big), \tag{4.35}$$

$$\Pi_{Z\gamma}^{\text{1PI, BSM}}(p^2) = -\frac{eg_Z}{16\pi^2}\Big(2(c_W^2 - s_W^2)B_5(p^2, m_{H^{++}}^2, m_{H^{++}}^2) + \frac{1}{2}(c_W^2 - s_W^2 - 1)B_5(p^2, m_{H^+}^2, m_{H^+}^2)\Big) \tag{4.36}$$

where $B_{0,1,00,11}(p^2, m_1^2, m_2^2)$ are the Passarino-Veltman two-point functions, which we evaluate using `LoopTools 2.16` [256]. The remaining loop-functions are given by

$$B_3(p^2, m_1^2, m_2^2) = -B_1(p^2, m_1^2, m_2^2) - B_{11}(p^2, m_1^2, m_2^2), \tag{4.37}$$

$$B_4(p^2, m_1^2, m_2^2) = -m_1^2 B_1(p^2, m_2^2, m_1^2) - m_2^2 B_1(p^2, m_1^2, m_2^2) \tag{4.38}$$

$$B_5(p^2, m_1^2, m_2^2) = A_0(m_1^2) + A_0(m_2^2) - 4B_{00}(p^2, m_1^2, m_2^2), \tag{4.39}$$

where $A_0(m^2)$ is the Passarino-Veltman one-point function.

The SM contributions to Δr (and $\sin^2\theta_{\text{eff}}$) can be separated into three classes: those from scalar bosons, fermions, and gauge bosons — i.e., $\Pi_i^{\text{1PI, SM}}(p^2) = \Pi_{i,S}^{\text{1PI, SM}}(p^2) + \Pi_{i,F}^{\text{1PI, SM}}(p^2) + \Pi_{i,V}^{\text{1PI, SM}}(p^2)$ where $i = WW, ZZ, \gamma\gamma, Z\gamma$. The scalar contributions are given by

$$\Pi^{\text{1PI, SM}}_{WW}(p^2)_S = \frac{g^2}{64\pi^2}\left(B_5(p^2, m_W^2, m_h^2) + B_5(p^2, m_W^2, m_Z^2)\right), \tag{4.40}$$

$$\Pi^{\text{1PI, SM}}_{ZZ}(p^2)_S = \frac{g_Z^2}{64\pi^2}\left((c_W^2 - s_W^2)^2 B_5(p^2, m_W^2, m_W^2) + B_5(p^2, m_h^2, m_Z^2)\right), \tag{4.41}$$

$$\Pi^{\text{1PI, SM}}_{Z\gamma}(p^2)_S = -\frac{eg_Z}{32\pi^2}(c_W^2 - s_W^2)B_5(p^2, m_W^2, m_W^2), \tag{4.42}$$

$$\Pi^{\text{1PI, SM}}_{\gamma\gamma}(p^2)_S = \frac{e^2}{16\pi^2}B_5(p^2, m_W^2, m_W^2), \tag{4.43}$$

$$\Pi'^{\text{1PI, SM}}_{\gamma\gamma}(p^2)_S = \frac{e^2}{16\pi^2}B'_5(p^2, m_W^2, m_W^2). \tag{4.44}$$

The fermionic contributions are given by

$$\Pi^{\text{1PI, SM}}_{WW}(p^2)_F = \frac{g^2}{16\pi^2}N_c^f(2p^2B_3(p^2, m_f^2, m_{f'}^2) - B_4(p^2, m_f^2, m_{f'}^2)), \tag{4.45}$$

$$\begin{aligned}\Pi^{\text{1PI, SM}}_{ZZ}(p^2)_F = \frac{g_Z^2}{8\pi^2}N_c^f\Big(&2p^2(2s_W^4Q_f^2 - 2s_W^2Q_fI_f + I_f^2)B_3(p^2, m_f^2, m_f^2) \\ &-I_f^2m_f^2B_0(p^2, m_f^2, m_f^2)\Big),\end{aligned} \tag{4.46}$$

$$\Pi^{\text{1PI, SM}}_{Z\gamma}(p^2)_F = \frac{eg_Z}{4\pi^2}N_c^f p^2(2s_W^2Q_f^2 - I_fQ_f)B_3(p^2, m_f, m_f), \tag{4.47}$$

$$\Pi^{\text{1PI, SM}}_{\gamma\gamma}(p^2)_F = \frac{e^2}{2\pi^2}N_c^fQ_f^2p^2B_3(p^2, m_f^2, m_f^2), \tag{4.48}$$

$$\Pi'^{\text{1PI, SM}}_{\gamma\gamma}(p^2)_F = \frac{e^2}{2\pi^2}N_c^fQ_f^2\left(B_3(p^2, m_f^2, m_f^2) + p^2B'_3(p^2, m_f^2, m_f^2)\right) \tag{4.49}$$

where m_f, Q_f, I_f, and N_c^f are the mass, electric charge, isospin, and color numbers of the SM fermion f, respectively. Here, we sum over all the SM quarks and leptons.

Finally, the gauge boson contributions are given by

$$\begin{aligned}
\Pi^{\text{1PI, SM}}_{WW}(p^2)_V = \frac{g^2}{16\pi^2}\Bigg(& m_W^2\left(B_0(p^2,m_h^2,m_W^2)+s_W^2B_0(p^2,m_W^2,0)+\frac{s_W^4}{c_W^2}B_0(p^2,m_W^2,m_Z^2)\right) \\
& - c_W^2(6D-8)B_{00}(p^2,m_Z^2,m_W^2)-2p^2c_W^2B_{11}(p^2,m_Z^2,m_W^2) \\
& - 2p^2c_W^2B_1(p^2,m_Z^2,m_W^2)-5p^2c_W^2B_0(p^2,m_Z^2,m_W^2)+c_W^2(D-1)A_0(m_Z^2) \\
& + (D-1)A_0(m_W^2)-s_W^2(6D-8)B_{00}(p^2,0,m_W^2)-2p^2s_W^2B_{11}(p^2,0,m_W^2) \\
& - 2p^2s_W^2B_1(p^2,0,m_W^2)-5p^2s_W^2B_0(p^2,0,m_W^2)\Bigg) \\
& - \frac{g^2}{4\pi^2}(p^2-m_W^2)\left(c_W^2B_0(p^2,m_Z^2,m_W^2)+s_W^2B_0(p^2,0,m_W^2)\right),
\end{aligned}\tag{4.50}$$

$$\begin{aligned}
\Pi^{\text{1PI, SM}}_{ZZ}(p^2)_V = \frac{g_Z^2}{16\pi^2}\Bigg(& m_Z^2B_0(p^2,m_h^2,m_Z^2)+2m_W^2s_W^4B_0(p^2,m_W^2,m_W^2) \\
& - c_W^4(6D-8)B_{00}(p^2,m_W^2,m_W^2)-2p^2c_W^4B_{11}(p^2,m_W^2,m_W^2) \\
& - 2p^2c_W^4B_1(p^2,m_W^2,m_W^2)-5p^2c_W^4B_0(p^2,m_W^2,m_W^2)+2(D-1)c_W^4A_0(m_W^2)\Bigg) \\
& - \frac{g_Z^2}{4\pi^2}(p^2-m_Z^2)c_W^4B_0(p^2,m_W^2,m_W^2),
\end{aligned}\tag{4.51}$$

$$\begin{aligned}
\Pi^{\text{1PI, SM}}_{Z\gamma}(p^2)_V = \frac{eg_Z}{16\pi^2}\Bigg(& c_W^2(6D-8)B_{00}(p^2,m_W^2,m_W^2)+2p^2c_W^2B_{11}(p^2,m_W^2,m_W^2) \\
& + 2p^2c_W^2B_1(p^2,m_W^2,m_W^2)+5p^2c_W^2B_0(p^2,m_W^2,m_W^2)-2c_W^2(D-1)A_0(m_W^2) \\
& + 2m_W^2s_W^2B_0(p^2,m_W^2,m_W^2)\Bigg)+\frac{eg_Z}{8\pi^2}\left(2p^2-m_Z^2\right)c_W^2B_0(p^2,m_W^2,m_W^2),
\end{aligned}\tag{4.52}$$

$$\begin{aligned}
\Pi^{\text{1PI, SM}}_{\gamma\gamma}(p^2)_V = -\frac{e^2}{16\pi^2}\Bigg(& (6D-8)B_{00}(p^2,m_W^2,m_W^2)+2p^2B_{11}(p^2,m_W^2,m_W^2)-2(D-1)A_0(m_W^2) \\
& + 2p^2B_1(p^2,m_W^2,m_W^2)+5p^2B_0(p^2,m_W^2,m_W^2)-2m_W^2B_0(p^2,m_W^2,m_W^2)\Bigg) \\
& - \frac{e^2}{4\pi^2}p^2B_0(p^2,m_W^2,m_W^2),
\end{aligned}\tag{4.53}$$

$$\begin{aligned}
\Pi'^{\text{1PI, SM}}_{\gamma\gamma}(p^2)_V = -\frac{e^2}{16\pi^2}\Bigg(& (6D-8)B'_{00}(p^2,m_W^2,m_W^2)+2B_{11}(p^2,m_W^2,m_W^2) \\
& + 2p^2B'_{11}(p^2,m_W^2,m_W^2)+2B_1(p^2,m_W^2,m_W^2)+2p^2B'_1(p^2,m_W^2,m_W^2) \\
& + 5B_0(p^2,m_W^2,m_W^2)+5p^2B'_0(p^2,m_W^2,m_W^2)-2m_W^2B'_0(p^2,m_W^2,m_W^2)\Bigg) \\
& - \frac{e^2}{4\pi^2}\left(B_0(p^2,m_W^2,m_W^2)+p^2B'_0(p^2,m_W^2,m_W^2)\right),
\end{aligned}\tag{4.54}$$

where $D = 4 - 2\epsilon$ with ϵ being the dimensional regulator. The divergences of the loop functions are given by

$$\begin{aligned}
A_0(m^2)_{\rm div} &= m^2\Delta, \quad B_0(p^2, m_1^2, m_2^2)_{\rm div} = \Delta \\
B_1(p^2, m_1^2, m_2^2)_{\rm div} &= -\frac{\Delta}{2}, \quad B_{11}(p^2, m_1^2, m_2^2)_{\rm div} = \frac{\Delta}{3} \\
B_{00}(p^2, m_1^2, m_2^2)_{\rm div} &= \left(\frac{m_1^2 + m_2^2}{4} - \frac{p^2}{12}\right)\Delta, \\
B'_{00}(p^2, m_1^2, m_2^2)_{\rm div} &= -\frac{\Delta}{12}, \\
B_3(p^2, m_1^2, m_2^2)_{\rm div} &= \frac{\Delta}{6}, B_4(p^2, m_1^2, m_2^2)_{\rm div} = \frac{m_1^2 + m_2^2}{2}\Delta \\
B_5(p^2, m_1^2, m_2^2)_{\rm div} &= \frac{p^2}{3}\Delta, \quad B'_5(p^2, m_1^2, m_2^2)_{\rm div} = \frac{\Delta}{3},
\end{aligned} \tag{4.55}$$

where $\Delta = \frac{1}{\epsilon} + \ln \mu^2$ with μ being the renormalization scale.

4.B The SM fitting formula

The SM prediction for the W boson mass, m_W, and the leptonic effective mixing angle, $\sin^2\theta_W$, are parameterized by the fitting formula in Ref. [250]) and Ref. ([251], respectively. We list them here for readers' convenience. The fitting formula for $m_{W,\rm SM}$ is given by

$$\begin{aligned}
m_{W,\rm SM} = m_W^0 &- c_1 dH - c_2 dH^2 + c_3 dH^4 + c_4(dh - 1) - c_5 d\alpha + c_6 dt \\
&- c_7 dt^2 - c_8 dH dt + c_9 dh dt - c_{10} d\alpha_s + c_{11} dZ,
\end{aligned} \tag{4.56}$$

where

$$\begin{aligned} dH &= \ln\left(\frac{m_h}{100\text{ GeV}}\right), & dh &= \left(\frac{m_h}{100\text{ GeV}}\right)^2, \\ dt &= \left(\frac{m_t}{174.3\text{ GeV}}\right)^2 - 1, & dZ &= \frac{m_Z}{91.1875\text{ GeV}} - 1, \\ d\alpha &= \frac{\Delta\alpha}{0.05907} - 1, & d\alpha_s &= \frac{\alpha_s(m_Z^2)}{0.119} - 1 \end{aligned} \tag{4.57}$$

and the coefficients are given by

$$\begin{aligned} m_W^0 &= 80.3799\text{ GeV}, & c_1 &= 0.05263\text{ GeV}, & c_2 &= 0.010239\text{ GeV}, \\ c_3 &= 0.000954\text{ GeV}, & c_4 &= -0.000054\text{ GeV}, & c_5 &= 1.077\text{ GeV}, \\ c_6 &= 0.5252\text{ GeV}, & c_7 &= 0.0700\text{ GeV}, & c_8 &= 0.004102\text{ GeV}, \\ c_9 &= 0.000111\text{ GeV}, & c_{10} &= 0.0774\text{ GeV}, & c_{11} &= 115.0\text{ GeV}. \end{aligned} \tag{4.58}$$

This fitting formula includes the complete one-loop and two-loop results [285, 286, 287, 288, 289, 290, 291, 292, 293, 294, 295, 296, 297, 298, 299, 300, 301, 251]). Moreover, partial higher-order corrections up to four-loop order are included ([302, 303, 304, 305, 306, 307, 308, 309, 310, 311].

The fitting formula for $\sin^2\theta^\ell_{\text{eff, SM}}$ is given by

$$\begin{aligned} \sin^2\theta^\ell_{\text{eff, SM}} = s_0 &+ d_1 L_H + d_2 L_H^2 + d_3 L_H^4 + d_4(\Delta_H^2 - 1) + d_5\Delta_\alpha + d_6\Delta_t \\ &+ d_7\Delta_t^2 + d_8\Delta_t(\Delta_H - 1) + d_9\Delta_{\alpha_s} + d_{10}\Delta_Z, \end{aligned} \tag{4.59}$$

where

$$\begin{aligned}
L_H &= \ln\left(\frac{m_h}{100\ \mathrm{GeV}}\right), \quad \Delta_H = \frac{m_h}{100\ \mathrm{GeV}}, \\
\Delta_\alpha &= \frac{\Delta\alpha}{0.05907} - 1, \quad \Delta_t = \left(\frac{m_t}{178.0\ \mathrm{GeV}}\right)^2 - 1, \\
\Delta_{\alpha_s} &= \frac{\alpha_s(m_Z^2)}{0.117} - 1, \quad \Delta_Z = \frac{m_Z}{91.1876\ \mathrm{GeV}} - 1
\end{aligned} \tag{4.60}$$

and the coefficients

$$\begin{aligned}
&s_0 = 0.2312527, && d_1 = 4.729 \times 10^{-4}, && d_2 = 2.07 \times 10^{-5}, \\
&d_3 = 3.85 \times 10^{-6}, && d_4 = -1.85 \times 10^{-6}, && d_5 = 2.07 \times 10^{-2}, \\
&d_6 = -2.851 \times 10^{-3}, && d_7 = 1.82 \times 10^{-4}, && d_8 = -9.74 \times 10^{-6}, \\
&d_9 = 3.98 \times 10^{-4}, && d_{10} = -0.655. &&
\end{aligned} \tag{4.61}$$

This fitting formula is based on the full one-, and two-loop corrections as well as the leading three- and four-loop corrections computed in Refs. [302, 303, 306, 307, 287, 288, 289, 290, 292, 312, 304, 291]. The corresponding $\Delta\kappa_{\mathrm{SM}}$ can then be derived by

$$\Delta\kappa_{\mathrm{SM}} = \frac{\sin^2\theta^{\ell}_{\text{eff, SM}}}{1 - m^2_{W,\mathrm{SM}}/m_Z^2} - 1. \tag{4.62}$$

4.C Soft $\mathbb{Z}_2$ breaking

Here we introduce a soft $\mathbb{Z}_2$ breaking term in the Higgs potential

$$\Delta V = \mu\Phi^{\mathrm{T}} i\sigma_2 \Delta^\dagger \Phi + h.c. = -\sqrt{2}\mu H h^2 + \mu(-\sqrt{2}H^- G^+ G^0 + H^{--} G^+ G^+ + h.c.) \tag{4.63}$$

where μ is assumed to be real. Such a term breaks the degeneracy between the two neutral states H, A, therefore it is expected that $m_H^2 - m_A^2 \propto \mu^2$. ΔV generates a non-zero v_Δ:

$$\begin{aligned} v_\Delta \approx& \frac{\sqrt{2}}{2M^2/v^2 + \lambda_4 + \lambda_5}\mu + \mathcal{O}(\mu^3), \\ v_\phi^2 \approx& -\frac{m^2}{\lambda_1} + \mathcal{O}(\mu^2) = v^2 - 2v_\Delta^2. \end{aligned} \tag{4.64}$$

Defining $\epsilon \equiv \sqrt{2}v_\Delta/v \ll 1$, the explicit $\mathbb{Z}_2$ breaking mixes the states of Φ and Δ with the same quantum numbers at $\mathcal{O}(\epsilon)$. To avoid confusion, we write the weak eigenstates as

$$\Phi' = \begin{pmatrix} H_1^+ \\ \frac{v_\phi + H_1 + iA_1}{\sqrt{2}} \end{pmatrix}, \quad \Delta' = \begin{pmatrix} \frac{H_2^+}{\sqrt{2}} & H^{++} \\ \frac{v_\Delta + H_2 + iA_2}{\sqrt{2}} & -\frac{H_2^+}{\sqrt{2}} \end{pmatrix} \tag{4.65}$$

The physical 125 GeV Higgs boson, and the Goldstone bosons that would become the longitudinal W and Z all have small mixtures of the corresponding component of the triplet:

$$h \approx H_1 + \frac{M^2}{M_\Delta^2 - 2\lambda_1 v^2}\sqrt{2}\epsilon H_2 \ , \ G^+ \approx H_1^+ + \epsilon H_2^+ \ , \ G^0 \approx A_1 + \sqrt{2}\epsilon A_2 \ , \tag{4.66}$$

where $M_\Delta^2 = M^2 + \frac{1}{2}(\lambda_4 + \lambda_5)v^2$. This mixture allows the mass eigenstates H and A to decay to fermions even though no Yukawa interactions are explicitly introduced in the triplet model. Up to quadratic order in ϵ, the physical states have masses given by

$$\begin{aligned} m_h^2 =& 2\lambda_1 v^2 - \left(2\lambda_1 v^2 + 2M^2 \frac{M^2}{M_\Delta^2 - 2\lambda_1 v^2}\right)\epsilon^2, \\ m_H^2 =& M_\Delta^2 + \left(v^2(\lambda_2 + \lambda_3) + M^2 \frac{M^2}{M_\Delta^2 - 2\lambda_1 v^2}\right)\epsilon^2, \\ m_A^2 =& M_\Delta^2 + 2M_\Delta^2\epsilon^2, \\ m_{H^+}^2 =& M_\Delta^2 - \frac{\lambda_5}{4}v^2 + M_\Delta^2\epsilon^2, \\ m_{H^{++}}^2 =& M_\Delta^2 - \frac{\lambda_5}{2}v^2 + \frac{\lambda_5 - \lambda_3}{2}v^2\epsilon^2. \end{aligned} \tag{4.67}$$

From (4.66), when $m_H^2 \to m_h^2$, the mixing parameter between H_1 and H_2 diverges. This means that h and H can be maximally mixed even when $\epsilon \ll 1$. In this limit, the $H - h$ mixing depends on the details of the Higgs potential parameters.

4.D Unitarity and Vacuum Stability Bounds

We follow the analysis of vacuum stability and unitarity constraints as given by [313, 247].

Demanding perturbative unitarity impose an upper bound on the eigenvalues of the $2 \to 2$ scattering matrix

$$|x_i| < 8\pi, \quad i = 1, 2, 3 \tag{4.68}$$

where

$$x_1 = 3\lambda_1 + 7\lambda_\Delta + \sqrt{(3\lambda_1 - 7\lambda_\Delta)^2 + \frac{3}{2}(2\lambda_4 + \lambda_5)^2},\ x_2 = \frac{1}{2}(2\lambda_4 + 3\lambda_5),\ x_3 = \frac{1}{2}(2\lambda_4 - \lambda_5)\cdot \tag{4.69}$$

Taking $\lambda_\Delta \equiv \lambda_2 = \lambda_3 > 0$, the necessary and sufficient condition for the Higgs potential to be bounded from below is

$$\lambda_1 > 0,\ \lambda_\Delta > 0,\ 2\sqrt{2\lambda_1\lambda_\Delta} + \lambda_4 + \min(0, \lambda_5) > 0 \tag{4.70}$$

The first two conditions are trivially satisfied. In terms of masses of physical states and M^2, the last condition can be written as

$$\frac{m_h}{v}\sqrt{\lambda_\Delta} + \frac{m_{H^{++}}^2 - M^2}{v^2} + \min\left(0, 2\frac{m_{H^+}^2 - m_{H^{++}}^2}{v^2}\right) > 0 \tag{4.71}$$

This can be easily satisfied if $\lambda_4 \geq 0$ and the mass spectrum is that $m_{A(H)} > m_{H^+} > m_{H^{++}}$. If the spectrum is $m_{A(H)} < m_{H^+} < m_{H^{++}}$, the vacuum stability condition places an upper bound on the mass of H^{++}:

$$m_h v\sqrt{\lambda_\Delta} + 2m_{H^+}^2 - m_{H^{++}}^2 > M^2 > 0 \tag{4.72}$$

While boundedness-from-below is only a necessary condition for vacuum stability, we do not expect a second minimum deeper than the electroweak vacuum to exists since we always assume that $v_\Delta \ll v$ recovering approximately the SM vacuum structure.

The conditions in Eq. 4.72 imposes absolute stability. One can slightly relax this assumption by demanding metastability with a lifetime longer than the age of the Universe. For large field values, the quartic term dominates allowing to solve analytical for the bounce action B [314]. Following Ref. [315, 316], we then demand that $B < 440$ resulting in the condition

$$\frac{1}{4}\lambda_1 \cos^4\varphi + (\lambda_2+\lambda_3)\sin^4\varphi + \frac{1}{8}(\lambda_4+\lambda_5)\cos^2\varphi\sin^2\varphi < -\frac{\pi^2}{165} \simeq -0.06 \tag{4.73}$$

for any $\varphi \in [0, 2\pi]$.

4.E Landau Pole

From Sec. 4.3, we see that a larger choice of m_{lightest} generically requires a larger value of λ_5. This generally tells us that the Landau pole could potentially be very close to m_{lightest}. For our purposes, we will denote the Landau pole as the scale at which the running coupling $\lambda_5(\mu)$ grows to 4π.

Here, we will compute the one-loop beta function for λ_5. For simplicity, we will only compute the leading λ_5^2 term. The one-loop counterterm for λ_5 in $d = 4 - 2\epsilon$ is given by

$$\delta^{(1)}\lambda_5 = \frac{\lambda_5^2}{8\pi^2}\left(\frac{1}{\epsilon} + \text{finite}\right). \tag{4.74}$$

At leading order in λ_5, the wave functions of Φ and Δ are not renormalized at the one-loop level. As such, the one-loop beta function for λ_5 is simply

$$\beta_{\lambda_5} = \frac{d\lambda_5}{d\ln\mu} = \frac{\lambda_5^2}{4\pi^2} \tag{4.75}$$

Solving the RGE yields

$$\Lambda_{\text{Landau-pole}} = m_{\text{lightest}} \exp\left(\frac{4\pi^2}{\lambda_5(m_{\text{lightest}})} - \pi\right). \tag{4.76}$$

The curve for $m_{\text{lightest}} = 1$ TeV in Fig. 4.1 crosses the CDF-II band at $|\lambda_5| \sim 7$. Inserting this value into Eq. (4.76) implies a Landau pole at $\sim 12 m_{\text{lightest}} = 12$ TeV. In this situation, additional BSM physics preventing the appearance of the Landau pole should appear in the multi-TeV range. For a more precise estimate also subleading RGE effects would need to be taken into account.

4.F Decoupling

In the literature, the one-loop corrected m_W is often presented as a function of $|\delta m| \equiv |m_{H^+} - m_{H^{++}}|$, as shown in Fig. 4.10. At first sight, it is confusing that to reach a given amount of m_W increment, $|\delta m|$ stays almost the same as m_{lightest} increases (for the type-I case, it even decreases). Naturally, one would expect that the BSM corrections go to zero in the limit $M \to \infty$.

To understand such behavior, we should notice that decoupling behavior is only manifest if $\Delta m^2 \equiv m_{H^\pm}^2 - m_{H^{\pm\pm}}^2$ or $\lambda_5 = 4\Delta m^2/v^2$ is fixed. If, however, $|\delta m|$ is fixed and M is increased, no decoupling occurs. This happens because

$$|\delta m| = |m_{H^\pm} - m_{H^{\pm\pm}}| = \left| \sqrt{M^2 - \frac{1}{4}\lambda_5 v^2} - \sqrt{M^2 - \frac{1}{2}\lambda_5 v^2} \right| = \frac{1}{8}|\lambda_5| \frac{v^2}{M}\left(1 + \mathcal{O}\left(\frac{v^2}{M^2}\right)\right) \tag{4.77}$$

and therefore $|\lambda_5| \sim M\delta m/v^2$ leads to $|\lambda_5| \to \infty$ in the limit $M \to \infty$. Consequently, this limit will unavoidably violate perturbative unitarity. (We truncated all the curves once $|\lambda_5|$ grows to 10 in Fig. 4.10.)

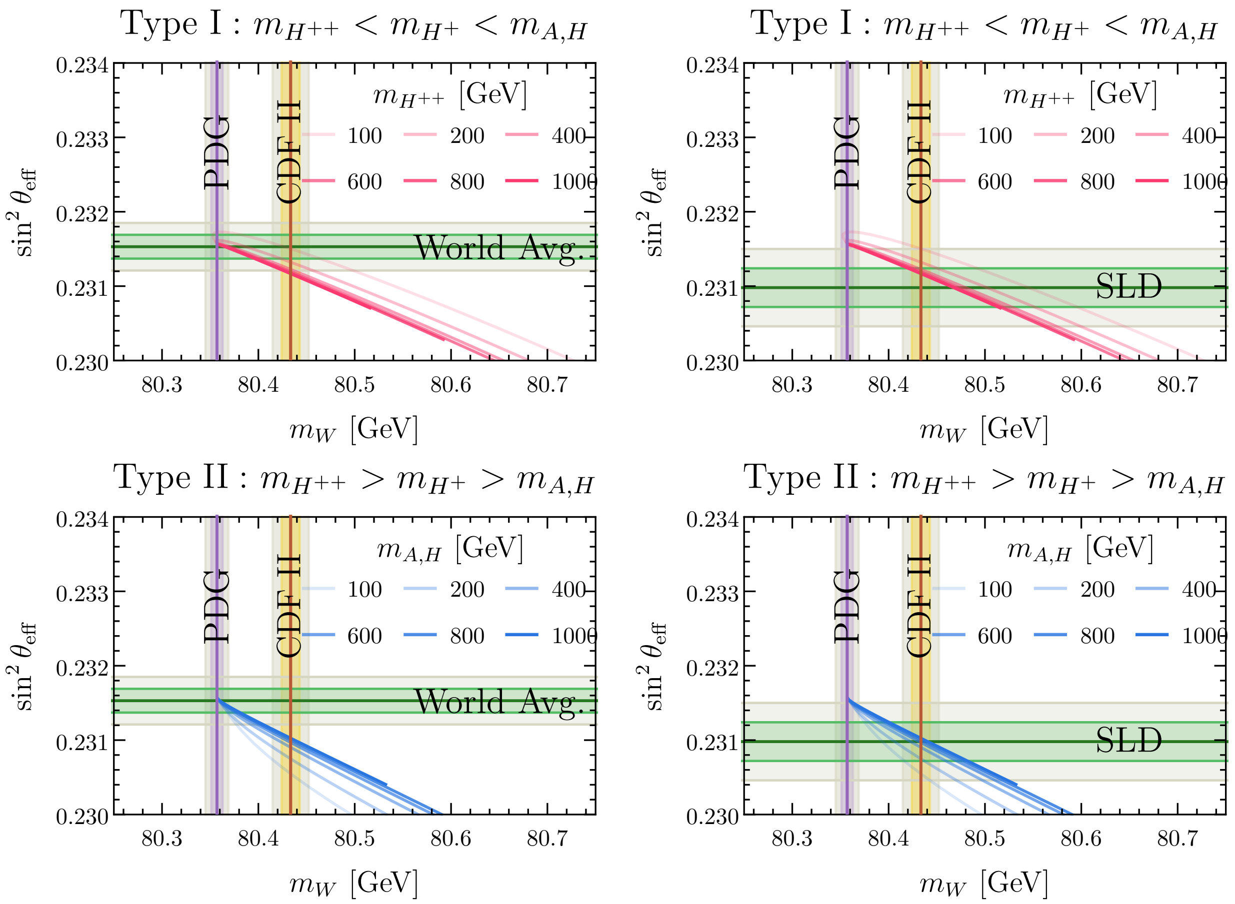

Figure 4.3: Effective weak mixing angle vs. W boson mass for the type I (upper row) and II (lower row) mass hierarchies. For each panel, the different curves represent models with different mass values for the lightest state. For each curve, we vary $|\lambda_5|$ from 0 (corresponds to the SM values) to 10. This finite range of $|\lambda_5|$ scanned results in the endpoints of the contours. The brown line represent the CDF II measured W boson mass and the yellow/gray band shows $1\sigma/2\sigma$ range. The dark purple line represent the PDG value for the W boson mass with the purple/gray band showing the $1\sigma/2\sigma$ range. The dark green line in the left (right) column represent the world averaged value 0.23153 ± 0.00016 [2, 3] (SLD measured value 0.23098 ± 0.00026 [2]) of $\sin^2\theta_{\rm eff}$ with the green/gray band shows $1\sigma/2\sigma$ range.

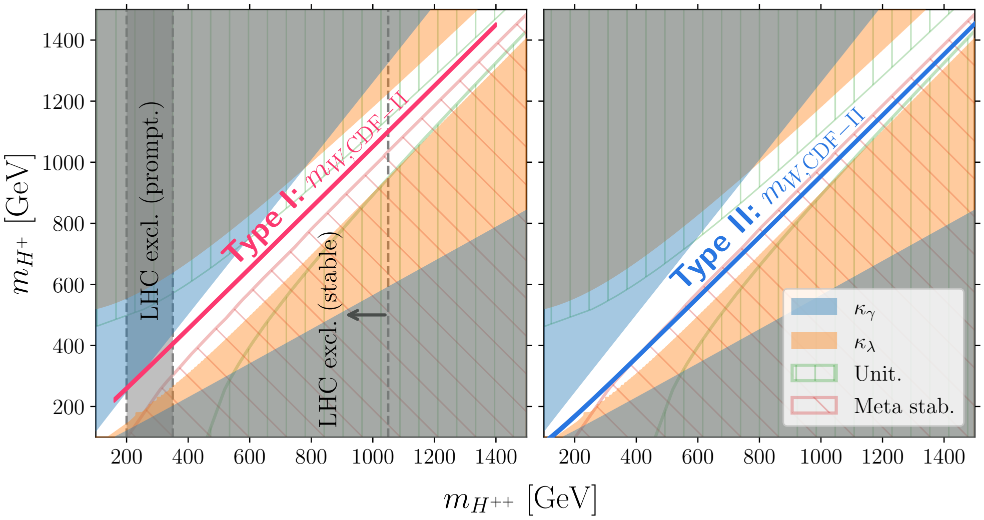

Figure 4.4: Constraints on $(m_{H^{++}}, m_{H^+})$ parameter space for the HTM from the measurement of Higgs-photon coupling (κ_γ, blue shaded region), Higgs self-coupling (κ_λ, orange shaded region), perturbative unitarity (green hatched region), and meta-stability condition of the vacuum (red hatched region). We set $\lambda_4 = 0$ and $\lambda_\Delta = 1$ for all panels. The left (right) column shows the 2σ favored parameter space that explained the measured m_W by CDF-II for the type-I (-II) model as red (blue) narrow bands. Note that we do not show the parameters for $|\lambda_5| > 10$ in drawing the narrow bands. The parameter space with $m_{H^{++}} \gtrsim 250\,\mathrm{GeV}$ ($m_{H^{++}} \lesssim 350\,\mathrm{GeV}$) for the type-I (-II) HTM remains unconstrained. We also show the LHC constraints on $m_{H^{++}}$ for type-I if H^{++} decays promptly (gray band) or if it is detector stable (left of the gray dash line). See Sec. 4.6.2 for more details.

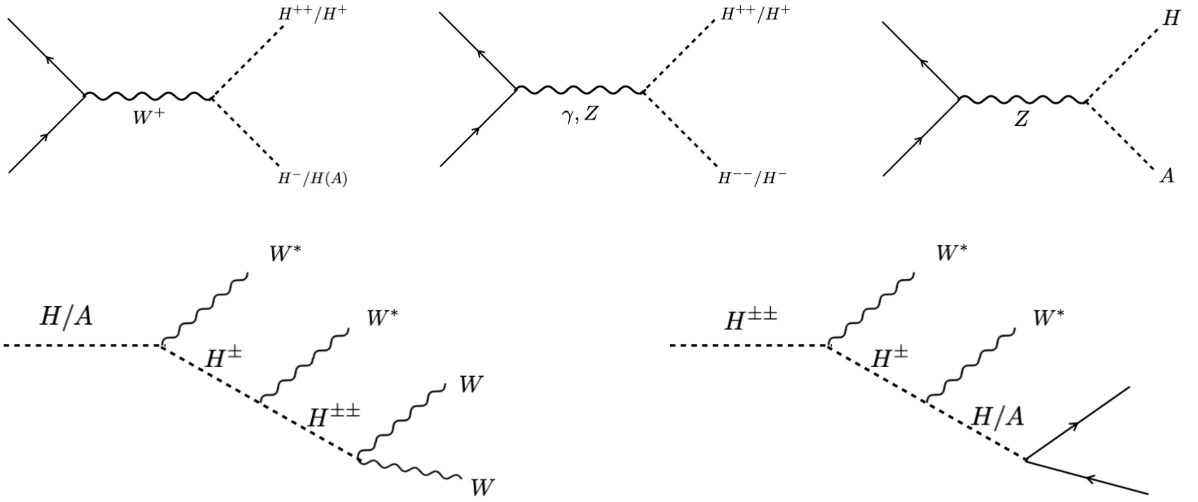

Figure 4.5: (Upper) Main production channels of the exotic Higgs states at the LHC. (Lower) Decay chains for the heaviest new Higgs state in type I (left) and type II (right). In type II, the lightest state H/A can decay to both SM fermions (as shown on the right) and the SM-like Higgs and gauge bosons.

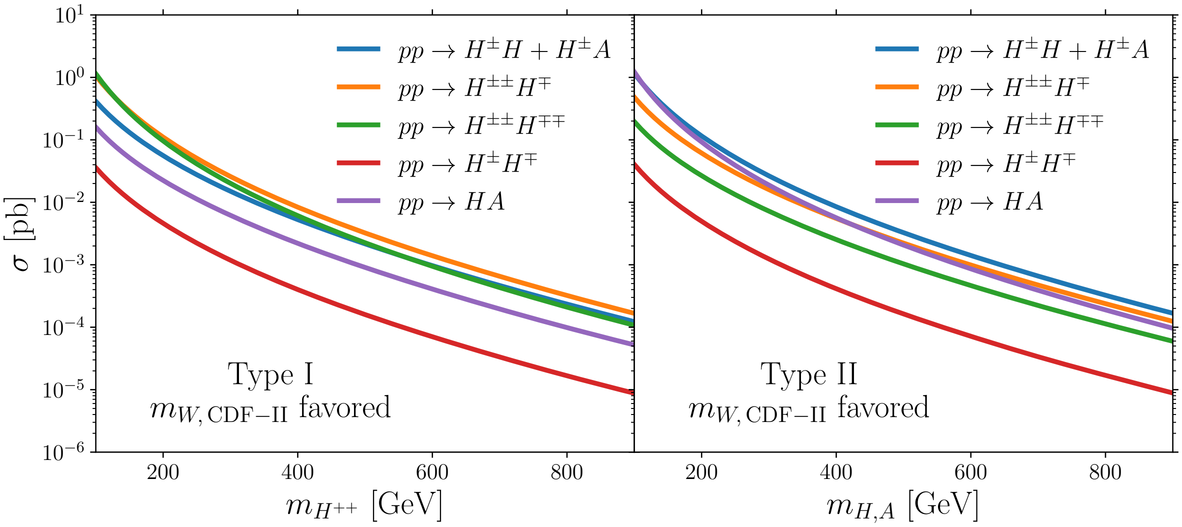

Figure 4.6: NLO pair production cross sections for Type-I (left) and Type-II (right) as a function of m_{lightest} at the 14 TeV run of the LHC.

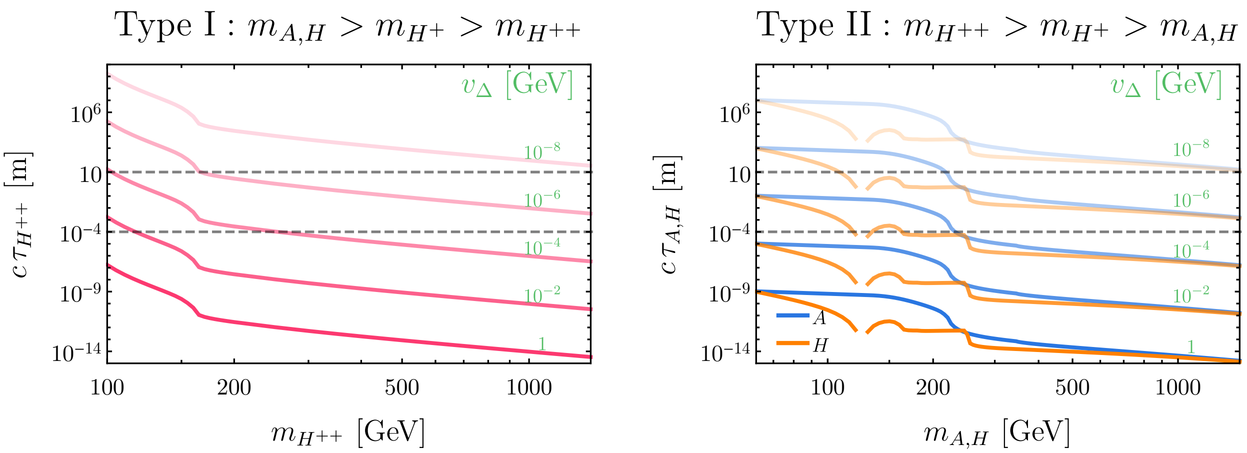

Figure 4.7: Lifetime (times the speed of light) of the lightest exotic Higgs state for type I (left) and type II (right) as a function of mass and v_Δ (setting $\lambda_2 = \lambda_3 = \lambda_4 = 0$). The remaining parameters are chosen such that CDF-II m_W value is explained. The sharp drop at around 160 GeV correspond to the threshold at which the WW decay becomes on shell. For type II (right), additional sharp drops occur at around 250 (215) GeV where $H \to hh$ ($A \to Zh$) becomes on shell; furthermore, m_H is restricted to be $\notin (120, 130)$ GeV since H maximally mixes with h there (see App. 4.C for more details). For reference, we have drawn dashed lines representing $c\tau = 10^{-4}$ meter (corresponding to $\sim 10^{-12}$ sec, which is the typical B meson lifetime) and 10 meter. This is the range in which long lived particle searches at the LHC could be sensitive.

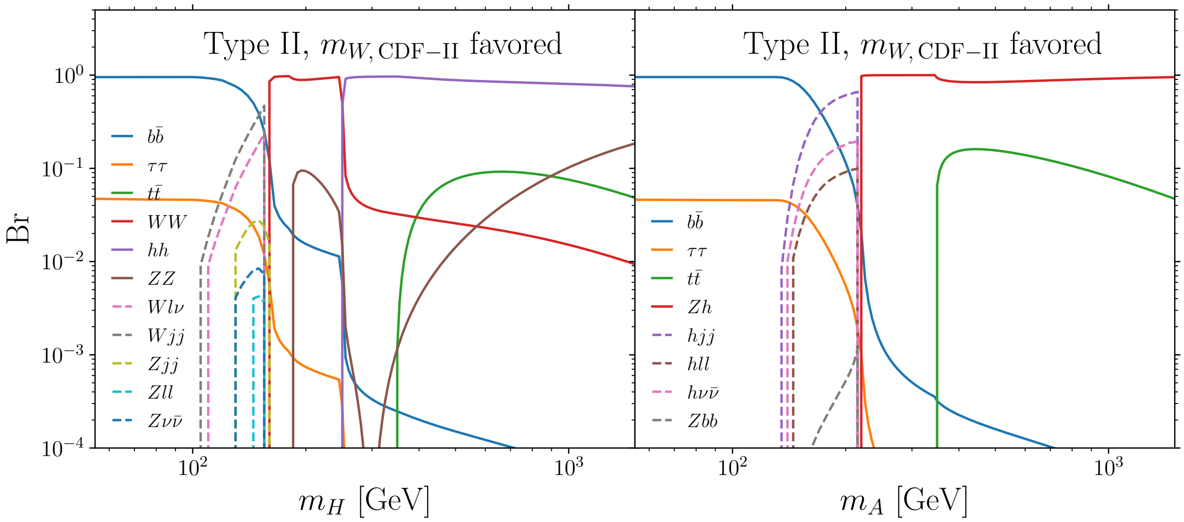

Figure 4.8: Branching ratios for H (left) and A (right) in the type-II HTM for $\lambda_2 = \lambda_3 = \lambda_4 = 0$, $v_\Delta = 1$ GeV, with a mass spectrum explaining the CDF-II m_W measurement. Branching ratios for two-body (three-body) decays are shown as solid (dashed) lines. Since all decay widths are proportional to v_Δ^2, the branching ratios do not depend on the choice of v_Δ provided that it is nonzero.

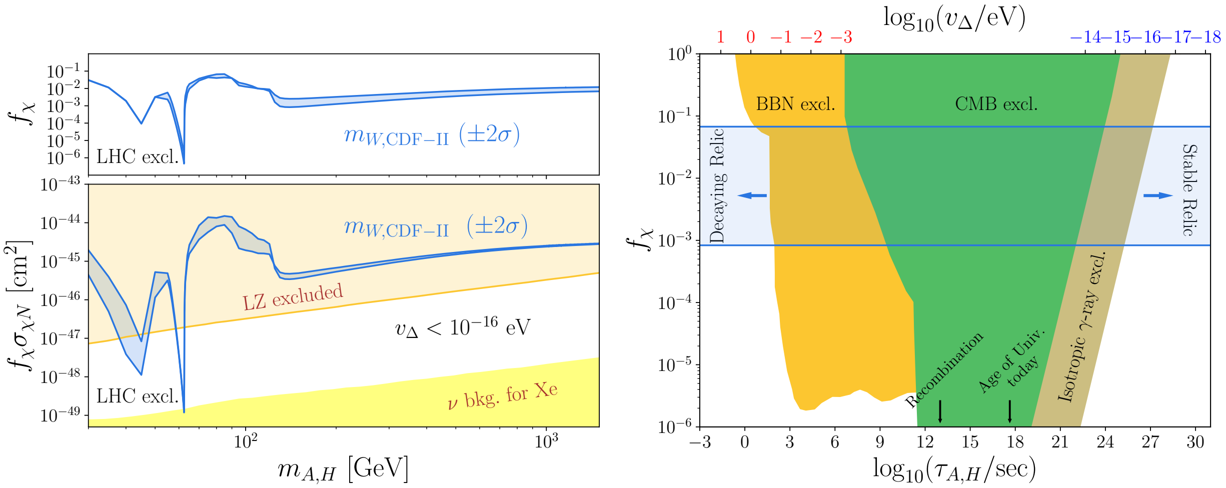

Figure 4.9: (Upper left) Sum of the relative relic abundances for H and A in the type-II HTM with respect to that of cold dark matter $f_\chi = \Omega_{H+A}/\Omega_c$ as a function of $m_{H,A} = m_H = m_A$ for parameters that explain the measured $m_{W,\text{CDF-II}}$ within 2σ. (Lower left) Sum of the direct detection cross sections times the relative abundance for cosmologically stable H and A for parameters that explain the measured m_W by CDF-II within 2σ (blue band) (assuming $v_\Delta < 10^{-16}\,\text{eV}$). 95% CL constraints from the LZ experiment with 5.5 ton$\cdot$ 60 day exposure [4] are shown as the orange shaded region. The neutrino background for a xenon target [5] is shown as the yellow shaded region. For both panels, we added constraints from the exotic decays of the SM-like Higgs as the gray shaded region. (Right panel) Constraints on the relative abundance of visibly decaying relic with respect to cold dark matter as a function of their lifetime. 95% CL constraints from BBN [6], CMB [7, 8], and isotropic γ-ray backgrounds [9] are shown as yellow, green, and brown shaded regions. We highlighted the range of f_χ that explains $m_{W,\text{CDF-II}}$ as the blue band with arrows indicating the allowed lifetimes for stable massive relic and decaying massive relic. In the lifetime axes, we indicate the age of Universe at recombination and today with black arrows. In the upper axes, we show the corresponding values of v_Δ for $m_A = 65\,\text{GeV}$ and $m_A = 1.5\,\text{TeV}$ as red and blue ticks, respectively. See text for more details.

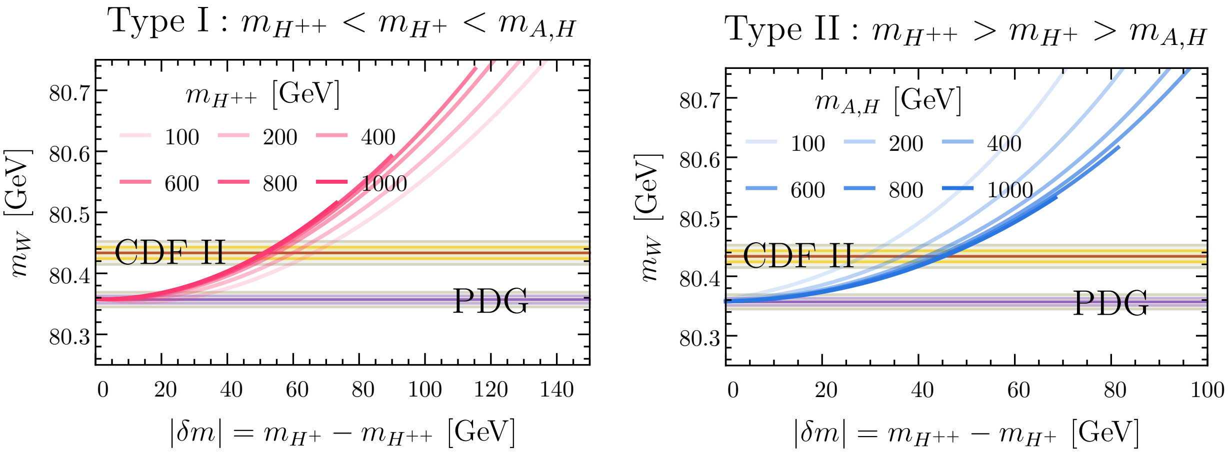

Figure 4.10: 1-loop corrected W boson mass m_W as a function of $|\delta m| = |m_{H^+} - m_{H^{++}}|$ for various masses of the lightest state in the HTM. We assume the mass hierarchy of the new states following $m_{H^{++}} < m_{H^+} < m_A$ ($m_{H^{++}} > m_{H^+} > m_A$) in the left (right) panel. We do not show the parameters for $|\lambda_5| > 10$ in drawing the curves. The color bands are the same as those in Fig. 4.1.

CHAPTER 5

DARK MATTER MODEL BUILDING

This chapter is reprinted with permission from:
Wen Han Chiu, Sungwoo Hong, and Lian-Tao Wang. Conformal freeze-in, composite dark photon, and asymmetric reheating. JHEP 03 (2023) 172.

5.1 Introduction

Dark sector models (see [317, 318] for overviews and relevant references) offer promising avenues beyond the weakly interacting massive particle (WIMP) paradigm. The mass scales in such models are often much lower than those we have in the Standard Model (SM). For phenomenological reasons, their coupling to the SM will need to be strongly suppressed as well. The production of dark matter is usually very different from the freeze-out mechanism commonly employed by the WIMP. Instead, a freeze-in mechanism [319, 320] is often invoked. The small coupling between the dark sector and the SM ensures they are not in thermal equilibrium. At the same time, the dark sector can't be populated during the reheating process like the SM. Implementing such an asymmetric reheating is a requirement for the success of a freeze-in model. While a simple parameterization with low energy degrees of freedoms is usually enough for phenomenological studies, such an array of different scales and small parameters usually call for dynamical explanations.

It is well known that large scale separation is present in theories which are nearly scale invariant, that is those close to being a conformal field theory (CFT). Starting at some UV scale where the theory is approximately conformal, a small deformation can lead to the emergence of an infrared scale which is exponentially lower than the UV scale. Hence, such CFTs are natural candidates for dark sector models. The deformation are generically present, for example, through the coupling with the SM. The small couplings required in such scenarios can be generated from scale separation as well. Motivated by this, there have been recent works [321, 322] studying the conformal freeze-in (COFI) process where the dark sector is conformal. The deformation would eventually lead to the confinement of the dark CFT, generating a mass gap, m_{gap}. A natural candidate of dark matter is one of the low lying composite resonances. Making an analogy with quantum chromodynamics (QCD), we will consider a dark matter candidate which is similar to the pion, with mass about one or two orders of magnitude below m_{gap}.

Building on the set of work on COFI, we set out to build a complete model which leads to the production of dark matter with the correct relic abundance. We consider a coupling (a portal) between the SM hypercharge gauge boson and an antisymmetric tensor operator in the dark sector CFT, which is the main driver for the COFI dark matter production. Other connections with the dark sector could also be (and have been [322]) considered. We offer a dynamical explanation of the smallness of the coupling between the SM and the dark CFT sector. In addition, we propose a scenario in which asymmetric reheating can be realized. Dark sector models are also subject to a host of astrophysical and cosmological constraints, including DM self-interaction, warm DM bound, and star cooling bounds. Taking these into account, we identify models in which correct dark matter relic abundance can be generated.

Our model predicts the existence of the dark photon as a composite vector meson in the dark sector with mass close to m_{gap}. The portal coupling introduced earlier will transform into a kinetic mixing between the dark photon and the SM hypercharge gauge boson in the IR once the conformal dark sector confines. The smallness of this coupling is explained by a large scale separation induced by a slow renormalization group (RG) running between Λ and m_{gap}. There is one important difference between our model and models with an elementary dark photon. While the freeze-in is mediated by the elementary dark photon in the latter case, the dark photon does not play a role during the COFI production. Hence, the relation between the relic abundance and the mass and coupling of the dark photon is very different, as illustrated in Figure 5.3.

The rest of the chapter is structured as follows. In section 5.2, we describe our theory and its IR effective theory. In particular, in subsection 5.2.1, we discuss UV theory and explain how the small coupling and asymmetric reheating required for the non-thermal freeze-in production can be achieved. Then, subsection 5.2.2 is devoted to describing the IR effective theory of dark matter and composite dark photon and mass gap generation. In section 5.3, we present detailed analysis of dark matter phenomenology, including freeze-in production, cosmological evolution, and various observational constraints. We then conclude in section 5.4. Several technical details are relegated to appendices. Dynamical small mass scale generations in COFI theories are explained in section 5.A. 5d dual picture of 4d COFI theories via AdS/CFT correspondence is described in section 5.B. Production of the dark sector in its hadronic phase (as opposed to conformal phase) can occur when $T < m_{\text{gap}}$ during the production and some details are presented in section 5.C. Details of rate computations needed for COFI production are discussed in section 5.D. Finally, useful ingredients of stellar evolution bounds for our theory are summarized in section 5.E.

5.2 The Setup

In this section, we introduce our theory and describe some of its key features. Our discussion in this section is mainly in the language of 4d QFT (CFT). Via the AdS/CFT correspondence, our theory admits a weakly coupled 5d gravity description which is presented in section 5.B. In addition, the production and evolution of the dark sector in cosmology and its phenomenology will be discussed in detail in section 5.3.

We are primarily interested in studying the conformal freeze-in production [321, 322] of the conformal dark sector coupled to the SM via a tensor interaction

$$\mathcal{L}_{\text{COFI}} \supset \frac{\lambda}{\Lambda^{d-2}} B_{\mu\nu} \mathcal{O}^{\mu\nu}.$$

Here, $B_{\mu\nu}$ is the field strength of $U(1)_Y$ gauge boson in the SM, and we assume $\Lambda \sim \mathcal{O}(1)$ TeV and $\lambda \ll 1$ as is the norm for freeze-in. Readers interested in phenomenology of this theory may skip subsection 5.2.1 and jump directly to subsection 5.2.2. subsection 5.2.1 (and section 5.B) is devoted to the description of microscopic theory which, through a cascade confinement, addresses the question of asymmetric reheating and results in the above effective theory, the starting point of our phenomenological study in the rest of the chapter.

5.2.1 UV theory and asymmetric reheating

In this section, we describe our UV theory and its RG evolution in a form of cascade confinement. The overall picture is depicted in Figure 5.1.

In the UV, our theory consists of a sector of CFT (denoted as CFT$_1$) coupled to a sector of elementary (as opposed to composite) particles. The elementary sector includes the inflaton Φ and a copy of the SM particle contents. The relevant particle contents and their interactions can be summarized by

$$\mathcal{L}_{\text{UV}} = \mathcal{L}_{\text{CFT}_1} + \mathcal{L}_{\Phi} + \mathcal{L}_{\text{ext}}\left(q, \ell, A_\mu\right) + \mathcal{L}_{\text{GW}_1} + \mathcal{L}_{\text{RH}} + \mathcal{L}_{\text{PC}} \tag{5.1}$$

where

1. $\mathcal{L}_{\text{ext}}$ represents terms for the external “SM” fields, $q = \text{quark}, \ell = \text{lepton}, A_\mu = \{G^a_\mu, W^i_\mu, B_\mu\} = \text{gauge fields}$[1]. These are not yet the SM fields. As described below, the SM fields are realized as admixtures of external (elementary) and composite

---

[1] Here, we do not include the SM Higgs as we wish to solve the EW hierarchy problem by treating the Higgs as composite. This, however, is not a necessary component of the model.

states, i.e. partial compositeness (PC), at energy scale below the confinement scale of CFT_1 by diagonalizing the elementary–composite mixing. Such a scheme is commonly used in the so called holographic Composite Higgs Model (CHM). For convenience, we will refer to the combination of external SM fields and the composite states they mix with as the CHM sector.

2. $\mathcal{L}_{\text{GW}_1} = \eta \mathcal{O}_{\text{GW}_1}$ describes a scalar deformation responsible for the running of the CFT_1 and generation of stable mass gap in the IR. This is the CFT dual of the Goldberger-Wise stabilization mechanism in 5d [323] and more details can be found in [324, 325, 326].

3. $\mathcal{L}_{\text{RH}}$ describes the interaction between the inflaton Φ and elementary fields, hence the reheating of the external sector. We emphasize that the inflaton is purely (or mostly) elementary with no (or little) composite mixture and hence it primarily couples only to the external sector.

4. $\mathcal{L}_{\text{PC}} = y_q \bar{q} \mathcal{O}_q + y_\ell \bar{\ell} \mathcal{O}_\ell + g A_\mu J_\mu + \frac{1}{M_{\text{pl}}} h_{\mu\nu} T^{\mu\nu}_{\text{CFT}_1}$ represents the linear interactions between the external fields and the CFT operators. When the CFT_1 confines in the IR, these will turn into the partial compositeness couplings between elementary fields and their composite partners.

The scalar deformation, $\mathcal{O}_{\text{GW}_1}$, triggers RG running of CFT_1 and the conformal invariance breaking effect grows in the IR if it is a relevant operator. Eventually, at a scale Λ_1, it becomes an $\mathcal{O}(1)$ violation and leads to a spontaneous breaking of CFT_1 measured by the vacuum expectation value (vev) of $\mathcal{O}_{\text{GW}_1}$. We assume that CFT_1 confines when this occurs. This event generates heavy composite particles which mixes linearly with the external fields. Upon diagonalizing this mass mixing, one gets mass eigenstates including massless states and these are identified as the SM particles. Heavy mass eigenstates correspond to the Kaluza-Klein (KK) excitations in the dual 5d picture.

In addition to the CHM sector described above, we assume that the confinement of CFT_1 also gives rise to a sector of composite "preons" which are singlets of the SM gauge group. These preons are similar to the quarks and gluons of QCD, and we assume that their dynamics bring them to an IR fixed point (denoted as CFT_2). [2] The dynamics of CFT_1 and the phase transition may result in various couplings between the CHM sector and CFT_2. We assume that the dominant interaction is given by

$$\mathcal{L}_{\Lambda_1} \supset \frac{1}{\Lambda_1}\rho_{B\mu\nu}\bar{\psi}_L\sigma^{\mu\nu}\chi_R + y_\Psi\bar{\psi}_L\mathcal{O}_R + y_\chi\bar{\mathcal{O}}_L\chi_R \tag{5.2}$$

where $\rho_{B\mu}$ is the composite $U(1)_Y$ vector meson which couples to SM singlet composite fermions (preons) ψ_L and χ_R via a dipole interaction. These latter SM singlet composite fermions couple to the CFT_2 through the linear mixing couplings. Since B^μ is external to the CFT_1, its coupling to the CFT_2 (which belongs to the composite sector) has to be through its mixing with composite partner ρ_B^μ. This mixing is analogous to the γ–ρ mixing realized in QCD and is given by g/g_{1s}, where g and g_{1s} are the $U(1)_Y$ gauge couping and composite coupling of confined CFT_1, respectively. See [326] for more discussion.

Below Λ_1, the above theory will undergo RG flow and the details depend on the scaling dimensions of the fermionic operators of CFT_2, $\mathcal{O}_{L,R}$. Denoting the scaling dimensions of these as d_L and d_R respectively, we first consider $d_L, d_R > 5/2$.

---

[2] Strictly speaking, the preon sector needs not be a CFT sector. For our purposes, it suffices that the dynamics of the composite preon sector has a slow RG running and an interacting IR fixed point at a much lower scale (this is our dark CFT). Provided this assumption, all our discussion below will be equally applicable.

(i) $d_L, d_R > 5/2$

In this case, the linear couplings are irrelevant operators, and they decrease towards the IR. At some lower scale $\mu < \Lambda_1$, we get

$$\mathcal{L}_{\mu<\Lambda_1} \supset \frac{1}{\Lambda_1}\rho_{B\mu\nu}\bar{\psi}_L\sigma^{\mu\nu}\chi_R + \tilde{y}_\Psi \left(\frac{\mu}{\Lambda_1}\right)^{d_R-\frac{5}{2}} \mu^{\frac{5}{2}-d_R}\bar{\psi}_L\mathcal{O}_R + \tilde{y}_\chi \left(\frac{\mu}{\Lambda_1}\right)^{d_L-5/2} \mu^{\frac{5}{2}-d_L}\bar{\mathcal{O}}_L\chi_R. \tag{5.3}$$

We have defined a dimensionless coupling $\tilde{y}_\psi$ by $y_\psi = \tilde{y}_\psi\Lambda_1^{5/2-d_R}$, and similarly for $\tilde{y}_\chi$.

We imagine that at a scale $\Lambda_2 < \Lambda_1$, the composite CFT_2 confines, generating composite particles and yet another composite CFT denoted as CFT_D. This CFT_D is the dark sector of our theory and carries dark $U(1)_\mathrm{D}$ global symmetry, hence reveals a coupling

$$\mathcal{L}_{\Lambda_2} \supset \mathcal{L}_{\mathrm{CFT}_\mathrm{D}} + g_\mathrm{D} A_{\mathrm{D}\mu} J^\mu_\mathrm{D} + \cdots . \tag{5.4}$$

Here, A^μ_D is a composite vector meson of confined CFT_2 and simultaneously plays the role of external $U(1)_\mathrm{D}$ gauge field coupled to CFT_D current J^μ_D. It also couples to a pair of composite fermions coming from $\mathcal{O}_{L,R}$ through a dipole interaction.

We can use an interpolation relation between the fermionic CFT operators and canonically normalized composite fermion fields, $\mathcal{O}_R \sim \Lambda_2^{d_R-3/2}\sum_n c_n\psi^{(n)}_{\mathrm{comp,R}}$ and $\mathcal{O}_L \sim \Lambda_2^{d_L-3/2}\sum_n d_n\chi^{(n)}_{\mathrm{comp},L}$ [3], to obtain an effective action at Λ_2

$$\begin{aligned}\mathcal{L}_{\Lambda_2} \quad &\supset \mathcal{L}_{\mathrm{CFT}_\mathrm{D}} + g_\mathrm{D} A_{\mathrm{D}\mu} J^\mu_\mathrm{D} + \frac{1}{\Lambda_1}\rho_{B\mu\nu}\bar{\psi}_L\sigma^{\mu\nu}\chi_R + \frac{1}{\Lambda_2}F_{\mathrm{D}\mu\nu}\bar{\psi}_{\mathrm{comp,R}}\sigma^{\mu\nu}\chi_{\mathrm{comp,L}} \\ &+\tilde{y}_\Psi\left(\frac{\Lambda_2}{\Lambda_1}\right)^{d_R-5/2}\Lambda_2\sum_n c_n\bar{\psi}_L\psi^{(n)}_{\mathrm{comp,R}} + \tilde{y}_\chi\left(\frac{\Lambda_2}{\Lambda_1}\right)^{d_L-5/2}\Lambda_2\sum_m d_m\bar{\chi}^{(m)}_{\mathrm{comp,L}}\chi_R.\end{aligned} \tag{5.5}$$

From this, we can estimate the effective kinetic mixing between the elementary $U(1)_Y$

---

[3] The sum is over the tower of composite fermions. c_n and d_n denote the "form factor"s.

gauge boson B_μ and $A_{\mathrm{D}\mu}$ by evaluating the diagram shown in Figure 5.2. From Figure 5.2 it is clear that the effective mixing is tiny due to two factors of fermion mixing since the latter two are very small by a RG evolution. In the end, we get

$$\tilde{\epsilon} \sim \frac{g}{g_{1s}} \frac{\tilde{y}_\Psi \tilde{y}_\chi}{16\pi^2} \left(\frac{\Lambda_2}{\Lambda_1}\right)^{d_L+d_R-4} . \tag{5.6}$$

The factor g/g_{1s} is from the elementary-composite mixing between B_μ and $\rho_{B\mu}$ as explained above, and we note that this estimation is up to possible $\log(\Lambda_2/\Lambda_1)$. We recall that $d_L + d_R > 10$ and therefore, $\tilde{\epsilon}$ can be highly suppressed by virtue of the RG running factor.

Since the dark CFT is uncharged under B_μ, the leading order interaction is expected to be the dipole-type. The interaction strength can be estimated to be (dropping the subscripts, e.g. $\Lambda_2 \to \Lambda$, to get an expression used in the rest of the chapter)

$$\mathcal{L}_{\mathrm{COFI}} \supset \frac{\lambda}{\Lambda^{d-2}} B_{\mu\nu}\mathcal{O}^{\mu\nu}. \tag{5.7}$$

where d is the scaling dimension of $\mathcal{O}^{\mu\nu}$ and $\lambda \sim g_{\mathrm{D}}\tilde{\epsilon}$ and thus can be readily very small.[4]

Finally, we show that asymmetric reheating requires $T_R < \Lambda_2$. Suppose that the decay of the inflaton reheats the *external* sector plasma to a temperature $\Lambda_2 < T_R \lesssim \Lambda_1$. This means that the correct description of the theory right after reheating is that of Equation 5.2. This comes with sizable coupling between the CHM sector and CFT_2. For a generic CFT, the entirety of CFT_2 will then be thermalized via this coupling. In particular, it is unlikely that there is a subsector of CFT_2 which is isolated and remains “cold”. Once the universe cools to $T \sim \Lambda_2$, CFT_2 confines and, in particular, a *thermal* $\mathrm{CFT}_{\mathrm{D}}$ appears. So for a generic CFT_2, $\mathrm{CFT}_{\mathrm{D}}$ will be at roughly the same temperature as the SM sector. On the other hand, if $T_R < \Lambda_2$, then the right description after reheating is Equation 5.7, which comes with

---

[4] The superficial IR-divergence from the intermediate $A_{\mathrm{D}\mu}$ propagator is absent thanks to two-derivatives from $\rho_{B\mu\nu}F_{\mathrm{D}}^{\mu\nu}$.

highly suppressed coupling.

(ii) $d_L, d_R < 5/2$

We briefly discuss the case with $d_L, d_R < 5/2$. The other choices of d_L and d_R are then simply mixture of the two cases we describe.

When $d < 5/2$, the linear mixing in Equation 5.2 is a relevant operator and grows in the IR. The RG running is described by (see e.g. [327, 328])

$$\mu \frac{dy}{d\mu} = \gamma y + c \frac{N}{16\pi^2} y^3 + \cdots \tag{5.8}$$

where $\gamma = d - 5/2 < 0$ is the anomalous dimension of the CFT operator $\mathcal{O}$, N denotes the number of "color" of the gauge theory describing the CFT, and c is an $\mathcal{O}(1)$ number. RG flow increases y and at some point the second term becomes as important as the first. Provided $c > 0$, there exists an IR fixed point where y stops running. We name the scale of the fixed point Λ_* and the coupling at the fixed point $y_* \sim \tilde{y}(\Lambda_*/\Lambda_1)^{d-5/2}$, which can be $\mathcal{O}(1)$. At the fixed point, the linear mixing terms become marginal operators and, at the same time, the fermion fields ψ_L and χ_R acquire sizable anomalous dimension. Explicitly, the scaling dimensions of them become $[\psi_L] = 4 - d_R > 3/2$, $[\chi_R] = 4 - d_L > 3/2$.

Unlike in the first case with $d_L, d_R > 5/2$, the fermion mixings are sizable and one may conclude that the effective mixing $\tilde{\epsilon}$ is not suppressed anymore. This, however, is not true. The anomalous dimensions of ψ_L and χ_R make the dipole interaction appearing in Equation 5.2 very irrelevant interaction with scaling dimension $10 - d_L - d_R > 5$. Via RG evolution, this means that this dipole operator becomes highly suppressed at Λ_2.

$$\frac{1}{\Lambda_1} \left(\frac{\Lambda_2}{\Lambda_*}\right)^{5-d_L-d_R} \Lambda_2^{d_L+d_R-5} \rho_{B\mu\nu} \bar{\psi}_L \sigma^{\mu\nu} \chi_R \tag{5.9}$$

It is then straightforward to estimate the effective mixing $\tilde{\epsilon}$. The final result is in fact the same as Equation 5.6. Interestingly, despite having very different RG evolutions, the product of the dipole interaction and the fermion mixings appearing in Figure 5.2 stays the same in both cases. A similar phenomenon appeared in the neutrino mass from a warped 5d model (and its 4d CFT dual) [328].

Summary for the UV theory

To sum up, asymmetric reheating is achieved by virtue of composite–elementary division[5] and the dynamically generated small coupling, provided the reheat temperature satisfies $T_R < \Lambda_2$. Specifically, the composite–elementary division makes it natural that the primordial reheating occurs only for the external states, hence only the SM sector. Then, the small coupling between the SM and dark CFT sectors, induced by RG running followed by a confining phase transition, forbids an efficient energy transfer from the SM to the dark CFT.

5.2.2 IR effective theory, mass gap, and composite dark photon

In this section, starting from Equation 5.7, we explain the mass gap generation, IR effective theory below the mass gap m_{gap} and comment on notable features of our model.

We first note that since our model is based on a tensor operator, the RG running of the CFT and dynamical mass scale generation do not go through the mechanisms introduced in [321, 322]. In particular, the operator mixing effects [322] which makes the COFI-mechanism generic for the case of scalar operator do not occur in our model. Instead, a necessary scalar deformation may arise from the operator product expansion (OPE) $\mathcal{O}_{\mu\nu} \times \mathcal{O}^{\mu\nu}$. We discuss this in detail in section 5.A. Here, we simply assume that such a scalar CFT operator exists

---

[5] It is this composite–elementary division that distinguishes our theory from the UV completion of COFI by a weakly coupled gauge theory with a IR fixed point proposed in [321]. In the latter case, unless symmetry forbids, generically there will be couplings between the gauge theory sector and the inflaton, and in turn the dark CFT sector will inherit a unsuppressed coupling to the inflaton.

and explore its implications on the IR EFT.

If such a deformation is close to being marginal, the theory described by Equation 5.7 undergoes a slow RG running (walking). At $E \sim m_{\text{gap}}$, the conformal invariance is spontaneously broken and a gap scale is generated. By virtue of walking, the separation between Λ_2 and m_{gap} are generically large.

We make a simplifying assumption that the spontaneous conformal symmetry breaking is a confining phase transition and a spectrum of composite hadrons become the relevant degrees of freedom in the IR. The operator $\mathcal{O}^{\mu\nu}$ is then interpolated by[6]

$$\mathcal{O}^{\mu\nu} \sim \frac{1}{g_s} m_{\text{gap}}^{d-2} \rho_{\mu\nu}, \tag{5.10}$$

where $\rho_{\mu\nu}$ is the field strength of the composite vector meson ρ^{μ}; the dark photon in our theory[7]. The dependence on m_{gap} is fixed by dimensional analysis and $g_s \sim \frac{4\pi}{\sqrt{N}}$ is the coupling constant among the composite states, where N is the number of "color" of the gauge group in the CFT.

The confined phase of the dark CFT may contain a (or a set of) Goldstone boson π and they can play the role of dark matter in our theory. Using Equation 5.10, we obtain the IR effective theory of hadrons from Equation 5.7

$$\mathcal{L}_{\text{IR}} \sim \frac{1}{2g_s^2} \rho_{\mu\nu}\rho^{\mu\nu} + \epsilon B_{\mu\nu}\rho^{\mu\nu} + \partial_\mu \pi^+ \partial^\mu \pi^- + m_{\text{DM}} \pi^+ \pi^- + i g_s \rho^\mu \pi^+ \overleftrightarrow{\partial}_\mu \pi^-, \tag{5.11}$$

with the kinetic mixing given by

$$\epsilon = \frac{\lambda}{g_s} \left(\frac{m_{\text{gap}}}{\Lambda} \right)^{d-2}. \tag{5.12}$$

---

[6] In principle, the operator can have a non-zero overlap with a composite 2-form field $C_{\mu\nu}$. For our purposes, it suffices to assume that $\mathcal{O}_{\mu\nu}$ has unsuppressed overlap with kinetic term of composite dark photon.

[7] Strictly speaking, the dark photon is a mixture of A_D and ρ, but it will be mostly comprised of ρ

We will now make a few comments on the low energy effective theory. The effective kinetic mixing ϵ shown in Equation 5.12 is naturally small. In particular, in addition to the small λ (whose natural smallness was explained earlier), it gets further suppressed by the RG running factor $\left(\frac{m_{\text{gap}}}{\Lambda}\right)^{d-2}$ (recall $d \geq 2$ by unitarity). This latter factor exhibits the interesting fact that a smaller m_{gap} implies a smaller mixing ϵ. This has a straightforward physics interpretation. We first note that m_{gap} is a consequence of conformal invariance breaking effect, thus the size of m_{gap} is positively correlated with the size of the breaking. In general, a smaller m_{gap} means slower (hence longer) RG running of the CFT sector. On the other hand, the mixing, ϵ, is induced from the coupling between the SM and CFT sectors in the UV theory. The unitarity bound $d \geq 2$ implies that the interaction Equation 5.7 is an irrelevant operator. This in turn suggests that smaller m_{gap} results in larger suppression of ϵ from longer RG running.

In addition to the kinetic mixing between the dark photon and hyper-charge gauge boson, we included terms for the dark matter candidate, $\pi^{\pm}$, and their interaction with the dark photon. Here, we assume that dark matter particles are pseudo-Nambu-Goldstone bosons (pNGB) of the spontaneously broken global symmetry of the CFT. Their mass is controlled by the size of the explicit breaking of the global symmetry, which we take to be a free parameter. The ratio $r \equiv m_{\text{DM}}/m_{\text{gap}}$ can be smaller than one, which ensures that dark matter can easily be lightest stable particle[8].

Dark matter will couple to the dark photon in the same manner as the pions in low energy QCD interact with the ρ-meson. The strength of the coupling is $g_s \sim \frac{4\pi}{\sqrt{N}}$. For a reasonable choice of N consistent with large-N treatment, we can take $g_s \sim \mathcal{O}(1)$. This coupling induces self-interaction among dark matter states. For $m_{\text{gap}} \lesssim \mathcal{O}(100)$MeV there are non-trivial constraints on this DM self-interaction, e.g. from observation of the bullet

---

[8] From the form of the effective Lagrangian, we've implicitly assumed that π has a dark charge which ensures stability. If we assumed no such dark charge, then one might expect $\mathcal{O}^{\mu\nu}$ can also interpolate to an operator of the form $\sim \pi\rho^{\mu\nu}$. After kinetic mixing, this will allow the process $\pi \to \gamma\gamma$. However, the LO decay rate will go as ϵ^4; ensuring that its cosmologically long-lived.

cluster. As we discuss later in subsection 5.3.4 (also discussed in [321, 322]), this constraint can be avoided with a proper choice of the ratio $m_{\text{DM}}/m_{\text{gap}} < 1$. Furthermore, any relevant processes involving the visible sector and the dark matter candidate is independent of g_s.

Other than the DM particles, the rest of the hadrons in the confined CFT are expected to have mass on the order of m_{gap}, which we assume to hold for our model. In particular, the dark photon, as one of the normal composite states, is assumed to have mass $\sim m_{\text{gap}}$. We suppress the rest of the hadrons from our effective theory.

5.3 Dark Matter Phenomenology

In this section, we describe the dark matter phenomenology of our theory. In subsection 5.3.1 we discuss the cosmological evolution of the energy density in the dark sector. In subsection 5.3.2, we present a parameter scan which reproduces the observed relic density for IR-dominant production and discuss the main characteristics. In subsection 5.3.3, we present a parameter-scan for UV-dominant production and discuss the associated physics. Lastly, in subsection 5.3.4, we discuss theoretical constraints and relevant observational constraints, including DM self-interaction, warm DM bound, star cooling bound and more. Throughout this section, in order to avoid interrupting the flow of the discussion, we relegate technical details to several appendices (see section 5.D and section 5.E).

5.3.1 Dark matter production mechanisms

The details of the freeze-in production of dark matter in this model depend on the nature of the coupling in Equation 5.7, especially the scaling dimension d of the operator $\mathcal{O}^{\mu\nu}$. At the same time, it also depend on various scales in the problem, including the temperature in the SM sector T, the temperature in the dark sector T_{ds}, m_{gap}, and the dark matter mass m_{DM}.

If the temperature of the SM sector T is larger than m_{gap}, then the freeze-in processes produce CFT objects in the final state. We denote this as COFI production. In the other regime, $T < m_{\text{gap}}$, the final state consists of the "hadronic" states of the confined CFT and the physics becomes that of standard particle production.

The dark sector is assumed to thermalize with itself.[9] When the dark sector is radiation-like, its temperature, T_{ds}, is given by

$$\rho_{\text{ds}} = A T_{\text{ds}}^4, \tag{5.13}$$

where A is the analog of $\frac{\pi^2}{30} \times$ dof appearing in the energy density of a relativistic fluid.

As shown in [321], IR-dominant COFI production can occur if the sum of the scaling dimensions of the operators appearing in the interaction term Equation 5.7 is less than or equal to 9/2. In our case, this requires $2 < d < 5/2$, where the lower limit is the unitarity bound. However, as we will show, this conclusion is based on the assumption that the dark sector is thermalized to a temperature $T_{\text{ds}} > m_{\text{DM}}$ during COFI production. In order to clarify this point, let us first briefly review the COFI production, obtain the bound $d < 5/2$, and generalize it to the case $T_{\text{ds}} < m_{\text{DM}}$.

$T_{\text{ds}} > m_{\text{DM}}$ during the COFI production

Starting from the general Boltzmann equation (BE), the relevant equation for COFI is (see [321] for details)

$$\frac{d}{dt}\rho_{\text{ds}} + 3H(\rho_{\text{ds}} + P_{\text{ds}}) = \Gamma, \tag{5.14}$$

where Γ is the energy transfer rate per volume from SM to CFT. We've dropped the energy transfer from the CFT sector to the SM sector due to the assumption that the CFT energy

---

[9] This condition can easily be satisfied in large-N CFT. Specifically, since we consider non-thermal freeze-in production, our conformal dark sector is a CFT at very low temperature which is strongly interacting. This also allows us to use AdS/CFT duality.

density is always small compared to the SM. In our case, Γ takes a general form

$$\Gamma = \left(\frac{\lambda}{\Lambda^{d-2}}\right)^2 \Gamma_d T^{2d+1} \tag{5.15}$$

with a process- and d-dependent coefficient Γ_d. In order to simplify expressions, we further define $B_d = \left(\frac{\lambda}{\Lambda^{d-2}}\right)^2 \Gamma_d$. For our model, the population of the dark sector can occur via $f\bar{f} \to B_\mu \to$ CFT: annihilation of SM fermion pairs through the exchange of the hypercharge gauge boson. In addition, at finite temperature, the photon acquires a thermal mass m_p. Following [329], we take m_p to be roughly the plasma frequency[10]

$$m_p \approx \omega_p \approx \frac{eT}{3} \approx 0.1T, \tag{5.16}$$

where e is the electric charge. The plasmon can directly decay into the CFT state which contributes to the production. At $T > v$, the intermediate state in the fermion annihilation is the $U(1)_Y$ gauge boson. Below v, it becomes a linear combination of the photon and Z gauge boson. At $T > m_{\text{gap}}$ the final state is the CFT state, while for $T < m_{\text{gap}}$ it is the hadronic state of the confined CFT.[11]

The collision terms take the general form Equation 5.15 and as we show in detail in subsection 5.D.1 the coefficients B_d are given by

$$B_d(\bar{f}f \to \text{CFT}) = \frac{12d}{(2\pi)^{2d+2}} \left(\frac{\lambda e}{\Lambda^{d-2}}\right)^2, \tag{5.17}$$

$$B_d(\gamma^* \to \text{CFT}) = \left(\frac{6A_d e^{2d-4}}{3^{2d-4}\pi^2}\right) \left(\frac{\lambda e}{\Lambda^{d-2}}\right)^2, \tag{5.18}$$

---

[10] The effective in-medium mass is generically a function of the momentum and the polarization mode.

[11] There is, in principle, contribution from pair annihilation of the Higgs doublet (equivalent to Zh annihilation below EWSB). In the case of IR freeze-in, since this process shuts off at scales well above the dark matter mass that we are considering. Its contribution to the overall relic density is negligible. In the case of UV freeze-in, due to the large number of fermions charged under $U(1)_Y$, its contribution is subleading compared to the fermion annihilation process.

where A_d is related to the phase space of CFT state and is defined in Equation 5.72.

Now, let's move onto the LHS of the Boltzmann equation. Rotational and conformal invariance (implying $T^{\mu\nu}$ is traceless) tells us that $P_{\rm ds} = \frac{1}{3}\rho_{\rm ds}$. Here, it is important to realize that usage of this dispersion relation is valid only if $T_{\rm ds} > m_{\rm DM}$.[12] With that, we have

$$-HT\rho_{\rm ds}' + 4H\rho_{\rm ds} = B_d T^{2d+1}, \tag{5.19}$$

where $'$ is a derivative with respect to T. In the radiation dominated epoch,

$$H = \sqrt{g_*}\frac{T^2}{\rm m_{pl}}, \quad {\rm m_{pl}} \equiv \frac{3\sqrt{5}}{2\pi^{3/2}}M_{\rm pl} \approx 7.35 \times 10^{18}{\rm GeV}. \tag{5.20}$$

Ignoring the temperature dependence of the number of relativistic degrees of freedom g_*[13], the solution to Equation 5.19 is of the form

$$\rho_{\rm ds}(T) = \frac{B_d {\rm m_{pl}}}{\sqrt{g_*}(5-2d)} T^4 \left(T^{2d-5} - T_R^{2d-5}\right), \tag{5.21}$$

where T_R is the reheat temperature (we take $T_R \sim \mathcal{O}(\text{TeV})$) and we have used the initial condition $\rho_{\rm ds}(T_R) = 0$. We factored out an overall factor of T^4 which allows us to interpret the expression in the parenthesis as the change of energy density in the comoving frame.

Whenever the production (for each channel) ends at T sufficiently lower than T_R, for $d < 5/2$, we can safely drop the T_R-dependent term. This shows that the production is insensitive to the UV physics (i.e. IR-dominant). Conversely, when $d > 5/2$, the T-terms gets dropped. This demonstrates that the production is only sensitive to the UV physics (i.e. UV-dominant).

---

[12] Strictly speaking, the dark sector plasma is that of a CFT (as opposed to the "hadronic" phase) only if $T_{\rm ds} > m_{\rm gap}$. However, here we are using the fact that so long as $T_{\rm ds} > m_{\rm DM}$ *and* if most of the energy density of the dark sector is rapidly transferred to dark matter state, then the energy density behaves as a relativistic gas.

[13] This is a simplification made here for illustrative purpose. In our numerical results, we include the effect of time dependence of g_*

$T_{\text{ds}} < m_{\text{DM}}$ during the COFI production

If T_{ds} drops below m_{DM} during the production, then the equation of state changes to $P_{\text{ds}} = 0$. The subsequent evolution of the energy density obeys

$$-HT\rho_{\text{ds}}' + 3H\rho_{\text{ds}} = B_d T^{2d+1}. \tag{5.22}$$

Here, we encounter another important temperature threshold, T_{NR}. This is the temperature of the SM bath when the dark sector temperature drops to m_{DM}. After this point, all particle states in the dark sector are non-relativistic.

The solution to the Boltzmann equation for temperatures below T_{NR} is then given by

$$\rho_{\text{ds}}(T)|_{T<T_{\text{NR}}} = \frac{B_d \text{m}_{\text{pl}}}{\sqrt{g_*}(4-2d)} T^3 \left(T^{2d-4} - T_{\text{NR}}^{2d-4}\right) + \left(\frac{T}{T_{\text{NR}}}\right)^3 \rho_{\text{ds}}(T_{\text{NR}}), \tag{5.23}$$

where again we pulled out the overall factor T^3 (the appropriate scaling for matter-like energy density). The second term is simply the evolution of the energy density produced prior to reach this point. As before, the expression in the parenthesis in the first term is the change of energy density in the comoving frame. Crucially, for all $d \geq 2$ (which is always the case for the interaction in Equation 5.7), the production is UV-sensitive. Hence, reaching T_{NR} provides an effective endpoint to COFI production.

For the special case where the dark sector was never relativistic, this corresponds to setting $T_{\text{NR}} = T_R$ and $\rho_{\text{ds}}(T_R) = 0$. In doing so, one can see that the late time energy density only depends on d, λ, T_R, and Λ (provided that the IR scale is much smaller than T_R).

"Hadronic" production

If production continues to occur when the temperature of the SM bath is less than m_{gap}, the characteristic energy of the initial SM states is also less than the mass gap. In this case, the produced final states are "dark hadrons" rather than CFT states[14]. While in principle, the relevant processes and their rates are model-dependent, in the region where m_{DM} is modestly smaller than m_{gap}[15] we obtain a reasonably reliable and simple description as follows. As we show in detail in section 5.C, the "hadronic" production process is (i) UV-dominant (i.e. most of the production occurs at $T \sim m_{\text{gap}}$) and is (ii) subdominant to the energy injected via COFI established at $T > m_{\text{gap}}$ (if at all).

Post-production evolution

Freeze-in production is terminated by a threshold effect. This can be a result of switching to non-relativistic production, switching to the "hadronic" production mode, or the initial states decoupling from the SM bath.

Let T_f be the threshold that puts an end to the production. The subsequent evolution depends on whether the dark sector is radiation-like or matter-like. If it were radiation-like, we get today's dark matter energy density, $\rho_{\text{ds},0}$, by first redshifting as radiation (i.e. as T^4) down to T_{NR} and further redshifting the energy density as matter (i.e. T^3) between T_{NR} and today:

$$\rho_{\text{ds},0} = \rho_{\text{ds}}(T_f)\left(\frac{T_{\text{NR}}}{T_f}\right)^4\left(\frac{T_0}{T_{\text{NR}}}\right)^3 = A m_{\text{DM}}^4\left(\frac{T_0}{T_{\text{NR}}}\right)^3. \tag{5.24}$$

---

[14] This "hadronic" production is strictly speaking not a conformal freeze-in and instead is the usual particle freeze-in.

[15] This will turn out to be a necessary condition in order to evade the DM self-interaction bound (see section 5.3.4).

5.3.2 IR-dominant freeze-in

Based on the discussion in subsection 5.3.1, we are in a position to compute relic abundances of dark matter and study its dependence on various parameters in this model. As is clear from Equation 5.7, the physics of COFI is controlled mainly by two parameters, λ and the scaling dimension d of the CFT operator. These can be traded with m_{gap} and d (see the discussion around Equation 5.48 and Equation 5.49). These parameters will be scanned over in our plots. The remaining model parameters: T_R, Λ, r, and A, are fixed for the plots. We are mainly interested in $T_R \approx \Lambda \sim \mathcal{O}(\text{TeV})$; with $T_R < \Lambda$ to ensure the validity of the theory throughout the entire freeze-in process and asymmetric reheating. The dependence on A is pretty mild. We consider two choices for r: $r = 0.1$ and $r = 0.01$. Finally, depending on scaling dimension d, we have two qualitatively different scenarios. We begin with the so called IR-dominant case, with $2 < d < 2.5$, leaving the UR-dominant production to the next subsection.

The contours of the observed relic density in the plane of (m_{DM}, d) (with the remaining parameters fixed) is shown in orange-red in Figure 5.3. For both panels, there is a general tendency for d to increase with m_{DM}. The physics behind this is that as m_{DM} increases, so does T_{NR} This in turn means that ρ_{ds} starts redshifting as matter at a higher temperature; leading to an effective increase of the final relic density, $\rho_{\text{ds},0}$. This increase must be compensated for by adjusting d so that $\rho_{\text{ds},0}$ matches a constant observed value. A larger d corresponds to a more irrelevant interaction, hence slower heating. Therefore, an increase in m_{DM} is generically balanced by an increase in d, as observed in Figure 5.3. Following this discussion, one can also determine how the general trend of the contour will behave as we lower our choice λ (or equivalently raising Λ). The scattering process will inject less energy into the dark sector. To compensate, m_{DM} can be raised so the dark sector can start redshifting as matter earlier or d can be lowered to make the interaction more relevant. As such, the contour will shift towards the bottom right.

Both plots exhibits some sharp change of slope for large $m_{\rm DM}$. In the case of the left plot, it plateaus; whereas the right plot drops sharply. Both of these correspond to the case with $T_{\rm NR} = T_R$. This can be verified by following the red curve in Figure 5.4. As discussed in section 5.3.1, this results in the late time energy density becoming independent of $m_{\rm DM}$. The discrepancy in the $r = 0.01$ plot is due to the fact that $T_{\rm SM} = m_{\rm gap}$ and $m_p(T_{\rm SM}) = m_{\rm gap}$ occur at scales close to T_R. When this happens, the first term in Equation 5.23 cannot be ignored and the interplay between the two terms determines the overall shape.

A sharp change of slope also occurs for low $m_{\rm DM}$: at $m_{\rm DM} \approx 50$ keV for the plot and $m_{\rm DM} \approx 5$ keV for the right figure. This is a result of $T_{\rm NR}$ dropping below the other possible endpoints of production. This can be verified by checking that the intersection of the blue curve with the black curve in Figure 5.4 does indeed occur at $m_{\rm DM} \approx 50$ keV for $r = 0.1$.

There are several localized bumps and dips in Figure 5.3. They arise from jumps in the number of relativistic degree of freedom, g_*, and the number of production channel. We explain this focusing on the left panel (with $r = m_{\rm DM}/m_{\rm gap} = 0.1$), but our discussion applies in general.

For example, there are noticeable bumps at $m_{\rm DM} \approx$ MeV, $d \approx 2.16$. These features are related to $T_{\rm NR}$ crossing some mass threshold: $\Lambda_{\rm QCD}$ followed by m_μ for the subsequent bump. This fact can be checked by finding the intersection of the yellow curve with the purple dashed line in Figure 5.4.

To understand this better, we note that $T_{\rm NR}$ decreases as we lower $m_{\rm DM}$. When $T_{\rm NR}$ happens to cross a threshold, e.g. the electron mass, there are potentially two effects. First, it reduces the number of production channels, effectively decreasing $\rho_{\rm ds,0}$. This must be compensated for by decreasing d which has an effect of increasing the rate of heating, and hence the final energy density. The second effect is the change of g_*. We incorporated the change of g_* numerically by evaluating the energy density exactly outside of any phase transitions, hence the "jump" in g_* across each mass threshold (except the QCD phase transition and neutrino decoupling) is rather smoothed out. The (smooth) decrease in g_* results in increase in $\rho_{\mathrm{ds},0}$, which then needs to be balanced by increasing d. This explains the smooth rising section right after the drop.

During the QCD phase transition, g_* drops sharply (increase in $\rho_{\mathrm{ds},0}$) and the up, down, and strange quarks decouple (decreasing the production channels, hence $\rho_{\mathrm{ds},0}$). Numerically, it turns out that the former effect dominates and is compensated by a sharp increase in d. Soon after, the muon decouples. This time, the effect of decreasing the number of production channels is larger; requiring a decrease in d.

While the qualitative feature described above is solid, the details of the shape appearing in Figure 5.3 is partly due to the way we implemented g_* and changes in the production channel. Furthermore, the impacts of neglecting the derivative of g_* in the BE can be large. As such, the shape of the contours in that region should not be taken to be exact.

For comparison, we have also drawn an estimate for the relic density contour for the particle freeze-in scenario based on the results given in [10] in green[16]. To obtain this curve, we assumed that the kinetic mixing parameter is given by Equation 5.12 and the dark photon mass obeys $rm_{A'} = m_{\mathrm{DM}}$. Using the right plot as an example, for low dark matter masses, we see that the contour exactly follows the contour of constant kinetic mixing parameter. As m_{DM} increases, the contour is interpolated to another contour of constant kinetic mixing parameter. This is due to the increase in $g_*(m_{A'})$ which needs to be compensated for by increasing the kinetic mixing. This illustrates that the predictions for COFI is very different from that of the particle dark photon scenario.

5.3.3 UV-dominant freeze-in

The contours of the observed relic density in the plane of (m_{DM}, λ) (with the remaining parameters fixed[17]) is shown in Figure 5.5. In both plots, we see the same behavior: two straight lines with constant, negative slope.

The physics of this scenario is simpler to describe compared to the IR-dominant freeze-in scenario. When $d > 5/2$, the T_R-dependent terms become the dominant contribution to the relic density at low temperatures. If the dark sector temperature increases rapidly beyond m_{DM} by the initial energy transfer, we can safely drop the T^{2d-5} term in Equation 5.21 and the energy density is of the form constant$\times T^4$. This tells us that the energy transfer from the SM sector has concluded and the dark sector energy density simply redshifts as radiation. This continues until the dark matter becomes non-relativistic, which occurs at

$$T_{\text{NR}} = \left[\frac{\text{m}_{\text{pl}}}{A\sqrt{g_*(T_R)}(2d-5)}B_d(\text{total})T_R^{2d-5}\right]^{-1/4} m_{\text{DM}}. \tag{5.25}$$

The energy density then continues to redshift as matter until today. This gives

$$\rho_{\text{ds},0} = \left[\frac{\text{m}_{\text{pl}}}{A\sqrt{g_*(T_R)}(2d-5)}B_d(\text{total})T_R^{2d-5}\right]^{3/4} A m_{\text{DM}} T_0^3 \tag{5.26}$$

Factoring out the m_{DM} and λ dependence, we see

$$\rho_{\text{ds},0} \propto \lambda^{3/2} m_{\text{DM}}. \tag{5.27}$$

So a log-log contour plot of constant ρ will look like a straight line.

---

[16] The exclusion contours shown in the figure do not apply to this contour.

[17] For a fixed d, changes to T_R and Λ consistent with $T_R < \Lambda$ is equivalent to redefining λ.

In the case where the dark sector was never relativistic, the energy density today is simply

$$\rho_{\text{ds},0} = \frac{\text{m}_{\text{pl}}}{\sqrt{g_*(T_R)}(2d-4)} B_d(\text{total}) T_R^{2d-4} T_0^3 \propto m_{\text{DM}}^0 \tag{5.28}$$

Here, we see that the relic density is independent of the dark matter mass[18]. Thus, a contour plot of fixed ρ is simply a flat line in λ

5.3.4 Phenomenological constraints

In this section, we discuss experimental as well as theoretical constraints on our model. Ones with non-trivial restrictions on the allowed parameter space are included in the plots of our main results Figure 5.3 and Figure 5.5.

Non-equilibrium

The dark sector must be out of equilibrium with the SM for the freeze-in assumption to be valid. Otherwise, the backreaction from the CFT to SM sector must be included in the Boltzmann equation. For this to be true, we must have

$$\Gamma = n\langle\sigma v\rangle < H \tag{5.29}$$

Using dimensional analysis, the LHS is roughly

$$\Gamma \sim \lambda^2 \frac{T^{2d-3}}{\Lambda^{2d-4}}, \tag{5.30}$$

while the RHS is roughly

$$H \sim \frac{T^2}{\text{m}_{\text{pl}}} \tag{5.31}$$

---

[18] Just like in the case of the IR-dominant production, there are higher order corrections which do depend on the dark matter mass.

Rearranging gives

$$\lambda^2 \lesssim \left(\frac{\Lambda}{T}\right)^{2d-4} \frac{T}{\mathrm{m_{pl}}}. \tag{5.32}$$

For IR-dominant production (i.e. $2 < d < 5/2$), it is sufficient to demand that it was out of equilibrium at the very last moment. A ballpark estimation can be made by considering $m_{\mathrm{DM}} \approx m_e$ and $d = 2.25$, $\Lambda = 1$ TeV for which we get $\lambda \lesssim 10^{-10}$. The above bound can be translated to a bound on the kinetic mixing

$$\epsilon \lesssim \frac{1}{g_s}\left(\frac{m_e}{\mathrm{m_{pl}}}\right)^{1/5}\left(\frac{m_{\mathrm{gap}}}{m_e}\right)^{d-2} \quad \text{for } m_{\mathrm{DM}} < m_e, \tag{5.33}$$

$$\epsilon \lesssim \frac{1}{g_s}\left(\frac{m_{\mathrm{DM}}}{\mathrm{m_{pl}}}\right)^{1/5}\left(\frac{m_{\mathrm{gap}}}{m_{\mathrm{DM}}}\right)^{d-2} \quad \text{for } m_{\mathrm{DM}} > m_e, \tag{5.34}$$

where $g_s \sim \mathcal{O}(1)$ is the coupling among hadrons of confining phase of the dark CFT.

For UV-dominate production (i.e. $d > 5/2$), exponent of T is positive. So we need non-equilibrium to hold at the onset. So this translates to

$$\lambda^2 < \left(\frac{\Lambda}{T_R}\right)^{2d-4} \frac{T_R}{\mathrm{m_{pl}}} \tag{5.35}$$

Choosing $\Lambda \sim T_R = 1$ TeV, we get $\lambda \lesssim 10^{-8}$.

DM self-interaction

Once the CFT confines, we expect that hadrons of the IR phase interact with each other with coupling strength g_s. Unlike the scenario studied in [321], we must have vector-boson-mediated self interactions in the dark sector. Here, the vector-meson is nothing but the composite dark photon coming from the CFT operator $\mathcal{O}_{\mu\nu}$. The estimate of the cross section via dimensional analysis is given by

$$\sigma_{\text{self}} \sim \frac{1}{8\pi}\frac{m_{\text{DM}}^2}{m_\rho^4} = \frac{1}{8\pi m_{\text{gap}}^2} r^2. \tag{5.36}$$

In this case (i.e dimension 4 vector mediation as opposed to dimension 5 scalar mediation), we see that the suppression is only r^2 rather than r^6 as in [321]. The DM self-interaction bound

$$\frac{\sigma_{\text{self}}}{m_{\text{DM}}} < 4500 \text{ GeV}^{-3} \tag{5.37}$$

becomes

$$m_{\text{DM}} \gtrsim 10 r^{4/3} \text{ MeV}. \tag{5.38}$$

Warm dark matter

For $m_{\text{DM}} \sim$ keV, our dark sector generically starts of as a relativistic plasma. Therefore, one needs to worry about a potentially large free streaming distance (λ_{FS}); suppressing structure formation below that length scale. Assuming collisionless dark matter, λ_{FS} is the comoving distance traveled until some late time when the dark matter becomes highly non-relativistic. Following original derivation in [322], we know that the mean-free path in COFI theories are given by

$$\lambda_{\text{FS, bound}} \sim \left.\frac{1}{T}\right|_{T_{\text{ds}}=m_{\text{DM}}} = \frac{1}{T_{\text{NR}}}. \tag{5.39}$$

By demanding the correct relic abundance, we can use Equation 5.24 to write T_{NR} as a constant times $m_{\text{DM}}^{4/3}$. With that constraint, the warm dark matter bound is constant in the dark matter mass[19].

---

[19] While the warm dark matter bound will be shown as a constant in m_{DM} in our plots, it is important to note that the relic density for all points above the orange-red line is less than the observed relic density. This implies that the dark sector is colder. In addition, as our dark matter is now a subcomponent, the warm dark matter bound is in-principle further relaxed. As such, the shaded region above the line should be interpreted as a conservative estimate for the exclusion.

Depending on the details of the modelling, the constraints on the mass of a warm thermal relic is given by [330]

$$m_{\mathrm{DM}} \gtrsim 3.5 - 5.3 \text{ keV}.$$

Constraints from searches at terrestrial experiments

In our model, the dark photon almost always decays invisibly. The dominant constraints from dark photons to invisible searches and LDMX projections are quoted in [331]. Since the kinetic mixing required to satisfy the out-of-equilibrium constraint is sufficiently small, we safely evade these bounds. Furthermore, as the dark photon is relatively heavy, we do not obtain a $1/v^2$ enhancement for direct detection experiments.

Stellar evolution

For a given stellar system with internal processes occurring at a scale T_S, there can be very distinct phenomenology depending on the mass of the dark matter candidate. If $m_{\mathrm{DM}} > T_S$, we are in the hadronic phase which prevents CFT states from being directly produced. Furthermore, the dark matter particle cannot be produced directly as it is kinematically forbidden. If $m_{\mathrm{DM}} \lesssim T_S \lesssim m_{\mathrm{gap}}$, then the dark matter production is no longer kinematically forbidden. Lastly, if $T_S \gtrsim m_{\mathrm{gap}}$, we are in the CFT phase, so CFT states are produced within the star. Only the latter two scenarios can rule out regions of parameter space. In the following subsections, we will briefly discuss the expected features of the constraints obtained via these two scenarios. The details of the estimate will be presented in section 5.E and we refer to [322] for a general discussion of star cooling bounds in COFI theories.

(i) $T_S \gtrsim m_{\mathrm{gap}}$

In this region, the only parameters of the model that influence the energy density loss rate, $\dot{\varepsilon}$, are Λ, λ, and d. Provided that Λ and λ are kept fixed, any constraints on $\dot{\varepsilon}$ will translate to a constant upper bound on d. An order-of-magnitude estimate on $\dot{\varepsilon}$ was performed and yielded an upper bound below the unitarity limit of d for all stellar systems. As such, this feature will not be seen on the plots. However, it should be noted that $\mathcal{O}(1)$ factors in $\dot{\varepsilon}$ can have sizable impacts on the bound on d. This could potentially alter our conclusion on the bounds for HB stars but not the other systems.

(ii) $m_{\rm DM} \lesssim T_S \lesssim m_{\rm gap}$

In this scenario, $\dot{\varepsilon}$ depends on all of the parameters of the model. In particular, as all of the dark matter production is mediated via the dark photon, the novel energy loss rate will always have the following dependence

$$\dot{\varepsilon} \propto \left(\frac{\lambda m_{\rm gap}^{d-2}}{\Lambda^{d-2}}\right)^2 \frac{1}{m_{\rm gap}^4} \tag{5.40}$$

As $m_{\rm gap} \ll \Lambda$, $\dot{\varepsilon}$ is a decreasing function of d. When $2 \leq d < 5/2$, $\dot{\varepsilon}$ is also a decreasing function of $m_{\rm gap}$. So the curve of constant $\dot{\varepsilon}$ will have negative slope on the $m_{\rm gap}$–d plane (and by extension, the $m_{\rm DM}$–d plane).

The systems which provide the strongest constraints are HB stars and RG cores. Both of these systems facilitate scattering processes with $T_S \sim 10$ keV; covering $10r$ keV$\lesssim m_{\rm DM} \lesssim$ 10 keV. The total allowed "novel" energy loss rate for these systems is typically constrained to be within the neutrino flux. Numerically, the constraints from both systems are derived from the "effective Fermi constant". So these constraints are both comparable.

MS stars provide a much weaker constraint. The total allowed "novel" energy loss is orders of magnitudes larger than the solar neutrino flux. This results in a much weaker constraint at r keV $\lesssim m_{\rm DM} \lesssim 1$ keV.

SN1987A does not provide any constraint for $30r$ MeV $\lesssim m_{\rm DM} \lesssim 30$ MeV. In the hadronic phase, our model is the usual dark photon particle freeze-in scenario with a heavy dark photon. This tells us that the novel energy loss is the same as the usual dark photon freeze-in models with an additional $(T_S/m_{\rm gap})^4$ suppression. Given that SN1987A does not constrain particle freeze-in, this is also true for us.

5.4 Conclusion of the Chapter

In this chapter, we have considered a scenario in which a dark sector is described by a CFT and it interacts with the Standard Model via an antisymmetric tensor coupling

$$\mathcal{L} \supset \frac{\lambda}{\Lambda^{d-2}} B_{\mu\nu} \mathcal{O}^{\mu\nu}, \tag{5.41}$$

where $B_{\mu\nu}$ is the field strength of the $U(1)_Y$ gauge boson of the SM and $\mathcal{O}^{\mu\nu}$ is an antisymmetric tensor operator of the dark CFT. Provided the coupling is sufficiently small, we show that the dark sector can be populated via Conformal Freeze-In [321, 322]. In our case, the freeze-in production is through a tensor (as opposed to scalar) coupling. A successful implementation of the freeze-in mechanism also requires the reheating to be preferential to the SM sector. We propose a scenario involving a cascade of CFTs, ending with the CFT describing the dark sector. This model provides a dynamical explanation of the hierarchy of scales, sizes of the couplings, as well as a natural realization of the asymmetric reheating.

Once the dark CFT confines, a composite dark photon emerges from the above coupling with a highly suppressed kinetic mixing with the $U(1)_Y$ gauge boson. This composite dark photon couples to a dark matter particle, which we assume to be a Goldstone boson of a spontaneously broken global symmetry. The size of kinetic mixing also has a unique positive correlation with the mass gap scale; hence the mass of the dark photon Equation 5.12.

All these features combined make the theory very predictive and, at the same time, represent an example where small couplings and mass scales significantly different from the ones appearing in the SM are explained rather than just assumed as inputs.

We study in detail the dark matter production, cosmological evolution, and relevant constraints from considerations of dark matter self-interaction, warm dark matter bound, and stellar evolution. We consider both possibilities where the dark matter production is UV- and IR-dominant, and show that the correct relic abundance can be obtained with reasonable choices of parameters. We found viable dark matter candidates in the range of MeV to GeV, with a dark sector confinement scale and dark photon mass a factor of approximately 10 –100 times higher.

There is one important distinction between our setup and the “usual" scenario with only an elementary dark photon with a tiny coupling to the SM. In our setup, the relic abundance is mainly determined by the conformal dynamics instead of being mediated by the dark photon. Hence, it leads to very different predictions for the correlation between the dark matter and dark photon properties. A richer dark sector can lead to richer physics as well. For example, the cascade of phase transitions between the transitions among the CFTs can leave their imprints in cosmological observations, such as the gravitational wave signals. We leave further exploration of these interesting possibilities for a future study.

5.A Dynamical Mass Scale Generation in COFI Theories

5.A.1 Gap scale in COFI theories with a scalar operator

In the UV, COFI theories assume a coupling between the SM sector and a CFT sector of the form

$$\mathcal{L} \supset \frac{\lambda}{\Lambda^{D-4}} \mathcal{O}_{\rm SM} \mathcal{O}_{\rm CFT} \tag{5.42}$$

where $\mathcal{O}_{\rm SM/CFT}$ is a gauge invariant operator (invariant under its own gauge group) and D is the sum of scaling dimensions of the two operators. The dimensionless coupling λ needs to be small for the dark matter relic density to be obtained via freeze-in. Such a small value can arise naturally from dimensional transmutation if the above theory emerges as an IR phase of a UV gauge theory with a IR-fixed point. See [321] for a UV completion via weakly coupled gauge theory and section 5.2 for a UV completion in terms of strongly coupled CFT with a 5d holographic dual.

In the absence of other conformal symmetry breaking terms, the interaction in Equation 5.42 is the main source of conformal symmetry breaking. The details of how this occurs depend on the nature of the SM operator $\mathcal{O}_{\rm SM}$. If the vacuum expectation value (vev) of $\mathcal{O}_{\rm SM}$ is non-zero, then the renormalization group (RG) flow ensures that the above theory flows to

$$\mathcal{L} \sim \frac{\lambda}{\Lambda^{D-4}} \langle \mathcal{O}_{\rm SM} \rangle \mathcal{O}_{\rm CFT} \tag{5.43}$$

at $E \sim \langle \mathcal{O}_{\rm SM} \rangle$. This can be recognized as a scalar deformation to the CFT and triggers running of the CFT (provided the CFT operator has dimension ≤ 4). The scale at which the conformal invariance is completely lost and a new IR phase (we assume that it is the usual confinement phase) arises is estimated to be [321]

$$m_{\rm gap} \sim \left(\frac{\lambda}{\Lambda^{D-4}} \langle \mathcal{O}_{\rm SM} \rangle \right)^{1/(4-d)}, \tag{5.44}$$

where d is the scaling dimension of the CFT operator. Below the gap scale (i.e. $E \leq m_{\rm gap}$), CFT states turn into composite particles states. Some of these composite states may be stable on a cosmological time scale and plays the role of DM.

Even when $\langle \mathcal{O}_{\rm SM} \rangle = 0$, conformality loss still occur due to “operator-mixing effects”[322]. The idea is that given the coupling in Equation 5.42, other sets of interactions are induced either at tree or loop level. This gives

$$\mathcal{L} \sim \sum_i b_i \mathcal{O}_{\rm CFT} + c_i \mathcal{O}^i_{\rm SM} \mathcal{O}_{\rm CFT} + d_i \mathcal{O}^2_{\rm CFT}, \tag{5.45}$$

where b_i, c_i and d_i are generic dimensionful coefficients which can be reliably estimated within a theory.

The first kind of mixing effect with a coefficient b_i arises by contracting all SM fields in $\mathcal{O}_{\rm SM}$ forming a loop diagram. An important example is the gluon portal with $\mathcal{O}_{\rm SM} = G^a_{\mu\nu} G^{a\mu\nu}$. In this case, one simply closes up gluon lines in a loop and it provides a dominant source for the CFT-breaking [322]. For the second kind with a coefficient c_i, some of the induced operators $\mathcal{O}^i_{\rm SM}$ can have non-vanishing vev leading to the breaking of conformal symmetry as described in the procedure above. For instance, starting with $\mathcal{O}_{\rm SM} = HL^\dagger \ell_R$, the operator $(H^\dagger H)\mathcal{O}_{\rm CFT}$ is generated at one-loop as shown in Figure 5.6. This provides a source of CFT breaking. In addition, $\mathcal{O}^2_{\rm CFT}$ may contribute to the breaking of conformal invariance if its scaling dimension is not greater than 4 (in the large-N limit, the scaling dimension of $\mathcal{O}^2_{\rm CFT}$ is roughly twice that of $\mathcal{O}_{\rm CFT}$). Ultimately, the mass gap scale is obtained by taking into account of all these effects, and is primarily determined by the largest breaking effect. See [322] for a comprehensive discussion.

5.A.2 Gap scale in COFI theory with an anti-symmetric tensor operator

At a UV scale, Λ, on the order of a few TeV, the Lagrangian of the theory is given by

$$\mathcal{L} \sim \frac{\lambda}{\Lambda^{d-2}} B_{\mu\nu}\mathcal{O}^{\mu\nu} \tag{5.46}$$

where $B_{\mu\nu}$ is the field strength of $U(1)_Y$ gauge boson of the SM. For freeze-in production of DM, we take $\lambda \sim \mathcal{O}(10^{-10}$–$10^{-11})$. This small coupling can arise naturally according to the construction described in section 5.2.

In order to study the RG evolution of the theory described by Equation 5.46 and the gap scale generation, we first note that no operator mixing effect of the first two kinds (b_i and c_i terms in Equation 5.45) can lead to a reliable source for the conformal symmetry breaking. This is simply because such induced operators are not scalar CFT operators.

Moving onto the third kind, at scales above the vev of the SM Higgs, v, the operator in Equation 5.46 does not mix with any other *local scalar* operators proportional to $\mathcal{O}_{\mu\nu}\mathcal{O}^{\mu\nu}$. This is because any diagram superficially generating such an operator involves massless propagator of the hypercharge gauge boson B_μ and hence is non-local. This changes once electroweak symmetry is broken. Now, $B_\mu = \cos\theta_W A_\mu + \sin\theta_W Z_\mu$. At $E < m_Z$, the exchange by Z-boson can generate other local operators. To see this we consider a scalar operator from OPE of two $\mathcal{O}_{\mu\nu}$'s

$$\mathcal{O}_{\mu\nu} \times \mathcal{O}^{\mu\nu} \supset \left[\mathcal{O}_{\mu\nu}\mathcal{O}^{\mu\nu}\right]_{n,\ell} \sim \mathcal{O}_{\mu\nu}\Box^n\partial_{\mu_1}\cdots\partial_{\mu_\ell}\mathcal{O}^{\mu\nu} \tag{5.47}$$

and the scaling dimension of the scalar operator $\mathcal{O}_s$ in the OPE expansion (i.e. $n = 0, \ell = 0$) is given by $d_s = 2d + \gamma$ where γ is the anomalous dimension. To the extent that negative anomalous dimension is possible, it is expected that such an operator can serve as a scalar deformation to the CFT.[20]

In fact, the Z-boson exchange generates the operator

$$\mathcal{L} \sim \left(\frac{\lambda}{\Lambda^{d-2}}\right)^2 \frac{e_s \sin^2\theta_W}{m_Z^{d_s-2d}}\mathcal{O}_s \tag{5.48}$$

where the scalar operator $\mathcal{O}_s$ is the lowest dimensional operator with dimension d_s in the OPE with dimensionless coefficient e_s.

In this work, we assume that there exists a CFT scalar operator $\mathcal{O}_s$ with scaling dimension d_s and there is a large gap in the CFT operator spectrum such that the scale of conformality lost is reliably estimated by the RG running of this single operator. To the best of our knowledge, no numerical CFT bootstrap bound on the scaling dimension of such a scalar operator from the OPE of antisymmetric rank-2 tensor operator is available in the literature. It would be interesting to compute the bound and to see if non-trivial constraints on our

---

[20] In AdS/CFT, the anomalous dimension $\gamma_{n,\ell}$ of a general spinned operator in the OPE expansion corresponds to the binding energy of the two antisymmetric tensor particles in the bulk. The scaling dimension is dual to the bulk energy of such a bound state and is given by $\Delta = 2d + 2n + \ell + \gamma_{n,\ell}$, where Δ and ℓ are the scaling dimension and the spin of the operator in the OPE expansion respectively. In the large-ℓ limit, it is known that the anomalous dimension takes the universal behavior $\gamma_{n,\ell} \sim \ell^{-\tau}$ where the twist τ is defined by $\tau = \Delta - \ell$. In particular, the energy momentum tensor (which exists in any QFT) satisfies $\tau = 2$ and $\gamma_{0,2} < 0$; the latter being the dual of the fact that the gravitational force is attractive. See e.g. [332] for more discussion.

scenario is imposed.

Given a scalar deformation term

$$\mathcal{L} \sim c_s \mathcal{O}_s, \tag{5.49}$$

the gap scale is estimated to be $m_{\text{gap}} \sim c_s^{1/(4-d_s)}$. Since we do not have prior knowledge of the scalar deformation generated from the OPE, we simply treat m_{gap} as a free parameter for our study of the dark matter phenomenology.

5.B AdS/CFT Correspondence for COFI

5.B.1 Details of the 5d dual

In this section, we discuss the AdS dual of the theory setup described in section 5.2.

A 4d theory of COFI can be thought of as the dual of a theory living on a slice of AdS_5. A simple cartoon level of this AdS_5 picture is depicted in Figure 5.7. Neglecting the first part of the bulk associated with the physics of inflation, roughly speaking, there is a bulk where all the SM fields propagate as in the standard Randall-Sundrum (RS) model [333, 334], which is dual to a CHM in 4d. There exists an additional bulk in the deeper IR (i.e. larger z) where dark sector (DS) fields propagate.[21] The two sectors communicate via brane-localized interactions.[22]

Inflation occurs at a very high energy scale, and so it is natural that the inflaton appears in the most UV part (small z) of the theory in 5d. In Figure 5.7, we added a "sector" of inflation depicted as an extra bulk slice beyond the SM slice. If the profile of the inflaton field, Φ, is inclined towards the UV brane, a completely natural picture emerges in which the SM sector gets reheated much more than the dark sector simply by the size of overlap with

---

[21] The theoretical framework for this type of generalization of the standard RS model with multiple branes was introduced in [326] and phenomenology was studied in [335, 336, 337, 338].

[22] In COFI, for simplicity, the SM sector is taken to be purely elementary. This may be realized by taking a limit in 5d in which the SM-bulk is taken to be a infinitely thin brane.

the inflaton field; in 5d, this is a consequence of the geometric (de)localization and in 4d, it is dual to the renormalization group flow effects. In order to simplify the discussion, we note that the details within the "inflation-bulk" is not important for us and we will simply take a thin brane limit for the inflaton sector (see Figure 5.8 but we still use Figure 5.7 for the discussion below).

The presence of a throat further in the deep IR (i.e. beyond $z = z_1$) in the 5d dual means that in 4d the confinement of CFT_1 at Λ_1 (associated with z_1) also creates a set of interacting *composite preons* (like quarks and gluons of the QCD). This sector carries no SM charges and their dynamics brings the sector into a strongly interacting IR fixed point at a scale not so much below Λ_1. This course of physics is not quite spelled out in the 5d physics when represented as a thin brane separating the two bulks.

In 5d, we add a $U(1)_{\mathrm{D}}$ gauge field in the DS-bulk and choose $(+,-)$ boundary conditions (BCs) (i.e. Neumann BC on the intermediate brane and Dirichlet BC on the IR brane). This ensures that there are no zero modes and at the same time allows us to write down a brane-localized interaction. The brane-localized interactions takes the form

$$\mathcal{L}_{\mathrm{brane}} \sim \epsilon_{5\mathrm{d}} B_{\mu\nu} F_{\mathrm{D}}^{\mu\nu} = \epsilon_{5\mathrm{d}} \sum_n \sum_m f_B^{(n)}(z_1) f_{\mathrm{D}}^{(m)}(z_1) B_{\mu\nu}^{(n)} F_{\mathrm{D}}^{(m)\mu\nu}. \tag{5.50}$$

Since the $U(1)_Y$ KK-modes, $B_\mu^{(n>0)}$, have profiles localized to the intermediate brane at $z = z_1$, they have sizable coupling with the dark $U(1)_{\mathrm{D}}$ gauge boson $A_{\mathrm{D}}^{(1)}$.[23] If $T_R \sim \Lambda_1$ (but less than confinement phase transition temperature), these KK modes can be excited and can easily populate the dark sector. If $T_R \ll \Lambda_1$, they are not produced cosmologically; leaving only the zero mode, $B_\mu^{(0)}$, (i.e. SM field) coupled to the dark CFT. If, on the other hand, $T_R > \Lambda_1$, a more appropriate description is in terms of the thermal CFT_1 in which

---

[23] To be more precise, the profile of $A_{\mathrm{D}}^{(1)}$ is peaked near the IR brane and suppressed at the intermediate brane. This may raise a question of whether the effective coupling is highly suppressed. From the discussion of elementary-composite mixing given in subsection 5.2.1, however, we know that this suppression is only $\mathcal{O}(g/g_s)$.

there is no clear distinction between the SM and the DS.

Next, we show that small λ appearing in Equation 5.7 requires the existence of an extra bulk (BZ-bulk) between the SM and DS bulk as shown in Figure 5.8. Let us first discuss the case with only SM and DS bulks (i.e. the BZ-bulk is shrunk to a thin brane). The $U(1)_{\mathrm{D}}$ gauge field living in the DS-bulk couples to the SM sector by a kinetic mixing written down on a brane, $B_{\mu\nu}F_{\mathrm{D}}^{\mu\nu}$. In the CFT picture, this means that the first confinement at Λ_1 gives rise to a "composite" CFT (called it $\mathrm{CFT_D}$ in section 5.2) and it interacts with the SM fields via

$$\mathcal{L} \sim \mathcal{L}_{\mathrm{CFT_D}} + \epsilon\rho_{B\mu\nu}F_{\mathrm{D}}^{\mu\nu} + g_{\mathrm{D}}A_{\mathrm{D}\mu}J_{\mathrm{D}}^{\mu} \tag{5.51}$$

where ρ_B^μ is a composite vector meson associated with $U(1)_Y$ and A_{D}^μ and $F_{\mathrm{D}}^{\mu\nu}$ is a composite vector boson and its field strength external to the dark CFT. The latter couples to the dark CFT through its coupling to $U(1)_{\mathrm{D}}$ current and to the composite SM sector via kinetic mixing with ρ_B^μ. Since $\mathrm{CFT_D}$ is purely composite, its interaction with the external field B_μ needs to be through its coupling to a composite state, ρ_B^μ, which then mixes with B_μ. The composite-elementary mixing is $\mathcal{O}(g/g_{1s})$, where $g(g_{1s})$ is the elementary (composite) gauge coupling[24]. If the reheat temperature is less than Λ_1, Equation 5.51 is the right description after the reheating. This, however, comes with a sizable interaction between the SM and DS. The SM interacts with the DS through B^μ–ρ_B^μ mixing and then ρ_B^μ–A_{D}^μ mixing, and finally A_{D}^μ coupling to the dark CFT. Generically, we expect that ϵ and g_{D} are not small, leading to a significant coupling which can be estimated to be

$$\mathcal{L} \sim \left(\frac{g}{g_{1s}}\right)\frac{\epsilon g_{\mathrm{D}}}{\Lambda_1^{d-2}}B_{\mu\nu}\mathcal{O}_{\mathrm{D}}^{\mu\nu}, \tag{5.52}$$

where d is the scaling dimension of the tensor operator $\mathcal{O}_{\mathrm{D}}^{\mu\nu}$ of the $\mathrm{CFT_D}$. We assumed that

---

[24] In more detail, the composite-elementary mixing is of the form $\frac{g}{g_{1s}}\Lambda_1^2 B_\mu\rho_B^\mu$, which originates from $gB_\mu J^\mu$ in the UV Lagrangian using the interpolation relation $J^\mu \sim \frac{\Lambda_1^2}{g_{1s}}\rho_B^\mu$. See section 2.3.2 of [326] for more details.

there is a coupling between $F_{\mathrm{D}}^{\mu\nu}$ and $\mathcal{O}_{\mathrm{D}}^{\mu\nu}$ which is on the order of g_{D}. We see that other than the mild suppression factor from the composite-elementary mixing, the net interaction is unsuppressed and the DS will be quickly equilibrated with the SM, invalidating both the asymmetric reheating and non-thermal freeze-in production.

To resolve this, we now introduce an extra bulk, the BZ-bulk, between the SM and DS bulks, as depicted in Figure 5.8. Intuitively, this BZ-bulk can be alternatively thought as a thick opaque brane. Due to the finite penetration depth, both B_μ and $A_{\mathrm{D}\mu}$ are attenuated, resulting in an extra reduction in their overlap. More explicitly, the interaction between the SM and DS is mediated by a field living in the BZ-bulk. For instance, it can be a pair of bulk fermions, ψ and χ, coupling to each side via dipole interactions

$$S \supset \int_{z=z_1} \frac{a}{\Lambda_1} B_{\mu\nu} \bar{\psi}_L \sigma^{\mu\nu} \chi_R(z_1) + \int_{z=z_1'} \frac{b}{\Lambda_2} F_{\mathrm{D}\mu\nu} \bar{\chi}_L \sigma^{\mu\nu} \psi_R(z_1'), \tag{5.53}$$

where a and b are dimensionless constants. In order to get the above interactions, we have chosen the following boundary conditions for the bulk fermions.

$$\psi = \begin{pmatrix} \psi_L(+,-) \\ \psi_R(-,+) \end{pmatrix}, \qquad \chi = \begin{pmatrix} \chi_L(-,+) \\ \chi_R(+,-) \end{pmatrix}. \tag{5.54}$$

Here, $+(-)$ denotes the Neumann (Dirichlet) boundary condition, and the above choice ensures that there are no fermion zero modes, thereby removing potential inconsistency with cosmological observations (e.g. ΔN_{eff}).

Crucially, if the reheat temperature is below Λ_2 (dual to $z = z_1'$), one can use KK-decomposition (as opposed to thermal CFT) to show that the exponentially suppressed profile leads to a very small the effective coupling between the SM and DS. This suppression is a 5d dual version of suppression seen in 4d picture from RG running (i.e. the discussion around Equation 5.5 and Equation 5.6 and analogous discussion for $d_{L,R} < 5/2$). More explicitly, if we choose bulk masses for ψ and χ such that their zero mode profiles are localized near the brane at $z = z_1$ (corresponding to $d_{L,R} > 5/2$ in subsection 5.2.1), then while a can be $\mathcal{O}(1)$, due to profile suppressions, b is exponentially suppressed. The effective coupling, denoted as $\tilde{\epsilon}$ in subsection 5.2.1 is proportional to the product ab and hence highly suppressed. A similar argument applies to the opposite case $d_{L,R} < 2/5$: this time b is $\mathcal{O}(1)$ but a is exponentially suppressed. Contributions from KK modes are also suppressed because KK profiles are all very inclined towards the IR brane at $z = z_1'$. The 4d dual picture is discussed in subsection 5.2.1 and the diagram Figure 5.2 represents the sum of both zero- and first KK-modes (in a sense of 2-site truncation of [339]).

An effective coupling between the SM and DS is obtained by computing the fermion loop stretched between the z_1 and z_1' branes which is UV-finite. The result should be on the order of what is shown in Equation 5.6.

5.B.2 Summary of 5d picture

The holographic dual picture of conformal freeze-in physics is shown in Figure 5.7. The feature that dark sector bulk (denoted as DS) appears at larger z (i.e. deeper IR) compared to the SM-bulk is a reflection of the SM being external to the dark CFT sector in the 4d picture. Furthermore, the fact that inflation occurs at very high energy scale makes it natural that the “inflation-bulk” appears in the deepest UV (i.e. smallest z). Due to the smaller overlap with the DS states, the SM states can be preferentially produced at reheating. To ensure asymmetric reheating, we need the coupling between the two sectors to be small. This necessitates another bulk (shown as “BZ” in Figure 5.8); providing effective sequestering of the DS bulk.

5.C Hadronic Production

Provided $m_{\text{DM}} \ll m_{\text{gap}}$ (in practice an $\mathcal{O}(1)$ separation suffices), at $T < m_{\text{gap}}$, most of the dark hadrons decouple and the effective theory is described by

$$\mathcal{L} \sim \epsilon B_{\mu\nu}\rho^{\mu\nu} + g_s J^{\mu}_{\text{DM}}\rho_{\mu} + eJ_{\mu}A^{\mu}, \tag{5.55}$$

where $J^{\mu} = \bar{\psi}\gamma^{\mu}\psi$ is the SM fermion (e.g. electron) current coupled to the photon, A_{μ}, and $J^{\mu}_{\text{DM}} = \left(\pi^{\dagger}\partial_{\mu}\pi + \text{h.c.}\right)$ is the DM current coupled to the dark photon, ρ_{μ}. As usual, the kinetic mixing can be diagonalized to get

$$\mathcal{L} \sim e\epsilon J^{\mu}\rho_{\mu} + g_s J^{\mu}_{\text{DM}}\rho_{\mu} + eJ^{\mu}A_{\mu}, \tag{5.56}$$

where the first term represents the coupling of the dark photon to the SM fermion current. Since the mass of the composite dark photon is $m_{\rho} \approx m_{\text{gap}}$, at $T < m_{\text{gap}}$, we can further integrate out the dark photon and acquire a higher-dimensional operator describing the interaction between the DM and the SM

$$\mathcal{L} \sim e\epsilon g_s \frac{J_{\mu}J^{\mu}_{\text{DM}}}{m^2_{\text{gap}}}. \tag{5.57}$$

The higher-dimensional nature of the operator reveals that the process is UV-dominant. More explicitly, the energy transfer rate from the fermion annihilation is estimated to be

$$\Gamma\left(\bar{\psi}\psi \to \pi\pi\right) \sim \frac{1}{8\pi}\frac{e^2\epsilon^2 g_s^2}{m^4_{\text{gap}}}T^9. \tag{5.58}$$

Here, T^6 is from n^2_{ψ}, a factor of T^2 from the derivative of π, and one factor of T from E_{transfer} (since we are computing a rate for the energy transfer).

We now show that this production is sub-dominant and therefore, to a good approximation, we can say that COFI production ends around $T \sim m_{\rm gap}$. In order to show the subdominance condition, we first consider the case where, in the UV, there was relativistic COFI production (i.e. $T_{\rm ds} > m_{\rm DM}$) and $T_{\rm NR} < m_{\rm gap}$. In this case, the Boltzmann equation Equation 5.14 can be solved using Equation 5.58 giving

$$\rho_{\rm ds,Had}(T < m_{\rm gap}) \approx \frac{\hat{B} {\rm m_{pl}}}{3\sqrt{g_*}} T^4 m_{\rm gap}^3, \quad \hat{B} = \frac{e^2 \epsilon^2 g_s^2}{m_{\rm gap}^4} = \frac{e^2 \lambda^2}{m_{\rm gap}^4} \left(\frac{m_{\rm gap}}{\Lambda}\right)^{2d-4}, \tag{5.59}$$

where we have kept only the leading term (valid at $T \ll m_{\rm gap}$). On the other hand, the energy density from COFI $T > m_{\rm gap}$ is

$$\rho_{\rm ds,R}(T < m_{\rm gap}) \approx \frac{B_d {\rm m_{pl}}}{(5-2d)\sqrt{g_*}} T^{2d-1}. \tag{5.60}$$

The ratio of the two is

$$\frac{\rho_{\rm ds,Had}}{\rho_{\rm ds,R}}(T < m_{\rm gap}) = \frac{e^2}{\Gamma_d} \left(\frac{T}{m_{\rm gap}}\right)^{5-2d}, \tag{5.61}$$

where Γ_d was previously defined in Equation 5.15. Since $2 < d < 5/2$ for IR-dominant COFI production, the above ratio is much smaller than 1. Therefore, we see that the hadronic production is insignificant when $T_{\rm NR} < m_{\rm gap}$.

Now, consider the complementary case with $T_{\rm NR} > m_{\rm gap}$. In this case, at $T > T_{\rm NR}$, the production is via the relativistic COFI process, and at $m_{\rm gap} < T < T_{\rm NR}$, it is through the process discussed in section 5.3.1. Finally, at $T < m_{\rm gap}$, further hadronic production occurs. The energy density from the hadronic production is obtained by solving Equation 5.22 with Equation 5.58 and we found

$$\rho_{\rm ds,Had}(T < m_{\rm gap}) \approx \frac{\hat{B} {\rm m_{pl}}}{4\sqrt{g_*}} T^3 m_{\rm gap}^4. \tag{5.62}$$

Contribution from the earlier production is found using Equation 5.21 and Equation 5.23:

$$\rho_{\text{ds,COFI}}(T < m_{\text{gap}}) \approx \frac{B_d \mathrm{m}_{\text{pl}}}{\sqrt{g_*}} \left(\frac{1}{(2d-4)} + \frac{1}{(5-2d)} \right) T^3 T_{\text{NR}}^{2d-4}. \tag{5.63}$$

The first term is from the non-relativistic COFI production ($m_{\text{gap}} < T < T_{\text{NR}}$) while the second term represents the relativistic COFI production ($T > T_{\text{NR}}$). The ratio is found to be

$$\frac{\rho_{\text{ds,Had}}}{\rho_{\text{ds,COFI}}} = \frac{e^2}{\Gamma_d} \frac{(2d-4)(5-2d)}{4} \left(\frac{m_{\text{gap}}}{T_{\text{NR}}} \right)^{2d-4}. \tag{5.64}$$

Since unitarity demands $d > 2$, the above ratio must be much smaller than one. Therefore, we conclude that the hadronic production makes only a small contribution to the DM energy density and hence may be ignored. This also means that while the naive kinematics suggest that the production must end at $T < m_{\text{DM}}$ (when it is not terminated already by SM fermion masses), in effect it ends around m_{gap}.

5.D Conformal Freeze-In Calculations

In this appendix, we present details of COFI computations used in the main text.

5.D.1 Fermion pair annihilation

We begin by writing down the $f\bar{f} \to$ CFT matrix element

$$\mathcal{M} = -\frac{2e\lambda}{\Lambda^{d-2}} \frac{1}{p^2} \bar{u}(p_2) \gamma^\mu u(p_1) p^\rho \langle p | \mathcal{O}_{\mu\rho} | 0 \rangle, \tag{5.65}$$

where $\mathcal{O}_{\mu\rho}$ is the antisymmetric 2-tensor operator corresponding to the CFT out state with momentum $p = p_1 + p_2$. Squaring and performing the spin sum in the massless fermion limit gives

$$\sum|\mathcal{M}|^2 = \frac{4e^2\lambda^2}{\Lambda^{2d-4}}\frac{4}{p^4}p_{1\beta}p_{2\gamma}(g^{\beta\nu}g^{\gamma\mu} - g^{\beta\gamma}g^{\mu\nu} + g^{\beta\mu}g^{\gamma\nu})p^\rho p^\alpha\langle 0|\mathcal{O}^\dagger_{\alpha\nu}|p\rangle\langle p|\mathcal{O}_{\mu\rho}|0\rangle \tag{5.66}$$

The collision term (rate of energy transfer through scattering) is given by

$$\begin{aligned} n_1n_2\langle\sigma_{1+2\to\mathrm{CFT}}v_{\mathrm{rel}}E_{\mathrm{tot}}\rangle = &\left(\int d\Pi_1 f(p_1)\right)\left(\int d\Pi_2 f(p_2)\right) \\ &\int\frac{d^4p}{(2\pi)^4}\rho(p^2)(2\pi)^4\delta^4(p_1+p_2-p)\left(\sum|\mathcal{M}|^2\right)(E_1+E_2), \end{aligned} \tag{5.67}$$

where f is the phase space distribution function of the incoming fermion and $\rho(p^2)$ is understood to be the appropriate normalization for the CFT state $|p\rangle$. Now notice that

$$\begin{aligned} \langle\mathcal{O}^\dagger_{\mu\nu}(x)\mathcal{O}_{\rho\sigma}(0)\rangle =&\int\frac{d^4p}{(2\pi)^4}\rho(p^2)\langle 0|e^{-iP\cdot x}\mathcal{O}^\dagger_{\mu\nu}(0)e^{iP\cdot x}|p\rangle\langle p|O_{\rho\sigma}(0)|0\rangle \\ =&\int\frac{d^4p}{(2\pi)^4}\rho(p^2)\langle 0|\mathcal{O}^\dagger_{\mu\nu}(0)|p\rangle\langle p|O_{\rho\sigma}(0)|0\rangle e^{ip\cdot x} \end{aligned}$$

Inverting the Fourier transform yields

$$\rho(p^2)\langle 0|\mathcal{O}^\dagger_{\mu\nu}(0)|p\rangle\langle p|O_{\rho\sigma}(0)|0\rangle = \int d^4x e^{-ip\cdot x}\langle\mathcal{O}^\dagger_{\mu\nu}(x)\mathcal{O}_{\rho\sigma}(0)\rangle \tag{5.68}$$

The (Euclidean) position-space two point functions in a CFT is fully fixed up to an overall normalization using conformal invariance and dimensional analysis. For the antisymmetric 2-tensor, it is given by [340]

$$\langle\mathcal{O}^\dagger_{\mu\nu}(x)\mathcal{O}_{\rho\sigma}(0)\rangle = C_{AT}\frac{1}{(2\pi)^2}\frac{(I_{\mu\rho}(x)I_{\nu\sigma}(x) - \frac{1}{4}g_{\mu\nu}g_{\rho\sigma}) - (\mu\leftrightarrow\nu)}{(x^2)^d}, \tag{5.69}$$

where d is the scaling dimension of the operator $\mathcal{O}_{\mu\nu}$, C_{AT} is an overall normalization, and

$$I_{\mu\nu} = g_{\mu\nu} - 2\frac{x_\mu x_\nu}{x^2}.$$

The Fourier transform is given by

$$\begin{aligned}\langle \mathcal{O}^{\dagger}_{\mu\nu}(x)\mathcal{O}_{\rho\sigma}(0)\rangle = \int \frac{d^4k}{(2\pi)^4} e^{ik\cdot x}\Bigg[& C_{AT}(-1)\frac{\Gamma(3-d)}{4^{d-1}\Gamma(d+1)}(k^2)^{d-2} \\ & \times \left(\Big(g_{\mu\rho}g_{\nu\sigma} - (\mu \leftrightarrow \nu)\Big) - 2\Big(g_{\mu\rho}\frac{k_\nu k_\sigma}{k^2} + g_{\nu\sigma}\frac{k_\mu k_\rho}{k^2} - (\mu \leftrightarrow \nu)\Big)\right)\Bigg]\end{aligned} \tag{5.70}$$

We analytically continue the above Euclidean expressions to Minkowski space in the mostly minus signature.

$$\begin{aligned}\rho(p^2)\langle 0|\mathcal{O}^{\dagger}_{\mu\nu}(0)|p\rangle\langle p|O_{\rho\sigma}(0)|0\rangle = & C_{AT}(-1)\frac{\Gamma(3-d)}{4^{d-1}\Gamma(d+1)}(-p^2)^{d-2} \\ & \times \left(\Big(g_{\mu\rho}g_{\nu\sigma} - (\mu \leftrightarrow \nu)\Big) - 2\Big(g_{\mu\rho}\frac{p_\nu p_\sigma}{p^2} + g_{\nu\sigma}\frac{p_\mu p_\rho}{p^2} - (\mu \leftrightarrow \nu)\Big)\right)\end{aligned} \tag{5.71}$$

To have an unparticle interpretation for the state generated by $\mathcal{O}_{\mu\nu}$, we need to choose the normalization such that the prefactor of p^2 corresponds to the phase space of d massless particles, i.e. choose C_{AT} such that the following relation holds:

$$(-1)^{d-2}C_{AT}\frac{\Gamma(3-d)}{4^{d-1}\Gamma(d+1)} \equiv A_d = \frac{16\pi^{5/2}}{(2\pi)^{2d}}\frac{\Gamma(d+1/2)}{\Gamma(d-1)\Gamma(2d)}. \tag{5.72}$$

We now perform the index contractions.

$$\begin{aligned}\rho(p^2)\sum|\mathcal{M}|^2 &\propto p_{1\beta}p_{2\gamma}p^{\rho}p^{\alpha}\left[\delta^{\beta}_{\rho}\delta^{\gamma}_{\alpha} + \delta^{\beta}_{\alpha}\delta^{\gamma}_{\rho} - g^{\beta\gamma}g_{\alpha\rho} - \frac{4}{p^2}(g_{\alpha\rho}p^{\beta}p^{\gamma} + g^{\beta\gamma}p_{\alpha}p_{\rho})\right] \\ &= -\Big(2(p_1\cdot p)(p_2\cdot p) + 5(p_1\cdot p_2)p^2\Big).\end{aligned}$$

Using the delta function and the fact that the particles are massless, we have the following:

$$(p_1+p_2)^2 = p^2 = 2p_1\cdot p_2, \qquad (p-p_2)^2 = p_1^2 = 0 = p^2 - 2p\cdot p_2,$$

$$(p-p_1)^2 = p_2^2 = 0 = p^2 - 2p\cdot p_1$$

Thus,

$$\rho(p^2)\sum|\mathcal{M}|^2 = A_d\frac{12e^2\lambda^2}{\Lambda^{2d-4}}(p^2)^{d-2} \tag{5.73}$$

Assuming the SM particles follow the Maxwell-Boltzmann distribution, we get

$$\begin{aligned} n_1 n_2\langle\sigma v E\rangle =& A_d\frac{48e^2\lambda^2}{\Lambda^{2d-4}}\frac{1}{(2\pi)^6}\int d^4p(p^2)^{d-2}\theta(p^2)\theta(p^0)p^0e^{-p_0/T} \\ &\times\int d^4p_1d^4p_2\delta(p_1^2)\delta(p_2^2)\theta(p_1^0)\theta(p_2^0)\delta^4(p_1+p_2-p) \end{aligned} \tag{5.74}$$

Computing the remaining integral yields

$$n_1n_2\langle\sigma v E\rangle = A_d\frac{48e^2\lambda^2}{4(2\pi)^5\Lambda^{2d-4}}\frac{1}{2}\frac{\Gamma(\frac{3}{2})\Gamma(d-1)}{\Gamma(d+\frac{1}{2})}\Gamma(2d+1)T^{2d+1} \tag{5.75}$$

5.D.2 Higgs annihilation

Next, we consider freeze-in through $H^\dagger H \to$ CFT (assuming only kinetic mixing through $U(1)_Y$ between the SM and the CFT sector). The matrix element is

$$\mathcal{M} = -\frac{2\lambda g}{\Lambda^{d-2}}\frac{1}{p^2}(p_1-p_2)_\mu p_\nu\langle p|\mathcal{O}^{\mu\nu}|0\rangle$$

Repeating the above in the massless limit yields

$$\rho(p^2)\sum|\mathcal{M}|^2 = \frac{4\lambda^2g^2}{\Lambda^{2d-4}}A_d(p^2)^{d-2} \tag{5.76}$$

After EWSB, the above process is matched onto $Zh \to$ CFT which then gets quickly shut off once the Higgs boson decouples from the thermal bath.

5.D.3 Gauge boson initial state

Due to thermal effects, the longitudinal mode of the photon picks up a thermal mass proportional to T. This allows the "decay" process of gauge bosons into unparticles. The matrix element for $A^\mu \to$ CFT is given by

$$\mathcal{M} = -\frac{2\lambda}{\Lambda^{d-2}} \epsilon^\mu p^\nu \langle p | \mathcal{O}_{\mu\nu} | 0 \rangle \tag{5.77}$$

Squaring and performing the polarization sum yields

$$\sum |\mathcal{M}|^2 = \frac{4\lambda^2}{\Lambda^{2d-4}} \left(-g^{\mu\sigma} + \cancel{\frac{p^\mu p^\sigma}{p^2}} \right) p^\nu p^\rho \langle 0 | \mathcal{O}^\dagger_{\rho\sigma} | p \rangle \langle p | \mathcal{O}_{\mu\nu} | 0 \rangle \tag{5.78}$$

where the second term vanishes by the antisymmetric property of $\mathcal{O}_{\mu\nu}$[25]. The rate of energy density transfer via this decay process is given by

$$\left(\int d\Pi_A f(p_A) \right) \int \frac{d^4 p}{(2\pi)^4} \rho(p^2) (2\pi)^4 \delta^4(p_A - p) \left(\sum |\mathcal{M}|^2 \right) (E_A) \tag{5.79}$$

As was done in the case of the fermion pair annihilation, we replace the "momentum-space wavefunctions" with the two-point function and use the correct normalization to yield the unparticle interpretation. So the right-most integral is equal to

$$\begin{aligned} \rho(p^2) \left(\sum |\mathcal{M}|^2 \right) =& \frac{4\lambda^2}{\Lambda^{2d-4}} A_d (p^2)^{d-2} g^{\mu\sigma} p^\nu p^\rho \\ & \times \left((g_{\mu\rho} g_{\sigma\nu} - (\mu \leftrightarrow \nu)) - 2 \left(g_{\mu\rho} \frac{p_\mu p_\sigma}{p^2} + g_{\nu\sigma} \frac{p_\mu p_\rho}{p^2} - (\mu \leftrightarrow \nu) \right) \right) \end{aligned} \tag{5.80}$$

Performing the index contractions yield

$$\rho(p^2) \left(\sum |\mathcal{M}|^2 \right) = \frac{4\lambda^2}{\Lambda^{2d-4}} A_d (p^2)^{d-2} (3p^2) \tag{5.81}$$

---

[25] Here, we used the polarization vectors for a massive gauge field. They are different from the dressed polarization vectors for photons in a thermal bath. This will generically result in functions of p arising in front of $g^{\mu\sigma}$ and $p^\mu p^\sigma$. This does not affect the fact that the second term cancels.

Thus, the collision term is

$$\left(\int d\Pi f(p)\right)\frac{4p^0\lambda^2}{\Lambda^{2d-4}}A_d(p^2)^{d-2}(3p^2) \tag{5.82}$$

The phase space integral includes a delta function which enforces the on-shell relation. Using that, the energy transfer rate simplifies down to

$$\frac{6\lambda^2 A_d m^{2d-2}}{\Lambda^{2d-4}}\int \frac{d^3p}{(2\pi)^3}f(p) \tag{5.83}$$

The final quantity is precisely the number density of a Boltzmann-distributed particle at temperature T. This is given by

$$\int \frac{d^3p}{(2\pi)^3}f(p) = \frac{1}{\pi^2}T^3 \tag{5.84}$$

Thus,

$$\Gamma = \frac{6\lambda^2 A_d}{\Lambda^{2d-4}}m(T)^{2d-2}\frac{1}{\pi^2}T^3 \tag{5.85}$$

5.E Details of Stellar Cooling Estimates

Here, we will discuss the estimation of the energy density loss rate in most stellar systems. A more detailed discussion of stellar evolution bound on COFI theories can be found in [322].

5.E.1 Main sequence and horizontal branch stars

In both main sequence and horizontal branch stars, the dominant mechanism for energy loss is via an analog of the Compton process [341]. An incoming photon is absorbed by an electron which subsequently radiates either DM pairs or unparticles.

In order for DM pairs to be directly produced, the temperature (or equivalently the scale of momentum transfer) must be below m_{gap}. We can integrate out the dark photon to obtain the effective operator

$$\mathcal{L} \supset i\frac{\epsilon e c_w g_s}{m_{\text{gap}}^2}(\bar{e}\gamma^\mu e)\left(\pi^+ \overset{\leftrightarrow}{\partial}_\mu \pi^-\right) \equiv i\frac{4G_{\text{eff}}}{\sqrt{2}}(\bar{e}\gamma^\mu e)\left(\pi^+ \overset{\leftrightarrow}{\partial}_\mu \pi^-\right) \tag{5.86}$$

Up to some $\mathcal{O}(1)$ factors from the difference in particle statistics, the kinematic factor of the spin-averaged amplitude is the same as that from neutrino pair emission. As such, one can take the existing computation of the energy density loss rate from neutrino emission and perform the replacement $G_F \to G_{\text{eff}}$. This gives

$$\dot{\varepsilon}_{\text{Comp, h}} \simeq \frac{7!}{\pi^2}\left(\frac{Y_e}{m_N}\right)\frac{\alpha}{8\pi^2}G_{\text{eff}}^2\frac{T^8}{m_e^2}, \tag{5.87}$$

where Y_e is the electron to nucleon ratio and m_N is the nucleon mass.

For unparticle production which occurs when $T > m_{\text{gap}}$, while the estimate is less robust, nevertheless a reasonable estimation is possible. This is done by rescaling the result of the energy loss via emission of a light scalar from the same Compton-like process [322]. The main difference between the two processes are the number of final state particles, average energy carried away by the final states and the couplings. Noting this, we can write

$$\frac{\dot{\varepsilon}_{\text{Comp, CFT}}}{\dot{\varepsilon}_{\text{scalar}}} \sim \frac{(e\lambda/\Lambda^{d-2})^2}{g^2}\frac{A_{d+1}}{A_2}T^{2d-4}, \tag{5.88}$$

where g is the Yukawa coupling of the electrons with the light scalar. The factors of T were added to ensure that the RHS is dimensionless.[26] Plugging in the known result for $\dot{\varepsilon}_{\text{scalar}}$ [341] gives

$$\dot{\varepsilon}_{\text{Comp, CFT}} \sim \alpha^2\lambda^2 A_{d+1}\frac{T^{2d}}{\Lambda^{2d-4}}\frac{Y_e}{m_u m_e^2}. \tag{5.89}$$

Here, we are missing potentially important numerical factors which may affect the bounds,

---

[26] Here, T is the right dimensionful parameter to balance the dimensions since the characteristic energy transfer is controlled by T. This is not always true. For example, in the case of electron-positron annihilation at the core of supernova, one has to use the fermi energy E_F instead. For more details, see [322].

but this is beyond the scope of this chapter.

5.E.2 SN 1987A

In supernova progenitor cores, the dominant energy loss mechanism is nuclear bremsstrahlung [342]. Since the nucleons are nearly degenerate in the core, the typical energy scale is $p_F \approx \sqrt{m_N T}$. Using a similar process as before, we can estimate the rate of energy loss by producing CFT states by rescaling the rate via emission of a light scalar

$$\frac{\dot{\varepsilon}_{\text{brem, CFT}}}{\dot{\varepsilon}_{\text{scalar}}} \sim \frac{(e\lambda/\Lambda^{d-2})^2}{g^2} \frac{A_{d+2}}{A_3} p_F^{2d-4}, \tag{5.90}$$

where g is now the Yukawa coupling of a nucleon pair to the light scalar. Plugging in the known result for $\dot{\varepsilon}_{\text{scalar}}$ [341], we get

$$\dot{\varepsilon}_{\text{brem, CFT}} \sim \frac{(e\lambda/\Lambda^{d-2})^2}{4\pi} \alpha_\pi^2 \frac{44}{15^3} \frac{A_{d+2}}{A_3} \left(\frac{T}{m_N}\right)^4 p_F^5 G_{\text{scalar}}(m_\pi/p_F), \tag{5.91}$$

where $\alpha_\pi \approx 15$ is the coupling of nucleons to pions and G_{scalar} is the correction to the bremsstrahlung rate for nonzero pion mass. For the density of the progenitor star core, $G_{\text{scalar}}(m_\pi/p_F) \approx 0.8$.

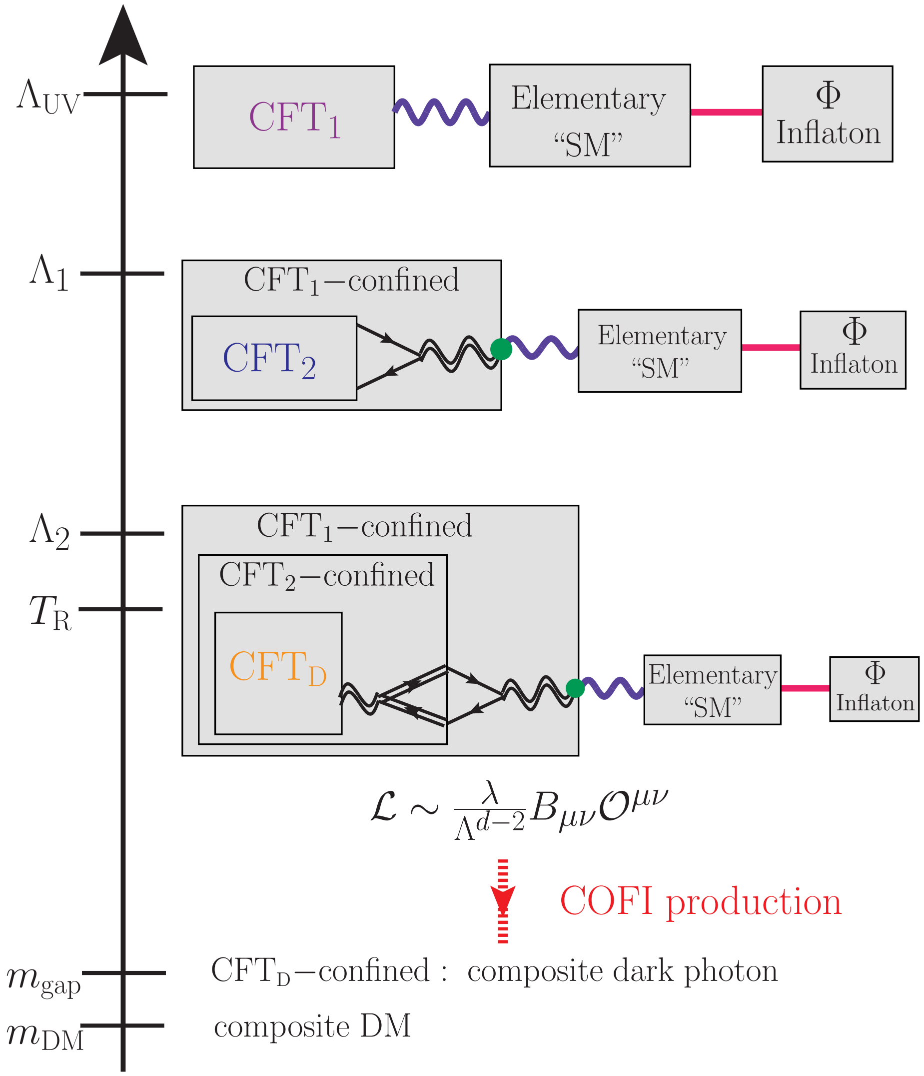

Figure 5.1: Our theoretical setup and its RG evolution. Cascade of confinement results in small effective coupling between the SM and dark CFT and asymmetric reheating.

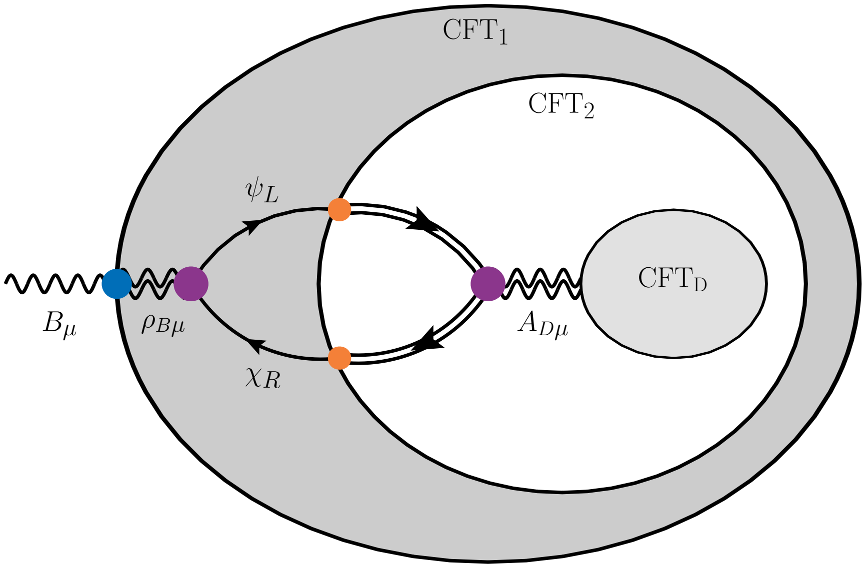

Figure 5.2: A diagram responsible for the effective mixing between B_μ and $A_{\mathrm{D}\mu}$. B_μ is an elementary gauge boson external to CFT$_1$ and $\rho_{B\mu}$ is a composite vector meson of confined phase of CFT$_1$. This latter phase also includes a pair of composite fermions denoted as ψ_L and χ_R which couples to a composite CFT$_2$ as described in Equation 5.2. These couplings lead to partial-compositeness coupling once CFT$_2$ confines. This is shown as orange blobs. The confined CFT$_2$ also contains a composite vector meson $A_{\mathrm{D}\mu}$ which itself is external to CFT$_\mathrm{D}$.

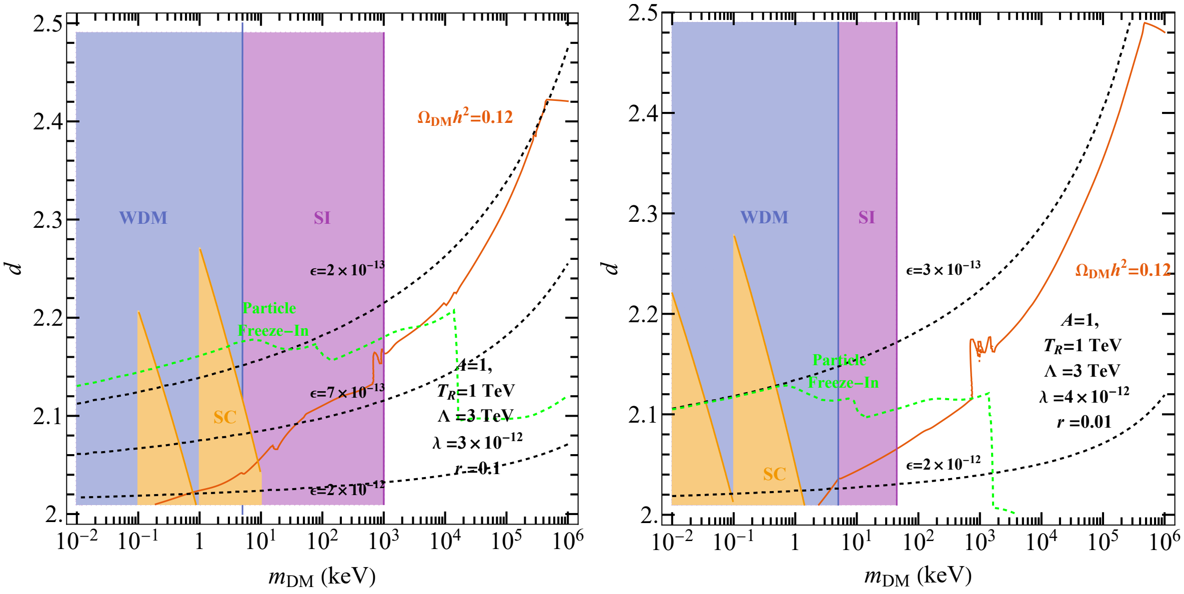

Figure 5.3: The dark matter mass and the CFT operator scaling dimension which reproduces the dark matter relic density (orange-red solid line) with $r = 0.1$ (left) and $r = 0.01$ (right). For comparison, the green dashed line shows an estimate for the expected parameters which reproduces the observed relic density for the “usual” freeze-in with kinetic mixing parameter given by Equation 5.12 and the same relation between the dark photon mass and dark matter mass [10]. The blue shaded region corresponds to the region of parameter space excluded by the warm dark matter bound. The yellow shaded region corresponds to the stellar cooling bound. The purple shaded region is excluded by the DM self-interaction bound coming from the observation of bullet-cluster. The dashed curves show contours of constant kinetic-mixing parameter, ϵ, with $g_s = 1$.

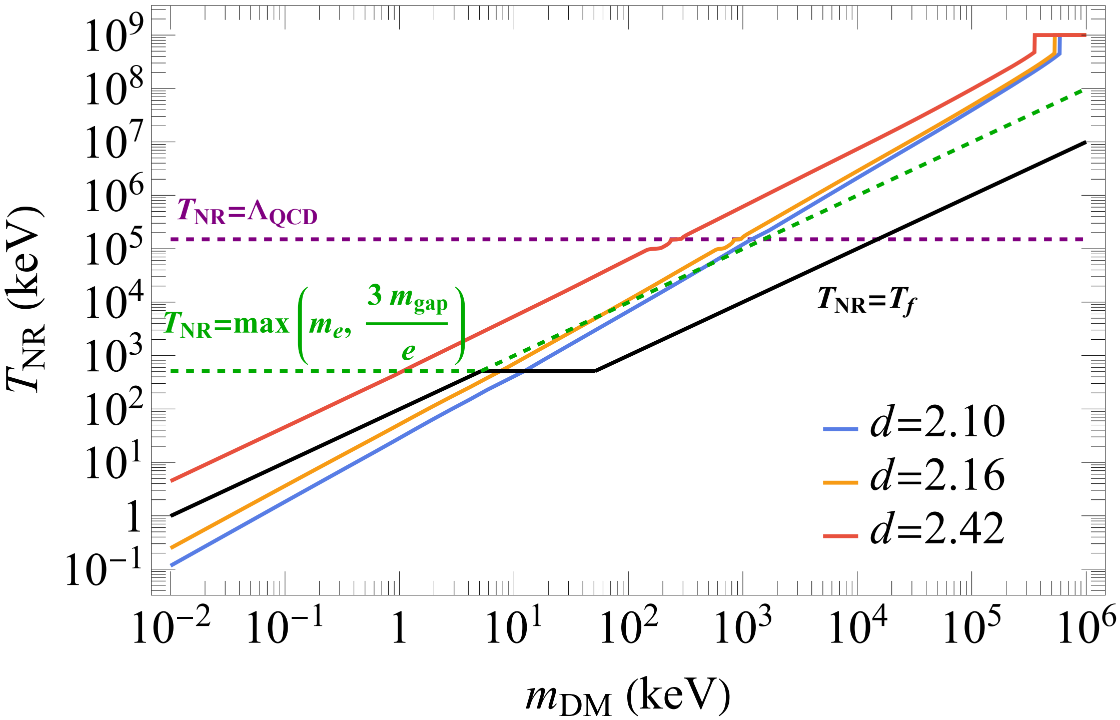

Figure 5.4: T_{NR} as a function of m_{DM} with a couple of choices of d for the parameters chosen in the left panel of Figure 5.3 (i.e. $r = 0.1$). The green-dashed curve shows the temperature when one of the two SM initial states decouple from the thermal bath. The black solid line shows the temperature when either all of the SM initial states decouple or when we switch to "hadronic" production. For data points below the black solid line, the transition into the non-relativistic phase occurs after the end of production.

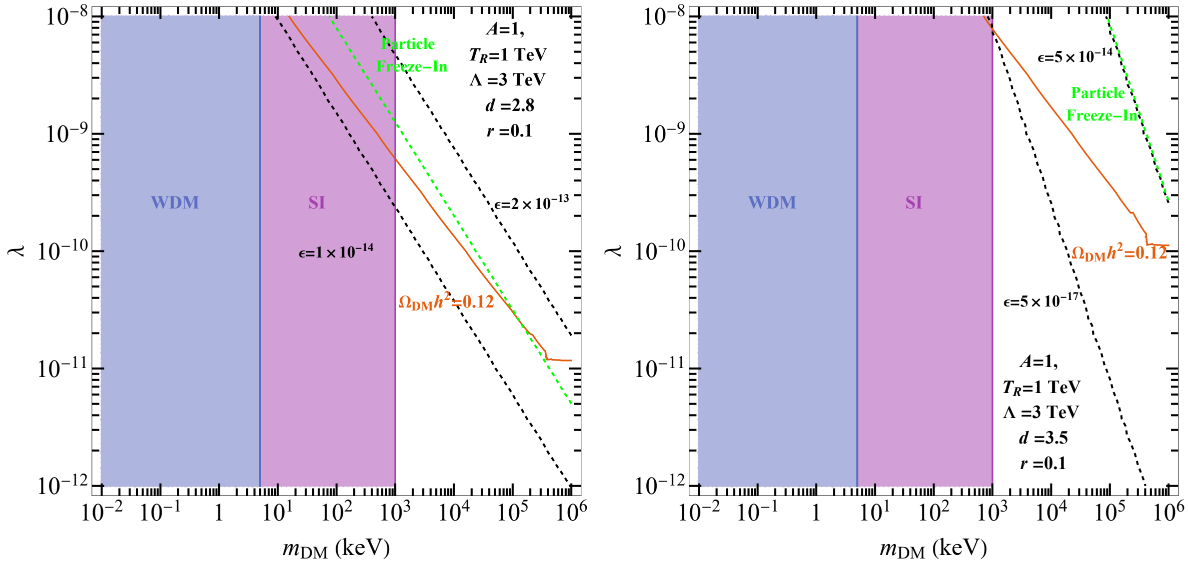

Figure 5.5: The dark matter mass (x-axis) and the SM-CFT mixing parameter, λ, (y-axis) which reproduces the observed dark matter relic density (orange-red solid line). The two plots have different scaling dimensions for our CFT operator; $d = 2.8$ (left) and $d = 3.5$ (right). For comparison, the green dashed line shows an estimate for the expected parameters which reproduces the observed relic density for the "usual" freeze-in with kinetic mixing parameter given by Equation 5.12 and the same relation between the dark photon mass and dark matter mass [10]. The blue shaded region corresponds to the region of parameter space excluded by the warm dark matter bound. The purple shaded region is excluded by DM self-interaction bound coming from the observation of the bullet-cluster. The dashed curves show contours of constant kinetic-mixing parameter, ϵ, with g_S=1.

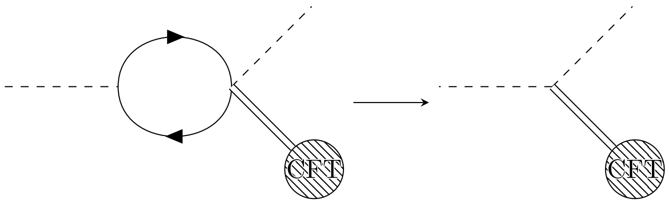

Figure 5.6: Example of the operator mixing effect

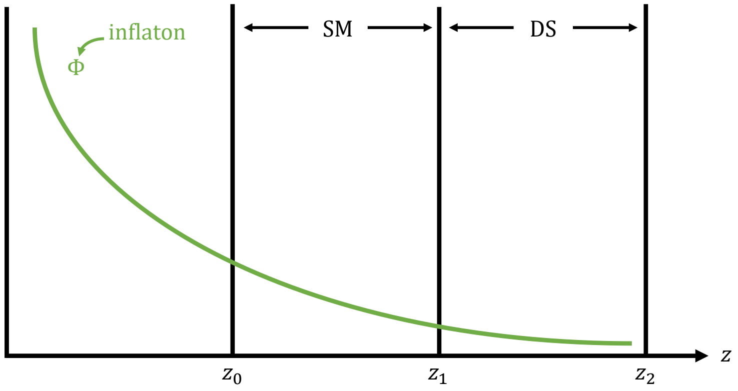

Figure 5.7: AdS$_5$ picture corresponding to the 4d COFI theory setup in section 5.2.

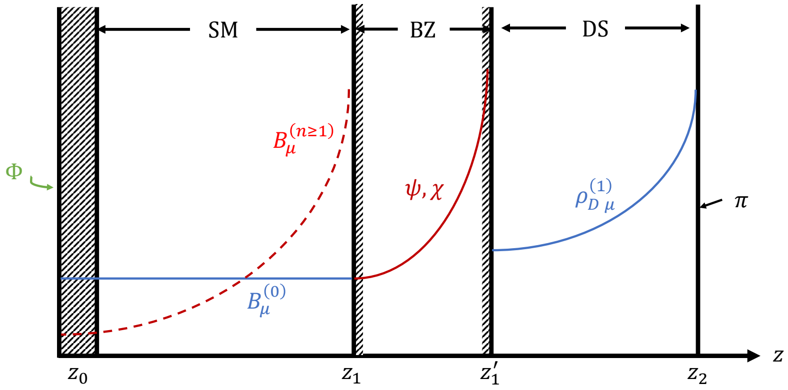

Figure 5.8: AdS$_5$ picture leading to a small portal coupling λ appearing in 4d CFT picture. An extra bulk (called BZ-bulk) is introduced between the SM and DS bulk. The interactions between the BZ-bulk fields with SM and DS states generate desired suppression in the effective coupling between the SM and DS. The inflaton sector is simplified to a thin-brane picture. π represents the DM state(s).

REFERENCES

[1] S. Kanemura, M. Kikuchi, K. Yagyu and H. Yokoya, *Bounds on the mass of doubly-charged Higgs bosons in the same-sign diboson decay scenario*, *Phys. Rev. D* **90** (2014) 115018 [`1407.6547`].

[2] ALEPH, DELPHI, L3, OPAL, SLD, LEP Electroweak Working Group, SLD Electroweak Group, SLD Heavy Flavour Group collaboration, *Precision electroweak measurements on the Z resonance*, *Phys. Rept.* **427** (2006) 257 [`hep-ex/0509008`].

[3] Particle Data Group collaboration, *Review of Particle Physics*, *PTEP* **2020** (2020) 083C01.

[4] J. Aalbers et al., *First Dark Matter Search Results from the LUX-ZEPLIN (LZ) Experiment*, .

[5] F. Ruppin, J. Billard, E. Figueroa-Feliciano and L. Strigari, *Complementarity of dark matter detectors in light of the neutrino background*, *Phys. Rev. D* **90** (2014) 083510 [`1408.3581`].

[6] M. Kawasaki, K. Kohri, T. Moroi and Y. Takaesu, *Revisiting Big-Bang Nucleosynthesis Constraints on Long-Lived Decaying Particles*, *Phys. Rev. D* **97** (2018) 023502 [`1709.01211`].

[7] S.K. Acharya and R. Khatri, *CMB anisotropy and BBN constraints on pre-recombination decay of dark matter to visible particles*, *JCAP* **12** (2019) 046 [`1910.06272`].

[8] S.K. Acharya and R. Khatri, *New CMB spectral distortion constraints on decaying dark matter with full evolution of electromagnetic cascades before recombination*, *Phys. Rev. D* **99** (2019) 123510 [`1903.04503`].

[9] C. Blanco and D. Hooper, *Constraints on Decaying Dark Matter from the Isotropic Gamma-Ray Background*, *JCAP* **03** (2019) 019 [`1811.05988`].

[10] M. Blennow, E. Fernandez-Martinez and B. Zaldivar, *Freeze-in through portals*, *JCAP* **01** (2014) 003 [`1309.7348`].

[11] M. Steinhauser, *Leptonic contribution to the effective electromagnetic coupling constant up to three loops*, *Phys. Lett. B* **429** (1998) 158 [`hep-ph/9803313`].

[12] D.J. Gross and F. Wilczek, *Ultraviolet behavior of non-abelian gauge theories*, *Phys. Rev. Lett.* **30** (1973) 1343.

[13] KOTO collaboration, *Search for the* $K_L \to \pi^0 \nu \overline{\nu}$ *and* $K_L \to \pi^0 X^0$ *decays at the J-PARC KOTO experiment*, *Phys. Rev. Lett.* **122** (2019) 021802 [`1810.09655`].

[14] CDF collaboration, *High-precision measurement of the W boson mass with the CDF II detector*, *Science* **376** (2022) 170.

[15] Muon $g-2$ Collaboration collaboration, *Measurement of the positive muon anomalous magnetic moment to 0.46 ppm*, *Phys. Rev. Lett.* **126** (2021) 141801.

[16] SNO collaboration, *Measurement of the rate of $\nu_e + d \to p + p + e^-$ interactions produced by ^8B solar neutrinos at the Sudbury Neutrino Observatory*, *Phys. Rev. Lett.* **87** (2001) 071301 [`nucl-ex/0106015`].

[17] A.D. Sakharov, *Violation of cp invariance, c asymmetry, and baryon asymmetry of the universe*, *Soviet Physics Uspekhi* **34** (1991) 392.

[18] V.C. Rubin and J. Ford, W. Kent, *Rotation of the Andromeda Nebula from a Spectroscopic Survey of Emission Regions*, *apj* **159** (1970) 379.

[19] M. Markevitch, A.H. Gonzalez, D. Clowe, A. Vikhlinin, L. David, W. Forman et al., *Direct constraints on the dark matter self-interaction cross-section from the merging galaxy cluster 1E0657-56*, *Astrophys. J.* **606** (2004) 819 [`astro-ph/0309303`].

[20] Planck collaboration, *Planck 2018 results. VI. Cosmological parameters*, *Astron. Astrophys.* **641** (2020) A6 [`1807.06209`].

[21] Weber, M. and de Boer, W., *Determination of the local dark matter density in our galaxy*, *A&A* **509** (2010) A25.

[22] K.V. Berghaus, A. Esposito, R. Essig and M. Sholapurkar, *The Migdal effect in semiconductors for dark matter with masses below $\sim$ 100 MeV*, *JHEP* **01** (2023) 023 [`2210.06490`].

[23] D. Adams, D. Baxter, H. Day, R. Essig and Y. Kahn, *Measuring the Migdal effect in semiconductors for dark matter detection*, *Phys. Rev. D* **107** (2023) L041303 [`2210.04917`].

[24] C. Dessert, J.W. Foster, Y. Park, B.R. Safdi and W.L. Xu, *Higgsino Dark Matter Confronts 14 years of Fermi Gamma Ray Data*, `2207.10090`.

[25] C. Csaki, A. Ismail and S.J. Lee, *The continuum dark matter zoo*, *JHEP* **02** (2023) 053 [`2210.16326`].

[26] K. Fraser, A. Parikh and W.L. Xu, *A Closer Look at CP-Violating Higgs Portal Dark Matter as a Candidate for the GCE*, *JHEP* **03** (2021) 123 [`2010.15129`].

[27] S. Tremaine and J.E. Gunn, *Dynamical role of light neutral leptons in cosmology*, *prl* **42** (1979) 407.

[28] J. Preskill, M.B. Wise and F. Wilczek, *Cosmology of the invisible axion*, *Physics Letters B* **120** (1983) 127.

[29] A. Banerjee, D. Budker, M. Filzinger, N. Huntemann, G. Paz, G. Perez et al., *Oscillating nuclear charge radii as sensors for ultralight dark matter*, `2301.10784`.

[30] J. Huang, A. Madden, D. Racco and M. Reig, *Maximal axion misalignment from a minimal model*, *JHEP* **10** (2020) 143 [`2006.07379`].

[31] A. Banerjee, G. Perez, M. Safronova, I. Savoray and A. Shalit, *The Phenomenology of Quadratically Coupled Ultra Light Dark Matter*, `2211.05174`.

[32] H.-Y. Zhang and S. Ling, *Phenomenology of wavelike vector dark matter nonminimally coupled to gravity*, `2305.03841`.

[33] K. Harigaya and I.R. Wang, *Axiogenesis from $SU(2)_R$ phase transition*, *JHEP* **10** (2021) 022 [`2107.09679`].

[34] A. Berlin and K. Zhou, *Discovering QCD-Coupled Axion Dark Matter with Polarization Haloscopes*, `2209.12901`.

[35] L. Lancaster, C. Giovanetti, P. Mocz, Y. Kahn, M. Lisanti and D.N. Spergel, *Dynamical Friction in a Fuzzy Dark Matter Universe*, *JCAP* **01** (2020) 001 [`1909.06381`].

[36] K. Kaneta, S.M. Lee and K.-y. Oda, *Boltzmann or Bogoliubov? Approaches compared in gravitational particle production*, *JCAP* **09** (2022) 018 [`2206.10929`].

[37] D. Brzeminski, Z. Chacko, A. Dev and A. Hook, *Time-varying fine structure constant from naturally ultralight dark matter*, *Phys. Rev. D* **104** (2021) 075019 [`2012.02787`].

[38] Z. Bogorad and N. Toro, *Ultralight millicharged dark matter via misalignment*, *JHEP* **07** (2022) 035 [`2112.11476`].

[39] B. Carr and F. Kuhnel, *Primordial black holes as dark matter candidates*, *SciPost Phys. Lect. Notes* **48** (2022) 1 [`2110.02821`].

[40] W. Qin, S.R. Geller, S. Balaji, E. McDonough and D.I. Kaiser, *Planck Constraints and Gravitational Wave Forecasts for Primordial Black Hole Dark Matter Seeded by Multifield Inflation*, `2303.02168`.

[41] C. Csáki, A. Gomes, Y. Hochberg, E. Kuflik, K. Langhoff and H. Murayama, *Super-resonant dark matter*, *JHEP* **11** (2022) 162 [`2208.07882`].

[42] M.A.G. Garcia, K. Kaneta, Y. Mambrini, K.A. Olive and S. Verner, *Freeze-in from preheating*, *JCAP* **03** (2022) 016 [`2109.13280`].

[43] E. Hall, R. McGehee, H. Murayama and B. Suter, *Asymmetric dark matter may not be light*, *Phys. Rev. D* **106** (2022) 075008 [`2107.03398`].

[44] Y. Sun, K. Schutz, A. Nambrath, C. Leung and K. Masui, *Axion dark matter-induced echo of supernova remnants*, *Phys. Rev. D* **105** (2022) 063007 [`2110.13920`].

[45] S. Bansal, J. Barron, D. Curtin and Y. Tsai, *Precision Cosmological Constraints on Atomic Dark Matter*, `2212.02487`.

[46] R. Ebadi et al., *Ultraheavy dark matter search with electron microscopy of geological quartz*, *Phys. Rev. D* **104** (2021) 015041 [`2105.03998`].

[47] C.P. Salemi et al., *Search for Low-Mass Axion Dark Matter with ABRACADABRA-10 cm*, *Phys. Rev. Lett.* **127** (2021) 081801 [`2102.06722`].

[48] D. Aloni, M. Joseph, M. Schmaltz and N. Weiner, *Dark Radiation from Neutrino Mixing after Big Bang Nucleosynthesis*, `2301.10792`.

[49] A.-K. Burns, M. Fieg, C.M. Karwin and A. Rajaraman, *Dark matter explanations of the gamma-ray excesses from the Galactic Center and M31*, *Phys. Rev. D* **103** (2021) 063023 [`2010.11650`].

[50] A.V. Manohar, *Effective field theories*, in *10th Lake Louise Winter Institute: Quarks and Colliders*, pp. 274–315, 6, 1995 [`hep-ph/9508245`].

[51] C. Cordova and S. Koren, *Higher Flavor Symmetries in the Standard Model*, `2212.13193`.

[52] ATLAS collaboration, *Observation of a new particle in the search for the Standard Model Higgs boson with the ATLAS detector at the LHC*, *Phys. Lett.* **B716** (2012) 1 [`1207.7214`].

[53] CMS collaboration, *Observation of a new boson at a mass of 125 GeV with the CMS experiment at the LHC*, *Phys. Lett.* **B716** (2012) 30 [`1207.7235`].

[54] B. Grzadkowski, M. Iskrzynski, M. Misiak and J. Rosiek, *Dimension-Six Terms in the Standard Model Lagrangian*, *JHEP* **10** (2010) 085 [`1008.4884`].

[55] G. Durieux, C. Grojean, J. Gu and K. Wang, *The leptonic future of the Higgs*, *JHEP* **09** (2017) 014 [`1704.02333`].

[56] J. Gu, H. Li, Z. Liu, S. Su and W. Su, *Learning from Higgs Physics at Future Higgs Factories*, *JHEP* **12** (2017) 153 [`1709.06103`].

[57] T. Barklow, K. Fujii, S. Jung, R. Karl, J. List, T. Ogawa et al., *Improved Formalism for Precision Higgs Coupling Fits*, *Phys. Rev.* **D97** (2018) 053003 [`1708.08912`].

[58] K. Fujii et al., *Physics Case for the 250 GeV Stage of the International Linear Collider*, `1710.07621`.

[59] S. Di Vita, G. Durieux, C. Grojean, J. Gu, Z. Liu, G. Panico et al., *A global view on the Higgs self-coupling at lepton colliders*, *JHEP* **02** (2018) 178 [`1711.03978`].

[60] W.H. Chiu, S.C. Leung, T. Liu, K.-F. Lyu and L.-T. Wang, *Probing 6D operators at future e^-e^+ colliders*, *JHEP* **05** (2018) 081 [`1711.04046`].

[61] CEPC Study Group collaboration, *CEPC Conceptual Design Report: Volume 2 - Physics & Detector*, `1811.10545`.

[62] J. de Blas et al., *The CLIC Potential for New Physics*, `1812.02093`.

[63] F. An et al., *Precision Higgs physics at the CEPC*, *Chin. Phys.* **C43** (2019) 043002 [`1810.09037`].

[64] FCC collaboration, *FCC-ee: The Lepton Collider*, *Eur. Phys. J. ST* **228** (2019) 261.

[65] J. De Blas, G. Durieux, C. Grojean, J. Gu and A. Paul, *On the future of Higgs, electroweak and diboson measurements at lepton colliders*, `1907.04311`.

[66] W. Altmannshofer, S. Gori and G.D. Kribs, *A Minimal Flavor Violating 2HDM at the LHC*, *Phys. Rev.* **D86** (2012) 115009 [`1210.2465`].

[67] M. Low, A. Tesi and L.-T. Wang, *Composite spin-1 resonances at the LHC*, *Phys. Rev.* **D92** (2015) 085019 [`1507.07557`].

[68] W. Altmannshofer, S. Gori, A.L. Kagan, L. Silvestrini and J. Zupan, *Uncovering Mass Generation Through Higgs Flavor Violation*, *Phys. Rev.* **D93** (2016) 031301 [`1507.07927`].

[69] J.A. Evans, D. Shih and A. Thalapillil, *Chiral Flavor Violation from Extended Gauge Mediation*, *JHEP* **07** (2015) 040 [`1504.00930`].

[70] M. Bauer, M. Carena and K. Gemmler, *Flavor from the Electroweak Scale*, *JHEP* **11** (2015) 016 [`1506.01719`].

[71] M. Bauer, M. Carena and K. Gemmler, *Creating the fermion mass hierarchies with multiple Higgs bosons*, *Phys. Rev.* **D94** (2016) 115030 [`1512.03458`].

[72] W. Altmannshofer, J. Eby, S. Gori, M. Lotito, M. Martone and D. Tuckler, *Collider Signatures of Flavorful Higgs Bosons*, *Phys. Rev.* **D94** (2016) 115032 [`1610.02398`].

[73] M. Bauer, M. Carena and A. Carmona, *Higgs Pair Production as a Signal of Enhanced Yukawa Couplings*, *Phys. Rev. Lett.* **121** (2018) 021801 [`1801.00363`].

[74] W. Altmannshofer, S. Gori, D.J. Robinson and D. Tuckler, *The Flavor-locked Flavorful Two Higgs Doublet Model*, *JHEP* **03** (2018) 129 [`1712.01847`].

[75] S. Gori, H.E. Haber and E. Santos, *High scale flavor alignment in two-Higgs doublet models and its phenomenology*, *JHEP* **06** (2017) 110 [`1703.05873`].

[76] M. Farina, G. Panico, D. Pappadopulo, J.T. Ruderman, R. Torre and A. Wulzer, *Energy helps accuracy: electroweak precision tests at hadron colliders*, *Phys. Lett.* **B772** (2017) 210 [`1609.08157`].

[77] A. Azatov, R. Contino, C.S. Machado and F. Riva, *Helicity selection rules and noninterference for BSM amplitudes*, *Phys. Rev.* **D95** (2017) 065014 [`1607.05236`].

[78] S. Alioli, M. Farina, D. Pappadopulo and J.T. Ruderman, *Precision Probes of QCD at High Energies*, *JHEP* **07** (2017) 097 [`1706.03068`].

[79] G. Panico, F. Riva and A. Wulzer, *Diboson Interference Resurrection*, *Phys. Lett.* **B776** (2018) 473 [`1708.07823`].

[80] R. Franceschini, G. Panico, A. Pomarol, F. Riva and A. Wulzer, *Electroweak Precision Tests in High-Energy Diboson Processes*, *JHEP* **02** (2018) 111 [`1712.01310`].

[81] WORKING GROUP 3 collaboration, *Beyond the Standard Model Physics at the HL-LHC and HE-LHC*, `1812.07831`.

[82] HL/HE WG2 GROUP collaboration, *Higgs Physics at the HL-LHC and HE-LHC*, `1902.00134`.

[83] FCC collaboration, *HE-LHC: The High-Energy Large Hadron Collider*, *Eur. Phys. J. ST* **228** (2019) 1109.

[84] M. Mangano, *Physics potential of a low-energy FCC-hh*, Tech. Rep. CERN-FCC-PHYS-2019-0001, CERN, Geneva (Jul, 2019).

[85] F. Zimmermann, "Fcc-ee design overview." conference, June, 2019.

[86] M. Ahmad et al., *CEPC-SPPC Preliminary Conceptual Design Report. 1. Physics and Detector*, .

[87] FCC collaboration, *FCC-hh: The Hadron Collider*, *Eur. Phys. J. ST* **228** (2019) 755.

[88] D. Liu and L.-T. Wang, *Prospects for precision measurement of diboson processes in the semileptonic decay channel in future LHC runs*, *Phys. Rev.* **D99** (2019) 055001 [`1804.08688`].

[89] C. Grojean, M. Montull and M. Riembau, *Diboson at the LHC vs LEP*, *JHEP* **03** (2019) 020 [`1810.05149`].

[90] S. Banerjee, C. Englert, R.S. Gupta and M. Spannowsky, *Probing Electroweak Precision Physics via boosted Higgs-strahlung at the LHC*, *Phys. Rev.* **D98** (2018) 095012 [`1807.01796`].

[91] J. Alwall, R. Frederix, S. Frixione, V. Hirschi, F. Maltoni, O. Mattelaer et al., *The automated computation of tree-level and next-to-leading order differential cross sections, and their matching to parton shower simulations*, *JHEP* **07** (2014) 079 [`1405.0301`].

[92] C. Degrande, C. Duhr, B. Fuks, D. Grellscheid, O. Mattelaer and T. Reiter, *UFO - The Universal FeynRules Output*, *Comput. Phys. Commun.* **183** (2012) 1201 [`1108.2040`].

[93] A. Alloul, N.D. Christensen, C. Degrande, C. Duhr and B. Fuks, *FeynRules 2.0 - A complete toolbox for tree-level phenomenology*, *Comput. Phys. Commun.* **185** (2014) 2250 [`1310.1921`].

[94] ATLAS collaboration, *Search for heavy resonances decaying into a W or Z boson and a Higgs boson in final states with leptons and b-jets in 36 fb^{-1} of $\sqrt{s} = 13$ TeV pp collisions with the ATLAS detector*, *JHEP* **03** (2018) 174 [`1712.06518`].

[95] G. Cowan, K. Cranmer, E. Gross and O. Vitells, *Asymptotic formulae for likelihood-based tests of new physics*, *Eur. Phys. J.* **C71** (2011) 1554 [`1007.1727`].

[96] D.B. Clark, E. Godat and F.I. Olness, *ManeParse : A Mathematica reader for Parton Distribution Functions*, *Comput. Phys. Commun.* **216** (2017) 126 [`1605.08012`].

[97] R.D. Ball et al., *Parton distributions with LHC data*, *Nucl. Phys.* **B867** (2013) 244 [`1207.1303`].

[98] A. Efrati, A. Falkowski and Y. Soreq, *Electroweak constraints on flavorful effective theories*, *JHEP* **07** (2015) 018 [`1503.07872`].

[99] O. Gedalia, Y. Grossman, Y. Nir and G. Perez, *Lessons from Recent Measurements of D0 - anti-D0 Mixing*, *Phys. Rev.* **D80** (2009) 055024 [`0906.1879`].

[100] Particle Data Group collaboration, *Review of Particle Physics*, *Phys. Rev.* **D98** (2018) 030001.

[101] Z. Liu, L.-T. Wang and H. Zhang, *Exotic decays of the 125 GeV Higgs boson at future e^+e^- lepton colliders*, *Chin. Phys.* **C41** (2017) 063102 [`1612.09284`].

[102] CMS collaboration, *Search for long-lived charged particles in proton-proton collisions at $\sqrt{s} = 13$ TeV*, *Phys. Rev. D* **94** (2016) 112004 [`1609.08382`].

[103] ATLAS collaboration, *Search for heavy charged long-lived particles in the ATLAS detector in 36.1 fb^{-1} of proton-proton collision data at $\sqrt{s} = 13$ TeV*, *Phys. Rev. D* **99** (2019) 092007 [`1902.01636`].

[104] CMS collaboration, *Search for decays of stopped exotic long-lived particles produced in proton-proton collisions at $\sqrt{s} = 13$ TeV*, *JHEP* **05** (2018) 127 [`1801.00359`].

[105] ATLAS collaboration, *A search for the decays of stopped long-lived particles at $\sqrt{s} = 13$ TeV with the ATLAS detector*, `2104.03050`.

[106] ATLAS collaboration, *Search for nonpointing and delayed photons in the diphoton and missing transverse momentum final state in 8 TeV pp collisions at the LHC using the ATLAS detector*, *Phys. Rev. D* **90** (2014) 112005 [`1409.5542`].

[107] CMS collaboration, *Search for long-lived particles using delayed photons in proton-proton collisions at $\sqrt{s} = 13$ TeV*, *Phys. Rev. D* **100** (2019) 112003 [`1909.06166`].

[108] J. Liu, Z. Liu and L.-T. Wang, *Enhancing Long-Lived Particles Searches at the LHC with Precision Timing Information*, *Phys. Rev. Lett.* **122** (2019) 131801 [`1805.05957`].

[109] M.D. Klimek, *The Time Substructure of Jets and Boosted Object Tagging*, `1911.11235`.

[110] Z. Flowers, Q. Meier, C. Rogan, D.W. Kang and S.C. Park, *Timing information at HL-LHC: Complete determination of masses of Dark Matter and Long lived particle*, *JHEP* **03** (2020) 132 [`1903.05825`].

[111] Z. Flowers, Q. Meier, C. Rogan, D.W. Kang and S.C. Park, *Timing information at HL-LHC: Complete determination of masses of Dark Matter and Long lived particle*, *JHEP* **03** (2020) 132 [`1903.05825`].

[112] S. Banerjee, B. Bhattacherjee, A. Goudelis, B. Herrmann, D. Sengupta and R. Sengupta, *Determining the lifetime of long-lived particles at the HL-LHC*, *Eur. Phys. J. C* **81** (2021) 172 [`1912.06669`].

[113] K.J. Bae, M. Park and M. Zhang, *Demystifying freeze-in dark matter at the LHC*, *Phys. Rev. D* **101** (2020) 115036 [`2001.02142`].

[114] S. El Hedri and M. de Vries, *Cornering Colored Coannihilation*, *JHEP* **10** (2018) 102 [`1806.03325`].

[115] O. Cerri, S. Xie, C. Pena and M. Spiropulu, *Identification of Long-lived Charged Particles using Time-Of-Flight Systems at the Upgraded LHC detectors*, *JHEP* **04** (2019) 037 [`1807.05453`].

[116] A. Abada, N. Bernal, M. Losada and X. Marcano, *Inclusive Displaced Vertex Searches for Heavy Neutral Leptons at the LHC*, *JHEP* **01** (2019) 093 [`1807.10024`].

[117] C. Frugiuele, E. Fuchs, G. Perez and M. Schlaffer, *Relaxion and light (pseudo)scalars at the HL-LHC and lepton colliders*, *JHEP* **10** (2018) 151 [`1807.10842`].

[118] G.D. Kribs, A. Martin, B. Ostdiek and T. Tong, *Dark Mesons at the LHC*, *JHEP* **07** (2019) 133 [`1809.10184`].

[119] A. Berlin and F. Kling, *Inelastic Dark Matter at the LHC Lifetime Frontier: ATLAS, CMS, LHCb, CODEX-b, FASER, and MATHUSLA*, *Phys. Rev. D* **99** (2019) 015021 [`1810.01879`].

[120] L.-X. Xu, J.-H. Yu and S.-H. Zhu, *Minimal neutral naturalness model*, *Phys. Rev. D* **101** (2020) 095014 [`1810.01882`].

[121] G. Bélanger et al., *LHC-friendly minimal freeze-in models*, *JHEP* **02** (2019) 186 [`1811.05478`].

[122] J.A. Evans and M.A. Luty, *Stopping Quirks at the LHC*, *JHEP* **06** (2019) 090 [`1811.08903`].

[123] C. Kilic, S. Najjari and C.B. Verhaaren, *Discovering the Twin Higgs Boson with Displaced Decays*, *Phys. Rev. D* **99** (2019) 075029 [`1812.08173`].

[124] A. Delgado, A. Martin and M. Quirós, *Higgsino Dark Matter in an economical Scherk-Schwarz setup*, *Phys. Rev. D* **99** (2019) 075015 [`1812.08019`].

[125] J. Liu, Z. Liu, L.-T. Wang and X.-P. Wang, *Seeking for sterile neutrinos with displaced leptons at the LHC*, *JHEP* **07** (2019) 159 [`1904.01020`].

[126] S. Chakraborti, V. Martin and P. Poulose, *Freeze-in and freeze-out of dark matter with charged long-lived partners*, *JCAP* **03** (2020) 057 [`1904.09945`].

[127] J. Serra, S. Stelzl, R. Torre and A. Weiler, *Hypercharged Naturalness*, *JHEP* **10** (2019) 060 [`1905.02203`].

[128] J.D. Mason, *Time-Delayed Electrons from Higgs Decays to Right-Handed Neutrinos*, *JHEP* **07** (2019) 089 [`1905.07772`].

[129] M. Du, Z. Liu and V.Q. Tran, *Enhanced Long-Lived Dark Photon Signals at the LHC*, *JHEP* **05** (2020) 055 [`1912.00422`].

[130] CMS collaboration, *The Phase-2 Upgrade of the CMS Level-1 Trigger*, .

[131] B. Shuve and D. Tucker-Smith, *Baryogenesis and Dark Matter from Freeze-In*, *Phys. Rev. D* **101** (2020) 115023 [`2004.00636`].

[132] C. Yuan, H. Zhang, Y. Zhao and G. Chen, *Producing and detecting long-lived particles at different experiments at the LHC*, `2004.08820`.

[133] J. Liu, Z. Liu, L.-T. Wang and X.-P. Wang, *Enhancing Sensitivities to Long-lived Particles with High Granularity Calorimeters at the LHC*, *JHEP* **11** (2020) 066 [`2005.10836`].

[134] E. Fuchs, O. Matsedonskyi, I. Savoray and M. Schlaffer, *Collider searches for scalar singlets across lifetimes*, *JHEP* **04** (2021) 019 [`2008.12773`].

[135] Y. Gershtein, S. Knapen and D. Redigolo, *Probing naturally light singlets with a displaced vertex trigger*, `2012.07864`.

[136] M. Borsato et al., *Unleashing the full power of LHCb to probe Stealth New Physics*, `2105.12668`.

[137] K. Cheung, K. Wang and Z.S. Wang, *Time-delayed electrons from neutral currents at the LHC*, `2107.03203`.

[138] K.R. Dienes, D. Kim, T. Leininger and B. Thomas, *Tumblers: A Novel Collider Signature for Long-Lived Particles*, `2108.02204`.

[139] B. Bhattacherjee, S. Mukherjee, R. Sengupta and P. Solanki, *Triggering long-lived particles in HL-LHC and the challenges in the rst stage of the trigger system*, *JHEP* **08** (2020) 141 [`2003.03943`].

[140] C. Allaire et al., *Beam test measurements of Low Gain Avalanche Detector single pads and arrays for the ATLAS High Granularity Timing Detector*, `1804.00622`.

[141] *TECHNICAL PROPOSAL FOR A MIP TIMING DETECTOR IN THE CMS EXPERIMENT PHASE 2 UPGRADE*, Tech. Rep. CERN-LHCC-2017-027. LHCC-P-009, CERN, Geneva (Dec, 2017).

[142] LHCb Collaboration collaboration, *Expression of Interest for a Phase-II LHCb Upgrade: Opportunities in flavour physics, and beyond, in the HL-LHC era*, Tech. Rep. CERN-LHCC-2017-003, CERN, Geneva (Feb, 2017).

[143] CMS collaboration, *Search for long-lived particles using nonprompt jets and missing transverse momentum with proton-proton collisions at* $\sqrt{s} = 13$ *TeV*, *Phys. Lett. B* **797** (2019) 134876 [`1906.06441`].

[144] G.P. Salam, *Towards Jetography*, *Eur. Phys. J. C* **67** (2010) 637 [`0906.1833`].

[145] CMS collaboration, C. Collaboartion, *Cms tracking pog performance plots for 2017 with phase i pixel detector*, May, 2017.

[146] M. Cacciari, G.P. Salam and G. Soyez, *The Catchment Area of Jets*, *JHEP* **04** (2008) 005 [`0802.1188`].

[147] D. Krohn, J. Thaler and L.-T. Wang, *Jets with Variable R*, *JHEP* **06** (2009) 059 [`0903.0392`].

[148] T. Sjöstrand, S. Ask, J.R. Christiansen, R. Corke, N. Desai, P. Ilten et al., *An introduction to PYTHIA 8.2*, *Comput. Phys. Commun.* **191** (2015) 159 [`1410.3012`].

[149] M. Cacciari, G.P. Salam and G. Soyez, *The anti-k_t jet clustering algorithm*, *JHEP* **04** (2008) 063 [`0802.1189`].

[150] M. Cacciari, G.P. Salam and G. Soyez, *FastJet User Manual*, *Eur. Phys. J. C* **72** (2012) 1896 [`1111.6097`].

[151] CMS collaboration, *CMS, the Compact Muon Solenoid: Technical proposal*, .

[152] ATLAS Collaboration collaboration, *ATLAS: technical proposal for a general-purpose pp experiment at the Large Hadron Collider at CERN*, LHC technical proposal, CERN, Geneva (1994).

[153] CMS collaboration, *A MIP Timing Detector for the CMS Phase-2 Upgrade*, .

[154] CMS collaboration, *Particle-flow reconstruction and global event description with the CMS detector*, *JINST* **12** (2017) P10003 [`1706.04965`].

[155] D. Krohn, J. Thaler and L.-T. Wang, *Jet Trimming*, *JHEP* **02** (2010) 084 [`0912.1342`].

[156] D. Krohn, M.D. Schwartz, M. Low and L.-T. Wang, *Jet Cleansing: Pileup Removal at High Luminosity*, *Phys. Rev. D* **90** (2014) 065020 [`1309.4777`].

[157] P. Berta, M. Spousta, D.W. Miller and R. Leitner, *Particle-level pileup subtraction for jets and jet shapes*, *JHEP* **06** (2014) 092 [`1403.3108`].

[158] D. Bertolini, P. Harris, M. Low and N. Tran, *Pileup Per Particle Identification*, *JHEP* **10** (2014) 059 [`1407.6013`].

[159] M. Cacciari, G.P. Salam and G. Soyez, *SoftKiller, a particle-level pileup removal method*, *Eur. Phys. J. C* **75** (2015) 59 [`1407.0408`].

[160] P.T. Komiske, E.M. Metodiev, B. Nachman and M.D. Schwartz, *Pileup Mitigation with Machine Learning (PUMML)*, *JHEP* **12** (2017) 051 [`1707.08600`].

[161] Tommaso Dorigo.

[162] C.-T. Lu, L. Wu, Y. Wu and B. Zhu, *Electroweak Precision Fit and New Physics in light of W Boson Mass*, `2204.03796`.

[163] L. Di Luzio, R. Gröber and P. Paradisi, *Higgs physics confronts the M_W anomaly*, `2204.05284`.

[164] H. Song, W. Su and M. Zhang, *Electroweak Phase Transition in 2HDM under Higgs, Z-pole, and W precision measurements*, `2204.05085`.

[165] K. Sakurai, F. Takahashi and W. Yin, *Singlet extensions and W boson mass in the light of the CDF II result*, `2204.04770`.

[166] Y. Cheng, X.-G. He, Z.-L. Huang and M.-W. Li, *Type-II seesaw triplet scalar effects on neutrino trident scattering*, *Phys. Lett. B* **831** (2022) 137218 [`2204.05031`].

[167] H. Bahl, J. Braathen and G. Weiglein, *New physics effects on the W-boson mass from a doublet extension of the SM Higgs sector*, `2204.05269`.

[168] Y. Heo, D.-W. Jung and J.S. Lee, *Impact of the CDF W-mass anomaly on two Higgs doublet model*, `2204.05728`.

[169] T. Biekötter, S. Heinemeyer and G. Weiglein, *Excesses in the low-mass Higgs-boson search and the W-boson mass measurement*, `2204.05975`.

[170] X.K. Du, Z. Li, F. Wang and Y.K. Zhang, *Explaining The New CDF II W-Boson Mass Data In The Georgi-Machacek Extension Models*, `2204.05760`.

[171] X.-F. Han, F. Wang, L. Wang, J.M. Yang and Y. Zhang, *A joint explanation of W-mass and muon g-2 in 2HDM*, `2204.06505`.

[172] Y.H. Ahn, S.K. Kang and R. Ramos, *Implications of New CDF-II W Boson Mass on Two Higgs Doublet Model*, `2204.06485`.

[173] P. Fileviez Perez, H.H. Patel and A.D. Plascencia, *On the W-mass and New Higgs Bosons*, `2204.07144`.

[174] A. Ghoshal, N. Okada, S. Okada, D. Raut, Q. Shafi and A. Thapa, *Type III seesaw with R-parity violation in light of m_W (CDF)*, `2204.07138`.

[175] S. Kanemura and K. Yagyu, *Implication of the W boson mass anomaly at CDF II in the Higgs triplet model with a mass difference*, *Phys. Lett. B* **831** (2022) 137217 [`2204.07511`].

[176] O. Popov and R. Srivastava, *The Triplet Dirac Seesaw in the View of the Recent CDF-II W Mass Anomaly*, `2204.08568`.

[177] G. Arcadi and A. Djouadi, *The 2HD+a model for a combined explanation of the possible excesses in the CDF $\mathbf{M_W}$ measurement and $(\mathbf{g-2})_\mu$ with Dark Matter*, `2204.08406`.

[178] K. Ghorbani and P. Ghorbani, *W-Boson Mass Anomaly from Scale Invariant 2HDM*, `2204.09001`.

[179] S. Lee, K. Cheung, J. Kim, C.-T. Lu and J. Song, *Status of the two-Higgs-doublet model in light of the CDF m_W measurement*, `2204.10338`.

[180] J. Heeck, *W-boson mass in the triplet seesaw model*, `2204.10274`.

[181] H. Abouabid, A. Arhrib, R. Benbrik, M. Krab and M. Ouchemhou, *Is the new CDF M_W measurement consistent with the two higgs doublet model?*, `2204.12018`.

[182] R. Benbrik, M. Boukidi and B. Manaut, *W-mass and 96 GeV excess in type-III 2HDM*, `2204.11755`.

[183] J. Kim, S. Lee, P. Sanyal and J. Song, *CDF W boson mass and muon $g-2$ in type-X two-Higgs-doublet model with a Higgs-phobic light pseudoscalar*, `2205.01701`.

[184] O. Atkinson, M. Black, C. Englert, A. Lenz and A. Rusov, *MUonE, muon $g-2$ and electroweak precision constraints within 2HDMs*, `2207.02789`.

[185] A. Strumia, *Interpreting electroweak precision data including the W-mass CDF anomaly*, `2204.04191`.

[186] J. de Blas, M. Pierini, L. Reina and L. Silvestrini, *Impact of the recent measurements of the top-quark and W-boson masses on electroweak precision fits*, `2204.04204`.

[187] J.M. Yang and Y. Zhang, *Low energy SUSY confronted with new measurements of W-boson mass and muon g-2*, `2204.04202`.

[188] G.-W. Yuan, L. Zu, L. Feng, Y.-F. Cai and Y.-Z. Fan, *Hint on new physics from the W-boson mass excess—axion-like particle, dark photon or Chameleon dark energy*, `2204.04183`.

[189] P. Athron, A. Fowlie, C.-T. Lu, L. Wu, Y. Wu and B. Zhu, *The W boson Mass and Muon $g-2$: Hadronic Uncertainties or New Physics?*, `2204.03996`.

[190] Y.-Z. Fan, T.-P. Tang, Y.-L.S. Tsai and L. Wu, *Inert Higgs Dark Matter for New CDF W-boson Mass and Detection Prospects*, `2204.03693`.

[191] K.S. Babu, S. Jana and V.P. K., *Correlating W-Boson Mass Shift with Muon $g-2$ in the 2HDM*, `2204.05303`.

[192] J.J. Heckman, *Extra W-Boson Mass from a D3-Brane*, `2204.05302`.

[193] J. Gu, Z. Liu, T. Ma and J. Shu, *Speculations on the W-Mass Measurement at CDF*, `2204.05296`.

[194] P. Athron, M. Bach, D.H.J. Jacob, W. Kotlarski, D. Stöckinger and A. Voigt, *Precise calculation of the W boson pole mass beyond the Standard Model with FlexibleSUSY*, `2204.05285`.

[195] P. Asadi, C. Cesarotti, K. Fraser, S. Homiller and A. Parikh, *Oblique Lessons from the W Mass Measurement at CDF II*, `2204.05283`.

[196] A. Paul and M. Valli, *Violation of custodial symmetry from W-boson mass measurements*, `2204.05267`.

[197] E. Bagnaschi, J. Ellis, M. Madigan, K. Mimasu, V. Sanz and T. You, *SMEFT Analysis of m_W*, `2204.05260`.

[198] H.M. Lee and K. Yamashita, *A Model of Vector-like Leptons for the Muon $g-2$ and the W Boson Mass*, `2204.05024`.

[199] X. Liu, S.-Y. Guo, B. Zhu and Y. Li, *Unifying gravitational waves with W boson, FIMP dark matter, and Majorana Seesaw mechanism*, `2204.04834`.

[200] J. Fan, L. Li, T. Liu and K.-F. Lyu, *W-Boson Mass, Electroweak Precision Tests and SMEFT*, `2204.04805`.

[201] R. Balkin, E. Madge, T. Menzo, G. Perez, Y. Soreq and J. Zupan, *On the implications of positive W mass shift*, *JHEP* **05** (2022) 133 [`2204.05992`].

[202] M. Endo and S. Mishima, *New physics interpretation of W-boson mass anomaly*, `2204.05965`.

[203] A. Crivellin, M. Kirk, T. Kitahara and F. Mescia, *Correlating $t \to cZ$ to the W Mass and B Physics with Vector-Like Quarks*, `2204.05962`.

[204] M. Blennow, P. Coloma, E. Fernández-Martínez and M. González-López, *Right-handed neutrinos and the CDF II anomaly*, `2204.04559`.

[205] G. Cacciapaglia and F. Sannino, *The W boson mass weighs in on the non-standard Higgs*, *Phys. Lett. B* **832** (2022) 137232 [`2204.04514`].

[206] T.-P. Tang, M. Abdughani, L. Feng, Y.-L.S. Tsai, J. Wu and Y.-Z. Fan, *NMSSM neutralino dark matter for W-boson mass and muon $g-2$ and the promising prospect of direct detection*, `2204.04356`.

[207] C.-R. Zhu, M.-Y. Cui, Z.-Q. Xia, Z.-H. Yu, X. Huang, Q. Yuan et al., *GeV antiproton/gamma-ray excesses and the W-boson mass anomaly: three faces of $\sim 60-70$ GeV dark matter particle?*, `2204.03767`.

[208] M.-D. Zheng, F.-Z. Chen and H.-H. Zhang, *The $W\ell\nu$-vertex corrections to W-boson mass in the R-parity violating MSSM*, `2204.06541`.

[209] N.V. Krasnikov, *Nonlocal generalization of the SM as an explanation of recent CDF result*, `2204.06327`.

[210] F. Arias-Aragón, E. Fernández-Martínez, M. González-López and L. Merlo, *Dynamical Minimal Flavour Violating Inverse Seesaw*, `2204.04672`.

[211] X.K. Du, Z. Li, F. Wang and Y.K. Zhang, *Explaining The Muon $g-2$ Anomaly and New CDF II W-Boson Mass in the Framework of (Extra)Ordinary Gauge Mediation*, `2204.04286`.

[212] J. Kawamura, S. Okawa and Y. Omura, *W boson mass and muon $g-2$ in a lepton portal dark matter model*, `2204.07022`.

[213] K.I. Nagao, T. Nomura and H. Okada, *A model explaining the new CDF II W boson mass linking to muon $g-2$ and dark matter*, `2204.07411`.

[214] K.-Y. Zhang and W.-Z. Feng, *Explaining W boson mass anomaly and dark matter with a $U(1)$ dark sector*, `2204.08067`.

[215] L.M. Carpenter, T. Murphy and M.J. Smylie, *Changing patterns in electroweak precision with new color-charged states: Oblique corrections and the W boson mass*, `2204.08546`.

[216] G. Senjanović and M. Zantedeschi, *$SU(5)$ grand unification and W-boson mass*, `2205.05022`.

[217] T.A. Chowdhury, J. Heeck, S. Saad and A. Thapa, *W boson mass shift and muon magnetic moment in the Zee model*, `2204.08390`.

[218] D. Borah, S. Mahapatra, D. Nanda and N. Sahu, *Type II Dirac Seesaw with Observable* ΔN_{eff} *in the light of W-mass Anomaly*, `2204.08266`.

[219] Y.-P. Zeng, C. Cai, Y.-H. Su and H.-H. Zhang, *Extra boson mix with Z boson explaining the mass of W boson*, `2204.09487`.

[220] M. Du, Z. Liu and P. Nath, *CDF W mass anomaly from a dark sector with a Stueckelberg-Higgs portal*, `2204.09024`.

[221] A. Bhaskar, A.A. Madathil, T. Mandal and S. Mitra, *Combined explanation of W-mass, muon* $g-2$*,* $R_{K^{(*)}}$ *and* $R_{D^{(*)}}$ *anomalies in a singlet-triplet scalar leptoquark model*, `2204.09031`.

[222] S. Baek, *Implications of CDF W-mass and* $(g-2)_\mu$ *on* $U(1)_{L_\mu - L_\tau}$ *model*, `2204.09585`.

[223] J. Cao, L. Meng, L. Shang, S. Wang and B. Yang, *Interpreting the W mass anomaly in the vectorlike quark models*, `2204.09477`.

[224] D. Borah, S. Mahapatra and N. Sahu, *Singlet-doublet fermion origin of dark matter, neutrino mass and W-mass anomaly*, *Phys. Lett. B* **831** (2022) 137196 [`2204.09671`].

[225] A. Batra, S. K. A., S. Mandal and R. Srivastava, *W boson mass in Singlet-Triplet Scotogenic dark matter model*, `2204.09376`.

[226] E.d.S. Almeida, A. Alves, O.J.P. Eboli and M.C. Gonzalez-Garcia, *Impact of CDF-II measurement of* M_W *on the electroweak legacy of the LHC Run II*, `2204.10130`.

[227] Y. Cheng, X.-G. He, F. Huang, J. Sun and Z.-P. Xing, *Dark photon kinetic mixing effects for CDF W mass excess*, `2204.10156`.

[228] A. Batra, S.K. A, S. Mandal, H. Prajapati and R. Srivastava, *CDF-II W Boson Mass Anomaly in the Canonical Scotogenic Neutrino-Dark Matter Model*, `2204.11945`.

[229] C. Cai, D. Qiu, Y.-L. Tang, Z.-H. Yu and H.-H. Zhang, *Corrections to electroweak precision observables from mixings of an exotic vector boson in light of the CDF W-mass anomaly*, `2204.11570`.

[230] Q. Zhou and X.-F. Han, *The CDF W-mass, muon g-2, and dark matter in a* $U(1)_{L_\mu - L_\tau}$ *model with vector-like leptons*, `2204.13027`.

[231] R.S. Gupta, *Running away from the T-parameter solution to the W mass anomaly*, `2204.13690`.

[232] J.-W. Wang, X.-J. Bi, P.-F. Yin and Z.-H. Yu, *Electroweak dark matter model accounting for the CDF W-mass anomaly*, `2205.00783`.

[233] B. Barman, A. Das and S. Sengupta, *New W-Boson mass in the light of doubly warped braneworld model*, `2205.01699`.

[234] J. Kim, *Compatibility of muon g-2, W mass anomaly in type-X 2HDM*, *Phys. Lett. B* **832** (2022) 137220 [`2205.01437`].

[235] R. Dcruz and A. Thapa, *W boson mass, dark matter and $(g-2)_\ell$ in ScotoZee neutrino mass model*, `2205.02217`.

[236] J. Isaacson, Y. Fu and C.P. Yuan, *ResBos2 and the CDF W Mass Measurement*, `2205.02788`.

[237] T.A. Chowdhury and S. Saad, *Leptoquark-vectorlike quark model for m_W (CDF), $(g-2)_\mu$, $R_{K^{(*)}}$ anomalies and neutrino mass*, `2205.03917`.

[238] S.-S. Kim, H.M. Lee, A.G. Menkara and K. Yamashita, *The $SU(2)_D$ lepton portals for muon $g-2$, W boson mass and dark matter*, `2205.04016`.

[239] J. Gao, D. Liu and K. Xie, *Understanding PDF uncertainty on the W boson mass measurements in CT18 global analysis*, `2205.03942`.

[240] G. Lazarides, R. Maji, R. Roshan and Q. Shafi, *Heavier W-boson, dark matter and gravitational waves from strings in an SO(10) axion model*, `2205.04824`.

[241] T.G. Rizzo, *Kinetic Mixing, Dark Higgs Triplets, M_W and All That*, `2206.09814`.

[242] D. Van Loi and P. Van Dong, *Novel effects of the W-boson mass shift in the 3-3-1 model*, `2206.10100`.

[243] S. Yaser Ayazi and M. Hosseini, *W boson mass anomaly and vacuum structure in vector dark matter model with a singlet scalar mediator*, `2206.11041`.

[244] N. Chakrabarty, *The muon $g-2$ and W-mass anomalies explained and the electroweak vacuum stabilised by extending the minimal Type-II seesaw*, `2206.11771`.

[245] S. Centelles Chuliá, R. Srivastava and S. Yadav, *CDF-II W boson mass in the Dirac Scotogenic model*, `2206.11903`.

[246] K.I. Nagao, T. Nomura and H. Okada, *An alternative gauged $U(1)_R$ symmetric model in light of the CDF II W boson mass anomaly*, `2206.15256`.

[247] M. Aoki, S. Kanemura, M. Kikuchi and K. Yagyu, *Radiative corrections to the Higgs boson couplings in the triplet model*, *Phys. Rev. D* **87** (2013) 015012 [`1211.6029`].

[248] M. Bohm, A. Denner and H. Joos, *Gauge theories of the strong and electroweak interaction* (2001), 10.1007/978-3-322-80160-9.

[249] S. Hessenberger, *Two-loop corrections to electroweak precision observables in Two-Higgs-Doublet-Models*, Ph.D. thesis, Munich, Tech. U., 2018.

[250] M. Awramik, M. Czakon, A. Freitas and G. Weiglein, *Precise prediction for the W boson mass in the standard model*, *Phys. Rev. D* **69** (2004) 053006 [`hep-ph/0311148`].

[251] M. Awramik, M. Czakon and A. Freitas, *Electroweak two-loop corrections to the effective weak mixing angle*, *JHEP* **11** (2006) 048 [`hep-ph/0608099`].

[252] P. Bechtle, S. Heinemeyer, O. Stål, T. Stefaniak and G. Weiglein, *HiggsSignals: Confronting arbitrary Higgs sectors with measurements at the Tevatron and the LHC*, *Eur. Phys. J. C* **74** (2014) 2711 [`1305.1933`].

[253] P. Bechtle, S. Heinemeyer, T. Klingl, T. Stefaniak, G. Weiglein and J. Wittbrodt, *HiggsSignals-2: Probing new physics with precision Higgs measurements in the LHC 13 TeV era*, *Eur. Phys. J. C* **81** (2021) 145 [`2012.09197`].

[254] H. Bahl, J. Braathen and G. Weiglein, *New constraints on extended Higgs sectors from the trilinear Higgs coupling*, `2202.03453`.

[255] T. Hahn, *Generating Feynman diagrams and amplitudes with FeynArts 3*, *Comput. Phys. Commun.* **140** (2001) 418 [`hep-ph/0012260`].

[256] T. Hahn and M. Perez-Victoria, *Automatized one loop calculations in four-dimensions and D-dimensions*, *Comput. Phys. Commun.* **118** (1999) 153 [`hep-ph/9807565`].

[257] N.D. Christensen and C. Duhr, *FeynRules - Feynman rules made easy*, *Comput. Phys. Commun.* **180** (2009) 1614 [`0806.4194`].

[258] ATLAS collaboration, *Combination of searches for non-resonant and resonant Higgs boson pair production in the $b\bar{b}\gamma\gamma$, $b\bar{b}\tau^+\tau^-$ and $b\bar{b}b\bar{b}$ decay channels using pp collisions at $\sqrt{s} = 13$ TeV with the ATLAS detector*, .

[259] ATLAS collaboration, *Combined measurements of Higgs boson production and decay using up to 80 fb^{-1} of proton-proton collision data at $\sqrt{s} = 13$ TeV collected with the ATLAS experiment*, *Phys. Rev. D* **101** (2020) 012002 [`1909.02845`].

[260] CMS collaboration, *Combined measurements of Higgs boson couplings in proton–proton collisions at $\sqrt{s} = 13$ TeV*, *Eur. Phys. J. C* **79** (2019) 421 [`1809.10733`].

[261] B. Fuks, M. Nemevšek and R. Ruiz, *Doubly Charged Higgs Boson Production at Hadron Colliders*, *Phys. Rev. D* **101** (2020) 075022 [`1912.08975`].

[262] D. Dercks, N. Desai, J.S. Kim, K. Rolbiecki, J. Tattersall and T. Weber, *CheckMATE 2: From the model to the limit*, *Comput. Phys. Commun.* **221** (2017) 383 [`1611.09856`].

[263] DELPHES 3 collaboration, *DELPHES 3, A modular framework for fast simulation of a generic collider experiment*, *JHEP* **02** (2014) 057 [`1307.6346`].

[264] M. Cacciari and G.P. Salam, *Dispelling the N^3 myth for the k_t jet-finder*, *Phys. Lett. B* **641** (2006) 57 [`hep-ph/0512210`].

[265] A.L. Read, *Presentation of search results: The CL(s) technique*, *J. Phys. G* **28** (2002) 2693.

[266] CMS collaboration, *Search for electroweak production of charginos and neutralinos in multilepton final states in proton-proton collisions at $\sqrt{s} = 13$ TeV*, *JHEP* **03** (2018) 166 [`1709.05406`].

[267] ATLAS collaboration, *Search for doubly charged scalar bosons decaying into same-sign W boson pairs with the ATLAS detector*, *Eur. Phys. J. C* **79** (2019) 58 [`1808.01899`].

[268] ATLAS collaboration, *Search for doubly and singly charged Higgs bosons decaying into vector bosons in multi-lepton final states with the ATLAS detector using proton-proton collisions at* $\sqrt{\mathrm{s}} = 13$ *TeV*, *JHEP* **06** (2021) 146 [`2101.11961`].

[269] S. Kanemura, M. Kikuchi, H. Yokoya and K. Yagyu, *LHC Run-I constraint on the mass of doubly charged Higgs bosons in the same-sign diboson decay scenario*, *PTEP* **2015** (2015) 051B02 [`1412.7603`].

[270] ATLAS collaboration, *Search for R-parity-violating supersymmetry in a final state containing leptons and many jets with the ATLAS experiment using* $\sqrt{s} = 13TeV$ *proton–proton collision data*, *Eur. Phys. J. C* **81** (2021) 1023 [`2106.09609`].

[271] ATLAS collaboration, *A strategy for a general search for new phenomena using data-derived signal regions and its application within the ATLAS experiment*, *Eur. Phys. J. C* **79** (2019) 120 [`1807.07447`].

[272] ATLAS collaboration, *Search for heavy long-lived multi-charged particles in the full Run-II pp collision data at* $\sqrt{s} = 13$ *TeV using the ATLAS detector*, .

[273] W.H. Chiu, Z. Liu, M. Low and L.-T. Wang, *Jet timing*, *JHEP* **01** (2022) 014 [`2109.01682`].

[274] ATLAS collaboration, *Search for heavy, long-lived, charged particles with large ionisation energy loss in pp collisions at* $\sqrt{s} = 13$ *TeV using the ATLAS experiment and the full Run 2 dataset*, `2205.06013`.

[275] G.F. Giudice, M. McCullough and D. Teresi, *dE/dx from boosted long-lived particles*, `2205.04473`.

[276] ATLAS collaboration, *Search for neutral long-lived particles in pp collisions at* $\sqrt{s} = 13$ *TeV that decay into displaced hadronic jets in the ATLAS calorimeter*, *JHEP* **06** (2022) 005 [`2203.01009`].

[277] C. Arina, J. Heisig, F. Maltoni, D. Massaro and O. Mattelaer, *Indirect dark-matter detection with MadDM v3.2 – Lines and Loops*, `2107.04598`.

[278] S. Ando and K. Ishiwata, *Constraints on decaying dark matter from the extragalactic gamma-ray background*, *JCAP* **05** (2015) 024 [`1502.02007`].

[279] T. Cohen, K. Murase, N.L. Rodd, B.R. Safdi and Y. Soreq, γ *-ray Constraints on Decaying Dark Matter and Implications for IceCube*, *Phys. Rev. Lett.* **119** (2017) 021102 [`1612.05638`].

[280] W. Liu, X.-J. Bi, S.-J. Lin and P.-F. Yin, *Constraints on dark matter annihilation and decay from the isotropic gamma-ray background*, *Chin. Phys. C* **41** (2017) 045104 [`1602.01012`].

[281] V. Poulin and P.D. Serpico, *Nonuniversal BBN bounds on electromagnetically decaying particles*, *Phys. Rev. D* **91** (2015) 103007 [`1503.04852`].

[282] T.R. Slatyer and C.-L. Wu, *General Constraints on Dark Matter Decay from the Cosmic Microwave Background*, *Phys. Rev. D* **95** (2017) 023010 [`1610.06933`].

[283] V. Poulin, J. Lesgourgues and P.D. Serpico, *Cosmological constraints on exotic injection of electromagnetic energy*, *JCAP* **03** (2017) 043 [`1610.10051`].

[284] J. Chluba, A. Ravenni and S.K. Acharya, *Thermalization of large energy release in the early Universe*, *Mon. Not. Roy. Astron. Soc.* **498** (2020) 959 [`2005.11325`].

[285] A. Sirlin, *Radiative Corrections in the SU(2)-L x U(1) Theory: A Simple Renormalization Framework*, *Phys. Rev. D* **22** (1980) 971.

[286] W.J. Marciano and A. Sirlin, *Radiative Corrections to Neutrino Induced Neutral Current Phenomena in the SU(2)-L x U(1) Theory*, *Phys. Rev. D* **22** (1980) 2695.

[287] A. Djouadi and C. Verzegnassi, *Virtual Very Heavy Top Effects in LEP / SLC Precision Measurements*, *Phys. Lett. B* **195** (1987) 265.

[288] A. Djouadi, *O(alpha alpha-s) Vacuum Polarization Functions of the Standard Model Gauge Bosons*, *Nuovo Cim. A* **100** (1988) 357.

[289] B.A. Kniehl, *Two Loop Corrections to the Vacuum Polarizations in Perturbative QCD*, *Nucl. Phys. B* **347** (1990) 86.

[290] F. Halzen and B.A. Kniehl, *Δ r beyond one loop*, *Nucl. Phys. B* **353** (1991) 567.

[291] B.A. Kniehl and A. Sirlin, *Dispersion relations for vacuum polarization functions in electroweak physics*, *Nucl. Phys. B* **371** (1992) 141.

[292] B.A. Kniehl and A. Sirlin, *On the effect of the $t\bar{t}$ threshold on electroweak parameters*, *Phys. Rev. D* **47** (1993) 883.

[293] F. Halzen, B.A. Kniehl and M.L. Stong, *Two loop electroweak parameters*, *Z. Phys. C* **58** (1993) 119.

[294] A. Freitas, W. Hollik, W. Walter and G. Weiglein, *Complete fermionic two loop results for the M(W) - M(Z) interdependence*, *Phys. Lett. B* **495** (2000) 338 [`hep-ph/0007091`].

[295] A. Freitas, W. Hollik, W. Walter and G. Weiglein, *Electroweak two loop corrections to the $M_W - M_Z$ mass correlation in the standard model*, *Nucl. Phys. B* **632** (2002) 189 [`hep-ph/0202131`].

[296] M. Awramik and M. Czakon, *Complete two loop bosonic contributions to the muon lifetime in the standard model*, *Phys. Rev. Lett.* **89** (2002) 241801 [`hep-ph/0208113`].

[297] M. Awramik and M. Czakon, *Complete two loop electroweak contributions to the muon lifetime in the standard model*, *Phys. Lett. B* **568** (2003) 48 [`hep-ph/0305248`].

[298] A. Onishchenko and O. Veretin, *Two loop bosonic electroweak corrections to the muon lifetime and M(Z) - M(W) interdependence*, *Phys. Lett. B* **551** (2003) 111 [`hep-ph/0209010`].

[299] M. Awramik, M. Czakon, A. Onishchenko and O. Veretin, *Bosonic corrections to Delta r at the two loop level*, *Phys. Rev. D* **68** (2003) 053004 [`hep-ph/0209084`].

[300] S. Bauberger and G. Weiglein, *Calculation of two loop top quark and Higgs boson corrections in the electroweak standard model*, *Nucl. Instrum. Meth. A* **389** (1997) 318 [`hep-ph/9611445`].

[301] S. Bauberger and G. Weiglein, *Higgs mass dependence of two loop corrections to* δ *r*, *Phys. Lett. B* **419** (1998) 333 [`hep-ph/9707510`].

[302] L. Avdeev, J. Fleischer, S. Mikhailov and O. Tarasov, $0(\alpha\alpha_s^2)$ *correction to the electroweak* ρ *parameter*, *Phys. Lett. B* **336** (1994) 560 [`hep-ph/9406363`].

[303] K.G. Chetyrkin, J.H. Kuhn and M. Steinhauser, *Corrections of order* $\mathcal{O}(G_F M_t^2 \alpha_s^2)$ *to the* ρ *parameter*, *Phys. Lett. B* **351** (1995) 331 [`hep-ph/9502291`].

[304] K.G. Chetyrkin, J.H. Kuhn and M. Steinhauser, *QCD corrections from top quark to relations between electroweak parameters to order alpha-s**2*, *Phys. Rev. Lett.* **75** (1995) 3394 [`hep-ph/9504413`].

[305] K.G. Chetyrkin, J.H. Kuhn and M. Steinhauser, *Three loop polarization function and O (alpha-s**2) corrections to the production of heavy quarks*, *Nucl. Phys. B* **482** (1996) 213 [`hep-ph/9606230`].

[306] M. Faisst, J.H. Kuhn, T. Seidensticker and O. Veretin, *Three loop top quark contributions to the rho parameter*, *Nucl. Phys. B* **665** (2003) 649 [`hep-ph/0302275`].

[307] J.J. van der Bij, K.G. Chetyrkin, M. Faisst, G. Jikia and T. Seidensticker, *Three loop leading top mass contributions to the rho parameter*, *Phys. Lett. B* **498** (2001) 156 [`hep-ph/0011373`].

[308] R. Boughezal, J.B. Tausk and J.J. van der Bij, *Three-loop electroweak correction to the Rho parameter in the large Higgs mass limit*, *Nucl. Phys. B* **713** (2005) 278 [`hep-ph/0410216`].

[309] Y. Schroder and M. Steinhauser, *Four-loop singlet contribution to the rho parameter*, *Phys. Lett. B* **622** (2005) 124 [`hep-ph/0504055`].

[310] K.G. Chetyrkin, M. Faisst, J.H. Kuhn, P. Maierhofer and C. Sturm, *Four-Loop QCD Corrections to the Rho Parameter*, *Phys. Rev. Lett.* **97** (2006) 102003 [`hep-ph/0605201`].

[311] R. Boughezal and M. Czakon, *Single scale tadpoles and O(G(F m(t)**2 alpha(s)**3)) corrections to the rho parameter*, *Nucl. Phys. B* **755** (2006) 221 [`hep-ph/0606232`].

[312] A. Djouadi and P. Gambino, *Electroweak gauge bosons selfenergies: Complete QCD corrections*, *Phys. Rev. D* **49** (1994) 3499 [`hep-ph/9309298`].

[313] A. Arhrib, R. Benbrik, M. Chabab, G. Moultaka, M.C. Peyranere, L. Rahili et al., *The Higgs Potential in the Type II Seesaw Model*, *Phys. Rev. D* **84** (2011) 095005 [`1105.1925`].

[314] K.-M. Lee and E.J. Weinberg, *TUNNELING WITHOUT BARRIERS*, *Nucl. Phys. B* **267** (1986) 181.

[315] W.G. Hollik, G. Weiglein and J. Wittbrodt, *Impact of Vacuum Stability Constraints on the Phenomenology of Supersymmetric Models*, *JHEP* **03** (2019) 109 [`1812.04644`].

[316] J. Wittbrodt, *Exploring Models of Electroweak Symmetry Breaking at the LHC and Beyond*, Ph.D. thesis, Hamburg U., Hamburg, 2019. 10.3204/PUBDB-2019-03809.

[317] M. Battaglieri et al., *US Cosmic Visions: New Ideas in Dark Matter 2017: Community Report*, in *U.S. Cosmic Visions: New Ideas in Dark Matter*, 7, 2017 [`1707.04591`].

[318] J. Alexander et al., *Dark Sectors 2016 Workshop: Community Report*, 8, 2016 [`1608.08632`].

[319] J. McDonald, *Thermally generated gauge singlet scalars as selfinteracting dark matter*, *Phys. Rev. Lett.* **88** (2002) 091304 [`hep-ph/0106249`].

[320] L.J. Hall, K. Jedamzik, J. March-Russell and S.M. West, *Freeze-In Production of FIMP Dark Matter*, *JHEP* **03** (2010) 080 [`0911.1120`].

[321] S. Hong, G. Kurup and M. Perelstein, *Conformal Freeze-In of Dark Matter*, *Phys. Rev. D* **101** (2020) 095037 [`1910.10160`].

[322] S. Hong, G. Kurup and M. Perelstein, *Dark Matter from a Conformal Dark Sector*, `2207.10093`.

[323] W.D. Goldberger and M.B. Wise, *Modulus stabilization with bulk fields*, *Phys. Rev. Lett.* **83** (1999) 4922 [`hep-ph/9907447`].

[324] N. Arkani-Hamed, M. Porrati and L. Randall, *Holography and phenomenology*, *JHEP* **08** (2001) 017 [`hep-th/0012148`].

[325] R. Rattazzi and A. Zaffaroni, *Comments on the holographic picture of the Randall-Sundrum model*, *JHEP* **04** (2001) 021 [`hep-th/0012248`].

[326] K. Agashe, P. Du, S. Hong and R. Sundrum, *Flavor Universal Resonances and Warped Gravity*, *JHEP* **01** (2017) 016 [`1608.00526`].

[327] R. Contino, *The Higgs as a Composite Nambu-Goldstone Boson*, in *Theoretical Advanced Study Institute in Elementary Particle Physics: Physics of the Large and the Small*, pp. 235–306, 2011, DOI [`1005.4269`].

[328] K. Agashe, S. Hong and L. Vecchi, *Warped seesaw mechanism is physically inverted*, *Phys. Rev. D* **94** (2016) 013001 [`1512.06742`].

[329] C. Dvorkin, T. Lin and K. Schutz, *Making dark matter out of light: freeze-in from plasma effects*, *Phys. Rev. D* **99** (2019) 115009 [`1902.08623`].

[330] V. Iršič et al., *New Constraints on the free-streaming of warm dark matter from intermediate and small scale Lyman-α forest data*, *Phys. Rev. D* **96** (2017) 023522 [`1702.01764`].

[331] A. Berlin, N. Blinov, G. Krnjaic, P. Schuster and N. Toro, *Dark Matter, Millicharges, Axion and Scalar Particles, Gauge Bosons, and Other New Physics with LDMX*, *Phys. Rev. D* **99** (2019) 075001 [`1807.01730`].

[332] J. Kaplan, *Lectures on AdS/CFT from the Bottom Up*, `2207.10093`.

[333] L. Randall and R. Sundrum, *A Large mass hierarchy from a small extra dimension*, *Phys. Rev. Lett.* **83** (1999) 3370 [`hep-ph/9905221`].

[334] L. Randall and R. Sundrum, *An Alternative to compactification*, *Phys. Rev. Lett.* **83** (1999) 4690 [`hep-th/9906064`].

[335] K.S. Agashe, J. Collins, P. Du, S. Hong, D. Kim and R.K. Mishra, *LHC Signals from Cascade Decays of Warped Vector Resonances*, *JHEP* **05** (2017) 078 [`1612.00047`].

[336] K. Agashe, J.H. Collins, P. Du, S. Hong, D. Kim and R.K. Mishra, *Dedicated Strategies for Triboson Signals from Cascade Decays of Vector Resonances*, *Phys. Rev. D* **99** (2019) 075016 [`1711.09920`].

[337] K. Agashe, J.H. Collins, P. Du, S. Hong, D. Kim and R.K. Mishra, *Detecting a Boosted Diboson Resonance*, *JHEP* **11** (2018) 027 [`1809.07334`].

[338] K. Agashe, M. Ekhterachian, D. Kim and D. Sathyan, *LHC Signals for KK Graviton from an Extended Warped Extra Dimension*, *JHEP* **11** (2020) 109 [`2008.06480`].

[339] R. Contino, T. Kramer, M. Son and R. Sundrum, *Warped/composite phenomenology simplified*, *JHEP* **05** (2007) 074 [`hep-ph/0612180`].

[340] B. Grinstein, K.A. Intriligator and I.Z. Rothstein, *Comments on Unparticles*, *Phys. Lett. B* **662** (2008) 367 [`0801.1140`].

[341] G.G. Raffelt, *Stars as laboratories for fundamental physics: The astrophysics of neutrinos, axions, and other weakly interacting particles*, University of Chicago Press (5, 1996).

[342] J.H. Chang, R. Essig and S.D. McDermott, *Supernova 1987A Constraints on Sub-GeV Dark Sectors, Millicharged Particles, the QCD Axion, and an Axion-like Particle*, *JHEP* **09** (2018) 051 [`1803.00993`].